Development and Application of Quantitative Gradient-Echo MRI Techniques for Assessment of Iron and Myelin in the Multiple Sclerosis Brain

by

Ahmed Elkady

A thesis submitted in partial fulfillment of the requirements for the degree of

Doctor of Philosophy

Department of Biomedical Engineering

University of Alberta

Abstract

Multiple Sclerosis (MS) is a progressive autoimmune and neurodegenerative disease of the Central Nervous System that results in demyelination and neuronal/axonal loss. Along with clinical evaluation, Magnetic Resonance Imaging (MRI) is the gold standard modality for diagnosing and monitoring MS, which has been conventionally carried out using T1 and T2-weighted pulse sequences. Gradient-echo T2*-weighted has been recently demonstrated as a sensitive predictor of MS disability and cognitive decline; however, more research is needed to implement gradient-echo based techniques into clinical practice and drug trials. The purpose of this thesis was to develop technical MRI innovations and study research applications to further the field of quantitative gradient-echo MRI of MS. Although gradient-echo acquisitions are most sensitive to iron, myelin also contributes to image contrast. The main clinical hypothesis was that quantitative gradient-echo MRI methods may serve as a biomarker of disease progression by assessing iron and myelin in the MS brain. This hypothesis was tested in one cross-sectional study and two longitudinal studies of MS subjects compared to age-matched controls, where we related MRI findings to clinical outcomes.

Since lesions are the most commonly indicator in MS clinical monitoring, we have explored their shape and conspicuity in Quantitative Susceptibility (QS) and Local Field Shift (LFS) maps that have been quantified from multi-echo gradient echo acuistions in Chapter 2 using postmortem and in vivo MS subjects. We have demonstrated that the use of LFS and QS contrast for lesion iron detection is sensitive, but not sufficiently specific, while the use of lesion dipole signature is specific but not sufficiently sensitive.

Although QS mapping is widely used in MS studies, its adoption is still lagging in clinical practice and trials. We investigated the sensitivity of QS mapping to field of view (FOV) reduction in Chapter 3, with the aim of determining whether restricted-FOV acquisition would affect QS accuracy. We have demonstrated through theoretical simulations and in vivo data that QSM is sensitive to FOV reduction, which was most sensitive in the direction of the static magnetic field.

Increased R2* and QS values in MS patients compared to controls in cross-sectional studies has been previously interpreted as increased iron accumulation in MS DGM. However, previous histochemical evaluations have indicated that the MS DGM also suffers from demyelinating lesions. We have developed in Chapter 4 an analysis technique using combined R2* and QS and sparse logistic regression to discriminate iron accumulation from demyelination MS cross-sectional studies. We have demonstrated the increased statistical power of the developed technique compared to conventional singular R2*/QS analysis. We have also demonstrated that iron accumulation occurs progressively with advanced MS phenotypes.

In Chapter 5 we present a novel longitudinal analysis technique for Discriminative Analysis of Regional Evolution (DARE) of brain iron/myelin changes in MS. Application of DARE to 2-year Relapsing-Remitting MS (RRMS) and Progressive (PMS) data compared to age-matched controls revealed that iron changes are prominent over 2 years in RRMS, whereas myelin changes are prominent in PMS compared to age-matched controls. Similar to the developed sparse logistic regression technique, I have demonstrated the increased statistical power of DARE compared to singular use of R2* and QS. Iron increase in identified DARE regions demonstrated the highest correlation with disease severity ($r=0.68$; $Q=0.0005$) from amongst all studied parameters.

No longitudinal evaluation of the MS DGM over 5-years has been previously conducted. In Chapter 6, we analyze 5-year longitudinal changes in RRMS DGM compared to controls using DARE and conventional bulk structure analysis, and correlate the identified significant results to clinical measures. We demonstrate that iron decrease and myelin increase is the most DGM prominent change in RRMS compared to controls, which is somewhat similar to the behavior of 2-year PMS DGM data. Using Pearson's regression, we have also demonstrated that iron decrease in the caudate nucleus is linearly related with disease severity ($r = 0.64$; $Q = 0.03$), and myelin increase in the substantia nigra is linearly related with disease duration ($r = 0.49$; $Q = 0.008$).

In conclusion, this thesis has developed and applied novel analysis techniques using gradient-echo acquisitions, which has provided important insight about pathological changes of iron and myelin in the MS brain.

Preface

Written informed consent was obtained from all patient and control subjects included in this thesis after the internal Institutional Review Board approved the study design. For all the published and unpublished chapters in this thesis, Dr. Alan Wilman (supervisor) shared unique ideas, helpful discussion and careful editing of the manuscripts. In all cases first drafts were written by the author.

The second chapter has been presented as an oral presentation: Elkady AM, Sun H, Walsh AJ, Blevins G, Zhuozi D and Wilman AH. Quantitative Susceptibility Mapping of Lesions in Multiple Sclerosis. Abstract #0281. In: ISMRM 23rd Annual Meeting & Exhibition, Toronto, Canada, 2015. All analyses and compilation of the abstract and presentation were implemented by the author. Dai Zhuozi verified lesions identified by the author. The postmortem patients studied came from the practice of Dr. Ken Warren with Ingrid Catz. The photographs and their processing were done by Andrew Walsh. The preparation of brain slices were performed by the neuropathologists Drs. Johnson and Lu.

The third chapter has been published: Elkady AM, Sun H & Wilman AH. Importance of extended spatial coverage for quantitative susceptibility mapping of iron-rich deep gray matter. Magn Reson Imaging 2016:34:574-578. The in vivo and theoretical simulation code was written by the author. All reconstruction, analyses and writing of the first draft of the paper were implemented by the author, while Hongfu Sun contributed to editing the final draft of the paper.

The fourth chapter has been published: Elkady AM, Cobzas D, Sun H, Blevins G & Wilman AH. Progressive iron accumulation across multiple sclerosis phenotypes revealed by sparse classification of deep gray matter. J Magn Reson Imaging 2017. Using sparse logistic regression was the contribution of Dana Cobzas, while utilizing combined analysis of R2* and Quantitative Susceptibility (QS) was the contribution of the author. The developed analysis framework was a fruit of discussion between the author, Dana Cobzas, and Dr. Alan Wilman. Dana Cobzas has written the Image Processing section of the paper, developed all code utilized in the study and contributed to statistical analysis and producing the figures. Except for the mentioned work by Dana Cobzas, the author has conducted all analyses and has written the first draft of the paper, while Hongfu Sun contributed to editing the final draft of the paper.

The fifth chapter has been published: Elkady AM, Cobzas D, Sun H, Blevins G & Wilman AH. Discriminative analysis of regional evolution of iron and myelin/calcium in deep gray matter of multiple sclerosis and healthy subjects. Journal of Magnetic Resonance Imaging 2018. The developed analysis framework was a fruit of discussion between the author, Dana Cobzas, and Dr. Alan Wilman. Dana Cobzas has written the Image Processing section of the paper, developed all code utilized in the study and contributed to statistical analysis and producing the figures. Dana Cobzas has written the Image Processing section of the paper, developed all code utilized in the study and contributed to producing the figures. Except for the mentioned work by Dana Cobzas, the author has conducted all analyses and has written the first draft of the paper.

For all QS and R2* maps, processing software was inherited from past graduate students Hongfu Sun and Marc Lebel, respectively. The author has performed all implemented R2* reconstruction after modifying the fitting code to allow for accurate quantification of high R2* values deepgray matter of some multiple sclerosis patients. With the exception of Chapter 3, all QS maps were reconstructed by Peter Seres using default reconstruction options set by Hongfu Sun. MRI pulse sequences were inherited from past graduate students: multiple-echo gradient echo & fast spin-echo imaging (Marc Lebel), and single-echo gradient-echo imaging (Amir Eissa). MPRAGE sequences were standard issued by the manufacturer. All *in vivo* patients included in this thesis from the practice of Dr. Gregg Blevins with Leah White. All volunteer subjects were recruited by Peter Seres, who has also carried out all MRI acquisitions included in this thesis.

Dedication

When I was little, my parents were giants to me.

Today, I stand on their shoulders to become a giant.

Tommorow, I will stand on my wife's shoulder to remain a giant.

Acknowledgements

The author gratefully acknowledges Queen Elizabeth II scholarship support from the Government of Alberta and grant support from the Multiple Sclerosis Society of Canada, the Canadian Institutes of Health Research, and the Natural Sciences and Engineering Research Council of Canada.

Table of Contents

List of Tables

List of Figures

Chapter 1: Introduction

The following chapter briefly outlines essential theoretical concepts needed to understand quantitative Magnetic Resonance Imaging (MRI) techniques used throughout this thesis. Furthermore, the chapter describes some of the functions of iron and myelin in the brain, as well as their effect on MRI. Finally, an overview of Multiple Sclerosis (MS) is presented, which is the disease focus of this research.

1.1. Magnetic Resonance Imaging

A Nobel-prize-winning experiment by Stern and Gerlach in 1922 established that particles possess an intrinsic angular momentum that resembles classical angular momentum of a spinning top, but the spin angular moment can only take discrete quantum values. Another Nobel Prize was awarded to Isidor Rabi for developing a "resonance method for recording the magnetic properties of atomic nuclei", which he used to detect the resonance frequencies of different molecules. Independently, Edward Purcell and Felix Bloch used a different method to measure nuclear magnetic resonance (NMR) in solids and liquids, which resulted in another Nobel Prize. The use of Fourier transform in NMR for spectroscopy, followed by its use in conjunction with magnetic field gradients in MRI awarded Ernst and Paul Lauterbur / Peter Mansfield Nobel Prizes in 1966 and 2003, respectively. The following section briefly outlines the basic physical principles of MRI and some relevant techniques that are used throughout the thesis. Relevant sources may be reviewed for further details about Nuclear Magnetic Resonance Imaging (1), Magnetic Resonance Imaging (2), tissue magnetism (3), contributors to R2* and susceptibility contrast (4), and quantitative susceptibility mapping (5).

1.1.1. Nuclear magnetic resonance

1.1.1.1. Physical phenomenon

Nuclear Magnetic Resonance (NMR) is a physical phenomenon that results from atomic nuclei with an odd pairing of nucleons (i.e. odd-odd, odd-even, or even-odd number of protons and neutrons). Since protons and neutrons possess a magnetic moment, also known as 'spin', such nuclei possess a net angular momentum that is the source of the NMR phenomenon. A sample at thermal equilibrium placed in a strong static magnetic field, B_o, experiences a nuclear magnetization, M_o, which can be approximated using Boltzman's statistics as a function of the spin density and thermal energy of the sample according to the following equation (1):

$$M_o(r) = \left(\frac{\gamma h}{4\pi}\right)^2 . \left(\frac{B_o}{k_b T}\right) . \rho(r) \qquad \textbf{(1.1)}$$

where $M_o(r) =$ Magnetization magnitude as a function of position r,
$h =$ Planck's constant,
$\gamma =$ Gyromagnetic ratio of the nucleus,
$k_b T =$ Average thermal energy of protons in the sample, and
$\rho(r) =$ Spin density of the sample as a function of position r.

In most cases where the NMR sample is biological tissue, the hydrogen proton is the main source of the NMR signal due to the biological abundance of water. Classical mechanics can be used to describe the behavior of the magnetization vector $\boldsymbol{M}$. By equating the rate of change of angular momentum to the torque caused by placing $\boldsymbol{M}$ in a static magnetic field $\boldsymbol{B_o}$, we obtain a magnetization vector $\boldsymbol{M}$ precessing at the Larmor frequency ω_o clockwise about the direction of $\boldsymbol{B_o}$ (1):

$$\omega_o = \gamma B_o \qquad \textbf{(1.2)}$$

This phenomenon can be exploited to produce an NMR signal that is proportional to the proton density of water molecules in biological tissue. A RadioFrequency (RF) pulse can be used to deviate the magnetization vector $\boldsymbol{M}$ with an angle α from the direction of $\boldsymbol{B_o}$ in a frame of reference rotating with an angular frequency ω_o (**Figure 1.1**), where α is proportional to the amplitude duration of the RF pulse. If the static magnetic field $\boldsymbol{B_o}$ is assumed to be parallel to the

z-axis in a frame of reference rotating at a frequency of ω_o, the vector **M** will be composed of a longitudinal component M_z parallel to $\boldsymbol{B_o}$ and a transverse component M_{xy} perpendicular to $\boldsymbol{B_o}$.

It can be shown that in the case of non-interacting protons, the detected NMR signal after an RF excitation is directly proportional to the sample's proton density $\rho(r)$ and B_o^2 (1). However, many interacting processes cause the NMR signal to evolve with respect to time, some of which are briefly discussed in the next section.

1.1.1.2.NMR Signal Evolution

The time evolution of the NMR signal is generally affected by interactions that occur on the microscopic, mesoscopic, and macroscopic scales. On the microscopic level, the magnetization vector $\boldsymbol{M}$ decays exponentially with a time constant T_2 due to a loss of spin phase coherence, which is induced by destructive interference from neighboring spins. Exponential signal recovery with a time constant T_1 also occurs due to microscopic interactions with the spin lattice.

Mesoscopic and macroscopic interactions also cause exponential signal decay with a time constant T_2' due to magnetic field inhomogeneities. Mesoscopic interactions are on the order of the voxel size and provide important information about variation in magnetic susceptibilities. Macroscopic interactions are usually of little interest in NMR because they represent signal decay due to geometries much larger than the voxel size, such as air-tissue interfaces. In total, the NMR signal decays with a time constant T_2^*, where $\frac{1}{T_2^*} = \frac{1}{T_2} + \frac{1}{T_2'}$, as a result of microscopic, mesoscopic and macroscopic signal decay processes, but returns to equilibrium with a time constant T_1.

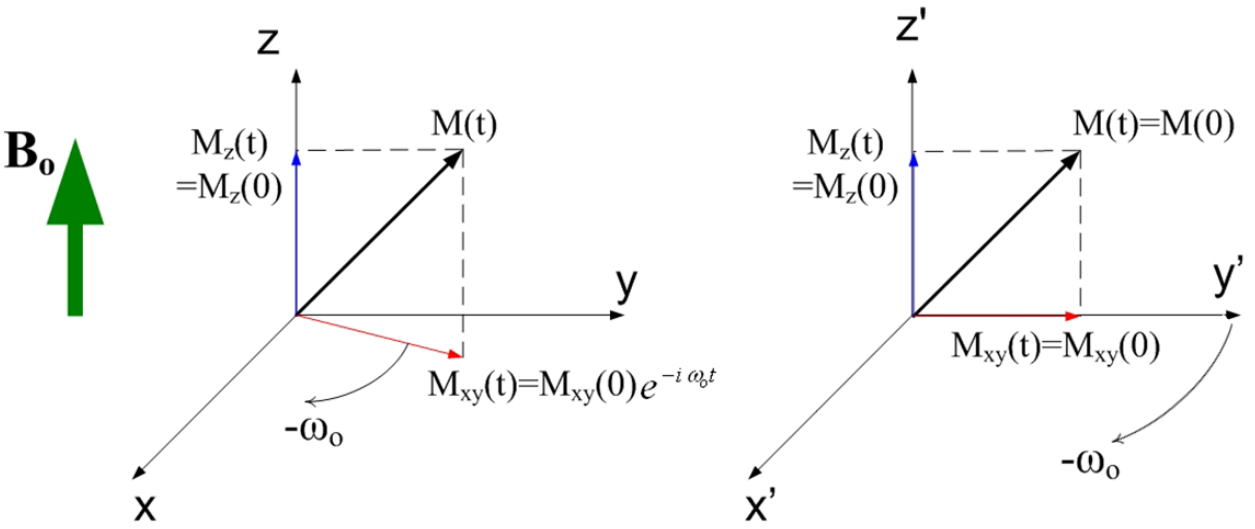

Figure 1.1 Laboratory frame of reference x-y-z (left) versus rotating frame of reference x'-y'-z' of angular frequency ω_o (right). Illustrated example is for magnetization excited by an RF pulse with an x-axis phase and a flip angle less than 90°. By convention, the static field is applied in the direction of the z-axis in the laboratory frame of reference, which is also the axis which the magnetization precesses around. In the rotating frame of reference, the precessing component of the transverse magnetization, $M_{xy}(0)$, becomes independent of time, and resides on the y'-axis.

1.1.1.3. Transverse Relaxation Rate Quantification

The following section presents the simplest techniques to quantify the transverse relaxation rates T_2 and T_2^*.

1.1.1.3.1. R2=1/T2

In a classic Carr-Purcell-Meiboom-Gill (CPMG) experiment (6,7) where ***M*** is tipped to the y' by an 90° RF pulse with an x'-phase, the transverse component begins to dephase into a fan due to static field inhomogeneities, depending on the true frequency experienced by each packet of spins (**Figure 1.2**). However, a 180° RF pulse with an y'-axis applied after the 90° pulse can refocus dephased transverse magnetization due to static field inhomogeneities by reversing the phase of each spin packet (**Figure 1.3**). Thus, the observed signal decay would be only due to irreversible spin-spin interactions. Pulse sequences that rely on refocusing pulse to refocus magnetization are called spin echo pulse sequences.

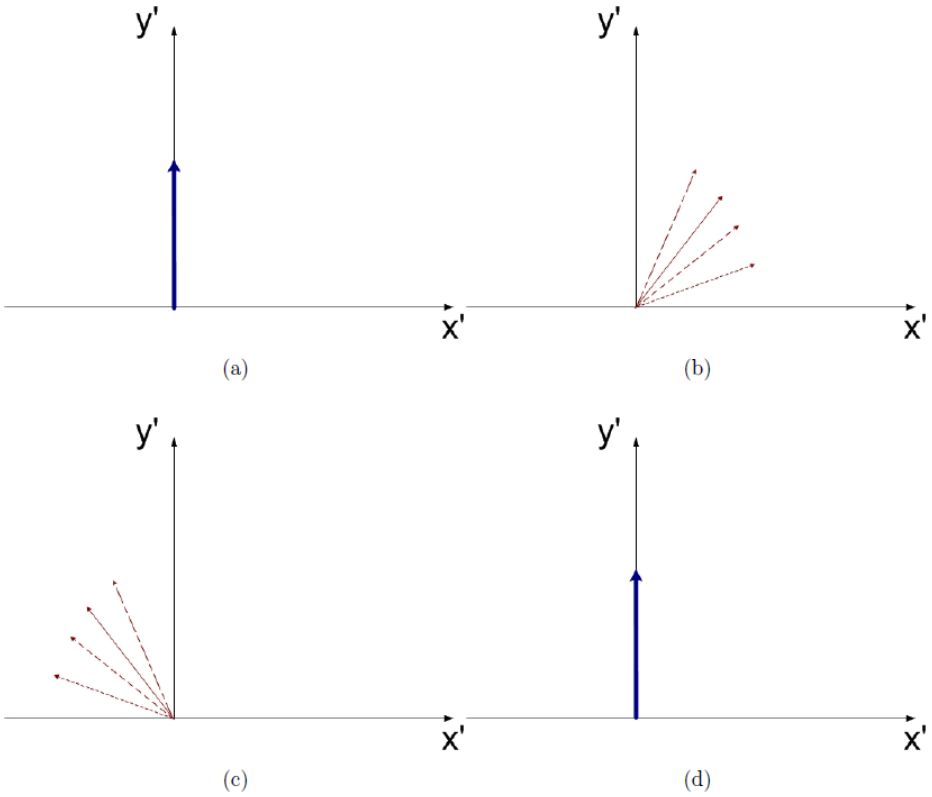

Figure 1.2 CPMG refocusing of dephased magnetization. (a) Immediately after an 90°-x RF pulse, there is a single magnetization vector on the y'-axis, (b) A fan of magnetization is produced due to dephasing in the x'-y' plane after a period τ_{CP} from the 90°-x RF pulse, where each vector represents a magnetization vector precessing at a unique frequency. The MRI signal during this period decays exponentially at a rate of $R_2 + R_2'$. (c) After a 180°-y RF pulse subsequent to the 90°-x RF pulse, the magnetization vector fan in the xy plane reverses phase around the y' axis. The MRI signal during this period decays exponentially at a rate of $R_2 - R_2'$. (d) After a period $2\tau_{CP}$, the magnetization refocuses on the y'-axis and the MRI signal is only affected by R_2 decay from the onset of the 90°-x RF pulse.

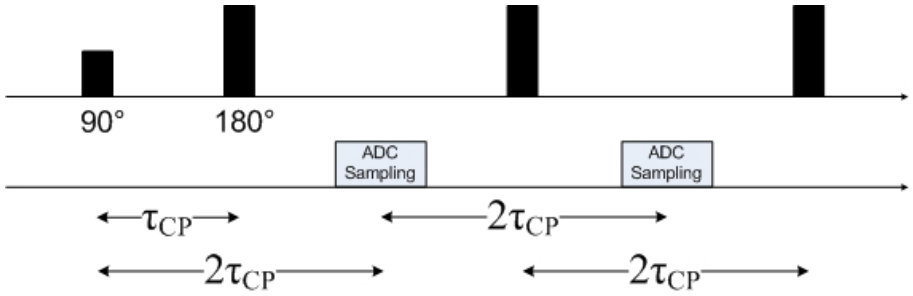

Figure 1.3 R_2 Quantification Using CPMG. CPMG is characterized by a 90°-x RF pulse followed by a series of 180°-y RF pulses after a delay, τ_{CP}, with the spacing between 180°-y pulses equal to $2\tau_{CP}$ and the signal being observed at TE(n) = 2*n after the first 90°-x RF pulse. Although the signal initially decays with an R2* relaxation rate after the 90° pulse, the reversible component of this decay (R2') is refocused by the time it is sampled after each 180° pulse. Thus, the resulting observed signal decay is purely weighted by an irreversible R_2 exponential decay.

1.1.1.3.2.R2*=1/T2*

As stated earlier, the transverse magnetization decays with a time constant T_2^* immediately after the application of an RF pulse due to microscopic, mesoscopic, and macroscopic processes. The signal observed is a result of this free induction decay process, and thus the relaxation rate can be quantified using an exponential fit of the observed signal after the application of the RF pulse (**Figure 1.4**). Pulse sequences that rely on dephasing and rephasing gradients to sample the free induction decay signal using are called gradient echo pulse sequences.

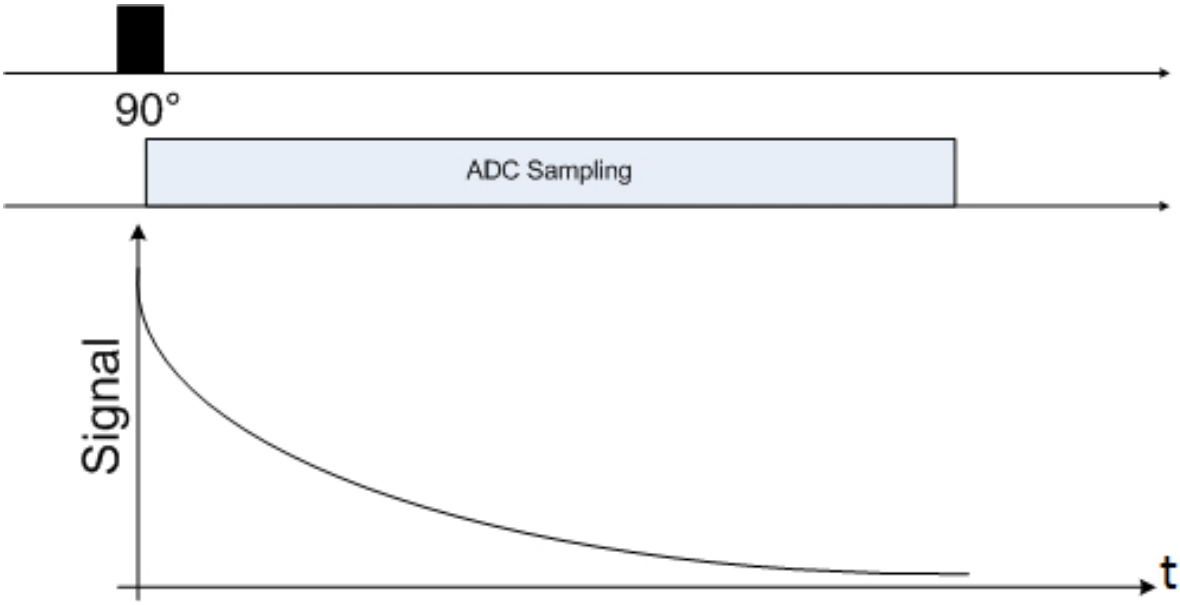

Figure 1.4 R2* quantification by sampling a free induction decay signal. Following a 90°-x excitation pulse, the magnetization is flipped unto the transverse plane and dephases, which produces a FID signal. The FID exponential decay curve can be sampled at different echo times (TEs) to quantify R2*.

1.1.2.Spatial Encoding using Magnetic Field Gradients

The key to utilizing the NMR signal for MRI is to be able to spatially localize the signal from a sample using magnetic field gradients. In 2D MRI imaging, an RF pulse of a bandwidth BW_{RF} and centered at the Larmor frequency is used to selectively excite a particular slice in the imaged

sample in combination with a linear gradient in the z-direction, G_z. Thus, the frequency of spins in the rotating reference frame of an axial slice at a location of z and with a thickness of Δz would be spatially encoded as (**Figure 1.5**):

$$\omega(z) = -\gamma.(z).G_z$$

$$\Delta z = \frac{BW_{RF}}{\gamma G_z} \qquad \textbf{(1.3)}$$

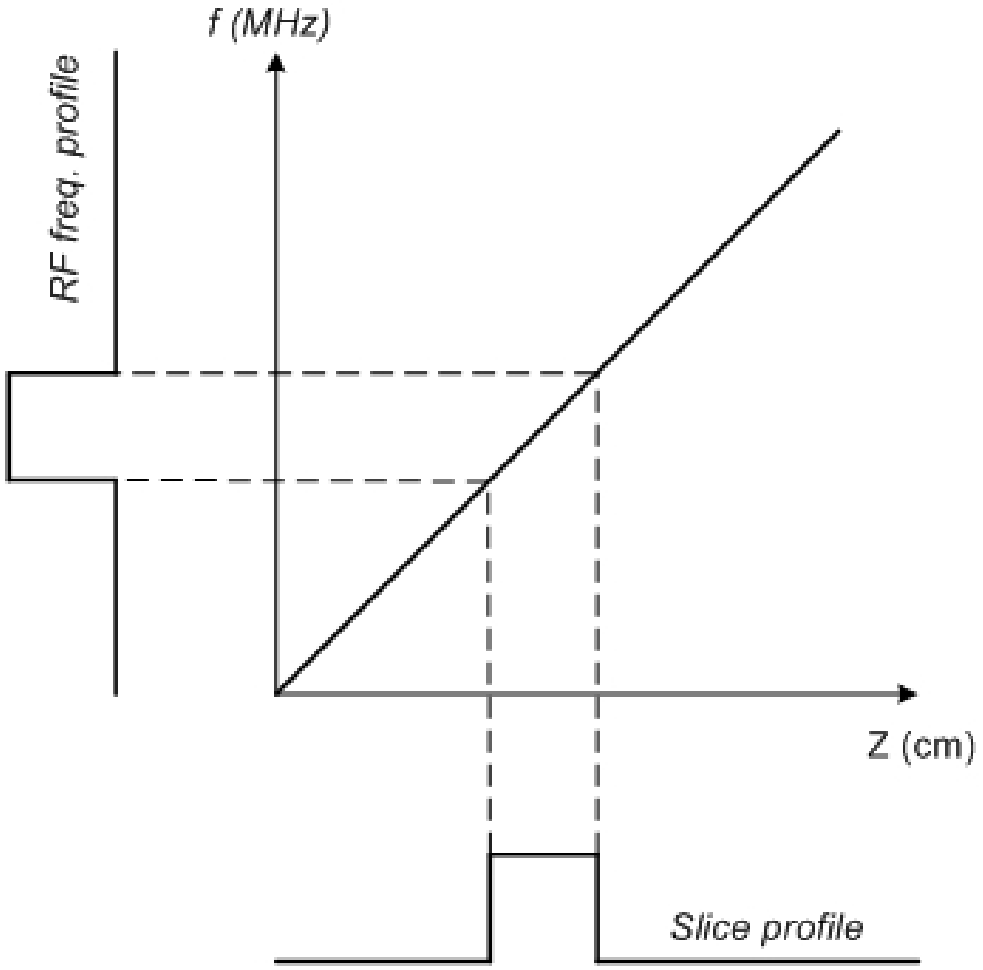

Figure 1.5 Selective slice selection uses pre-designed RF pulses to selectively excite a specific slice in the presence of linear magnetic gradients in the slice selection direction. Design of the RF bandwidth can be used to determine the slice thickness, while design of the RF center frequency can be used to determine the slice location.

Magnetic gradients G_x and G_y are used to encode the in-plane x and y directions to the Fourier domain, which is named k-space. Encoding in the y-direction is performed by turning on a magnetic gradient G_y for a period τ_{PE} before the data acquisition to accumulate phase as a function of:

$$\varphi(G_y, \tau_{PE}) = -\gamma y G_y \tau_{PE} \quad \textbf{(1.4)}$$

In-plane frequency encoding is achieved by turning on a magnetic gradient G_x during data acquisition to encode the data phase as a function of the acquisition time t:

$$\varphi(x, t) = -\gamma x G_x t \quad \textbf{(1.5)}$$

Thus, the slice becomes encoded on a Cartesian grid with increments of Δk, where:

$$\Delta k_x = \frac{\gamma}{2\pi} G_x \Delta t$$
$$\Delta k_y = \frac{\gamma}{2\pi} G_y \tau_{PE} \quad \textbf{(1.6)}$$

The k-space signal is thus encoded to be the Fourier transform of the image domain (**Figure 1.6**):

$$S(k_x, k_y) = \iint \rho(x, y) e^{-i2\pi(k_x x + k_y y)} dx.dy \quad \textbf{(1.7)}$$

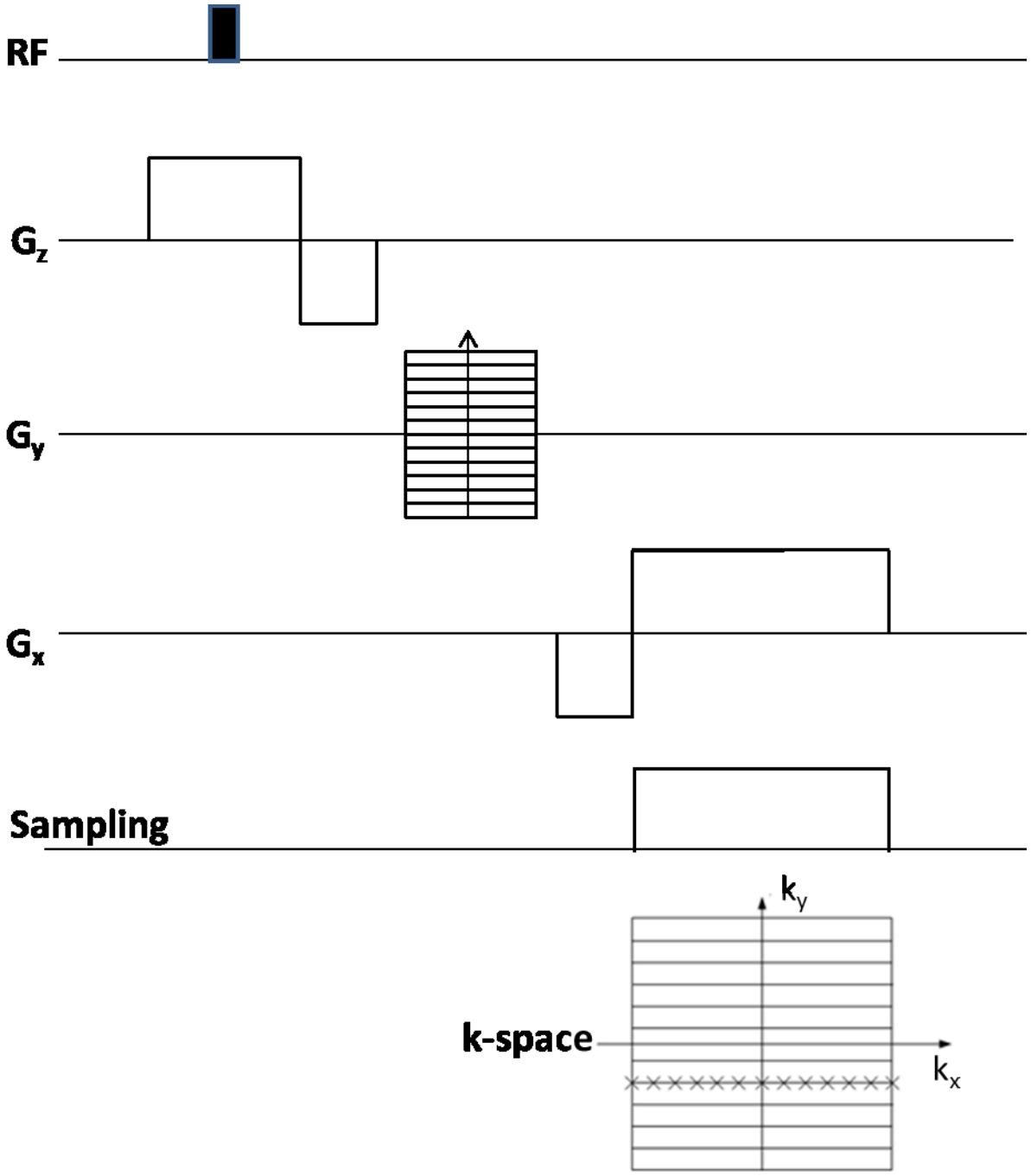

Figure 1.6 Pulse sequence diagram for a 2D gradient-echo axial acquisition showing the slice-select gradient applied in the z-direction to select a specific slice, phase-encoding gradients applied in the y-direction applied prior to sampling the signal to encode a particular ky line, and frequency-econding gradients applied in the x-direction in conjunction with sampling of the signal to sample all kx points.

The inverse Fourier Transform can be used to transfer the image back to image domain:

$$I(x,y)= \iint S(k_x,k_y)e^{i2\pi(k_x x+k_y y)}dk_x.dk_y \quad \textbf{(1.8)}$$

The minimum Field Of View (FOV) to acquire a number of points N is set according to Nyquist criterion to prevent aliasing:

$$\begin{aligned} FOV_x &= \frac{1}{\Delta k_x} = \frac{2\pi}{\gamma G_x \Delta t} \\ FOV_y &= \frac{1}{\Delta k_y} = \frac{2\pi}{\gamma G_y \tau_{PE}} \\ \Delta x &= \frac{1}{N_x \Delta k_x} = \frac{FOV_x}{N_x} \\ \Delta y &= \frac{1}{N_y \Delta k_y} = \frac{FOV_y}{N_y} \end{aligned} \quad \textbf{(1.9)}$$

3D Imaging can also be used by replacing the RF slice selection with a phase encoding gradient in the slab-select direction.

1.1.3. Contributors to the MRI Signal

The following section will briefly discuss some relevant contributors to the MRI signal in light of the scope of this thesis.

1.1.3.1. Susceptibility Effects

Materials typically encountered in MRI can be categorized as paramagnetic that have a positive susceptibility and strengthen the applied field, or diamagnetic that have a negative susceptibility and weaken the applied field. (3).

The magnetic properties of an atom are a function of the arrangement of its electrons, which exist around a nucleus in shells representing states of successively higher energy. Within a shell, electrons exist in orbitals, with each orbital containing no more than two electrons that have

opposite spins. Since a moving electrically charged particle produces a magnetic field, the magnetic properties of a material are defined by electron orbital angular momentum due to the orbital motion of an electron around the nucleus, and are also defined by electron magnetic moment (which is coupled to its spin angular momentum).

An atom possesses a net magnetic moment where there are unpaired electrons in an orbit (i.e. no cancellation of spin moments due to spin pairing). The maximum achievable spin magnetic moment occurs when the outer shell is half full, and decreases when further electrons are added. In ferromagnetic solids, atoms are closely packed such that shared electrons between atoms cause a strong parallel coupling of electron spin moments, which gives rise to a strong permanent magnetic moment within a ferromagnetic domain. In paramagnetic solids, such as iron in biological tissue (**Figure 1.7**), unpaired electrons exist but without coupling, hence there is no net permanent magnetization due to thermal activation at temperatures above the Curie temperature.

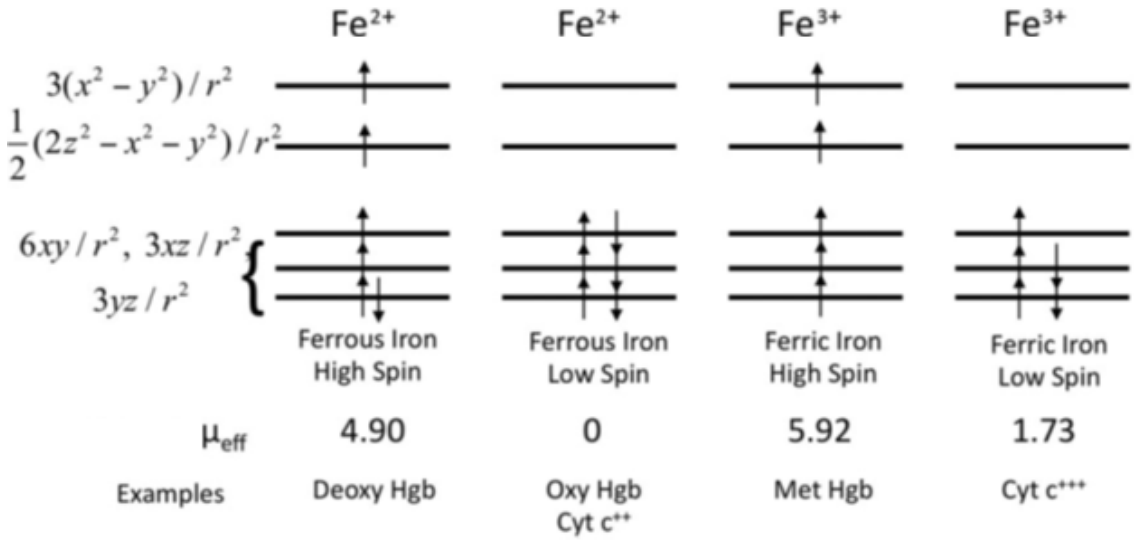

Figure 1.7 The angular momentum (μ_{eff}) of tissue iron depends on depends on its oxidation and spin state, with Methemoglobin Ferric iron exhibiting the strongest paramagnetic properties due to the presence of five half-full orbitals (adapted from (4)). Deoxy Hgb = Deoxygenated Hemoglobin; Oxy Hgb = Oxygenated Hemoglobin; Met Hgb = Methemoglobin; Cyt c = Cytochrome complex.

Regardless of the electron arrangement, any material will exhibit a response to an external magnetic field. Magnetic susceptibility χ is a property that measures the response of a material when placed in an external magnetic field. All materials exhibit a diamagnetic response to an external field that opposes the field due to an induced orbital angular momentum of paired electrons. However, this property is swamped in materials that possess atomic moments, since paramagnetism a much stronger effect than diamagnetism. Unpaired electrons in paramagnetic materials align in the direction of the field, which creates a parallel dipole field that strengthens the applied field.

In any given NMR sample, the induced electron magnetization $\boldsymbol{M}$ (which is distinct from the nuclear magnetization which has been defined earlier) is a function of the susceptibility of the sample to be magnetized and the applied field:

$$\boldsymbol{M} = \chi \boldsymbol{H} = \chi \frac{\boldsymbol{B}}{\mu} = \frac{\chi}{\mu_o(1+\chi)} \boldsymbol{B} \tag{1.10}$$

where $\boldsymbol{H}$ is the applied magnetic field in Am^{-1}, μ is the permeability of the material, and μ_o is the permeability of vacuum. By assuming the static magnetic field z component is dominant, tissue susceptibilities are much smaller than 1, and isotropic susceptibility properties, **Equation (1.10)** can be simplified to calculate the induced field shift ΔB:

$$\Delta B = \mu_o M_z \approx \chi B_o \tag{1.11}$$

According to **Equation (1.2)** and **Equation (1.11)**, spins in different materials precessing at differing frequencies as a function of the magnetic fields that they experience, which are a function of their susceptibilities. The NMR signal phase difference of two pools with different susceptibilities that is observed a time t after the application of the RF excitation pulse is decreased by a factor of $\Delta\varphi$ (8):

$$\Delta\varphi(t) = \gamma . \Delta\chi . B_o . t \tag{1.12}$$

Additionally, the T2* decay of the NMR signal magnitude is modulated over time by a factor of $sinc(\gamma . \Delta\chi . B_o . t/2)$ because of the linear field gradients between different susceptibilities (9), where $\Delta\chi$ represents the susceptebility difference between the boundaries of the voxel.

1.1.3.2.Diffusion Effects

Diffusion in NMR refers to the random thermal Brownian motion of water molecules, which are ^{1}H protons in the conventional case of MRI of biological tissue. For a proton diffusing in a field created by a magnetic perturber, two regimes may be defined based on the size of the magnetic perturber: (a) the "small size" regime (also known as the narrowing regime (10)), where motional averaging of protons reduces the observed susceptibility effects of the perturber on the MRI signal and thus diffusion becomes the most important contributor to the signal, (b) the "large size" regime (also known as the static dephasing regime (11)), where diffusion effects are insignificant in comparison to susceptibility effects because the signal decays faster than diffusion effects, and the intermediate exchange regime, where the diffusion partially contributes to the signal (11).

A simple distinction between these regimes can be made based the diffusion distance in time, d_τ, of a proton diffusing in a magnetic field perturbation created by a susceptibility difference $\Delta\chi$, which can be calculated as (4,10):

$$d_\tau = \sqrt{\frac{D}{\gamma . \Delta\chi . B_o}} \qquad \textbf{(1.13)}$$

where D is the apparent diffusion coefficient and $\Delta\chi$ is the susceptibility difference of the perturber with the surrounding medium. The "small size" regime occurs when d_τ is much greater than the radius of the perturber inducing the magnetic field at the equator (i.e. the radius for the case of a sphere, and the cross-sectional radius for the case of a cylinder parallel to the main field), whereas the "large size" regime occurs when d_τ is much smaller than this radius (10).

For a ferritin iron molecule with $\Delta\chi = 520$ ppm (theoretical susceptibility for fully loaded case with 4500 Fe^{3+} ions) and assuming D = 1 $\mu m^2/ms$ and field strength of 4.7T (which was employed throughout this thesis), **Equation (1.13)** is used to calculate the diffusion distance d_τ to be 100 nm, which is substantially larger than the typical radius of an isolated ferritin particle (i.e. 6 nm) (4). Similarly, the diffusion distance for a crude model of a white matter fiber with 20% myelin volume fraction is in the range of 20 to 12 μm for susceptibilities in the range of -13 to -34 ppb, which is larger than a white matter fiber of radius 1 μm (4). These simple calculations

for a single perturber demonstrate that diffusion should theoretically contribute to reducing the observed NMR transverse relaxation rates around ferritin particles and white matter fibers. For the case of a volume with many perturbers, more sophisticated modelling of the magnetic environment at the sub-voxel scale has been proposed (11,12). Although diffusion may indeed be a contributor to the MRI signal, the effects of diffusion is beyond the scope of this thesis and has not been considered.

1.1.3.3. Orientation Effects

White matter fiber bundles are oriented at various angles in the brain (**Figure 1.8**). Orientation of white matter fiber bundles relatic to the direction of the static field has been shown to substantially affect the observed frequency and R2* distribution (13-17). For white matter structure crudely approximated as a set of parallel cylindrical sheaths oriented at angle θ with main magnetic field, the increase in the transverse relaxation rate can be calculated as (11):

$$\Delta R_2^* = 0.5 * \sin^2\theta * \gamma * \Delta\chi_{myelin} \qquad \textbf{(1.14)}$$

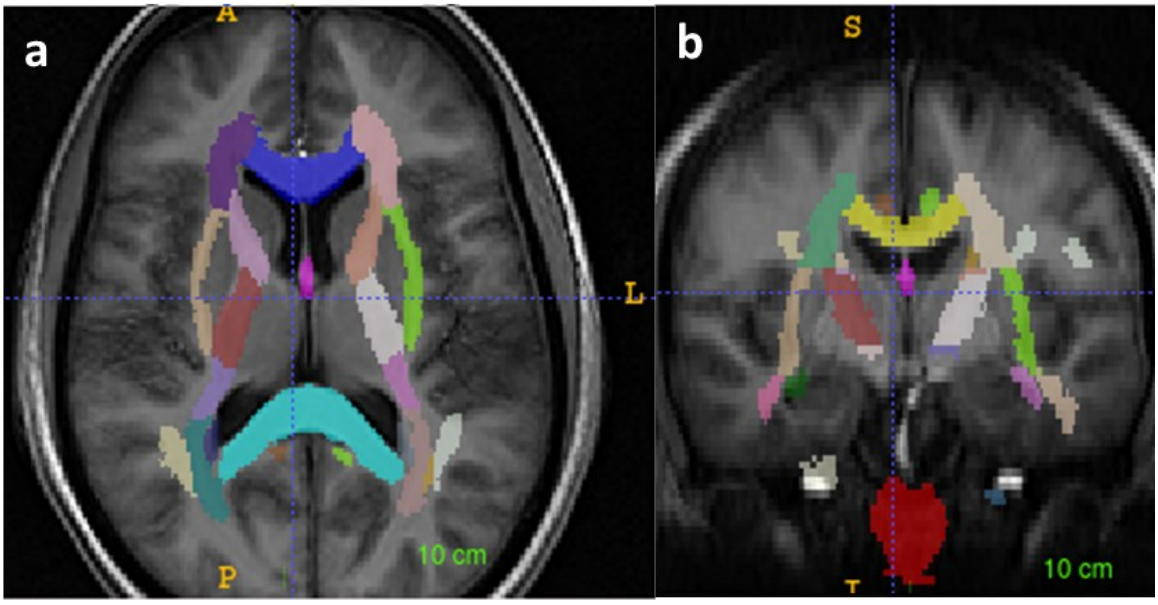

Figure 1.8 Forty eight segmented labels of white matter fiber tracts (coloring is to distinguish different white matter fibers) overlaid on the axial (**a**) and coronal (**b**) views of the T1-weighted MPRAGE of a control subject demonstrating different orientations of white matter fiber tracts. Segmentation was performed by registering the John Hopkins Eve atlas (23) to patient space (see (23) for a description of the tract labels).

A tensor representation of susceptibility can be used with the parallel and perpendicular components (relative to the fiber direction) used as diagonal elements, which may be used to produce orientation maps of white matter fibers (18). Furthermore, the organized arrangement (19,20) of anisotropic (20) phospholipid molecules in the lipid bilayer of myelin introduces anisotropic properties for the susceptibility of white matter fibers, which is also observed on a macroscopic scale (21) (**Figure 1.9**).

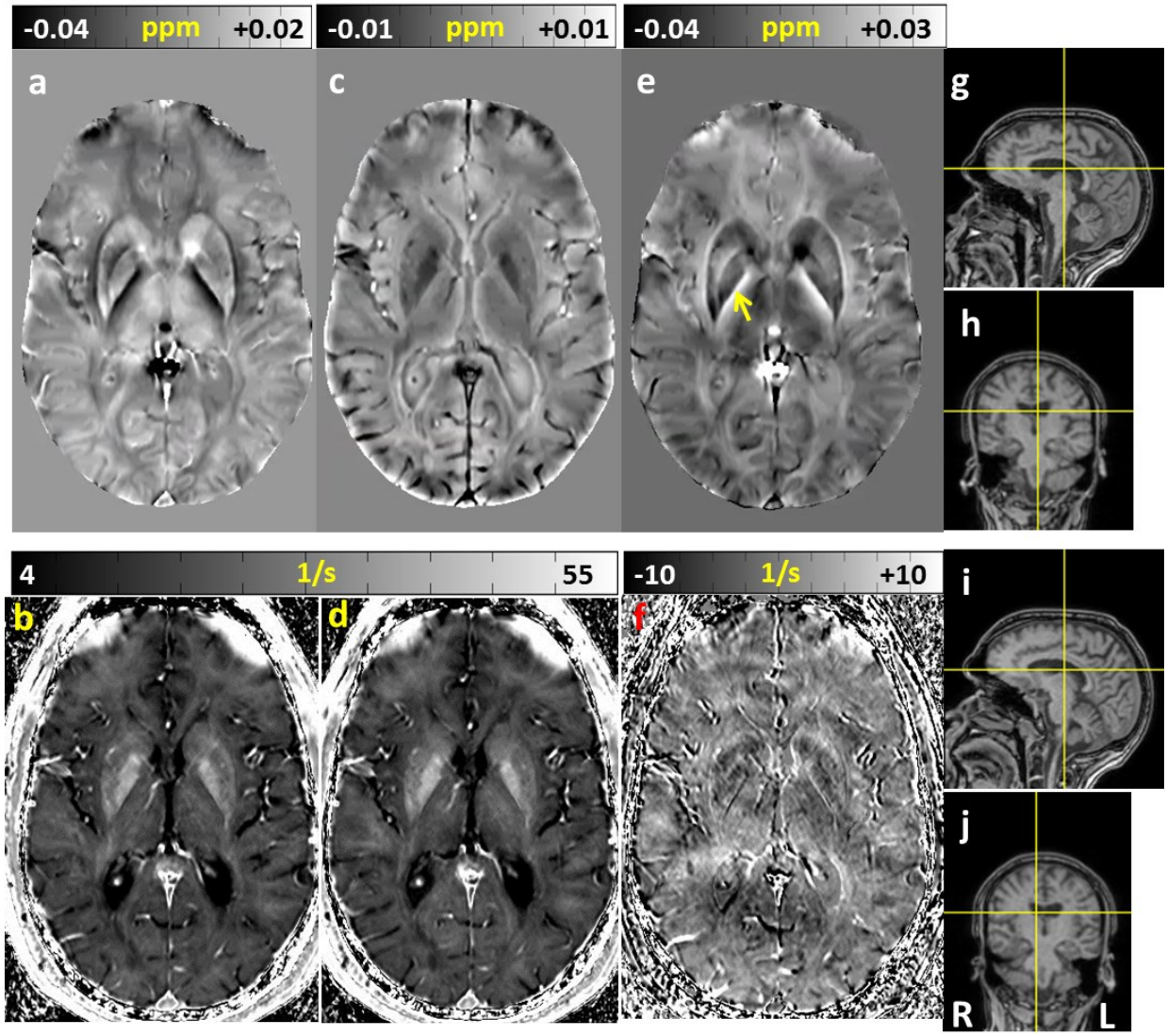

Figure 1.9 Axial Frequency (**a**,**c**), R2* (**b**,**d**) maps, sagittal (**g**,**i**), and coronal (**h**,**j**) T1-weighted localizer images of a volunteer subject with coil-centered (**a**,**b**,**g**,**h**) and left-tilted (**c**,**d**,**i**,**j**) positions (radiological convention), where the FOV was tilted so the slice was matched in both acquisitions (matching has been confirmed post-acquisition by comparing Image. Orientation values in DICOM headers). Tilting was achieved by putting a cushion beside the subject's head, leading to approximately 8 and 4 degrees of tilting from y and z axes, respectively (calculated using FSL FLIRT). The sensitivity of frequency and R2* to the orientation of the head relative to the main magnetic field is apparent in the corresponding difference images (**e**,**f**), especially in the internal capsule white matter tract for the frequency difference image (highlighted by yellow arrows). Frequency maps were calculated using RESHARP (described later in detail) and R2* maps were calculated using a mono-exponential fit.

1.1.3.4.Microstructure Effects

In the simple case of the existence of a single paramagnetic perturber of the magnetic field and neglecting effects other than the field perturbation, the mesoscopic transverse relaxation rate loss due to this perturber can be simply calculated as $R_2' = \gamma \Delta B$ (11). In this case, the average magnetic environment seen by a proton is a reflection of the field shape induced by the susceptibility difference and the shape of the perturber (11). However, protons frequently experience the effect of several microscopic perturbers, such as iron, myelin, deoxyhemoglobin. Thus, the micro-distribution of the perturber distribution can significantly influence the measured transverse relaxation effect and field shift (4). Furthermore, these perturbers can be distributed non-uniformly throughout the voxel with limited exchange, such as the case of the compartmentalization of water within myelin, which would cause the observed transverse relaxation rate to deviate from the mono-exponential case (25) (**Figure 1.10**). One of the limitations of this thesis is that it only consideres field perturbations on the scale of the voxel neglecting effects of perturber distribution, and thus assumed a mono-exponential time evolution of transverse relaxation.

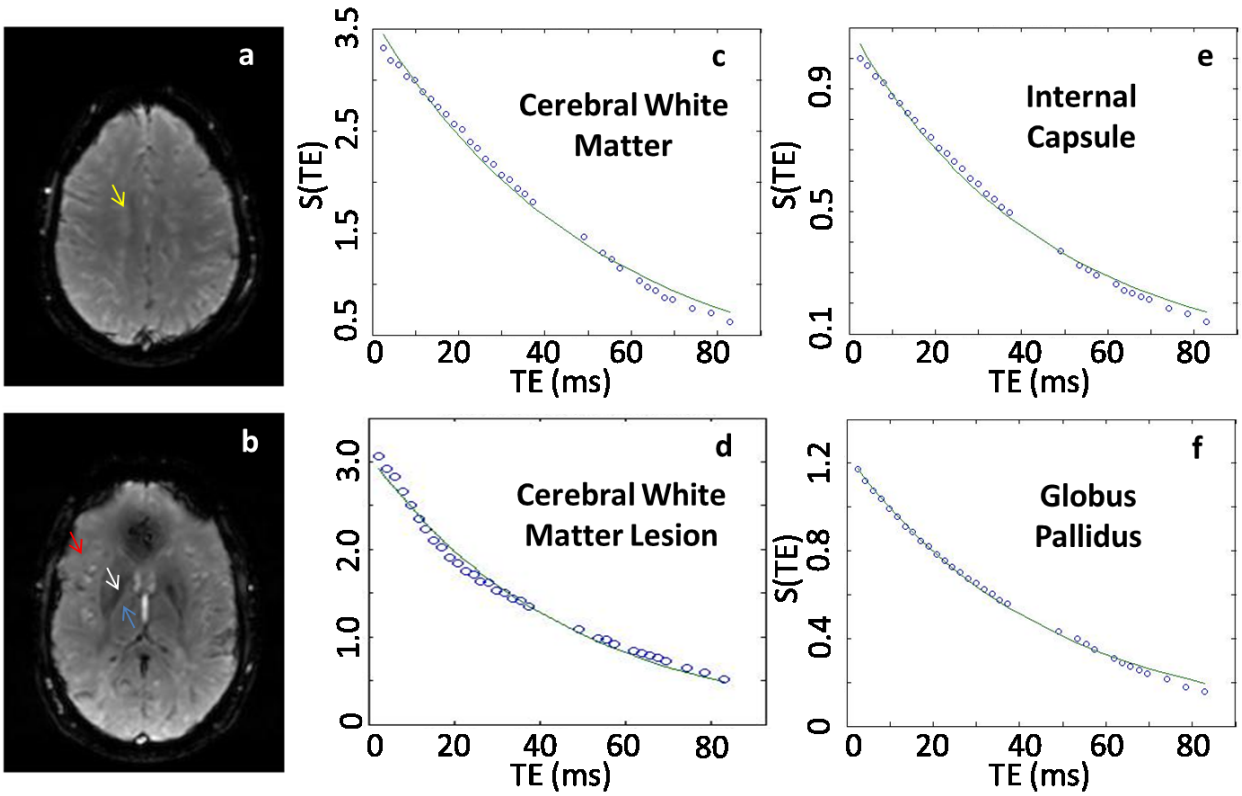

Figure 1.10 Axial slices of the cerebellum (**a**) and deep gray (**b**) from 2 separate multi-echo gradient-echo acquisitions of a 32 year old male MS patient. The corresponding magnitude time evolution curves (**c**-**f**) demonstrates that a mono-exponential fit (solid line) of the signal magnitude (circles) for the cerebral white matter lesion (**d**, yellow arrow) and the globus pallidus (**f**, white arrow) is a more appropriate model compared to the mono-exponential fit of the time evolution of the cerebral white matter (**c**, red arrow) and internal capsule (**e**, blue arrow) signal. This effect underscores the multi-component exponential relaxation which occurs in white matter due to the compartmentalization of water protons within myelin. Sequence parameters were: number of slices =1; slice thickness = 3mm; FOV = 187.5 x 240 mm^3; in-plane pixel size = 0.94 x 0.94 mm^3; number of averages = 50; number of echoes = 32; time to first echo = 2.5ms; echo spacing for echoes 2:20 = 1.8ms; echo spacing between echo 20 & 21 = 11.8ms; echo spacing for echoes 22:28 = 1.9ms; echo spacing for echoes 29:32 = 4.5ms.

1.1.4. Quantitative Susceptibility Mapping

Quantitative Susceptibility Mapping (QSM) is a signal post-acquisition processing technique that computes magnetic susceptibilities from a measured free induction decay MRI signal, which is usually acquired using a gradient-echo sequence (26-31). The technique consists of a number of signal pre-processing steps, phase processing steps, and a field inversion procedure.

1.1.4.1.Signal Pre-processing

1.1.4.1.1.Coil combination

Most modern MRI systems have multiple receiver coils (32). A reference scan using a volume coil with uniform sensitivity can be used to estimate the sensitivity function of each of the coils, which is ideally needed to reconstruct the combined image from all coils. However, not all MRI have a body coil, especially high-field coils such as the one used throughout this thesis.

The simplest method for coil combination that does not require prior knowledge of the coil sensitivity function is sum-of-squares of the signal magnitude from all coils. However, this method does not account for the signal phase, which is an essential component of QSM. Coil combination implemented through this thesis utilizes a complex summation of signals from multiple coils, but after estimating and subtracting the phase offset from each coil (33,34).

1.1.4.1.2.Brain Extraction

Most QSM methods only use the useful phase information from brain tissue, hence a mask is used to extract brain tissue using the magnitude MR image. This mask was calculated throughout this thesis by applying the Brain Extraction Tool (BET) (33) of FMRIB software library (FSL) to the first echo of the magnitude signal. The resultant mask was multiplied to the combined MRI signal magnitude and phase. The masked MRI signal was used in all phase processing and field inversion steps.

1.1.4.2.Phase processing

After combining the signal from the multiple coil elements using using complex summation, the MRI signal phase is unwrapped and contributions from background field are removed.

1.1.4.2.1.Phase Unwrapping

MRI phase represents the vector angle of the complex signal, where measurement of MRI phase spans $[-\pi,\pi)$. However, phase is a continuous parameter that physically represents the evolution of phase in a voxel from the time of application of the RF excitation pulse. Thus, aliasing occurs

during phase measurements, and phase images need to be unwrapped to remove phase wrap-arounds that exceed [-π,π). Path-based methods perform unwrapping by adding multiple 2πs to remove phase jumps, while Laplacian unwrapping applies the Laplacian function in Fourier space to estimate the true values of unwrapped phase. Spatial path-based phase unwrapping was implemented throughout this thesis using Phase Region Expanding Labeller for Unwrapping Discrete Estimates (PRELUDE) (35), which is a package from the FMRIB Software Library (FSL) (**Figure 1.11**).

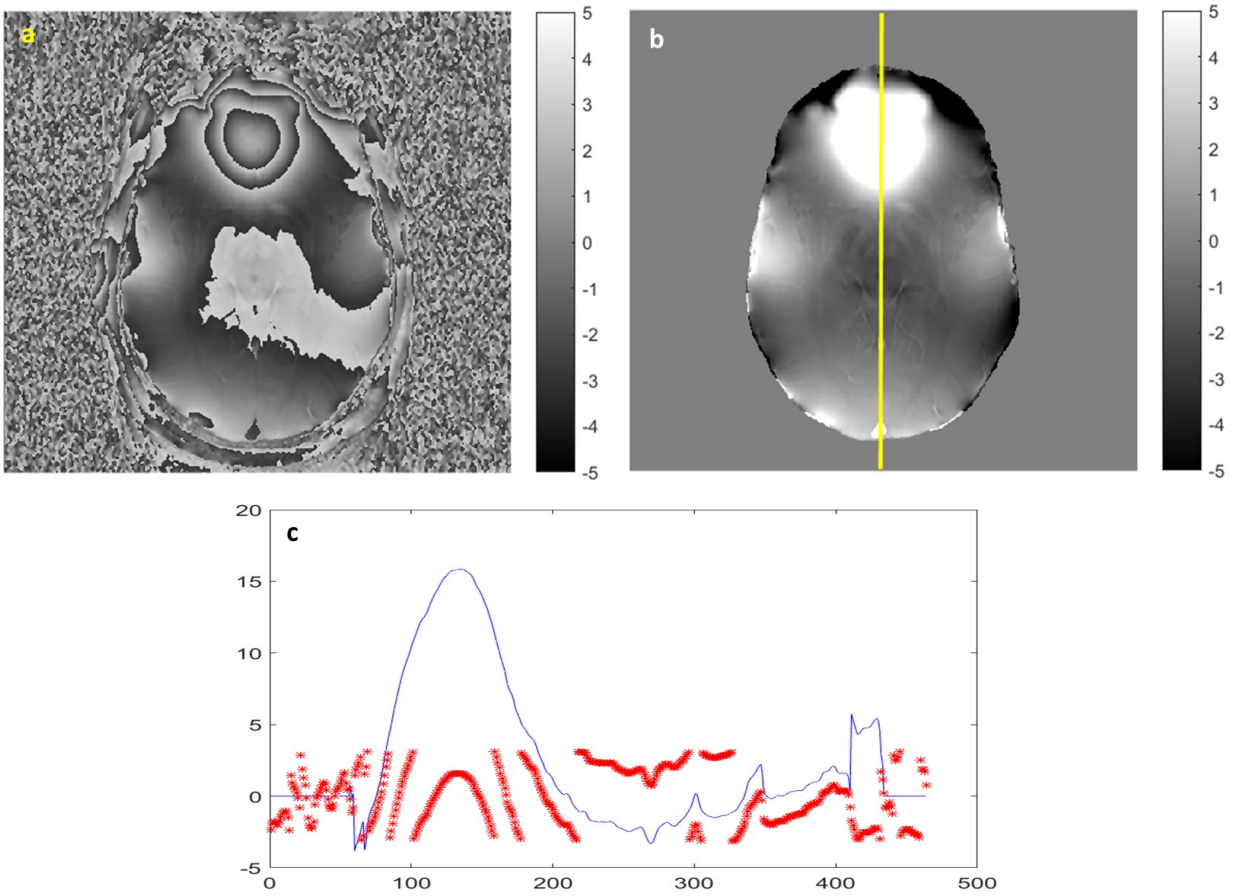

Figure 1.11 Raw MRI phase of volunteer subject (**a**) only ranges from [-π,π), and thus exhibits phase jumps at ±π.n. PRELUDE can be used to unwrap these phase jumps to produce an unwrapped phase image (**b**). The yellow line indicates the position of the line plot in (**c**), where red stars represent wrapped phase values, and the blue line represents the unwrapped phase (units of y-axis are radians). PRELUDE was applied after brain extraction using BET.

1.1.4.2.2. Calculation of Total Field Perturbation

Total Field Shift (TFS) relative to the static field was calculated in this thesis using magnitude weighted least square fitting of unwrapped phase values, φ, of multiple gradient-echoes (36):

$$argmin_{TFS} \left\| W^{\frac{1}{2}}(\varphi + \gamma.TE.B_o.TFS) \right\|^2 \quad \textbf{(1.15)}$$

where W is the weighting matrix assigned as the magnitude intensity and TE is the time to the echo signal from the application of the RF excitation pulse.

In the case of single echo acquisitions, TFS was calcuated by assuming it scales linearly with TE and B_o:

$$TFS = -\frac{\varphi}{\gamma.TE.B_o} \quad \textbf{(1.16)}$$

1.1.4.2.3. Background Field Removal

From **Equation (1.10)**, the field experienced by a voxel containing brain tissue is a function of the applied magnetic field, as well as the susceptibility of the voxel:

$$B_{seen} = (1 + \chi)B_{applied} \quad \textbf{(1.17)}$$

The field applied to the voxel has two components: the static magnetic field B_o and a field component induced by dipole magnetic fields of other voxels. However, background fields of air voxels external to the brain contaminate local magnetic fields from brain voxels. Since there is no MRI signal outside the brain, several methods have been proposed to solve the ill-posed problem of removing background field contribution using only information of MRI signal within the brain. The easiest background field removal approach is to apply a homodyne filter to remove low frequency components representative of background fields (37). Although this technique has been applied frequently to susceptibility-weighted imaging, it is disadvantaged by being sensitive to changes in filter width, structure size, shape and local environment (38).

Regularization-Enabled SopHisticAted Removal of Harmonic Fields (RESHARP) (24) has been applied through this thesis for background field removal. According to Maxwell's equations, the

background field sources outside the brain should only introduce harmonic fields within the brain (39,40). By utilizing the Spherical Mean Value property of harmonic functions, the background field can be removed by convolving the total field with a nonnegative, radially symmetric, normalized convolution kernel (31). However, the SMV theorem is violated wherever the kernel overlaps the brain edge. Thus, RESHARP employs L2 norm (Tikhonov) regularization to solve this problem by exploiting the fact that background fields fit the majority of the induced total field (24) (**Figure 1.12**).

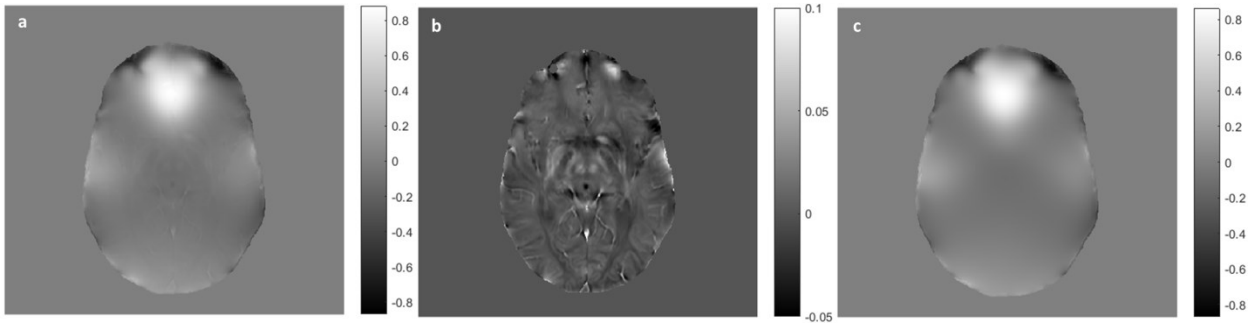

Figure 1.12 The Total Field Shift (**a**) is calculated by fitting the unwrapped phase of multiple echoes (**Figure 1.10b**) according to **Equation (1.16)**, which is then convolved with a spherical kernel of radius 3mm to calculate the local field shift using RESHARP (**b)** by removing the background field (**c**). RESHARP was carried out using a Tikhonov regularization parameter of 0.001 for a maximum number of 500 iterations, and the displayed fields are expressed in parts per million.

Using a larger spherical kernel size reduces the background field component, but more brain tissue is eroded at the edge of the brain (**Figure 1.13**). All patient studies employed in this thesis utilized a 3mm kernel radius, which was empirecially determined to produce a reasonable balance of contrast to noise ratio and preservation of brain edges. Modified SHARP background removal techniques, such as Extended RESHARP (ESHARP) (41) and Variable-kernel SHARP (V-SHARP) (42), try to minimize edge effects. As for the Tikhonov regularization parameter, using a larger value will increase the smoothness of the image without affecting the energy of the image (i.e. it will reduce the standard deviation without affecting the mean) (**Figure 1.14**), and thus images would have a similar contrast (**Figure 1.15**).

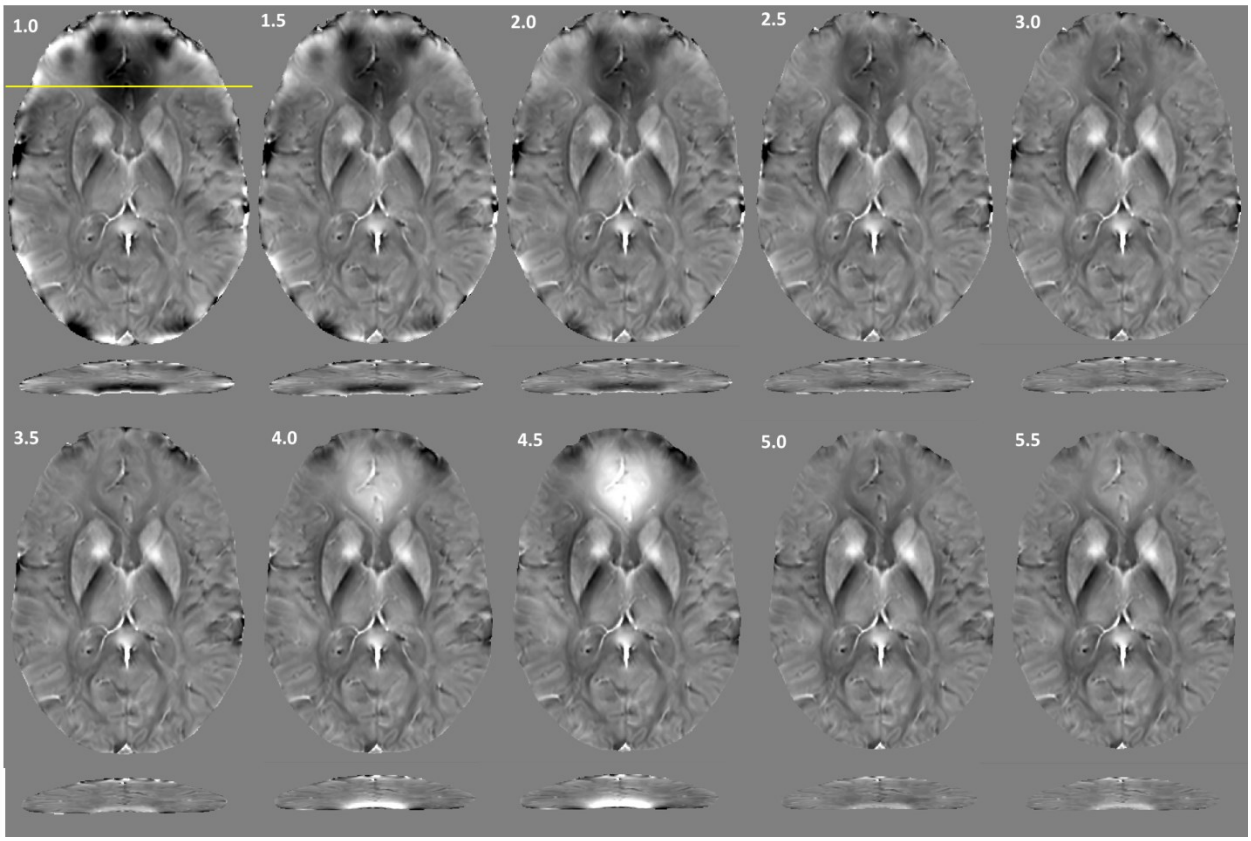

Figure 1.13 Axial view (first and third rows) of local field shift maps calculated using RESHARP with spherical kernel sizes of radius 1 to 5mm in steps of 0.5mm and corresponding coronal view sectioned at yellow line (second and fourth rows) demonstrate the increased contribution of background field and erosion of brain edges at larger kernel sizes, where the slicing location causes smaller brain tissue to appear in coronal views. Increased kernel size is shown to reduce the bakround field component. Note that the effect of background field appears to be reduced in kernel sizes of 5 and 5.5mm compared to 4.5mm, but this effect is only for the displayed slice. Choice of optimum kernel radius for an MRI scanner should be performed empirically to ensure reasonable reduction of background field while preserving as much brain edge tissue as possible. Images are scaled between -0.05 and 0.05 ppm. All patient studies employed in this thesis utilized a 3mm kernel radius.

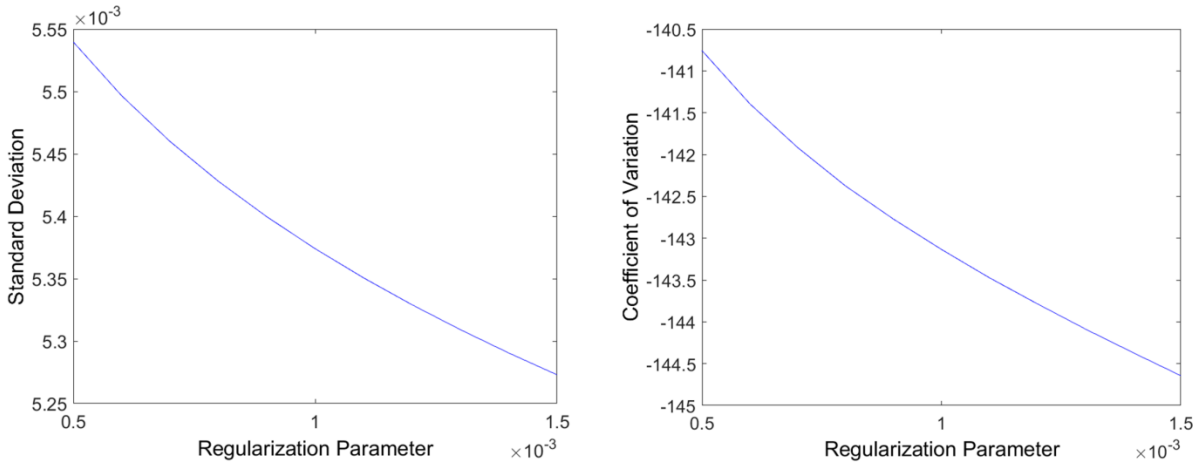

Figure 1.14 Standard deviation of LFS (left; units of y-axis are in ppm) decreases exponentially with increase in Tikhonov regularization parameter for RESHARP. Since this regularization procedure is a linear process, the coefficient of variation (right) behaves in the same manner, thus there is no visual difference in image contrast that the naked eye can observe when employing different regularization parameters (see **Figure 1.15**).

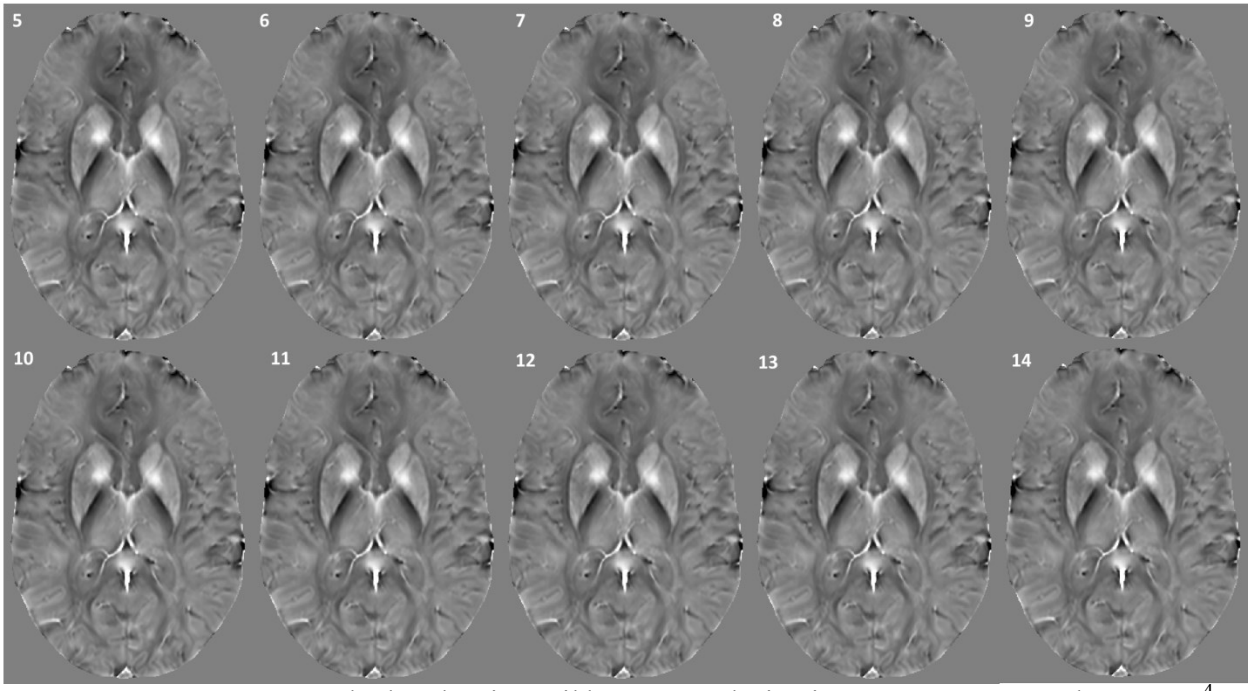

Figure 1.15 LFS maps calculated using Tikhonov regularization parameters equal to $5x10^{-4}$ to $14x10^{-4}$ in steps of $1x10^{-4}$ demonstrate the visual similarity of maps despite the reduced image variation with increased regularization parameters.

1.1.4.3.Magnetic Field Inversion

The magnetic field induced by a susceptibility distribution can be expressed using a volume integral of the magnetization (5):

$$\Delta \boldsymbol{B}(\boldsymbol{r}) = \frac{\mu_o}{4\pi} \int d^3r' \left\{ \frac{\mathbf{3}\boldsymbol{M}(\boldsymbol{r}').(\boldsymbol{r}-\boldsymbol{r}').}{|\boldsymbol{r}-\boldsymbol{r}'|^5}(r-r') - \frac{\boldsymbol{M}(\boldsymbol{r}')}{|\boldsymbol{r}-\boldsymbol{r}'|^3} \right\} \quad \textbf{(1.18)}$$

which can be simplified by expressing it in MRI-relevant k-space assuming isotropic susceptibility:

$$\Delta \boldsymbol{B}(\boldsymbol{k}) = \frac{\mu_o}{3} \frac{3cos^2\beta - 1}{2} (M(\boldsymbol{k}) - 3\boldsymbol{M_z}(\boldsymbol{k})) \quad \textbf{(1.19)}$$

Where β is the angle between the main field and the vector $\boldsymbol{k}$, such that:

$$cos^2\beta = \frac{k_z^2}{k_x^2 + k_y^2 + k_z^2} \quad \textbf{(1.20)}$$

Since only the z component of the magnetic field is important, **Equation (1.19)** can be simplified as:

$$\Delta \boldsymbol{B_z}(\boldsymbol{k}) = -\frac{\mu_o(3cos^2\beta - 1)}{3} \boldsymbol{M_z}(\boldsymbol{k}) \quad \textbf{(1.21)}$$

By substituting M_z from **Equation (1.11)** and $cos^2\beta$ from **Equation (1.20)**, the Local magnetic Field Shift (LFS) relative to the static magnetic field can be calculated as (43):

$$LFS(\boldsymbol{k}) = \frac{\Delta \boldsymbol{B_z}(\boldsymbol{k})}{B_o} = \left(\frac{1}{3} - \frac{k_z^2}{k_x^2 + k_y^2 + k_z^2} \right) . \chi(\boldsymbol{k}) \quad \textbf{(1.22)}$$

This equation can be inverted to calculate the susceptibility distribution from $LFS(\boldsymbol{k})$, where $LFS(\boldsymbol{r})$ can be calculated as the time evolution of a phase difference $\Delta\varphi$ between two voxels, as per **Equation (1.12)**.

However, **Equation (1.22)** cannot be solved when $k_z^2 = k_x^2 + k_y^2$, which occurs at the 'magic angle 'when $\beta = 54.7°$. Thus, the inversion process is ill-posed, and must be solved numerically using regularized methods. Susceptibility maps are calculated throughout this thesis using Total

Variation (TV) regularization (44,45), which is a form of L1 regularization. TV regularization is a convex minimization procedure via a non-linear recovery scheme, which means that the coefficient of variation of the signal does not behave in the same manner as its standard deviation (**Figure 1.16**), as was observed earlier in Tikhonov regularization employed in RESHARP (**Figure 1.14**). This translates to a visible difference contrast with different TV regularization parameters (**Figure 1.17**).

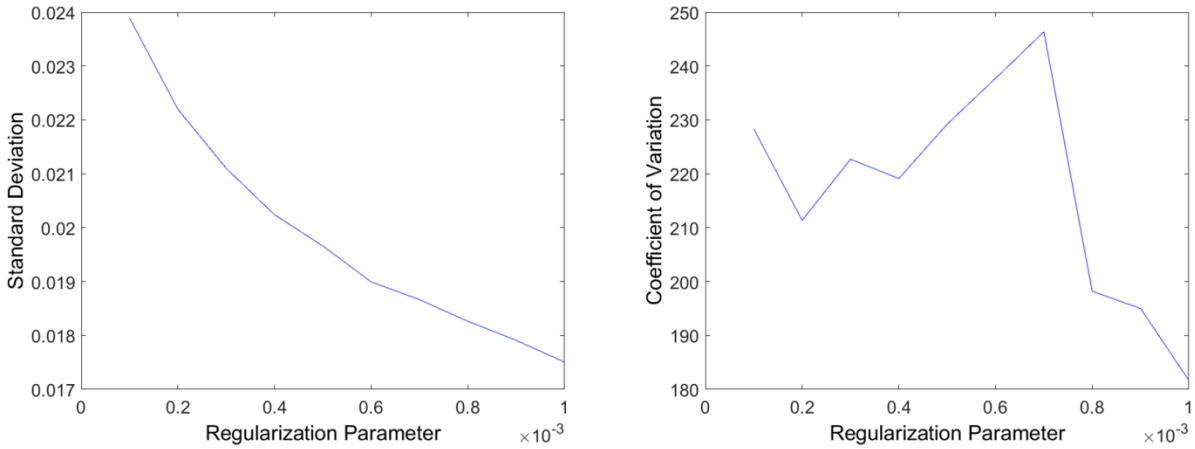

Figure 1.16 Standard deviation of QS (left; units of y-axis are in ppm) decreases exponentially with increase in TV regularization parameter. Since this regularization procedure is a non-linear process, the coefficient of variation (right) behaves in a non-linear fashion.

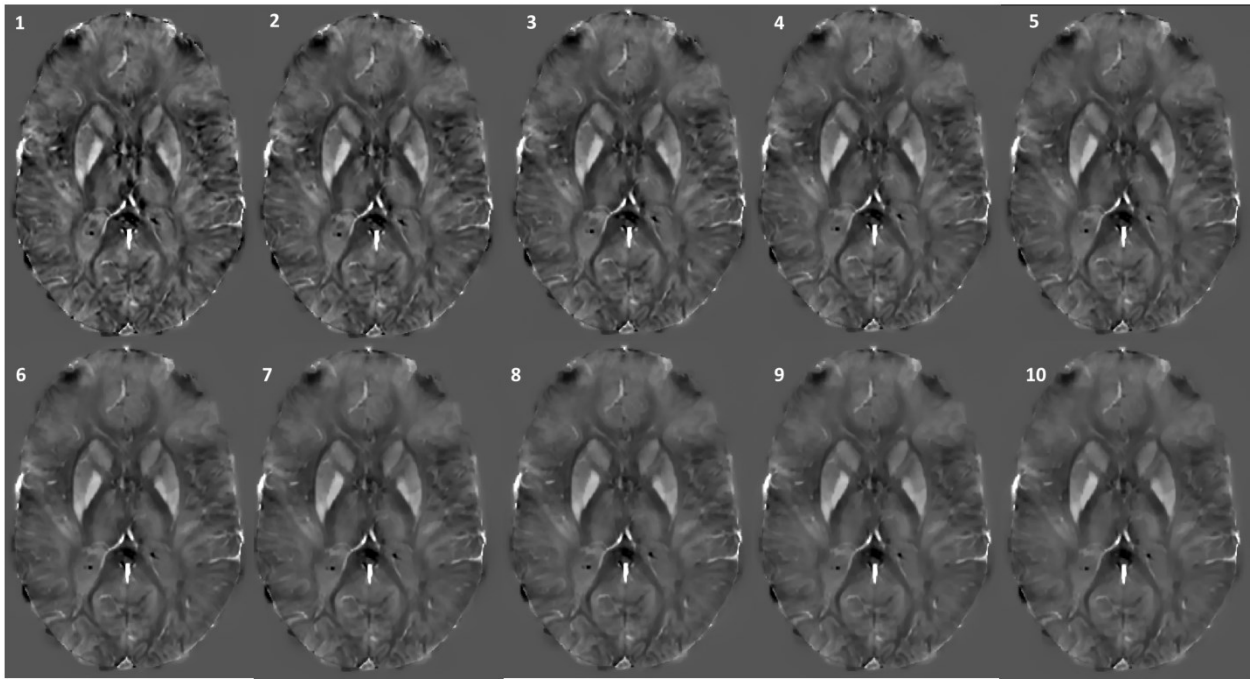

Figure 1.17 Quantitative susceptibility maps calculated using Total Variation (TV) regularization with regularization parameters from $1x10^{-4}$ to $1x10^{-3}$ in steps of $1x10^{-4}$ demonstrate the increased smoothness of maps with increasing RV regularization parameter, decreased structural details, and the non-linear dependence of the coefficient of variation of the maps with increasing regularization parameters. Similar to RESHARP parameters, choice of field inversion reconstruction parameters should be performed empirically to ensure reasonable smoothness of the image while preserving as much structural details as possible. Images are scaled between -0.1 and 0.2 ppm.

1.2.Iron & Myelin in the Brain

1.2.1.Biodistribution

1.2.1.1.Iron

There is a total amount of approximately 5 grams of iron in the body, with 65% present in red blood cells/reticulocytes, 30% as ferritin in macrophages/microglia in the reticuloendothelial system (e.g. the liver and the spleen), 4% as myoglobin within the muscle, 1% oxidation-promoting intra-cellular heme compounds, and 0.1% transported in blood plasma as Fe3+ bound to transferrin. Since iron is an essential component of metabolic processes in the brain, several pathways exist to transport iron across the blood brain barrier. The most important pathway is through transferrin receptors expressed on endothelial cells of the blood brain barrier. These

receptors capture circulating transferring compounds with bound Fe3+, internalize them into an endosome, and transport them using divalent metal transporter 1 (DMT 1) (5).

In addition to transporting iron across the blood brain barrier, the brain maintains a homeostasis of iron by regulating its traffic into neurons, oligodendrocytes, and glial cells. Iron has been observed in various brain tissues; very little iron has been detected in major white matter fiber bundle regions, such as the corpus callosum and optic radiation (46), some iron has been observed in cortical gray matter, cortical white matter and subcortical white matter (WM) (47-49). The highest concentrations of brain iron are observed in deep gray matter structures, which are often associated with glial cells (49). At the microscopic scale, the most consistent iron staining is typically observed in microglia and oligodendrocytes (47).

Iron can exist in biological tissue in a stored form of Ferric iron (Fe^{3+}) or a reactive form of Ferrous iron (Fe^{2+}). Despite its requirement in various metabolic processes, the cell maintains a zero cytosolic level of 'free' ferrous iron because of its ability to form toxic free radicals. Thus, a *labile iron pool* of approximately 1 μM ferrous iron is maintained within the cell's cytosol using aqua-irons and/or low-molecular-weight ligands. The bulk of cellular iron is present as Ferric iron in a *storage iron pool* bound to various proteins, with the majority stored associated with the ferritin protein. In an incompletely understood process, the *labile iron pool* and the *stored iron pool* are regulated through iron metellochaperones that direct iron to ferritin and iron-requiring enzymes, and also through ferritinophagy, where bound ferric iron is released from ferritin after being autophagocytosyzed in a lysosome (4).

1.2.1.2.Myelin

The Central Nervous system (CNS) is characterized by myelin sheaths to accelerate nerve conduction through the long axons of the CNS. Myelin consists of multiple (5,20) phospholipid bilayers and is formed and maintained by oligodendrocytes, which are the most frequent glial cell in the brain. Dimensions of CNS myelin sheaths are coupled with the axon diameter, with myelin sheaths of large axons differing in lipid and protein composition compared to small axons (50).

1.2.2.Effects of on Healthy Development & Aging

1.2.2.1.Iron

In addition to its utility in various metabolic processes in the brain, iron accumulation is a well-established effect that occurs with healthy aging. In a landmark study by Halggren & Sourander (49), samples from 98 *postmortem* subject of various ages were quantitatively analyzed for iron content on a fresh-weight basis. The highest concentration of the body was found to be in the Globus Pallidus (21.30 mg iron/100 g fresh weight), which was even higher than the liver (13.44 mg iron/100 g fresh weight). Very little iron is found in the deep gray matter (DGM) at birth, but increases rapidly during the first two decades. For the globus pallidus, no further increase occurs after age of 30, but for the caudate nucleus and putamen iron increases somewhat slowly until it reaches a maximum value before the age of 50-60. Although the red nucleus and subtantia nigra demonstrated similar rapid increases in the first two decades, quantified iron levels demonstrated large variations partly due to difficulties in dissecting these small structures. The thalamus displayed a unique non-linear iron accumulation trajectory which peaked at the age of around 35.

Iron deficiency due to diet choices has been found to significantly ($P<0.05$) affect the cognitive performance among non-anemic school-aged children and adolescents (51). Furthermore, diet choices were found to influence iron levels in the DGM of healthy adults, as measured by phase MRI (52). Moreover, transverse MRI relaxation rate, R2*, in the neocortex was found to be associated with body mass index, while smoking status was associated with R2* in the DGM (53).

1.2.2.2.Myelin

Studies investigating white matter changes with aging have been less subtle. Histological studies in the rhesus monkey have observed a decrease in the total number of myelinated nerve fibers and alterations in the myelin sheath (54). In human neuroimaging studies, there was a global and regional decrease in white matter volume with aging (55). Diffusion tensor imaging studies have also pointed out reduced diffusivity and increased anisotropy throughout childhood and

adolescence development stages (56). The correlation of improved cognitive performance with decreased diffusivity and increased anisotropy (57) has led to the assumption that these observations characterize myelination and axonal pruning (58). As young adults age, a decrease in global WM volume, and increase in global diffusivity are observed, with individuals older than 60 years old demonstrating the strongest correlations with white matter tissue deterioration measures (59).

Myelin integrity, as measured by diffusion tensor imaging, was also found to be strongly correlated with blood iron levels in healthy young adults (60), which links iron and myelin in the process of healthy development/aging.

1.2.3. Effects on MRI Contrast

1.2.3.1. Iron

Ferric iron is the main contributor to MRI contrast in the brain, because ferrous iron is diamagnetic, and its distribution is too low and diffuse to be detected by MRI. Theoretical estimates of iron's contribution indicate that a susceptibility difference of 1.4 ppb is observed for each 1 μg iron / 1 g tissue (3). Field inhomogeneities created by susceptibility differences between iron and biological tissue should theoretically cause an increase in the transverse relaxation rate, R2*, of 0.11 $s^{-1}.T^{-1}$ for each 1 ppb susceptibility difference caused by spherical iron particles (11). However, actual estimates of proportionality constant relating $\Delta\chi$ and R_2^* are close to half the values predicted theoretically (61,62), most likely due to diffusion averaging due to motion of spins through field gradients surrounding a ferritin particle (4).

1.2.3.2. Myelin

Water protons are thought to be compartmentalized within the axonal space, the interstitial space, and between myelin wraps. The latter is often a target for MRI quantification of myelin using quantification of the short component (<20 ms) of T2 relaxation (63). In terms of susceptibility, myelin presents as diamagnetic compared to cerebrospinal fluid, mainly due to the

phospholipid bilayers in myelin (64). QSM provides estimates of myelin's susceptibility range from -13 to -34 ppb (4). However, the cylindrical shape and orientation of nerve fibers encapsulated by myelin affects the measured susceptibility of myelin. Theoretical estimates predict R2* linearly increases with axonal myelin susceptibility as a function of the fiber orientation (**Equation 1.14**), which assumes diffusion effects and susceptibility anisotropy can be neglected (11). However, experimentally determined values for the proportionality coefficient between $\Delta R2^*$ and $\Delta\chi \sin^2\theta$ is somewhat lower than theoretical estimates, which confirms the importance of considering diffusion effects and anisotropic properties of myelin's bilayers (4). Additionally, compartment-specific R2* relaxation and frequency shifts of WM has been confirmed experimentally (65,66), but simulations indicate the effects of NMR-invisible microstructure on WM susceptibility contrast may be larger than the anisotropic effects of susceptibility (67).

1.2.4. Confounding Effects of Myelin and Iron

Not only does iron co-localize with myelin in normal appearing subcortical WM (68), but iron and myelin changes are associated closely in the brains of MS patients. For instance, iron-laden macrophages at the edges and demyelination-associated centric iron-loss are found in WM (69) and DGM (70) lesions.

R2* and susceptibility quantified from gradient echo MRI acquisitions can offer complementary information about iron and myelin concentrations. While iron and myelin have opposing para/diamagnetic susceptibilities, they exhibit similar effects on the transverse relaxation rate R_2^*. Joint regression of myelin and iron tissue concentration with quantified R2* and susceptibility values has produced better correlations compared to independent regressions of iron and myelin (71). Furthermore, multi-angle QSM combined with R2* quantification has been shown to produce brain maps indicative of iron and myelin concentrations (72). Accordingly, combined R2* and QSM has been used to qualitatively stage Gd-enhancing WM lesions in MS (73).

1.3.Multiple Sclerosis

Multiple Sclerosis (MS) is a chronic inflammatory disease of the brain and spinal cord occurring on a background of axonal and neuronal loss (74). The following section briefly outlines some aspects of the disease, in addition to a brief discussion of brain iron and myelin in MS compared to the healthy brain.

1.3.1.Epidemiology

MS is primarily diagnosed in young adults, with age of onset inversely correlating with distance from equator (75). Incidence also increases with distance from equator, with Canada reportedly having the highest rate worldwide. However, fewer diagnostic tools are available in countries closer to equator, which may contribute to a larger number of underreported cases in those countries (76), which is also confirmed by the attenuation of the latitude gradient after 1980 (77).

1.3.2.Clinical features

MS risk factors include age between 15 and 60, female gender, family history of MS, previous viral infections, Caucasian race, residence in northern hemisphere, comorbidity of certain autoimmune diseases, such as thyroid disease, type 1 diabetes, or inflammatory bowel disease, Vitamin D deficiency, and smoking (78,79).

Symptoms vary widely between different MS patients, depending on their disease course and the location of affected nerve fibers. These symptoms may include motor symptoms, imbalance, sensory and/or cognitive impairment, depression, fatigue, bladder and bowel dysfunction, heat sensitivity, headache, and double vision (80).

1.3.3. Clinical phenotypes

The US National Multiple Sclerosis Society Advisory Committee on Clinical Trials in Multiple Sclerosis has adopted the following consensus terminology to describe different MS clinical phenotypes (81,82):

- *Clinically Isolated Syndrome (CIS)*: The first clinical presentation of MS showing potential MS inflammatory demyelination, but has not yet fulfilled the MacDonald's criteria of time dissemination.
- Relapsing-remitting MS (RRMS): A disease course that features relapses that are clearly defined, but with full recovery or sequalae and residual deficit after recovery. Remission periods are characterized by a lack of disease progression.
- Secondary Progressive MS (SPMS): Subsequent to an initial RRMS disease course, a progressive disease course with or without intermittent relapses, minor remissions, and plateaus.
- Primary progressive MS (PPMS): Progressive disease course from onset, with intermittent plateaus that may include temporary minor improvements.

1.3.4. Pathology

1.3.4.1. The Blood Brain Barrier

The Blood Brain Barrier (BBB) is a barrier formed of tight junctions of epithelial cells that separates the circulating blood in the brain from the extracellular fluid in the central nervous system. The BBB selectively allows passage of some substances, such as glucose and amino acids, and blocks the passage of neurotoxins and immune white blood cells that may disrupt the function of the brain. In MS, BBB leakage occurs at the time of an MS attack, which can be detected using Gd-enhanced T1-weighted MRI (83).

1.3.4.2.Immune Cells

The main mediator of MS pathology is thought to be T-cells. CD4 and CD8 are T cells that cross the leaking BBB, propagate an inflammatory immune response, and initiate cellular damage in the brain. CD4 are helper T cells that divide rapidly and secrete small proteins called cytokines upon activation by antigens on the surface of Antigen Presenting Cells (APC). In MS, CD 4 cells stimulate an inflammatory response and produce pro-inflammatory cytokines upon activation by APCs such as dendritic cells, microglia, astrocytes and B-cells. Interferon therapies in MS aim to convert the pro-inflammatory response of CD4 cells to an anti-inflammatory response. CD 8 cells, on the other hand, have a non-specific immune response and release cytokines that cause damage to glial cells, axons, and promotes BBB dysfunction. CD 8 cell also cause damage directly in the brain by releasing toxic proteins, such as perforin, granzyme, and lymphotoxin (84).

Other immune cells that are associated with the secondary response in MS pathology include B-cells, peripheral macrophages and microglial cells. B-cells are white blood lymphocytes that secret antibodies that take part in the humoral immunity component of the adaptive immune system. In MS, B-cells can contribute to pathology by several mechanisms, such as forming meningeal follicles, producing an immune response to myelin oligodendrocyte glycoprotein or myelin basic protein, or upregulating general immunoglobin production secondary to white matter injury. In addition to their role in phagocytosis of debris from demyelinating lesions and other cellular debris, macrophages and microglial cells mediate cellular damage by producing proteolytic and lipolytic enzymes, complement component, cytotoxic cytokines, and nitric-oxide free radicals (85).

1.3.4.3.Damage & Repair Cells

MS damage in the brain can occur to myelin sheath, myelin-producing oligodendrocytes, and neurons. Damage to myelin and oligodendrocytes is primarily caused by pro-inflammatory cytokines, oxidative stress and excitotoxicity, while neuronal dysfunction occurs to mechanisms

such as damage of naked axons by reactive oxygen species and proteases, direct damage by CD8 cells and macrophages, mitochondrial dysfunction, glutamate mediated excitotoxicity, energy imbalance from dysfunction of ions channels, and loss of trophic support from absent myelin or synapses. Repair of myelin is performed by oligodendrocytes, while replenishment of oligodendrocytes is achieved by neighboring cursor cells that are stimulated to differentiate and propagate. To account for absence of other cells during MS neurodegeneration, astrocytes form a dense fibrillary network in chronic MS tissue (85).

1.3.4.4.Lesions

Regions of the central nervous system that incur an apparent damage are called lesions. Two classifications of lesions exists: a staging system based on postmortem samples that has been developed by Bo and Trapp that labels lesions as active, chronic active, and chronic inactive, and a classification based on in vivo biopsied samples that classifies lesions into early active, late active, early remyelinating, and late remyelinating lesions.

Earlier lesions are characterized by the presence of macrophage and microglia, fewer oligodendrocytes, decreased myelin density compared to normal appearing white matter, and hypercellularity. Chronic lesions are hypocellular, contain few mature oligodendrocytes, have decreased presence of T-cells and macrophages, suffer from severe axonal loss, and scar-forming astrocyte networks replace absent healthy tissue. Chronic active lesion are a temporary stage that connects early and chronic lesions, and they have an active border with a chronic center (84).

1.3.5.Diagnosis

Although more updated diagnosis guidelines have been published (86), patient studies included in this thesis have utilized the 2010 Revised MacDonald Criteria for diagnosis of MS (87). These criteria employ clinical and MRI evidence of CNS damage to confirm an MS diagnosis, as shown in **Figure 1.18**. Clinical evidence of MS damage can be demonstrated by two or more attacks, where an attack, also known as a relapse or exacerbation, are defined as “patient-

reported or objectively observed events typical of an acute inflammatory demyelinating event in the CNS, current or historical, with duration of at least 24 hours, in the absence of a fever or infection." MRI evidence can be demonstrated by dissemination in space or time. Dissemination in space can be demonstrated by hyperintense lesions on T2-weighted MRI in two or more of periventricular, juxtacortical, infratentroial, or spinal cord regions. Dissemination in time can be demonstrated by MRI evidence of a new T2 and/or gadolinium enhancing lesion on follow-up MRI over time (irrespective of the time of baseline scanning), or asymptomatic gadolinium-enhancing lesion occurring simultaneously with non-enhancing lesions. Not shown in **Figure 1.18** is the diagnosis of insidious neurological progression suggestive of MS, also known as PPMS, which can be diagnosed using 1 year of disease progression (retrospectively or prospectively determine), in addition to evidence of dissemination in space in the brain for ≥1 lesions or the spinal cord for ≥2 lesions, or positive cerebrospinal isoelectric focusing evidence of oligoclonal bands and/or elevated IgG index (87).

1.3.6. Treatment

Introduced in the 1990s, injectable Disease Modifying Therapy (DMT) beta-interferons have been used as the first-line of MS treatment because of their established efficacy and safety. More recently, alternative DMT options have been introduced, including intravenous monoclonal antibodies, and oral therapies, which are usually presented after disease modifying therapies are deemed ineffective, or in the case of highly aggressive disease course (88). Currently, 16 drugs are approved by Health Canada and the United States Food and Drug Administration for treating RRMS, 10 are approved for treating SPMS, but the only drug approved for treating PPMS is Ocrevus™ (ocrelizumab) (89), which is a monoclonal antibody.

1.3.7. MRI as an Outcome Measure in MS Clinical Trials

For every new MS attack, 10 to 15 new lesions are formed (90). New lesion formation, as measured by gadolinium-enhanced MRI, has been shown to accurately predict the effect of therapy in phase II clinical trials (91). However, gadolinium has been shown to accumulate in the

dentate nucleus (92), bones, and kidneys, and there is significant *in vitro*, animal and human data that suggests the potential for rare (2-4% of patients) acute reactions and Nephrogenic systemic fibrosis in patients with renal failure for repeated exposure to gadolinium (93). Additionally, gadolinium MRI only detects some newly formed lesions upon leakage of the BBB, and not all lesions (94). Moreover, Gadolinium contrast adds substantial expense to the evaluation of MS by MR imaging, because of the cost of the contrast, its administration cost, and the additional scanning time necessary to obtain the postgadolinium images (95). Thus, alternative MRI biomarkers that correlate with clinical disease measures are needed.

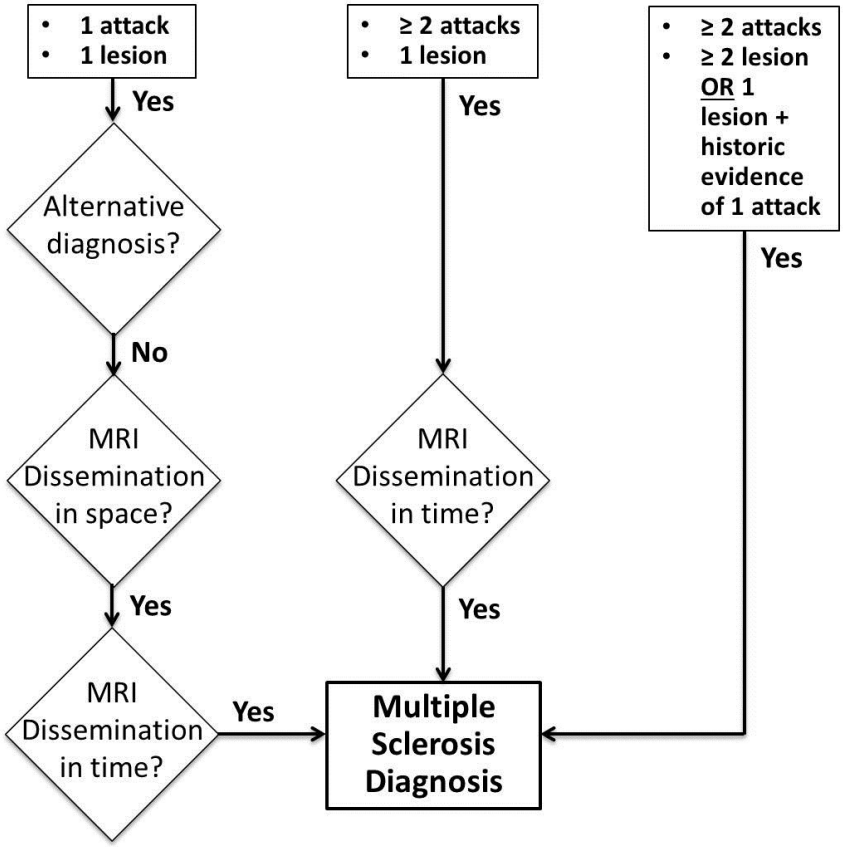

Figure 1.18 MS diagnosis flowchart according to the 2010 revised MacDonald criteria.

Furthermore, gadolinium-enhanced MRI is only a measure of BBB leakage in new demyelinating white matter lesions enhanced with gadolonium. Although neurodegeneration has generated much interest in MS (96), a similarly widely accepted phase II outcome measure for

assessing neurodegeneration in MS is still unavailable (97), although whole brain atrophy (98) has been recently adopted as a primary outcome measure in phase II SPMS clinical trials (99,100). Other MRI measures of neurodegeneration that have been suggested as phase II outcomes, such as gray matter atrophy (101) and gray matter lesions (102), have been proposed as potential surrogate outcomes for neurodegeneration in clinical trials, but none of the proposed methods have been widely adopted yet (97).

1.4. Brain Deep Gray Matter Tissue

1.4.1. Function

Deep gray matter tissue of the brain includes subcortical gray matter nuclei that contain neuronal cell bodies which project and receive connections to other parts of the Central Nervous System, including the cortex, brainstem, other subcortical nuclei, and the spinal cord. The deep grey matter structures studied in this thesis include the Caudate Nucleus (CN), Putamen (PU), Globus Pallidus (GP), Substantia Nigra (SN), Red Nucleus (RN), Dentate Nucleus (DN), and Thalamus (TH).

The CN, PU, GP, and SN are part of the basal ganglia, which is responsible for regulating motor functions, various cognitive functions, procedural learning, and emotional functions (103). Feedback loops are used by the brain to modulate cortical areas or nuclei after processing in basal ganglia nuclei via five major feedback loops: a motor circuit, an oculomotor circuit, a dorsolateral prefrontal circuit, a lateral orbitofrontal circuit, and an anterior cingulate circuit. Dysfunction in the CN was associated with cognitive deficits in Huntington's disease, while PU dysfunction was linked to positive motor symptoms such as chorea. Dysfunction in the ventral striatum (consisting of the ventral part of the CN and PU) has also been associated with emotional changes. Negative motor and emotional symptoms in Parkinson's disease has been also been linked to loss of dopaminergic neurons in the SN pars compacta. Regardless of the basal ganglia region being affected, dysfunction in one nucleus can have a cascading in one or several additional nuclei because of their interdependence within cortical circuitry.

In contrast to the diffuse anatomical regions of the basal ganglia, the thalamus contains many distinct anatomic and functional regions. All sensory information into the cortex (excluding the olfactory system) must first pass through the thalamus. Functionally, the thalamus can be classified into relay nuclei that receive a distinct input bundle and project to a specific cortical area, and association nuclei that contribute to gating cortical information and project to cortical areas.

Located in the rostral midbrain, the RN receives afferents from deep cerebellar nuclei and the cerebral cortex. The DN is the largest single structure linking the cerebellum to the rest of the brain. The DN and RN are thought to be part of cerebellar circuitry responsible for planning, initiation and control of voluntary movements.

1.4.2.Pathology in MS

DGM pathology in MS has been studied using animal models, postmortem human tissue, and nuclear medicine examinations. Invasive examination of the experimental autoimmune encephalomyelitis (EAE) rat model has associated changes in cannabinoid receptors in the DGM with motor behavior, cognition, and memory (104).

1.4.2.1.Animal Studies

Demyelinating cuprizone injections in the basal ganglia of mice have demonstrated increased fatigue, cognitive dysfunction, and movement disturbances (105). However, animal studies were unable to decipher whether DGM damage in MS is a result of primary or secondary pathology (106).

1.4.2.2.Postmortem Studies

As early as 2002 (107), several studies have investigated DGM pathology in postmortem MS samples (70,108,109). Mean thalamic neuronal density and mean volumes of thalamic medial

dorsal nucleus was reduced in MS patients compared to controls, indicating a total 35% MS-associated reduction in thalamic neuronal numbers (107). Frequent demyelinating DGM lesions were observed in a histologic examination of 14 MS patient compared to 6 control brains. Most of these lesions involved both gray and white matter damage, but the extent of white matter damage was less. Inflammation in active DGM lesion was intermediate between disparaging white matter lesions and low inflammation of cortical lesions. Activated microglia were abundant in DGM lesions, but myelin-laden macrophages were rare (108). A more recent study (70) of 75 MS autopsy sample compared to 12 controls confirmed these findings, and revealed that demyelination of the caudate nucleus and hypothalamus were the most prominent, and could already be seen in early MS stages. Furthermore, the study revealed that DGM demyelination and neurodegeneration was associated with oxidative injury, and iron that was stored in oligodendrocytes was released upon demyelination. Regression analysis of Expanded Disability Status Scale (EDSS) on different variables indicated that focal lesions and diffuse neurodegeneration in the DGM appeared to contribute to disability.

1.4.2.3.Nuclear Medicine Studies

Fludeoxyglucose (^{18}F) is a radiopharmaceutical label used in Positron Emission Tomography (PET) to measure tissue glucose as a metabolic indicator of brain function (110). PET studies have revealed that the thalamus of the MS patients is significantly different compared to controls (111), which has correlated with memory dysfunction (112). Additionally, glucose reduction in the putamen and associated basal ganglia circuitry regions of the prefrontal cortex and supplemental motor area have correlated with fatigue (113).

1.4.2.4.In Vivo MRI Studies

In vivo, iron accumulation has been a common interpretation of observed cross-sectional increase in phase imaging (38,114-118), magnetic field correlation (119), quantitative susceptibility (120-122), R2' (123), R2 (38,124-130), and R2* (120,131-135) of the DGM. Combined analysis of atrophy and R2* of the DGM of MS patients compared to controls has been interpreted as due to

iron decrease in the MS DGM (136). Similarly, decreased thalamic susceptibility in MS patients compared to controls (137) and decreased susceptibility changes in the caudate nucleus compared to expected changes from theoretical simulations (121) were interpreted as iron decrease.

T1-weighted imaging has been used extensively to study changes in DGM atrophy in MS, which has been commonly interpreted as glial or neuronal loss. A study of PPMS patients (138) revealed that DGM volume loss was more pronounced compared to controls. Thalamic changes in volume and structural connectivity predicted cognitive performance in MS (139). DGM atrophy was also found to be correlated with T2 lesion volume (140). A large *in vivo* MRI study of 1,214 MS patients has demonstrated that DGM volume loss drives disease progression, especially in progressive forms of the disease (101). The most commonly involved DGM structures experiencing atrophy are the CN, PU and TH, which may be caused by dysfunction of afferent cortical connections that can potentiate pathology through loss of trophic support, excitotoxicity, and other factors.

Dynamic susceptibility contrast perfusion of MS patients has demonstrated a significant difference in tissue perfusion compared to controls, which has been associated with fatigue severity (141). Thalamic magnetization transfer ratio was reduced in MS compared to controls, and the extent of their volume loss was correlated with long term disability (142). Although diffusion MRI is an important tool that measures the restricted/hindered motion of water molecules and has been used to study the DGM of pediatric spina bifida (143), thalamus connectivity in MS (139), and gray matter of MS (144), no diffusion MRI study has yet been dedicated for evaluating MS DGM, to the best of our knowledge. Additionally, myelin water fraction has not been applied to MS DGM, despite its valuable application to studying MS white matter lesions (145).

1.5.Thesis Overview

1.5.1.Problem Statement

Although gray matter damage has been shown as the only longitudinal predictor of disability and cognitive impairment in MS after 13 years (146), the focus of most MRI research has been developing and applying T2-weighted and Gd-enhanced T1-weighted MRI to evaluate lesions (97). More research is needed to develop and apply gradient-echo MRI to the study of MS to elucidate the neurodegenerative component of the disease. By producing "maps of meaningful physical or chemical variables that can be measured in physical units and compared between tissue regions and among subjects" (147), quantitative gradient-echo MRI techniques offer the potential to replace conventional qualitative MRI techniques as a sensitive measure of pathological changes and clinical measures in MS.

1.5.2.Global Hypothesis

The purpose of this thesis is to develop technical MRI innovations and to study research applications to further the field of quantitative gradient-echo MRI of MS. The main clinical hypothesis is that quantitative gradient-echo MRI methods may serve as a biomarker of disease progression in MS. We will test this hypothesis in one cross-sectional study and two longitudinal studies of MS subjects compared to age-matched controls, and relate MRI findings to clinical outcomes.

1.5.3.Technical Innovations

Although lesions are the main focus of MRI research, the shape and conspicuity of lesions in MS using quantitative gradient-echo MRI has not been thoroughly studied at the time of performing this research. We have presented in Chapter 2 an evaluation of the contrast of Local Frequency Shift (LFS) and Quantitative Susceptibility (QS), quantified from multiple-echo gradient-echo acquisitions, in lesions relative to surrounding normal appearing white matter tissue. We have

also evaluated the feasibility of using dipole signature as an indication of the presence of lesion iron in MS.

To explore the clinical relevance of using QS mapping in the clinic, we explored in Chapter 3 the feasibility of accelerating acquisitions by restricting the field of view (FOV) to deep gray matter structures. Patient compliance and motion are common issues that MS studies, and the simplest solution for accelerating an MRI acquisition is using a smaller field of view. We have demonstrated through theoretical simulations and *in vivo* data that QSM is sensitive to field of view, and presented the limits of accurate quantification of DGM susceptibility.

Using combined R2* and QS maps of MS patients compared to controls, we have presented in Chapter 4 a novel sparse logistic regression technique for localized cross-sectional analysis of sparse regions indicative of DGM pathological iron and myelin. We have also presented in Chapter 5 a novel technique for discriminative analysis of regional evolution (DARE) of iron and myelin/calcium in longitudinal MS data compared to controls using combined R2* and QS data.

1.5.4. Research Applications

In Chapter 4, we have applied sparse logistic regression to 16 CIS subjects, 41 RRMS, 40 SPMS, and 13 PPMS patients, and corresponding age-matched controls, and present the results of this analysis compared to conventional singular R2* and QS analysis. We also correlate all measurements with clinical measures.

Longitudinally, we have studied in Chapter 5 2-year changes in R2* and QS of bulk structures and regions identified by DARE in 27 RRMS and 17 PMS subjects compared to age-matched controls. Similarly, in Chapter 6 we have evaluated longer term changes over 5-years in R2* and QS of bulk structures and regions identified by DARE in 22 RRMS subjects compared to age/sex-matched controls. We also correlate measurements that were significantly different between patients and controls with clinical measures.

References

1. Paul T. Callaghan. Principles of nuclear magnetic resonance microscopy. Oxford University Press on Demand: 1993.
2. Haacke EM & Reichenbach JR. Susceptibility weighted imaging in MRI: basic concepts and clinical applications. John Wiley & Sons: 2014.
3. Schenck JF. Health and Physiological Effects of Human Exposure to Whole-Body Four-Tesla Magnetic Fields during MRI. Ann N Y Acad Sci 1992:649:285-301.
4. Duyn JH & Schenck J. Contributions to magnetic susceptibility of brain tissue. NMR Biomed 2017:30.
5. Wang Y. Quantitative susceptibility mapping: magnetic resonance imaging of tissue magnetism. CreateSpace: 2013.
6. Carr HY & Purcell EM. Effects of diffusion on free precession in nuclear magnetic resonance experiments. Physical review 1954:94:630.
7. Meiboom S & Gill D. Modified spin-echo method for measuring nuclear relaxation times. Rev Sci Instrum 1958:29:688-691.
8. Haacke EM, Liu S, Buch S, Zheng W, Wu D & Ye Y. Quantitative susceptibility mapping: current status and future directions. Magn Reson Imaging 2015:33:1-25.
9. Fernández-Seara M & Wehrli F. Postprocessing technique to correct for background gradients in image-based R* 2 measurements. Magnetic resonance in medicine 2000:44:358-366.
10. Muller RN, Gillis P, Moiny F & Roch A. Transverse relaxivity of particulate MRI contrast media: from theories to experiments. Magnetic resonance in medicine 1991:22:178-182.
11. Yablonskiy DA & Haacke EM. Theory of NMR signal behavior in magnetically inhomogeneous tissues: the static dephasing regime. Magnetic resonance in medicine 1994:32:749-763.
12. He X & Yablonskiy DA. Biophysical mechanisms of phase contrast in gradient echo MRI. Proc Natl Acad Sci U S A 2009:106:13558-13563.
13. CJ Wiggins, V. Gudmundsdottir, D. Le Bihan, V. Lebon and M. Chaumeil. Orientation dependence of white matter T2* contrast at 7 T: a direct demonstration. In: Proceedings of the 16th Annual Meeting of ISMRM, Toronto, Canada, 2008.
14. Bender B & Klose U. The in vivo influence of white matter fiber orientation towards B0 on T2* in the human brain. NMR Biomed 2010:23:1071-1076.
15. Denk C, Torres EH, MacKay A & Rauscher A. The influence of white matter fibre orientation on MR signal phase and decay. NMR Biomed 2011:24:246-252.
16. Lee J, van Gelderen P, Kuo L, Merkle H, Silva AC & Duyn JH. T2*-based fiber orientation mapping. Neuroimage 2011:57:225-234.
17. Sati P, Silva AC, van Gelderen P, et al. In vivo quantification of T2 anisotropy in white matter fibers in marmoset monkeys. Neuroimage 2012:59:979-985.
18. Liu C. Susceptibility tensor imaging. Magnetic resonance in medicine 2010:63:1471-1477.
19. Bloom M, Burnell EE, MacKay AL, Nichol CP, Valic MI & Weeks G. Fatty acyl chain order in lecithin model membranes determined from proton magnetic resonance. Biochemistry (N Y) 1978:17:5750-5762.
20. Lounila J, Ala-Korpela M, Jokisaari J, Savolainen M & Kesäniemi Y. Effects of orientational order and particle size on the NMR line positions of lipoproteins. Phys Rev Lett 1994:72:4049.
21. Lonsdale K. Diamagnetic anisotropy of organic molecules. Proc.R.Soc.Lond.A 1939:171:541-568.

22. Lee J, Shmueli K, Fukunaga M, et al. Sensitivity of MRI resonance frequency to the orientation of brain tissue microstructure. Proc Natl Acad Sci U S A 2010:107:5130-5135.
23. Lim IAL, Faria AV, Li X, et al. Human brain atlas for automated region of interest selection in quantitative susceptibility mapping: application to determine iron content in deep gray matter structures. Neuroimage 2013:82:449-469.
24. Sun H & Wilman AH. Background field removal using spherical mean value filtering and Tikhonov regularization. Magn Reson Med 2013:71:1151-7.
25. Alonso-Ortiz E, Levesque IR & Pike GB. MRI-based myelin water imaging: A technical review. Magnetic resonance in medicine 2015:73:70-81.
26. de Rochefort L, Liu T, Kressler B, et al. Quantitative susceptibility map reconstruction from MR phase data using bayesian regularization: validation and application to brain imaging. Magn Reson Med 2010:63:194-206.
27. Liu J, Liu T, de Rochefort L, et al. Morphology enabled dipole inversion for quantitative susceptibility mapping using structural consistency between the magnitude image and the susceptibility map. Neuroimage 2012:59:2560-2568.
28. Shmueli K, de Zwart JA, van Gelderen P, Li TQ, Dodd SJ & Duyn JH. Magnetic susceptibility mapping of brain tissue in vivo using MRI phase data. Magn Reson Med 2009:62:1510-1522.
29. Liu T, Spincemaille P, De Rochefort L, Kressler B & Wang Y. Calculation of susceptibility through multiple orientation sampling (COSMOS): a method for conditioning the inverse problem from measured magnetic field map to susceptibility source image in MRI. Magnetic Resonance in Medicine 2009:61:196-204.
30. Liu C, Li W, Tong KA, Yeom KW & Kuzminski S. Susceptibility-weighted imaging and quantitative susceptibility mapping in the brain. Journal of magnetic resonance imaging 2015:42:23-41.
31. Schweser F, Deistung A, Lehr BW & Reichenbach JR. Quantitative imaging of intrinsic magnetic tissue properties using MRI signal phase: an approach to in vivo brain iron metabolism? Neuroimage 2011:54:2789-2807.
32. Roemer, P.B., Edelstein, W.A., Hayes, C.E., Souza, S.P. and Mueller, O.M., 1990. The NMR phased array. Magnetic resonance in medicine, 16(2), pp.192-225.
33. Robinson S, Grabner G, Witoszynskyj S & Trattnig S. Combining phase images from multi-channel RF coils using 3D phase offset maps derived from a dual-echo scan. Magnetic resonance in medicine 2011:65:1638-1648.
34. Sun H. Quantitative Susceptibility Mapping in Human Brain: Methods Development and Applications 2015.
35. Jenkinson M. Fast, automated, N-dimensional phase-unwrapping algorithm. Magn Reson Med 2003:49:193-197.
36. Gilbert G, Savard G, Bard C & Beaudoin G. Quantitative comparison between a multiecho sequence and a single-echo sequence for susceptibility-weighted phase imaging. Magn Reson Imaging 2012:30:722-730.
37. Haacke EM, Xu Y, Cheng YC & Reichenbach JR. Susceptibility weighted imaging (SWI). Magn Reson Med 2004:52:612-618.
38. Walsh AJ & Wilman AH. Susceptibility phase imaging with comparison to R2 mapping of iron-rich deep grey matter. Neuroimage 2011:57:452-461.
39. Li L & Leigh JS. High-precision mapping of the magnetic field utilizing the harmonic function mean value property 2001.

40. Jackson JD. Classical Electrodynamics John Wiley & Sons. Inc., New York, 1999.
41. Topfer R, Schweser F, Deistung A, Reichenbach JR & Wilman AH. SHARP edges: recovering cortical phase contrast through harmonic extension. Magn Reson Med 2015:73:851-856.
42. Fang J, Bao L, Li X, van Zijl PC & Chen Z. Background field removal using a region adaptive kernel for quantitative susceptibility mapping of human brain. Journal of Magnetic Resonance 2017:281:130-140.
43. Salomir R, de Senneville BD & Moonen CT. A fast calculation method for magnetic field inhomogeneity due to an arbitrary distribution of bulk susceptibility. Concepts in Magnetic Resonance Part B: Magnetic Resonance Engineering 2003:19:26-34.
44. Bilgic B, Pfefferbaum A, Rohlfing T, Sullivan EV & Adalsteinsson E. MRI estimates of brain iron concentration in normal aging using quantitative susceptibility mapping. Neuroimage 2012:59:2625-2635.
45. Bilgic B, Fan AP, Polimeni JR, et al. Fast quantitative susceptibility mapping with L1-regularization and automatic parameter selection. Magnetic resonance in medicine 2014:72:1444-1459.
46. Norton WT & Cammer W. Isolation and characterization of myelin. In: Anonymous Myelin. Springer: 1984. 147-195 p.
47. Morris C, Candy J, Oakley A, Bloxham C & Edwardson J. Histochemical distribution of non-haem iron in the human brain. Cells Tissues Organs (Print) 1992:144:235-257.
48. Connor J, Menzies S, St Martin S & Mufson E. Cellular distribution of transferrin, ferritin, and iron in normal and aged human brains. J Neurosci Res 1990:27:595-611.
49. Hallgren B & Sourander P. The effect of age on the non-haemin iron in the human brain. J Neurochem 1958:3:41-51.
50. Hildebrand C, Remahl S, Persson H & Bjartmar C. Myelinated nerve fibres in the CNS. Prog Neurobiol 1993:40:319-384.
51. Halterman JS, Kaczorowski JM, Aligne CA, Auinger P & Szilagyi PG. Iron deficiency and cognitive achievement among school-aged children and adolescents in the United States. Pediatrics 2001:107:1381-1386.
52. Hagemeier J, Tong O, Dwyer MG, Schweser F, Ramanathan M & Zivadinov R. Effects of diet on brain iron levels among healthy individuals: an MRI pilot study. Neurobiol Aging 2015:36:1678-1685.
53. Pirpamer L, Hofer E, Gesierich B, et al. Determinants of iron accumulation in the normal aging brain. Neurobiol Aging 2016:43:149-155.
54. Peters A. The Effects of Normal Aging on Nerve Fibers and Neuroglia in the Central Nervous System. In: Riddle DR, editor. Brain Aging: Models, Methods, and Mechanisms. Taylor & Francis Group, LLC: Boca Raton (FL): 2007.
55. Salat DH. The declining infrastructure of the aging brain. Brain connectivity 2011:1:279-293.
56. Cascio CJ, Gerig G & Piven J. Diffusion tensor imaging: Application to the study of the developing brain. J Am Acad Child Adolesc Psychiatry 2007:46:213-223.
57. Beaulieu C, Plewes C, Paulson LA, et al. Imaging brain connectivity in children with diverse reading ability. Neuroimage 2005:25:1266-1271.
58. Suzuki Y, Matsuzawa H, Kwee IL & Nakada T. Absolute eigenvalue diffusion tensor analysis for human brain maturation. NMR Biomed 2003:16:257-260.
59. Salat DH, Lee SY, Yu P, Setty B, Rosas HD & Grant PE. DTI in development and aging. In: Anonymous Diffusion MRI. Elsevier: 2009. 205-236 p.

60. Jahanshad N, Kohannim O, Hibar DP, et al. Brain structure in healthy adults is related to serum transferrin and the H63D polymorphism in the HFE gene. Proc Natl Acad Sci U S A 2012:109:E851-9.
61. Deistung A, Schafer A, Schweser F, Biedermann U, Turner R & Reichenbach JR. Toward in vivo histology: a comparison of quantitative susceptibility mapping (QSM) with magnitude-, phase-, and R2*-imaging at ultra-high magnetic field strength. Neuroimage 2013:65:299-314.
62. Sun H, Walsh AJ, Lebel RM, et al. Validation of quantitative susceptibility mapping with Perls' iron staining for subcortical gray matter. Neuroimage 2015:105:486-492.
63. MacKay A, Whittall K, Adler J, Li D, Paty D & Graeb D. In vivo visualization of myelin water in brain by magnetic resonance. Magn Reson Med 1994:31:673-677.
64. Liu C, Li W, Johnson GA & Wu B. High-field (9.4 T) MRI of brain dysmyelination by quantitative mapping of magnetic susceptibility. Neuroimage 2011:56:930-938.
65. Wharton S & Bowtell R. Fiber orientation-dependent white matter contrast in gradient echo MRI. Proc Natl Acad Sci U S A 2012:109:18559-18564.
66. Sati P, van Gelderen P, Silva AC, et al. Micro-compartment specific T2□ relaxation in the brain. Neuroimage 2013:77:268-278.
67. Wharton S & Bowtell R. Effects of white matter microstructure on phase and susceptibility maps. Magnetic resonance in medicine 2015:73:1258-1269.
68. Fukunaga M, Li TQ, van Gelderen P, et al. Layer-specific variation of iron content in cerebral cortex as a source of MRI contrast. Proc Natl Acad Sci U S A 2010:107:3834-3839.
69. Bagnato F, Hametner S & Welch EB. Visualizing iron in multiple sclerosis. Magn Reson Imaging 2013:31:376-384.
70. Haider L, Simeonidou C, Steinberger G, et al. Multiple sclerosis deep grey matter: the relation between demyelination, neurodegeneration, inflammation and iron. J Neurol Neurosurg Psychiatry 2014:85:1386-1395.
71. Stuber C, Morawski M, Schafer A, et al. Myelin and iron concentration in the human brain: a quantitative study of MRI contrast. Neuroimage 2014:93 Pt 1:95-106.
72. F. Schweser, A. Deistung, K. Sommer and J. R. Reichenbach. Disentangling contributions from iron and myelin architecture to brain tissue magnetic susceptibility by using Quantitative Susceptibility Mapping (QSM). In: Proc. Int. Soc. Magn. Reson. Med. , 2012. (Volume 20, p. 409).
73. Zhang Y, Gauthier SA, Gupta A, et al. Quantitative Susceptibility Mapping and R2* Measured Changes during White Matter Lesion Development in Multiple Sclerosis: Myelin Breakdown, Myelin Debris Degradation and Removal, and Iron Accumulation. AJNR Am J Neuroradiol 2016:37:1629-1635.
74. Minagar A, Toledo EG, Alexander JS & Kelley RE. Pathogenesis of brain and spinal cord atrophy in multiple sclerosis. Journal of Neuroimaging 2004:14.
75. Tao C, Simpson S,Jr, van der Mei I, et al. Higher latitude is significantly associated with an earlier age of disease onset in multiple sclerosis. J Neurol Neurosurg Psychiatry 2016:87:1343-1349.
76. Browne P, Chandraratna D, Angood C, et al. Atlas of Multiple Sclerosis 2013: A growing global problem with widespread inequity. Neurology 2014:83:1022-1024.
77. Alonso A & Hernan MA. Temporal trends in the incidence of multiple sclerosis: a systematic review. Neurology 2008:71:129-135.

78. O'Gorman C, Lucas R & Taylor B. Environmental risk factors for multiple sclerosis: a review with a focus on molecular mechanisms. International journal of molecular sciences 2012:13:11718-11752.
79. Disanto G, M Morahan J & V Ramagopalan S. Multiple sclerosis: risk factors and their interactions. CNS & Neurological Disorders-Drug Targets (Formerly Current Drug Targets-CNS & Neurological Disorders) 2012:11:545-555.
80. Gelfand JM. Multiple sclerosis: diagnosis, differential diagnosis, and clinical presentation. In: Anonymous Handbook of clinical neurology. Elsevier: 2014. 269-290 p.
81. Lublin FD & Reingold SC. Defining the clinical course of multiple sclerosis: results of an international survey. National Multiple Sclerosis Society (USA) Advisory Committee on Clinical Trials of New Agents in Multiple Sclerosis. Neurology 1996:46:907-911.
82. Lublin FD, Reingold SC, Cohen JA, et al. Defining the clinical course of multiple sclerosis: the 2013 revisions. Neurology 2014:83:278-286.
83. Montagne A, Toga AW & Zlokovic BV. Blood-brain barrier permeability and gadolinium: benefits and potential pitfalls in research. JAMA neurology 2016:73:13-14.
84. Loma I & Heyman R. Multiple sclerosis: pathogenesis and treatment. Current neuropharmacology 2011:9:409-416.
85. Wu GF & Alvarez E. The immunopathophysiology of multiple sclerosis. Neurol Clin 2011:29:257-278.
86. Thompson AJ, Banwell BL, Barkhof F, et al. Diagnosis of multiple sclerosis: 2017 revisions of the McDonald criteria. The Lancet Neurology 2017.
87. Polman CH, Reingold SC, Banwell B, et al. Diagnostic criteria for multiple sclerosis: 2010 revisions to the McDonald criteria. Ann Neurol 2011:69:292-302.
88. Cross A & Naismith R. Established and novel disease-modifying treatments in multiple sclerosis. J Intern Med 2014:275:350-363.
90. Barkhof F, Scheltens P, Frequin ST, et al. Relapsing-remitting multiple sclerosis: sequential enhanced MR imaging vs clinical findings in determining disease activity. AJR Am J Roentgenol 1992:159:1041-1047.
91. Sormani MP & Bruzzi P. MRI lesions as a surrogate for relapses in multiple sclerosis: a meta-analysis of randomised trials. The Lancet Neurology 2013:12:669-676.
92. Schlemm L, Chien C, Bellmann-Strobl J, et al. Gadopentetate but not gadobutrol accumulates in the dentate nucleus of multiple sclerosis patients. Multiple Sclerosis Journal 2017:23:963-972.
93. Rogosnitzky M & Branch S. Gadolinium-based contrast agent toxicity: a review of known and proposed mechanisms. Biometals 2016:29:365-376.
94. Kermode AG, Tofts PS, Thompson AJ, et al. Heterogeneity of blood-brain barrier changes in multiple sclerosis: an MRI study with gadolinium-DTPA enhancement. Neurology 1990:40:229-235.
95. Shinohara RT, Goldsmith J, Mateen FJ, Crainiceanu C & Reich DS. Predicting breakdown of the blood-brain barrier in multiple sclerosis without contrast agents. AJNR Am J Neuroradiol 2012:33:1586-1590.
96. Trapp BD & Nave K. Multiple sclerosis: an immune or neurodegenerative disorder? Annu Rev Neurosci 2008:31:247-269.
97. Ontaneda D & Fox RJ. Imaging as an outcome measure in multiple sclerosis. Neurotherapeutics 2017:14:24-34.

98. Calabrese M, Filippi M & Gallo P. Cortical lesions in multiple sclerosis. Nature Reviews Neurology 2010:6:438.
99. Chataway J. MS-SMART: Multiple Sclerosis-Secondary Progressive Multi-Arm Randomisation Trial-ClinicalTrials.gov .
100. Chataway J, Schuerer N, Alsanousi A, et al. Effect of high-dose simvastatin on brain atrophy and disability in secondary progressive multiple sclerosis (MS-STAT): a randomised, placebo-controlled, phase 2 trial. The Lancet 2014:383:2213-2221.
101. Eshaghi A, Prados F, Brownlee W, et al. Deep grey matter volume loss drives disability worsening in multiple sclerosis. Ann Neurol 2017.
102. Calabrese M, Agosta F, Rinaldi F, et al. Cortical lesions and atrophy associated with cognitive impairment in relapsing-remitting multiple sclerosis. Arch Neurol 2009:66:1144-1150.
103. DeLong M & Wichmann T. Update on models of basal ganglia function and dysfunction. Parkinsonism Relat Disord 2009:15 Suppl 3:S237-40.
104. Fernandez-Ruiz J, Lastres-Becker I, Cabranes A, Gonzalez S & Ramos J. Endocannabinoids and basal ganglia functionality. Prostaglandins, Leukotrienes and Essential Fatty Acids (PLEFA) 2002:66:257-267.
105. Pott F, Gingele S, Clarner T, et al. Cuprizone effect on myelination, astrogliosis and microglia attraction in the mouse basal ganglia. Brain Res 2009:1305:137-149.
106. Geurts JJ & Barkhof F. Grey matter pathology in multiple sclerosis. The Lancet Neurology 2008:7:841-851.
107. Cifelli A, Arridge M, Jezzard P, Esiri MM, Palace J & Matthews PM. Thalamic neurodegeneration in multiple sclerosis. Ann Neurol 2002:52:650-653.
108. Vercellino M, Masera S, Lorenzatti M, et al. Demyelination, inflammation, and neurodegeneration in multiple sclerosis deep gray matter. J Neuropathol Exp Neurol 2009:68:489-502.
109. Walsh AJ, Lebel RM, Eissa A, et al. Multiple sclerosis: validation of MR imaging for quantification and detection of iron. Radiology 2013:267:531-542.
110. Newberg A, Alavi A & Reivich M. Determination of regional cerebral function with FDG-PET imaging in neuropsychiatric disorders. Semin Nucl Med 2002:32:13-34.
111. Derache N, Marie RM, Constans JM & Defer GL. Reduced thalamic and cerebellar rest metabolism in relapsing-remitting multiple sclerosis, a positron emission tomography study: correlations to lesion load. J Neurol Sci 2006:245:103-109.
112. Paulesu E, Perani D, Fazio F, et al. Functional basis of memory impairment in multiple sclerosis: a [18F] FDG PET study. Neuroimage 1996:4:87-96.
113. Roelcke U, Kappos L, Lechner-Scott J, et al. Reduced glucose metabolism in the frontal cortex and basal ganglia of multiple sclerosis patients with fatigue: a 18F-fluorodeoxyglucose positron emission tomography study. Neurology 1997:48:1566-1571.
114. Walsh AJ, Blevins G, Lebel RM, Seres P, Emery DJ & Wilman AH. Longitudinal MR imaging of iron in multiple sclerosis: an imaging marker of disease. Radiology 2014:270:186-196.
115. Zivadinov R, Heininen-Brown M, Schirda CV, et al. Abnormal subcortical deep-gray matter susceptibility-weighted imaging filtered phase measurements in patients with multiple sclerosis: a case-control study. Neuroimage 2012:59:331-339.
116. Hagemeier J, Yeh EA, Brown MH, et al. Iron content of the pulvinar nucleus of the thalamus is increased in adolescent multiple sclerosis. Mult Scler 2013:19:567-576.

117. Hagemeier J, Weinstock-Guttman B, Bergsland N, et al. Iron deposition on SWI-filtered phase in the subcortical deep gray matter of patients with clinically isolated syndrome may precede structure-specific atrophy. AJNR Am J Neuroradiol 2012:33:1596-1601.
118. Hammond KE, Metcalf M, Carvajal L, et al. Quantitative in vivo magnetic resonance imaging of multiple sclerosis at 7 Tesla with sensitivity to iron. Ann Neurol 2008:64:707-713.
119. Ge Y, Jensen JH, Lu H, et al. Quantitative assessment of iron accumulation in the deep gray matter of multiple sclerosis by magnetic field correlation imaging. AJNR Am J Neuroradiol 2007:28:1639-1644.
120. Cobzas D, Sun H, Walsh AJ, Lebel RM, Blevins G & Wilman AH. Subcortical gray matter segmentation and voxel-based analysis using transverse relaxation and quantitative susceptibility mapping with application to multiple sclerosis. J Magn Reson Imaging 2015:42:1601-10.
121. Hagemeier J, Zivadinov R, Dwyer MG, et al. Changes of deep gray matter magnetic susceptibility over 2years in multiple sclerosis and healthy control brain. NeuroImage: Clinical 2017.
122. Hagemeier J, Ferdinand S, Dwyer M, et al. Quantitative Susceptibility Mapping Study of Deep Gray Matter Iron at 3T in Large Cohort of Multiple Sclerosis Patients (P4. 162). Neurology 2016:86:P4. 162.
123. Holst B, Siemonsen S, Finsterbusch J, et al. T2' imaging indicates decreased tissue metabolism in frontal white matter of MS patients. Mult Scler 2009:15:701-707.
124. Uddin MN, Lebel RM, Seres P, Blevins G & Wilman AH. Spin echo transverse relaxation and atrophy in multiple sclerosis deep gray matter: A two-year longitudinal study. Mult Scler 2015.
125. Lebel RM & Wilman AH. Transverse relaxometry with stimulated echo compensation. Magn Reson Med 2010:64:1005-1014.
126. Ceccarelli A, Rocca MA, Neema M, et al. Deep gray matter T2 hypointensity is present in patients with clinically isolated syndromes suggestive of multiple sclerosis. Mult Scler 2010:16:39-44.
127. Ceccarelli A, Filippi M, Neema M, et al. T2 hypointensity in the deep gray matter of patients with benign multiple sclerosis. Mult Scler 2009:15:678-686.
128. Bakshi R, Benedict RH, Bermel RA, et al. T2 hypointensity in the deep gray matter of patients with multiple sclerosis: a quantitative magnetic resonance imaging study. Arch Neurol 2002:59:62-68.
129. Tjoa CW, Benedict RH, Weinstock-Guttman B, Fabiano AJ & Bakshi R. MRI T2 hypointensity of the dentate nucleus is related to ambulatory impairment in multiple sclerosis. J Neurol Sci 2005:234:17-24.
130. Zhang Y, Zabad R, Wei X, Metz L, Hill M & Mitchell J. Deep grey matter "black T2" on 3 tesla magnetic resonance imaging correlates with disability in multiple sclerosis. Mult Scler 2007:13:880-883.
131. Khalil M, Langkammer C, Ropele S, et al. Determinants of brain iron in multiple sclerosis: a quantitative 3T MRI study. Neurology 2011:77:1691-1697.
132. Ropele S, Kilsdonk ID, Wattjes MP, et al. Determinants of iron accumulation in deep grey matter of multiple sclerosis patients. Mult Scler 2014:20:1692-1698.
133. Khalil M, Langkammer C, Pichler A, et al. Dynamics of brain iron levels in multiple sclerosis: A longitudinal 3T MRI study. Neurology 2015:84:2396-2402.

134. Khalil M, Enzinger C, Langkammer C, et al. Quantitative assessment of brain iron by R(2)* relaxometry in patients with clinically isolated syndrome and relapsing-remitting multiple sclerosis. Mult Scler 2009:15:1048-1054.
135. Lebel RM, Eissa A, Seres P, Blevins G & Wilman AH. Quantitative high-field imaging of sub-cortical gray matter in multiple sclerosis. Mult Scler 2012:18:433-441.
136. E. Hernández-Torres, V. Wiggermann, D. K. Li, et al. Iron loss occurs in the deep gray matter of multiple sclerosis patients. In: Proc. Intl Soc. Mag. Reson Med. Hawaii, .
137. Schweser F, Martins, Ana Luiza Raffaini Duarte, Hagemeier J, et al. Mapping of thalamic magnetic susceptibility in multiple sclerosis indicates decreasing iron with disease duration: A proposed mechanistic relationship between inflammation and oligodendrocyte vitality. Neuroimage 2017.
138. Eshaghi A, Bodini B, Ridgway GR, et al. Temporal and spatial evolution of grey matter atrophy in primary progressive multiple sclerosis. Neuroimage 2014:86:257-264.
139. Schoonheim MM, Hulst HE, Brandt RB, et al. Thalamus structure and function determine severity of cognitive impairment in multiple sclerosis. Neurology 2015:84:776-783.
140. Ceccarelli A, Rocca MA, Pagani E, et al. A voxel-based morphometry study of grey matter loss in MS patients with different clinical phenotypes. Neuroimage 2008:42:315-322.
141. Inglese M, Park S, Johnson G, et al. Deep gray matter perfusion in multiple sclerosis: dynamic susceptibility contrast perfusion magnetic resonance imaging at 3 T. Arch Neurol 2007:64:196-202.
142. Rocca MA, Mesaros S, Pagani E, Sormani MP, Comi G & Filippi M. Thalamic damage and long-term progression of disability in multiple sclerosis. Radiology 2010:257:463-469.
143. Ware AL, Juranek J, Williams VJ, Cirino PT, Dennis M & Fletcher JM. Anatomical and diffusion MRI of deep gray matter in pediatric spina bifida. NeuroImage: Clinical 2014:5:120-127.
144. Tóth E, Szabó N, Csete G, et al. Gray matter atrophy is primarily related to demyelination of lesions in multiple sclerosis: a diffusion tensor imaging MRI study. Frontiers in neuroanatomy 2017:11:23.
145. Vargas WS, Monohan E, Pandya S, et al. Measuring longitudinal myelin water fraction in new multiple sclerosis lesions. NeuroImage: Clinical 2015:9:369-375.
146. Filippi M, Preziosa P, Copetti M, et al. Gray matter damage predicts the accumulation of disability 13 years later in MS. Neurology 2013:81:1759-1767.
147. Pierpaoli C. Quantitative brain MRI. Top Magn Reson Imaging 2010:21:63.

Chapter 2: Lesion Shape and Conspicuity in postmortem and in vivo Multiple Sclerosis Subjects using Phase and Quantitative Susceptibility Mapping [1]

Abstract

Purpose: To evaluate lesion shape and conspicuity in *postmortem* and *in vivo* Multiple Sclerosis (MS) brains using phase imaging and Quantitative Susceptibility Mapping (QSM), and to confirm iron sensitivity and prevalence of phase dipole signature.

Methods: Lesions from 20 *in vivo* and 2 *postmortem* MS subjects were examined with phase imaging and QSM. Neuropathological identification was performed for *postmortem* lesions, while *in vivo* lesions were verified by a radiologist. Lesion core and rim contrast relative to surrounding normal appearing white matter was examined. Lesions were also inspected for phase dipole signature in orthogonal views. Iron sensitivity was further examined using Perls' iron stain of *postmortem* lesions.

Results: Out of 23 *postmortem* lesions, 9 lesions were positive for Perls' iron stain, of which 8 were visible on QSM. Of the 14 lesions negative for iron staining, 5 were visible on QSM. Dipole signature was only detected in 1 of the 8 Perls' stained *postmortem* lesions that were visible in phase/QSM. Approximately half of the 351 *in vivo* lesions were visible using QSM (50.4%) and phase imaging (54.1%), mostly with hyper-intense core and iso-intense rim contrast using QSM (25.1%) and phase imaging (43.3%), while dipole patterns were only detected in 12% of visible *in vivo* lesions.

Conclusion: QSM hyper-intense core and iso-intense rim contrast was the most common appearance of MS lesions, which is sensitive, but not sufficiently specific for iron detection in

[1] A version of this chapter has been presented as an oral presentation: *Elkady AM, Sun H, Walsh AJ, Blevins G, Zhuozi D and Wilman AH. Quantitative Susceptibility Mapping of Lesions in Multiple Sclerosis. Abstract #0281. In: ISMRM 23rd Annual Meeting & Exhibition, Toronto, Canada, 2015.*

lesions in MS. Dipole signature, on the other hand, is specific but not sufficiently sensitive for lesion iron detection.

2.1. Introduction

Magnetic susceptibility in White Matter (WM) lesions has recently emerged as a relevant inflammation biomarker in Multiple Sclerosis (MS) (1) because of its sensitivity to demyelination and paramagnetic ferric iron (2-8). Increased ferric iron in the vicinity of lesions in MS suggests the presence of pro-inflammatory non-phagocytizing M1 macrophages. Conversely, actively demyelinating lesions contain a high number of myelin-laden M2 anti-inflammatory macrophages, which contain small amounts of ferric iron (1). Detection of patchy iron presence in the center of lesions may suggest the presence of hemosiderin typical of microbleeds (8). Susceptibility variations have been shown to correlate with lesion age and activation status (9), while phase variations have been shown to predict the appearance of lesions in conventional T2-weighted MRI (6). Clinically, susceptibility changes in lesions and normal appearing WM have shown correlation with age-adjusted disability scores in MS patients (10).

MRI techniques based on signal phase, such as such as Susceptibility Weighted Imaging (SWI) (3) and phase/frequency imaging (4-7,11,12), have been used extensively for lesion evaluation, but are compounded by artifacts due to non-local magnetic dipole effects (13). Nonetheless, dipole patterns in phase/frequency images have been suggested as a unique qualitative tool for evaluating lesion iron, and their sporadic appearance in MS patients has been attributed to the scarcity of lesion iron (5).

On the other hand, Quantitative Susceptibility Mapping (QSM) (2,14,15) offers the potential to extract local lesion information from phase images. QSM is a new quantitative technique that has evolved from phase imaging, and relies on deconvoluting susceptibilities of magnetic dipole sources. QSM has been validated for detection of iron in deep gray matter (16) and correlated with MS disease progression (10,12,17) and pathology (18). However, interpretation of iron detection in WM lesions using QSM is hindered by demyelination effects, which are a dominant contributor to WM susceptibility contrast (19).

Prior studies have confirmed that in vivo phase imaging (13) and QSM (15) can be used for lesion detection in MS, and their sensitivities for iron detection has been evaluated post mortem (4,7,8). However, the shape and conspicuity of lesions in MS using susceptibility sensitive MRI techniques revealed various lesion contrast patterns of center and rim (3,4,13,15,20), and

numerical simulations and phantom studies demonstrated that core and shell lesions may exhibit similar shapes and contrast in phase images, but different in QSM (20). Nonetheless, interpretation of observed contrast variations using histopathological studies has not been sufficiently studied. Furthermore, although phase dipole signature offers a tool uniquely sensitive to MS lesion iron, no assessment of this technique has been carried out postmortem. Using in vivo and postmortem MS subjects, the goal of this study was to gain further information on the shape and conspicuity of lesions in phase imaging and QSM, in addition to assessing the feasibility of phase dipole signature as an indicator of lesion iron.

2.2.Materials and Methods

2.2.1.Postmortem

Institutional ethical approval was obtained, and informed consent from the subjects and/or their families was received prior to investigation. Detailed description of *post mortem* subjects, MRI protocols and pathology examination procedure has been previously described (7,16). The MRI methods were similar to the in vivo protocol discussed below. Briefly, two secondary progressive MS subjects with focal lesions (males with age of 63 and 60 years) underwent *in situ* imaging hours after death, followed by formalin fixation and Perls' iron staining to detect ferric iron in lesions.

2.2.2.In Vivo

Institutional ethical approval and informed consent were obtained from all participants prior to the study. Twenty subjects with clinically confirmed relapsing-remitting MS (4/16 M/F, 33.5 ± 8.3 years) who had received MRI examinations using a 4.7T system were studied retrospectively. Axial whole brain coverage was acquired using two dimensional Fast Spin Echo (FSE), FLuid-Attenuated Inversion Recovery (FLAIR), single echo flow-compensated Gradient Echo (GE), and T1 weighted magnetization prepared Rapid Acquisition of Gradient Echo (mp-RAGE).

FSE acquisitions were performed using repetition time (TR) 5750 ms, echo time (TE) 60 ms, number of echoes 4, echo spacing 15 ms, field of view 192.0 x 288.0 x 160.0 mm, and voxel size 0.375 x 0.375 x 4.0 mm^3. FLAIR was acquired with TR/TE 20021/136 ms, flip angle 58°, field of view 192 x 256 x 120 mm^3, and voxel size 0.5x0.5x4 mm. Single-echo GE was carried out using TR/TE 1540/15 ms, flip angle 65°, number of contiguous sections 50, field of view 192.5 x 256.0 x 100.0 mm^3, and voxel size 0.75 x 0.5 x 2 mm^3. T1 weighted mp-RAGE acquisitions were carried out using TE/TR 4.5/8.5 ms, inversion time 300ms, flip angle 10°, field of view 200 x 256 x 168 mm^3, voxel size 0.45 x 0.45 x 2.0 mm^3, and acquisition time 5 minutes.

2.2.3.Image Processing

Postmortem images were interpolated to an isotropic resolution of 0.25 mm, then manually registered to neuropathology slides. *In vivo* images were interpolated to a resolution of 0.38 x 0.38 x 2.0 mm^3, then manually registered to FSE. Raw phase images from GE acquisitions were unwrapped using PRELUDE/FSL (21), and then the brain was extracted using FSL Brain Extraction Tool (22), followed by background field removal using Regularization-Enabled Sophisticated Harmonic Artifact Reduction for Phase data (RESHARP) (23). Local Field Shift (LFS) maps were calculated from phase imaging by normalizing local phase φ_{local} extracted using RESHARP to the main magnetic field B_0 (11):

$$\text{LFS} = -\frac{\varphi_{local}}{\gamma.TE.B_o} \quad \textbf{(2.23)}$$

Quantitative Susceptibility (QS) maps were calculated by magnetic field deconvolution using total variation dipole inversion (24).

2.2.4.Lesion Classification

MS lesions were identified as hyper-intensities on T2-weighted FSE and FLAIR, and hypo-intensities on non-enhanced T1-weighted mp-RAGE with validation from a radiologist (Z.D.) with three years of experience. LFS images were inspected for magnetic dipole field patterns (5), which were defined as a hyper or iso-intensive core and hypo-intensive rim in axial view, in conjunction with hyper/hypo-intensive poles in coronal and sagittal views, with the hyper-intensive dipole portion oriented along the main magnetic field direction (**Figure 2.1**). Contrast patterns of lesion core and rim on QS and LFS maps were classified as hypo-, hyper-, iso-intense, or heterogeneous contrast relative to surrounding normal appearing WM.

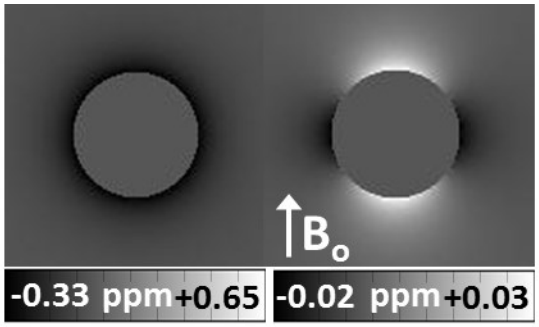

Figure 2.1 Dipole field patterns of a sphere in axial (*left*) and coronal (*right*) planes.

2.2.5.Numerical Simulations

Nine spherical objects (**A**,**B**,**C**) with sizes (diameters 1/32, 1/16 and 1/8th of 10 cm FOV) and susceptibilities (0.015, 0.03, 0.045 ppm) typical of MS lesions (9) were simulated using MATLAB, and LFS was calculated using a forward Fourier transform method (26,27) to investigate dipole visibility in the presence of white Gaussian noise with mean of 0 and standard deviation 20 times less the maximum LFS value in the image (equivalent to a phase SNR of 20). The effect of lesion geometry and orientation was also examined using spheroidal and ellipsoidal objects, with description below including semi-principal axes (a,b,c) and oblique angles (phi, psi): two spheroidal objects (**G** (susceptibility 0.5ppm, a,b 4.6mm, c 5mm), **F** (susceptibility 0.4ppm, a,b 4.6mm, c 5mm)) and three ellipsoidal objects (**D** (susceptibility 0.1ppm, a 11mm, b 31mm, c 22mm, phi -18°, psi 10°), **E** (susceptibility 0.3ppm, a 21mm, b 25mm, c 41mm), **H** (susceptibility 0.2ppm, a 16mm, b 41mm, c 28mm, phi 18°, psi 10°).

2.3.Results

2.3.1.Postmortem

Table 2.1 shows QS lesion contrast compared to Perls' iron stain status for 23 lesions identified by a neuropathologist in the 2 *postmortem* subjects. Dipole patterns in phase imaging were detected in only 1 out of 8 visible iron-positive lesions, which suggests that dipole signature is not sufficiently sensitive for affirmation of iron absence.

Table 2.1 Quantitative Susceptibility core/rim contrast and dipole visibility of 23 MS lesions from 2 *postmortem* subjects in terms of Perl's iron stain status as a percentage.

Center+Rim Contrast	Iron-positive (%)	Iron-negative (%)
Not Visible	11.1	64.3
hyper+iso	55.6	21.4
iso+hyper	22.2	0.0
hypo+iso	0.0	7.1
hetero+iso	11.1	7.1
Total	100.0	100.0
Dipole visibility %	12.5	-

Figure 2.2 demonstrates 9 lesions identified from gross pathology and corresponding iron-stain and *in-situ* QS slice from a *postmortem* subject, with lesion details in **Table 2.2**. The only dipole pattern identified in *postmortem* lesions is highlighted with yellow arrows in axial LFS, coronal, and sagittal images. **Table 2.2** shows QS contrast for 9 *postmortem* lesions displayed in **Figure 2.2**.

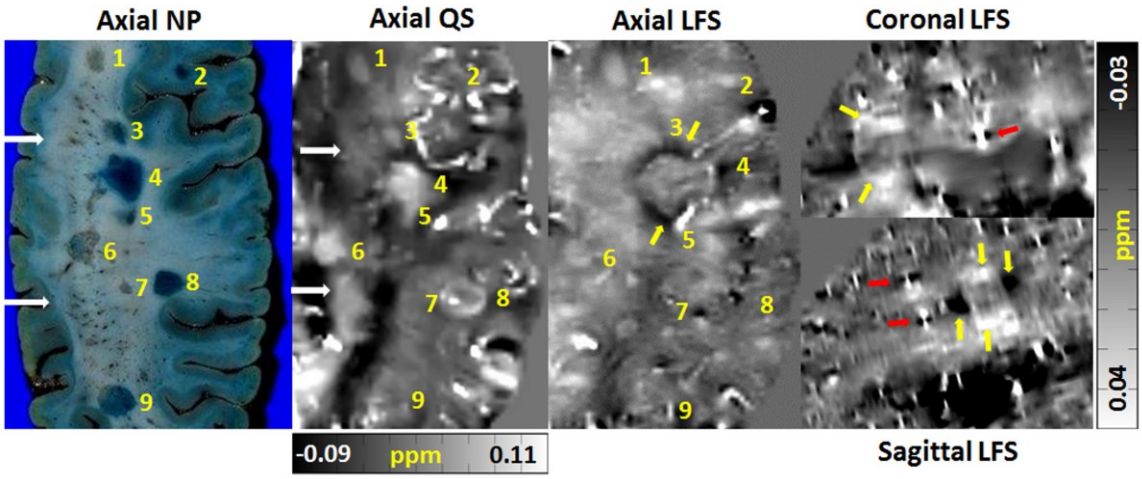

Figure 2.2 Lesions 1-9 identified from gross pathology from an axial postmortem MS brain stained for ferric iron using Perls' stain, and matched to registered QS and LFS from in-situ MRI. Orthogonal coronal and sagittal LFS views (rotated to display upright brain) were used to confirm phase dipole patterns of lesion 4 (yellow arrows in LFS maps). White arrows in pathology and QS highlight non-MS related congested blood vessels that are likely surrounded by micro-angiopathic changes in WM, which appear as hyper-intense contrast in QS, while red arrows point to blood vessel dipole signature in LFS maps. Dipole lobes in phase imaging appear tilted in sagittal/coronal views because of oblique slicing as a result of registration to pathology sections.

Table 2.2 Quantitative Susceptibility contrast of *postmortem* lesions shown in Figure 2.

Lesion #	Perls' Stain	QS Center/Rim Contrast
1,3,4,5	+	hyper/iso
8,9	+	iso/hyper
2	+	hetero
6	-	hyper/iso
7	-	not visible

2.3.2.In Vivo

Table 2.3 presents lesion core/rim contrast as a percentage of the total 351 lesions identified *in vivo*. In agreement with previous reports (3,9,15), lesions with hyper-core contrast were abundantly observed in QSM (31.7%) and phase imaging (44.2%). Nonetheless, rare occurrences of other contrast patterns highlight the complexity of QSM contrast mechanisms, which also depend on orientation and magnetic microarchitecture of WM fiber bundles (28-30).

Table 2.3 Center/rim contrast of 351 lesions identified from T1/T2-weighted MRI.

Center+Rim Contrast	QS[1] (%)	LFS[2] (%)
Not Visible	49.6	45.9
hypo+hypo	0.0	0.0
hyper+hyper	1.1	1.1
hypo+hyper	3.1	1.7
hypo+iso	2.6	3.1
hyper+hypo	6.6	0.9
hyper+iso	25.1	43.3
hetero+hyper	2.6	0.9
hetero+iso	2.3	0.9
iso+hyper	5.4	2.0
iso+hypo	1.7	0.3
Total	100.0	100.0
Dipole visibility %	-	12

Figure 2.3 shows one slice from a relapsing remitting MS subject identifying 11 lesions from T2-weighted MRI, and corresponding images from QSM and phase imaging in axial, coronal, and sagittal views. Hyper/iso-intense contrast for center/rim are apparent in all lesions in QS, except for lesion 5 which shows hyper/hyper-intense contrast, and lesions are visible in LFS but with mixed contrast patterns. Yellow arrows and white crosshairs in phase imaging highlight the presence of dipole patterns in lesions 6 and 7, while red arrows highlight lesions 3 and 5 where dipoles are not visible.

2.3.3. Simulations

The effect of noise, lesion size, shape and susceptibility is evident in **Figure 2.4**. The dipole patterns from spherical phantoms (**Figure 2.4** *top*), are less visible in smaller size and smaller susceptibility sources which can be masked by surrounding noise, whereas the largest spheres with the highest susceptibility displayed the most vivid dipole signature. However, the orientation of the source plays a significant role in dipole visibility because the slicing of the image determines the visible shape of the lesion and its surrounding contrast (**Figure 2.4** *bottom*). Unexpected contrast of dipole signature is evident in sources (**E**) and (**H**) in axial view, (**H**) in coronal, and (**D**) in sagittal.

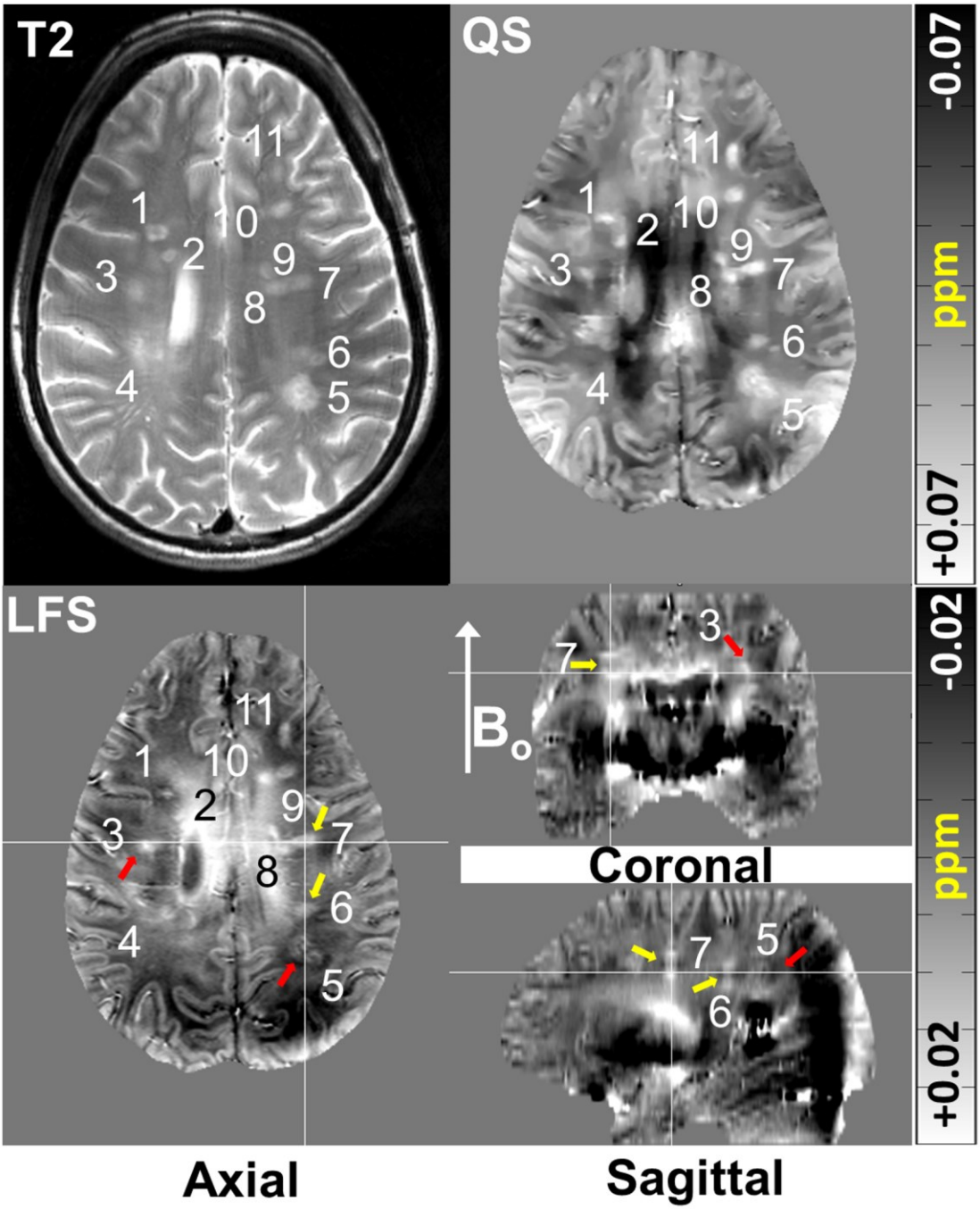

Figure 2.3 Example T2-weighted, QS, and LFS axial images from a 34 year old female relapsing remitting MS subject showing 11 lesions. Orthogonal coronal and sagittal LFS views (rotated to display upright brain) were used to confirm dipole patterns for lesions 6 and 7 (yellow arrows), which agree to displayed hypo-ring in axial view, in contrast to lesions 3 and 5 where dipole signature is not visible in axial and orthogonal views.

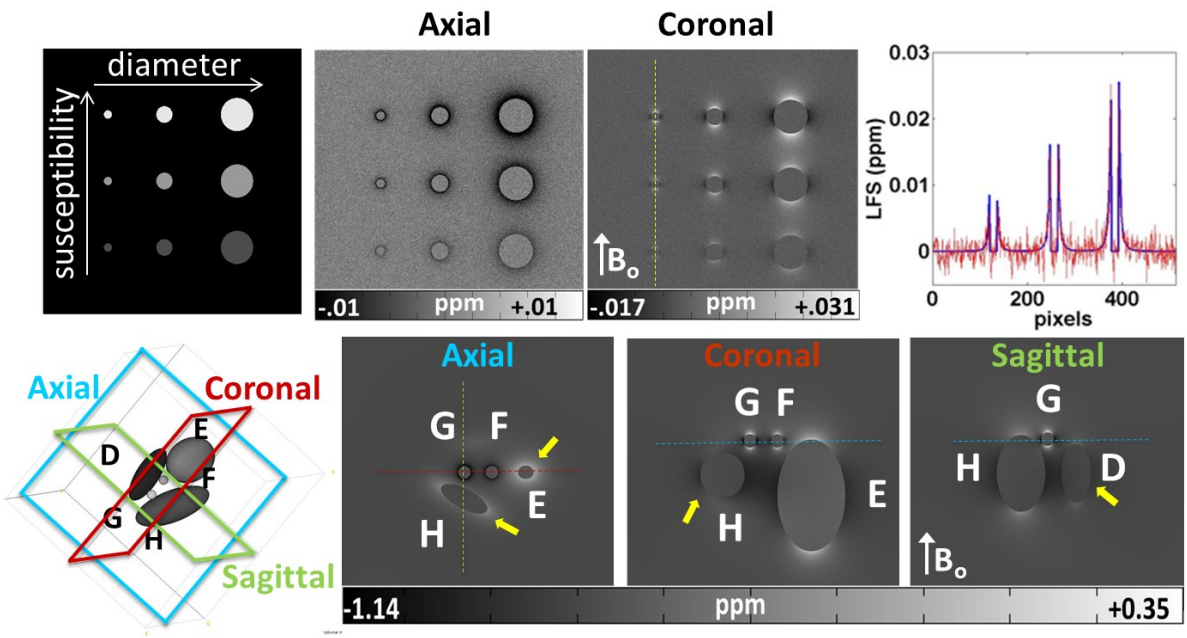

Figure 2.4 Susceptibility and LFS simulations of object size and susceptibility (*top row*) and orientation and shape (*bottom row*). Yellow dashed line in top row corresponds to LFS profile parallel to B_o, which is shown at the right, while dashed lines in bottom row correspond to slicing location, with blue for axial, red for coronal, and green for sagittal.

2.4.Discussion

In agreement with theoretical predictions of lesions with positive susceptibility (31), the dominance of hyper-core contrast in QS maps in *postmortem* iron-positive lesions confirms the usefulness of QSM for detection of lesion iron in MS. Also, the small percentage of iron-positive lesions which did not display hyper-contrast using QSM confirms previous reports describing dependence of QS contrast on factors other than susceptibility differences, such as fiber orientation and tissue micro-architecture (28-30). Nonetheless, QS contrast of iron-positive lesions also presented as iso-intense core with a hyper-intense ring (22.2%) or heterogeneous contrast (11.1%), which may be indicative of the lesion age and type (9). QS invisibility of most iron-negative lesions (64.3%) suggests that the presence of lesion iron improves conspicuity in QS maps, and also highlights the locality of QSM relative to phase imaging. Variable contrast of iron-positive lesions in phase imaging (4,7,8) and QSM (9,15) have previously been reported, which also highlights dependence of phase and susceptibility on fiber orientation and tissue

micro-architecture (28,29), but may be also indicative of the heterogeneity of the pathological process (32).

In terms of *in vivo* lesion conspicuity, phase imaging (54.1%) was most successful in lesion visualization followed by QSM (50.4%) (**Table 2.1**). Previous investigations reported different conspicuities of T2-weighted WM lesions using SWI (73%) (3), or only HF phase imaging (16%) (33), which may be attributed to patient group and imaging method differences. SWI images may offer improved lesion conspicuity by exploiting information from both HF phase and magnitude images (34), but SWI composite images are not quantitative. HF phase exploits background field frequency properties to extract local phase/field, which creates a tradeoff between losing valuable phase information with narrow filter sizes, and introducing image artifacts due to inadequate background field removal (25). In contrast, RESHARP extracts true local phase/field using regularized spherical mean value filtering of phase data (23). QS visibility of WM lesions was less than similar investigations at 7T (66.2%) (15), which may be indicative of improved QS lesion visualization with higher resolution imaging or larger induced susceptibility fields. A limitation of the current study is that it did not consider lesions which were visible in susceptibility MRI but not visible in T2-weighted imaging. Instead, for *in vivo* studies, we used the standard clinical definition of a lesion on T2 and T1-weighted MRI. Previous studies have noted that a number of phase lesions may be invisible on standard MRI (3,33), and that phase lesions may appear before T2 lesions in some cases (6).

Dipole signature was only observed in 12% of visible lesions *in vivo* and 1 out of 8 visible lesions *postmortem*, which is on the order of, but larger than, previous studies (4%) that utilized HF filtering for background field removal (5). The small percentage of dipoles observed in phase imaging *in vivo* has been previously attributed to the scarcity of iron in lesions (5). However, although dipole patterns in phase imaging could affirm probable presence of iron (**Figure 2.2**), they could not be used to conclude its absence. This conclusion can be drawn from the fact that the majority of iron-positive visible lesions from Perls' staining (7 out of 8) did not demonstrate dipole patterns in phase imaging. The rare conspicuity of lesions with dipole patterns in *postmortem* and *in vivo* phase imaging can be attributed to factors which can impair dipole identification, such as iron concentration, SNR level, lesion geometry & orientation, and other contrast contributors in the vicinity of the lesion.

Non-invasive detection of lesion iron in MS has many implications in furthering current understanding of this elusive disease. Dysregulation of brain iron metabolism has been closely associated with the pathogenesis and progression of MS (35). In the MS brain, decreased iron levels were found in normal appearing white matter and remyelinated plaques (8), in contrast to elevated iron levels in microglia and macrophages at the center and edges of active WM lesions (8,36). One obvious source of immune uptake of free iron in the vicinity of lesions is oligodendrocyte destruction in MS, which contain profound amounts of iron because of their role in myelin production. Other possible sources of iron include post vascular hemorrhage heme release, dysregulation of iron transport pathways, and other pathologies (37). However, the exact mechanism that determines the fate of iron is still unclear, which has left the question about the etiologic role of iron unanswered (37-39). One reason for this controversy is the confounding effects of iron accumulation and demyelination in lesions. In addition to its cellular cytotoxic effects, iron-mediated oxidative stress is also implicated with reduced demyelination and increased inflammation in active lesions (37). Combined histological and MRI studies has been proposed in context of elucidating this dilemma (7,8,40), however, the origin of MRI susceptibility contrast in WM lesions in MS remains unclear. Susceptibility-sensitive MRI is unable to delineate iron accumulation and demyelination because both effects result in the same outcome of susceptibility increase. Hence, complementary MRI techniques, such as R2* mapping, offer the opportunity to dismantle these compounding effects (41,42).

A limitation of this study is that it did not perform neuropathological assessment of demyelination in *postmortem* lesions, which affects QS contrast in a similar manner to iron accumulation (31). Also, the effect of WM fiber orientation and microarchitecture has not been considered, which are major contributors to WM QSM contrast. Nonetheless, contribution of WM fiber orientation and microarchitecture should be less significant for focal demyelinated lesions that have been confirmed by hyper-intensity on T2-weighted and hypo-intensity on T1-weighted imaging. Another limitation is that Perls' iron stain does not provide quantitative information about iron distribution in lesions, which can be performed using laser ablation inductively coupled mass spectroscopy (31). However, the purpose of the study was to evaluate QS contrast and dipole patterns of iron-laden lesions in MS compared to iron-negative lesions, which does not require lesion iron maps. Dipole visibility inspected in this study was also limited by the larger size of voxels (2mm) in the static field direction, which can be improved by using

sagittal or 3D isotropic acquistions. *In vivo* lesion identification was also limited to lesions that are conspicuous on both T1 and T2-weighted images, which implies that the conducted analyses are limited to lesions with oedema or axonal loss (43).

2.5.Conclusions

In conclusion, Perls' iron stained *postmortem* lesions suggest that dipole patterns in phase imaging are not sufficiently sensitive for iron detection, which explains their rare conspicuity in *in vivo* lesions. QSM hyper/iso core/rim contrast, which is the most common appearance of lesions in MS, is sensitive, but not sufficiently specific for lesion iron detection.

References

1. Mehta V, Pei W, Yang G, et al. Iron is a sensitive biomarker for inflammation in multiple sclerosis lesions. PLoS One 2013:8:e57573.
2. Chawla S, Kister I, Herbert J, et al. Assessment of iron deposition pattern in multiple sclerosis and neuromyelitis optica lesions with ultra-high field quantitative susceptibility mapping. Mult Scler 2014:20 S1:14-66.
3. Haacke EM, Makki M, Ge Y, et al. Characterizing iron deposition in multiple sclerosis lesions using susceptibility weighted imaging. J Magn Reson Imaging 2009:29:537-544.
4. Yao B, Bagnato F, Matsuura E, et al. Chronic multiple sclerosis lesions: characterization with high-field-strength MR imaging. Radiology 2012:262:206-215.
5. V. Wiggermann, L. E. Lee, E. Hernandez Torres, et al. Iron accumulation is a rare feature in multiple sclerosis lesions. In: Proceedings of the 22nd Joint Annual Meeting of ISMRM-ESMRB, Milano, 2014. (abstract 0895).
6. Wiggermann V, Hernandez Torres E, Vavasour IM, et al. Magnetic resonance frequency shifts during acute MS lesion formation. Neurology 2013:81:211-218.
7. Walsh AJ, Lebel RM, Eissa A, et al. Multiple sclerosis: validation of MR imaging for quantification and detection of iron. Radiology 2013:267:531-542.
8. Bagnato F, Hametner S, Yao B, et al. Tracking iron in multiple sclerosis: a combined imaging and histopathological study at 7 Tesla. Brain 2011:134:3602-3615.
9. Chen W, Gauthier SA, Gupta A, et al. Quantitative susceptibility mapping of multiple sclerosis lesions at various ages. Radiology 2014:271:183-192.
10. Rudko DA, Solovey I, Gati JS, Kremenchutzky M & Menon RS. Multiple sclerosis: improved identification of disease-relevant changes in gray and white matter by using susceptibility-based MR imaging. Radiology 2014:272:851-864.
11. Hammond KE, Metcalf M, Carvajal L, et al. Quantitative in vivo magnetic resonance imaging of multiple sclerosis at 7 Tesla with sensitivity to iron. Ann Neurol 2008:64:707-713.

12. Walsh AJ, Blevins G, Lebel RM, Seres P, Emery DJ & Wilman AH. Longitudinal MR imaging of iron in multiple sclerosis: an imaging marker of disease. Radiology 2014:270:186-196.
13. Walsh AJ & Wilman AH. Susceptibility phase imaging with comparison to R2 mapping of iron-rich deep grey matter. Neuroimage 2011:57:452-461.
14. Al-Radaideh AM, Wharton SJ, Lim SY, et al. Increased iron accumulation occurs in the earliest stages of demyelinating disease: an ultra-high field susceptibility mapping study in Clinically Isolated Syndrome. Mult Scler 2013:19:896-903.
15. X. Li, H. Liu, D. Harrison, et al. Magnetic Susceptibility Contrast Variations in Multiple Sclerosis (MS) Lesions Observed at 7T. In: Proceedings of the 22nd Joint Annual Meeting of ISMRM-ESMRB, Milan, Italy, 2014. (abstract 0895).
16. Sun H, Walsh AJ, Lebel RM, et al. Validation of quantitative susceptibility mapping with Perls' iron staining for subcortical gray matter. Neuroimage 2015:105:486-492.
17. Hagemeier J, Weinstock-Guttman B, Heininen-Brown M, et al. Gray matter SWI-filtered phase and atrophy are linked to disability in MS. Front Biosci (Elite Ed) 2013:5:525-532.
18. Haider L, Simeonidou C, Steinberger G, et al. Multiple sclerosis deep grey matter: the relation between demyelination, neurodegeneration, inflammation and iron. J Neurol Neurosurg Psychiatry 2014:85:1386-1395.
19. Langkammer C, Krebs N, Goessler W, et al. Susceptibility induced gray-white matter MRI contrast in the human brain. Neuroimage 2012:59:1413-1419.
20. Eskreis-Winkler S, Deh K, Gupta A, et al. Multiple sclerosis lesion geometry in quantitative susceptibility mapping (QSM) and phase imaging. J Magn Reson Imaging 2014.
21. Jenkinson M. Fast, automated, N-dimensional phase-unwrapping algorithm. Magn Reson Med 2003:49:193-197.
22. Smith SM. Fast robust automated brain extraction. Hum Brain Mapp 2002:17:143-155.
23. Sun H & Wilman AH. Background field removal using spherical mean value filtering and Tikhonov regularization. Magn Reson Med 2013:71:1151-7.
24. Wu B, Li W, Guidon A & Liu C. Whole brain susceptibility mapping using compressed sensing. Magn Reson Med 2012:67:137-147.
25. Reichenbach JR, Barth M, Haacke EM, Klarhofer M, Kaiser WA & Moser E. High-resolution MR venography at 3.0 Tesla. J Comput Assist Tomogr 2000:24:949-957.
26. Salomir R, de Senneville BD & Moonen CT. A fast calculation method for magnetic field inhomogeneity due to an arbitrary distribution of bulk susceptibility. Concepts in Magnetic Resonance Part B: Magnetic Resonance Engineering 2003:19:26-34.
27. Marques J & Bowtell R. Application of a Fourier-based method for rapid calculation of field inhomogeneity due to spatial variation of magnetic susceptibility. Concepts in Magnetic Resonance Part B: Magnetic Resonance Engineering 2005:25:65-78.
28. He X & Yablonskiy DA. Biophysical mechanisms of phase contrast in gradient echo MRI. Proc Natl Acad Sci U S A 2009:106:13558-13563.
29. Yablonskiy DA, Luo J, Sukstanskii AL, Iyer A & Cross AH. Biophysical mechanisms of MRI signal frequency contrast in multiple sclerosis. Proc Natl Acad Sci U S A 2012:109:14212-14217.
30. Sukstanskii AL & Yablonskiy DA. On the role of neuronal magnetic susceptibility and structure symmetry on gradient echo MR signal formation. Magn Reson Med 2014:71:345-353.

31. Wisnieff C, Ramanan S, Olesik J, Gauthier S, Wang Y & Pitt D. Quantitative susceptibility mapping (QSM) of white matter multiple sclerosis lesions: Interpreting positive susceptibility and the presence of iron. Magn Reson Med 2014.
32. Yao B, Ikonomidou VN, Cantor FK, Ohayon JM, Duyn J & Bagnato F. Heterogeneity of Multiple Sclerosis White Matter Lesions Detected With T2*-Weighted Imaging at 7.0 Tesla. J Neuroimaging 2015.
33. Eissa A, Lebel RM, Korzan JR, et al. Detecting lesions in multiple sclerosis at 4.7 tesla using phase susceptibility-weighting and T2-weighting. J Magn Reson Imaging 2009:30:737-742.
34. Haacke EM, Xu Y, Cheng YC & Reichenbach JR. Susceptibility weighted imaging (SWI). Magn Reson Med 2004:52:612-618.
35. LeVine SM & Chakrabarty A. The role of iron in the pathogenesis of experimental allergic encephalomyelitis and multiple sclerosis. Ann N Y Acad Sci 2004:1012:252-266.
36. Craelius W, Migdal MW, Luessenhop CP, Sugar A & Mihalakis I. Iron deposits surrounding multiple sclerosis plaques. Arch Pathol Lab Med 1982:106:397-399.
37. Stephenson E, Nathoo N, Mahjoub Y, Dunn JF & Yong VW. Iron in multiple sclerosis: roles in neurodegeneration and repair. Nat Rev Neurol 2014:10:459-468.
38. Khalil M, Teunissen C & Langkammer C. Iron and neurodegeneration in multiple sclerosis. Mult Scler Int 2011:2011:606807.
39. Zivadinov R, Weinstock-Guttman B & Pirko I. Iron deposition and inflammation in multiple sclerosis. Which one comes first? BMC Neurosci 2011:12:60-2202-12-60.
40. Laule C, Vavasour IM, Leung E, et al. Pathological basis of diffusely abnormal white matter: insights from magnetic resonance imaging and histology. Mult Scler 2011:17:144-150.
41. Deistung A, Schafer A, Schweser F, Biedermann U, Turner R & Reichenbach JR. Toward in vivo histology: a comparison of quantitative susceptibility mapping (QSM) with magnitude-, phase-, and R2*-imaging at ultra-high magnetic field strength. Neuroimage 2013:65:299-314.
42. Wu B, Li W, Avram AV, Gho SM & Liu C. Fast and tissue-optimized mapping of magnetic susceptibility and T2* with multi-echo and multi-shot spirals. Neuroimage 2012:59:297-305.
43. Bagnato F., Jeffries N., Richert N.D., Stone R.D., Ohayon J.M., McFarland H.F. & Frank, J.A. Evolution of T1 black holes in patients with multiple sclerosis imaged monthly for 4 years. Brain 2003: 126(8), pp.1782-1789.

Chapter 3: Importance of Extended Spatial Coverage for Quantitative Susceptibility Mapping of Iron-Rich Deep Grey Matter [2]

Abstract

Quantitative Susceptibility Mapping (QSM) is an emerging area of brain research with clear application to brain iron studies in deep gray matter. However, acquisition of standard whole brain QSM can be time-consuming. One means to reduce scan time is to use a focal acquisition restricted only to the regions of interest such as deep gray matter. However, the non-local dipole field necessary for QSM reconstruction extends far beyond the structure of interest. We demonstrate the practical implications of these non-local fields on the choice of brain volume for QSM. In an illustrative numerical simulation and then in human brain experiments, we examine the effect on QSM of volume reduction in each dimension. For the globus pallidus, as an example of iron-rich deep gray matter, we demonstrate that substantial errors can arise even when the field-of-view far exceeds the physical structural boundaries. Thus, QSM reconstruction requires a non-local field-of-view prescription to ensure minimal errors. An axial QSM acquisition, centered on the globus pallidus, should encompass at least 76 mm in the superior–inferior direction to conserve susceptibility values from the globus pallidus. This dimension exceeds the physical coronal extent of this structure by at least five-fold. As QSM sees wider use in the neuroscience community, its unique requirement for an extended field-of-view needs to be considered.

[2] A version of this chapter has been published: *Elkady AM, Sun H & Wilman AH. Importance of extended spatial coverage for quantitative susceptibility mapping of iron-rich deep gray matter. Magn Reson Imaging 2016:34:574-578.*

3.1. Introduction

Elevated iron levels in the basal ganglia and thalamus have been implicated using *ex vivo* histopathological studies in the pathogenesis of several neurodegenerative disorders including: Parkinson's (1-3), Alzheimer's (4,5), Huntington's disease (2,3), Neurodegenerative Brain Iron Accumulation (NBIA) (6), and Multiple Sclerosis (MS) (5), as well as healthy aging (7). Quantitative Susceptibility Mapping (QSM) (8-11), which performs dipole inversion on phase images usually from gradient echo acquisitions, has been shown to be highly sensitive to iron in Deep Grey Matter (DGM) in postmortem studies (12-14). The use of QSM has enabled confirmation of iron dependencies *in vivo* for Parkinson's (15), Alzheimer's (16), Huntington's disease (17), healthy aging (18), and its application for iron-chelating therapy evaluation in NBIA (19), early detection of Clinical Isolated Syndrome (CIS) (20), and for monitoring MS disease progression (21).

Reconstruction of QSM requires the dipole field, which has non-local components that extend beyond the structures of interest, thus QSM acquisitions have typically used whole brain coverage. However, whole brain coverage at moderate to high resolution is time-consuming. For example, a typical scan without acceleration techniques may take ~8 minutes (8). Standard approaches to accelerate QSM acquisitions include use of parallel imaging and partial k-space acquisition. Extreme reductions in acquisition time can also be made by shifting from conventional acquisition schemes to a single-shot 2D gradient echo planar acquisition (22) or multi-shot 3D echo planar versions (23). When focused only on iron-rich DGM, further acceleration of the acquisition may also be achieved by targeting only the area of interest, rather than acquiring the whole brain volume, using a field-of-view (FOV) restricted to structures of interest. In particular, FOV reduction by reducing the number of acquired slices in 2D or 3D acquisitions, reduces scan time proportionally without aliasing effects and may be combined with any other acceleration technique. Restricted-FOV QSM acquisitions may also enable increases in spatial resolution given the same scan time, to identify local iron accumulation (24) or regional substructures such as thalamic nuclei (25).

However, unlike standard brain imaging where FOV minimization is a trivial process, the FOV prescription for QSM requires consideration of the dipole effects that extend beyond the object

of interest, but are not visible in a standard magnitude scout image. While recognition of the unit dipole is well known to follow a magnetic field pattern $\delta B(r) = \frac{3\cos^2\theta - 1}{4\pi r^3}$, where δB is the induced magnetic field by a unit susceptibility source relative to the static magnetic field strength; θ is the angle between position r and the static magnetic field (26-29), the effects of FOV restriction have not been studied in depth for human brain. Using the globus pallidus as an example of iron-rich DGM, we demonstrate the practical implications of these non-local fields on the choice of brain volume for QSM, and investigate the dependence of QSM on the FOV dimensions in each dimension using numerical simulation for illustration and human brain experiments on healthy volunteers. These experiments illustrate the sensitivity of QSM to FOV changes, and provide practical guidelines for FOV choice for each acquisition direction, including the smallest FOV that maintains accurate QSM in iron-rich globus pallidus.

3.2.Materials & Methods

3.2.1.Numerical Simulation

To illustrate non-local field effects, a simple intuitive simulation was performed. Analytical field solutions from a sphere of 32-pixel diameter with susceptibilities relative to background ranging from 1 to 10 ppm were generated (28), with the sphere centered within a FOV that was eight times the sphere diameter in each direction, yielding a 256x256x256 matrix. The number of slices in the volume was reduced either symmetrically from both sides or asymmetrically from one side only. Axial, sagittal and coronal volumes were considered separately. For each resulting volume, susceptibility inversion was performed using total variation regularization, which is a form of L1 normalization (10,18,30), then the mean susceptibility of the sphere relative to background was calculated.

3.2.2.MRI Acquisitions

Five healthy males (age 33.3 ± 8.7 yrs) received a 2D axial whole brain susceptibility-weighted acquisition at 4.7 T. Local research ethics board approval and informed consent were obtained

prior to study. These datasets were used for analysis of FOV reduction on QSM accuracy *in vivo*. Acquisitions parameters included: TR/TE 1540/15 ms, flip angle 65°, first-order gradient moment nulling in read and slice directions, fifty contiguous 2 mm axial slices with 0.5(y) x 0.75(x) mm^2 spatial resolution yielding a FOV of 256(y) x 192(x) x 100(z) mm^3.

From this full FOV, the volume was incrementally truncated separately in left–right (x-direction), anterior–posterior (y-direction), or superior–inferior (z-direction). For each truncation direction, only one direction of FOV reduction was considered representing the slice select direction of axial, sagittal or coronal acuiquistions. The minimum FOVs were 65(x), 50(y), or 12(z) mm, centered on the globus pallidus (GP) and also including putamen and caudate head in the x-y plane as illustrated in **Figure 3.1b–e**. For each direction, only slice select reduction was performed because there is no significant scan time savings by reducing the frequency encode dimension, and the phase encode dimension size is constrained by aliasing.

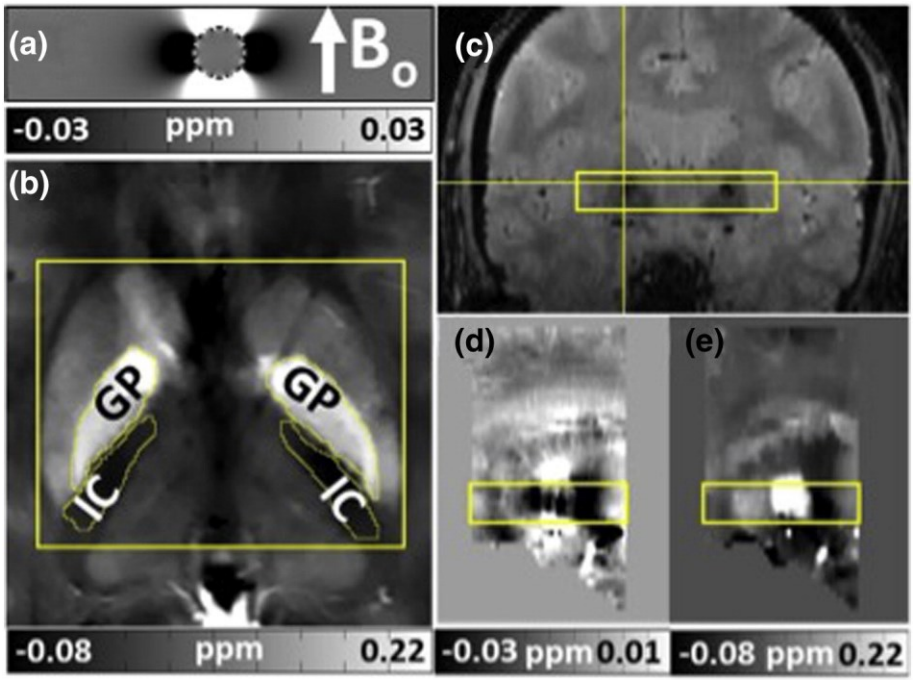

Figure 3.1 Sagittal view of field dipole patterns of a sphere (a) and Globus Pallidus (GP) (d), with non-local hyper-intense lobes in main field direction and perpendicular hypo-intense ring. Axial QSM (b) shows the ROIs of GP and IC. The minimal FOV dimension used was either 65 (x), 50 (y) or 12 (z) mm, as outlined by yellow boxes shown on coronal magnitude (c), axial and sagittal QSM (b, e), and sagittal phase (d). In contrast to magnitude and QSM, non-local dipole effects are clearly evident in the phase image (d). Lines in c indicate slice position in b–e.

QSM reconstruction utilized PRELUDE/FSL (31) for phase unwrapping, Brain Extraction Tool (BET) (32) for skull stripping using the full FOV dataset. Each FOV reduction implemented unique instances of background phase removal with Regularization-Enabled Sophisticated Artifact Reduction for Phase data (RESHARP) (33) and susceptibility inversion using total variation regularization (18). RESHARP utilized a spherical kernel radius of 6mm and Tikhonov regularization of 5×10^{-4}, and total variation used regularization parameter of 5×10^{-4}. Two-dimensional manual region of interests (ROIs) from six central axial slices were used to quantify susceptibility values using QSM, then normalized relative to Internal Capsule (IC) by subtraction (**Figure 3.1b**). Finally, quantification errors of normalized susceptibilities for restricted FOVs relative to the full FOV were recorded.

3.3.Results

Figure 1a demonstrates the dipole field patterns of a sphere in the coronal plane, where parts of the dipole field are truncated along the **Bo** direction due to limited FOV (75% increase from sphere diameter). The DGM regions-of-interest are shown in **Figure 3.1b-e**. Figure 1c illustrates a coronal magnitude image, while 1d,e are sagittal images of phase and QSM. Strong non-local dipole effects from iron-rich DGM are evident in Fig 1d, which extends far beyond the minimal FOV indicated by the yellow boxes.

Figure 3.2 exhibits the effects of FOV reduction on QSM accuracy. In **Figure 3.2a**, numerical simulation of a unity (susceptibility = 1 ppm) sphere for symmetric and asymmetric FOV reduction is shown. The symmetric FOV reduction in the z-direction exceeds the 5% error cut-off for FOVs smaller than 88 pixels, which is 2.75 times larger than the sphere diameter. Results of spherical simulations with higher susceptibility strengths are not shown because they are identical to the shown simulation in this zero noise case. Also, FOV reduction in the x-direction was identical to the y-direction (not shown). In **Figure 3.2b**, errors in in vivo GP susceptibility are shown for FOV restriction in z, y, and x-directions, corresponding to axial, coronal and sagittal acquisitions since FOV reduction is in the slice select direction. The QSM percent errors were calculated relative to the full FOV acquisitions. Largest errors can be observed in the $\mathbf{B_o}$ field direction in both numerical simulations and in vivo data.

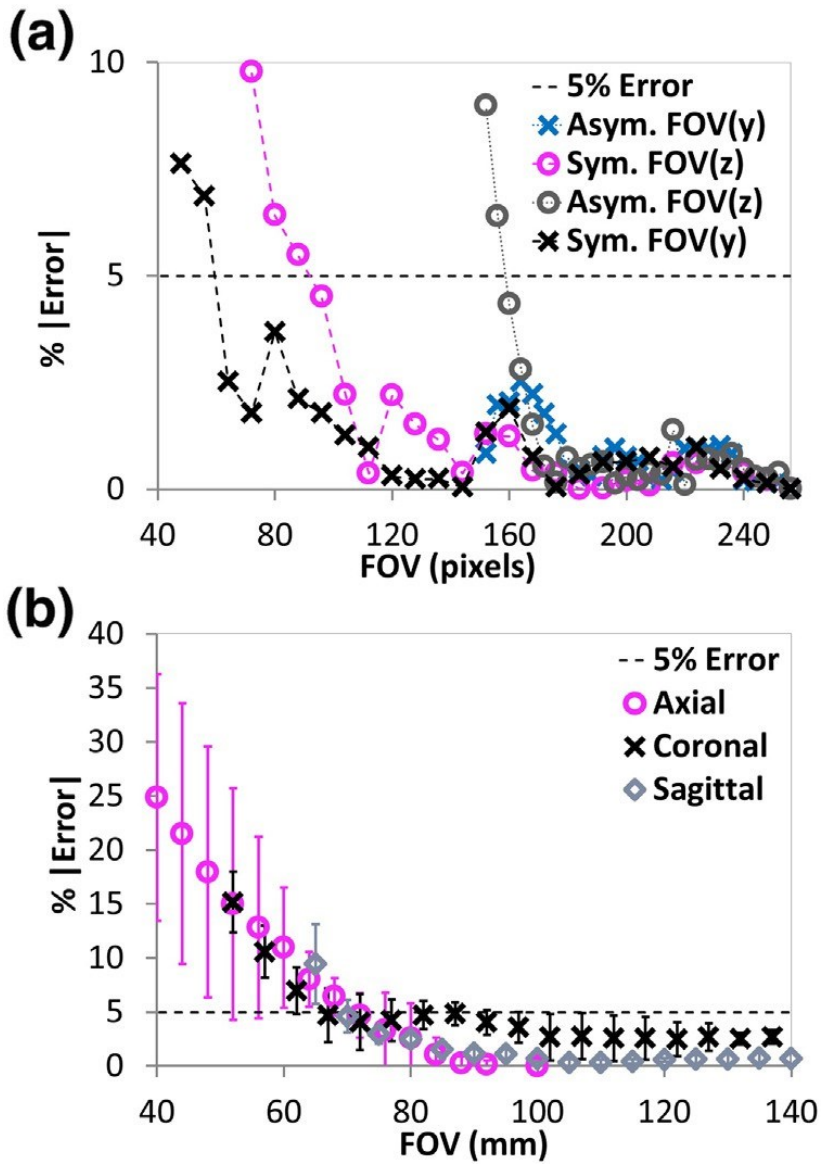

Figure 3.2 The dependence of susceptibility (%) error on FOV. (a) Numerical simulations from a 32-pixel diameter uniform sphere of unity susceptibility for symmetric and asymmetric FOV reduction, with FOV size shown in absolute pixels. (b) Mean susceptibility error of GP from 5 subjects for symmetric slice select FOV reduction for axial (z), coronal (y), and sagittal (x) acquisitions, with error bars corresponding to standard deviation of quantification error between subjects. QSM quantification errors for FOVs larger than 140 mm are not shown because of their insignificant errors. The minimum in vivo FOV considered was 65(x), 50(y) or 12(z) mm, which corresponds to the yellow boxes in Fig. 1, and represents the least FOV that encompasses typical structures of interest in the DGM (GP, IC, Putamen, and Caudate Head).

The effects on QSM of FOV reduction in the $\mathbf{B_0}$ field (z-direction) are shown in **Figure 3.3** for one volunteer. The full 100 mm FOV **(a)** is compared to reduced FOVs of 68, 48, and 28 mm

(b–d), with corresponding difference images **(f–h)**. The coronal image in e illustrates the extent of FOV reduction. Susceptibility values of brain structures are affected differently for each FOV change as each has a different shape and position.

For each subject, the minimal FOV coverage with less than 5% error in GP susceptibility values was calculated for axial, coronal, and sagittal acquisitions. The mean and standard deviation of the minimal FOV coverage are reported in **Table 3.1**, along with its size relative to the extent of the GP (x = 52.2 ± 1.5 mm, y = 26.8 ± 1.6 mm, z = 13.6 ± 1.1 mm). Although sagittal acquisitions would require only 1.3 times the bilateral extent of the GP in the x-direction (left–right), axial acquisitions have a similar minimum FOV requirement.

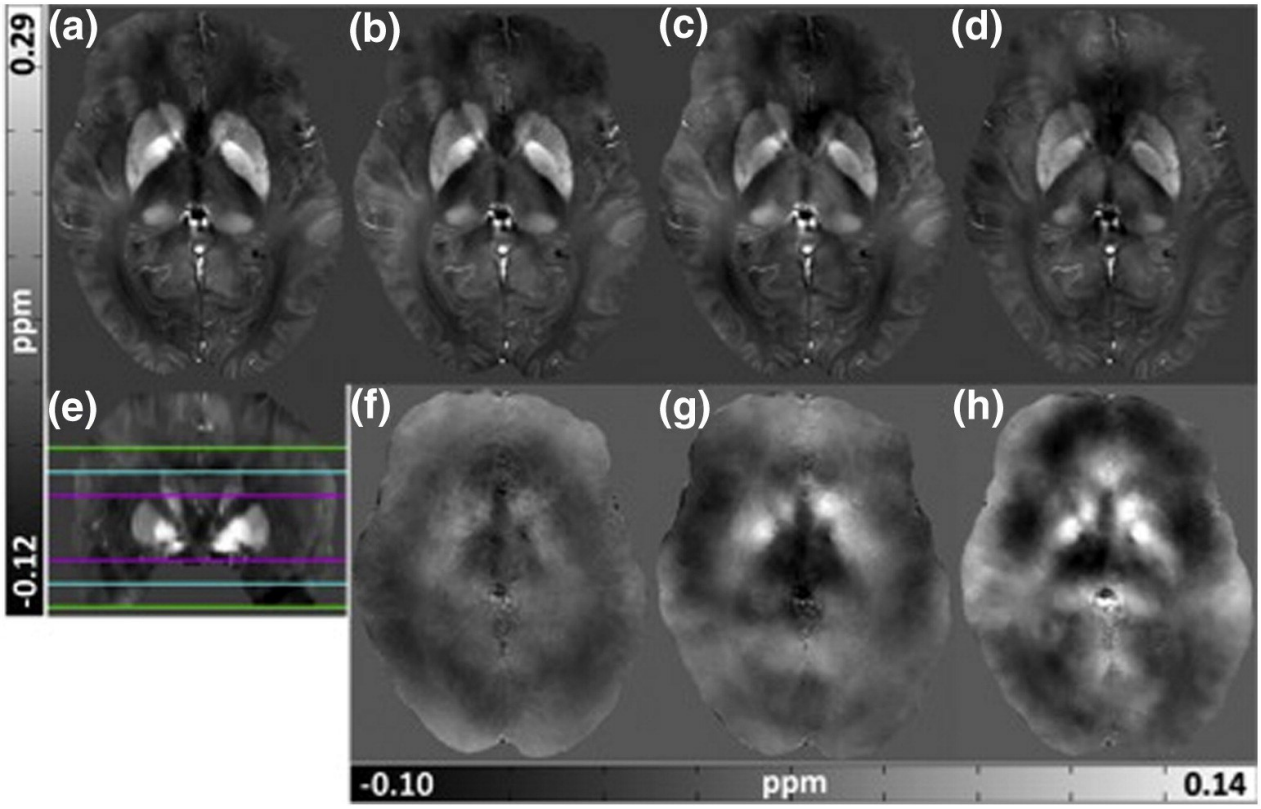

Figure 3.3 Axial susceptibility maps (a–d) calculated from full FOVz = 100 mm (a), and reduced FOVz = 68 mm (b), 48 mm (c), and 28 mm (d). The coronal view of the full FOV acquisition is shown in e, with reduced FOVs positions highlighted in green, cyan, and magenta lines. Corresponding difference images (f, g, h) were calculated between full FOV (a), and reduced FOVs (b, c, d).

3.4.Discussion

Two FOV dependent steps in QSM are background field removal and dipole inversion. Background field removal using RESHARP was found to be insensitive to FOV changes (data not shown), which can be explained by the removal of the common harmonic background component within the defined ROI. As for the inversion process, it has been previously shown that the forward calculation of phase from susceptibility may be accurately solved up to an FOV 2.5 times larger than the diameter of a sphere or cylinder of interest (26). However, in vivo effects of FOV reduction were not considered and only one FOV reduction axis was used. The current study demonstrates that the inverse problem is dependent on the FOV restriction axis, where restriction parallel to $\mathbf{B_0}$ is the most sensitive due to the asymmetric nature of the dipole field as shown by simulations and in vivo MRI brain acquisitions.

Spherical simulations without noise demonstrated that the accuracy of QSM calculations in the case of FOV reduction is independent of the strength of the relative susceptibility shift. This is a natural consequence of the equation used to model the forward problem (26-29), where the dipole field linearly scales with the strength of the susceptibility source. Additionally, loss of phase information due to FOV reduction can be interpreted by the inversion algorithm as either an increased or decreased susceptibility of the magnetic source in a structurally dependent manner, leading to variation of quantification error between subjects, and different field patterns for each FOV change.

The non-local effects of FOV reduction may influence the choice of acquisition orientation. To accelerate the acquisition without introducing aliasing artifacts, the FOV, centered on the structures of interest, was reduced in the orthogonal slice-select direction. While the z-dimension has the greatest dipole extent for a single sphere, the 3D orientation of the DGM nuclei considered gives rise to large x and y FOVs already being necessary to encompass the span of the physical structures. In vivo results indicate that the x and y FOVs need to be 1.3 and 3.3 times the longest GP dimension, while the z FOV must be more than 5.6 times. Although the z-direction requires the greatest FOV percent expansion from actual structure size, axial acquisitions may offer reduced in-plane dimensions versus sagittal and coronal due to head dimensions. Thus, both the in-plane and through-plane FOVs need to be considered to determine

minimum scan time. For example, when GP and additional iron-rich DGM structures that are more inferior are also of interest, such as substantia nigra, red nucleus and dentate nucleus, a sagittal or coronal volume would more effectively encompass this territory.

Table 3.4 Minimal FOV* slice coverage for QSM of globus pallidus with less than 5% error for all five subjects in x-, y-, and z-directions.

Direction	**Minimum FOV (mm, mean ± SD)**	**Ratio of Min. FOV to GP size**
z-dimension (superior-inferior)	76.0 ± 13.6	5.6
y-dimension (anterior-posterior)	87.6 ± 23.9	3.3
x-dimension (left-right)	70.0 ± 3.3	1.3

* FOV centered on Globus Pallidus

Although this study was performed at 4.7 T, these results may be generalized to other field strengths, since susceptibility contrast is similar across field strengths. Limitations of this study include that only the GP was evaluated. However, this iron-rich structure of the basal ganglia provides a representative evaluation of the FOV dependence, providing practical limits for FOV minimization. A second limitation is the use of a standard background phase removal method, i.e. RESHARP, which erodes the brain by the kernel radius (6 mm). This further reduces the actual FOV of the field map for dipole inversion. Recent advanced methods, such as extended-SHARP (34) and Laplacian boundary value (35), can overcome this limitation.

3.5. Conclusions

Non-local field effects, especially in the $\mathbf{B_0}$ field direction, limit restricted-FOV QSM acquisitions of DGM. For example, axial FOVs should be at least 76 mm coverage to conserve the accuracy of GP susceptibility values when using standard QSM reconstruction. This dimension exceeds the physical coronal extent of this structure by at least five-fold. The unique requirement for an extended, non-local FOV leads to a strong dependence of QSM on FOV

choice. Comparisons between studies should consider effects of FOV differences on QSM quantification.

References

1. Dexter DT, Wells FR, Lees AJ, et al. Increased nigral iron content and alterations in other metal ions occurring in brain in Parkinson's disease. J Neurochem 1989:52:1830-1836.
2. Dexter DT, Carayon A, Javoy-Agid F, et al. Alterations in the levels of iron, ferritin and other trace metals in Parkinson's disease and other neurodegenerative diseases affecting the basal ganglia. Brain 1991:114 (Pt 4):1953-1975.
3. Chen JC, Hardy PA, Kucharczyk W, et al. MR of human postmortem brain tissue: correlative study between T2 and assays of iron and ferritin in Parkinson and Huntington disease. AJNR Am J Neuroradiol 1993:14:275-281.
4. Bouras C, Giannakopoulos P, Good PF, Hsu A, Hof PR & Perl DP. A laser microprobe mass analysis of brain aluminum and iron in dementia pugilistica: comparison with Alzheimer's disease. Eur Neurol 1997:38:53-58.
5. LeVine SM. Iron deposits in multiple sclerosis and Alzheimer's disease brains. Brain Res 1997:760:298-303.
6. Haraguchi T, Terada S, Ishizu H, et al. Coexistence of TDP-43 and tau pathology in neurodegeneration with brain iron accumulation type 1 (NBIA-1, formerly Hallervorden-Spatz syndrome). Neuropathology 2011:31:531-539.
7. Hallgren B & Sourander P. The effect of age on the non-haemin iron in the human brain. J Neurochem 1958:3:41-51.
8. de Rochefort L, Liu T, Kressler B, et al. Quantitative susceptibility map reconstruction from MR phase data using bayesian regularization: validation and application to brain imaging. Magn Reson Med 2010:63:194-206.
9. Shmueli K, de Zwart JA, van Gelderen P, Li TQ, Dodd SJ & Duyn JH. Magnetic susceptibility mapping of brain tissue in vivo using MRI phase data. Magn Reson Med 2009:62:1510-1522.
10. Liu J, Liu T, de Rochefort L, et al. Morphology enabled dipole inversion for quantitative susceptibility mapping using structural consistency between the magnitude image and the susceptibility map. Neuroimage 2012:59:2560-2568.
11. Schweser F, Sommer K, Deistung A & Reichenbach JR. Quantitative susceptibility mapping for investigating subtle susceptibility variations in the human brain. Neuroimage 2012:62:2083-2100.
12. Langkammer C, Schweser F, Krebs N, et al. Quantitative susceptibility mapping (QSM) as a means to measure brain iron? A post mortem validation study. Neuroimage 2012:62:1593-1599.
13. Zheng W, Nichol H, Liu S, Cheng YC & Haacke EM. Measuring iron in the brain using quantitative susceptibility mapping and X-ray fluorescence imaging. Neuroimage 2013:78:68-74.
14. Sun H, Walsh AJ, Lebel RM, et al. Validation of quantitative susceptibility mapping with Perls' iron staining for subcortical gray matter. Neuroimage 2015:105:486-492.
15. Barbosa JH, Santos AC, Tumas V, et al. Quantifying brain iron deposition in patients with Parkinson's disease using quantitative susceptibility mapping, R2 and R2*. Magn Reson Imaging 2015.

16. Acosta-Cabronero J, Williams GB, Cardenas-Blanco A, Arnold RJ, Lupson V & Nestor PJ. In vivo quantitative susceptibility mapping (QSM) in Alzheimer's disease. PLoS One 2013:8:e81093.
17. C. Poynton, J. Lupo, C. Hess and S. Nelson. Quantitative susceptibility mapping of Huntington's disease at 7 Tesla. In: Proceedings of the 22nd Joint Annual Meeting of ISMRM-ESMRB, Milan, Italy, 2014. (abstract 0896).
18. Bilgic B, Pfefferbaum A, Rohlfing T, Sullivan EV & Adalsteinsson E. MRI estimates of brain iron concentration in normal aging using quantitative susceptibility mapping. Neuroimage 2012:59:2625-2635.
19. Lobel U, Schweser F, Nickel M, et al. Brain iron quantification by MRI in mitochondrial membrane protein-associated neurodegeneration under iron-chelating therapy. Ann Clin Transl Neurol 2014:1:1041-1046.
20. Al-Radaideh AM, Wharton SJ, Lim SY, et al. Increased iron accumulation occurs in the earliest stages of demyelinating disease: an ultra-high field susceptibility mapping study in Clinically Isolated Syndrome. Mult Scler 2013:19:896-903.
21. Rudko DA, Solovey I, Gati JS, Kremenchutzky M & Menon RS. Multiple sclerosis: improved identification of disease-relevant changes in gray and white matter by using susceptibility-based MR imaging. Radiology 2014:272:851-864.
22. Sun H & Wilman AH. Quantitative susceptibility mapping using single-shot echo-planar imaging. Magn Reson Med 2014.
23. Langkammer C, Bredies K, Poser BA, et al. Fast quantitative susceptibility mapping using 3D EPI and total generalized variation. Neuroimage 2015:111:622-630.
24. Cobzas D, Sun H, Walsh AJ, Lebel RM, Blevins G & Wilman AH. Subcortical gray matter segmentation and voxel-based analysis using transverse relaxation and quantitative susceptibility mapping with application to multiple sclerosis. J Magn Reson Imaging 2015:42:1601-10.
25. Liu T, Eskreis-Winkler S, Schweitzer AD, et al. Improved subthalamic nucleus depiction with quantitative susceptibility mapping. Radiology 2013:269:216-223.
26. Salomir R, de Senneville BD & Moonen CT. A fast calculation method for magnetic field inhomogeneity due to an arbitrary distribution of bulk susceptibility. Concepts in Magnetic Resonance Part B: Magnetic Resonance Engineering 2003:19:26-34.
27. Marques J & Bowtell R. Application of a Fourier-based method for rapid calculation of field inhomogeneity due to spatial variation of magnetic susceptibility. Concepts in Magnetic Resonance Part B: Magnetic Resonance Engineering 2005:25:65-78.
28. Cheng YC, Neelavalli J & Haacke EM. Limitations of calculating field distributions and magnetic susceptibilities in MRI using a Fourier based method. Phys Med Biol 2009:54:1169-1189.
29. Schafer A, Wharton S, Gowland P & Bowtell R. Using magnetic field simulation to study susceptibility-related phase contrast in gradient echo MRI. Neuroimage 2009:48:126-137.
30. Wu B, Li W, Guidon A & Liu C. Whole brain susceptibility mapping using compressed sensing. Magn Reson Med 2012:67:137-147.
31. Jenkinson M. Fast, automated, N-dimensional phase-unwrapping algorithm. Magn Reson Med 2003:49:193-197.
32. Smith SM. Fast robust automated brain extraction. Hum Brain Mapp 2002:17:143-155.
33. Sun H & Wilman AH. Background field removal using spherical mean value filtering and Tikhonov regularization. Magn Reson Med 2013:71:1151-7.

34. Topfer R, Schweser F, Deistung A, Reichenbach JR & Wilman AH. SHARP edges: recovering cortical phase contrast through harmonic extension. Magn Reson Med 2015:73:851-856.
35. Zhou D, Liu T, Spincemaille P & Wang Y. Background field removal by solving the Laplacian boundary value problem. NMR Biomed 2014:27:312-319.

Chapter 4: Progressive Iron Accumulation Across Multiple Sclerosis Phenotypes [3] Revealed by Sparse Classification of Deep Gray Matter

Abstract

Purpose: To create an automated framework for localized analysis of Deep Gray Matter (DGM) iron accumulation and demyelination using sparse classification by combining Quantitative Susceptibility (QS) and transverse relaxation rate (R2*) maps, for evaluation of DGM in Multiple Sclerosis (MS) phenotypes relative to healthy controls.

Materials and Methods: R2*/QS maps were computed using a 4.7T 10-echo gradient echo acquisition from 16 clinically isolated syndrome (CIS), 41 relapsing-remitting (RR), 40 secondary-progressive (SP), 13 primary-progressive (PP) MS patients, and 75 controls. Sparse classification for R2*/QS maps of segmented Caudate Nucleus (CN), Putamen (PU), Thalamus (TH), and Globus Pallidus (GP) structures produced localized maps of iron/myelin in MS patients relative to controls. Paired t-tests, with age as a covariate, were used to test for statistical significance ($p \leq 0.05$).

Results: In addition to DGM structures found significantly different in patients compared to controls using whole region analysis, singular sparse analysis found significant results in RRMS PU R2* ($p=0.03$), TH R2* ($p=0.04$), CN QS ($p=0.04$); in SPMS CN R2* ($p=0.04$), GP R2* ($p=0.05$); and in PPMS CN R2* ($p=0.04$), TH QS ($p=0.04$). All sparse regions were found to conform to an iron accumulation pattern of changes in R2*/QS, while none conformed to demyelination. Intersection of sparse R2*/QS regions also resulted in RRMS CN R2* becoming significant, while RRMS R2* TH and PPMS QS TH becoming insignificant. Common iron-associated volumes in MS patients and their effect size progressively increased with advanced phenotypes.

[3] A version of this chapter has been published: *Elkady AM, Cobzas D, Sun H, Blevins G & Wilman AH. Progressive iron accumulation across multiple sclerosis phenotypes revealed by sparse classification of deep gray matter. J Magn Reson Imaging 2017.*

Conclusion: A localized technique for identifying sparse regions indicative of iron or myelin in the DGM was developed. Progressive iron accumulation with advanced MS phenotypes was demonstrated, as indicated by iron-associated sparsity and effect size.

4.1. Introduction

Iron accumulation, demyelination, and neuronal/axonal loss are common features of the Deep Gray Matter (DGM) of Multiple Sclerosis (MS) patients (1). Magnetic Resonance Imaging (MRI) evaluation of DGM iron levels has been shown to be a sensitive marker for MS progression, using R2* (2) and R2 (3) mapping, susceptibility weighted imaging (4), and phase imaging (5). Quantitative Susceptibility (QS) mapping is a newer quantitative technique that has evolved from phase imaging, and relies on deconvoluting susceptibilities of magnetic dipole sources (6). R2* mapping, on the other hand, quantifies the exponential signal decay rate of a multi-echo gradient echo experiment. Both QS and R2* increase with iron accumulation, but they also have opposing sensitivity to myelin changes (7). Therefore, their combined use (8-10) can delineate iron accumulation from demyelination in MS.

Previous cross-sectional MS studies established elevated iron levels in MS DGM compared to healthy controls. However, the majority of these studies have utilized whole structure analysis of DGM structures (2,11-13). Whole structure analysis does not provide information about spatial distributions within relevant structures. To overcome this limitation, Hagemeier et al. proposed a voxel based analysis (VBA) method for the identification of abnormal phase voxels (14). Although this method has confirmed the role of DGM in clinically isolated syndrome (CIS) (15,16), relapsing-remitting (RR) (4,14), and secondary progressive (SP) MS (14), it may be compounded by non-local phase effects and characteristics of the reference sample. Similarly, VBA has been used for localized analysis of the DGM of CIS (17,18) and RRMS (18-20) patients using mass univariate statistical tests at each voxel to identify significant regional differences between patients and controls (21). VBA generates statistical maps consisting of p-values characterizing significant differences at the voxel level. These methods have limited ability to identify complex population differences because they do not consider multivariate relationships in data and do not capture the full pathological complexity of the contribution of multiple anatomies in MS. More sophisticated methods, like random field theory (22) can overcome this issue, but do not provide a principled way to set parameter values. This problem can be overcome with sparse methods, which simultaneously select several significant areas related to disease pathology and have a principled way of computing optimal parameters using

cross validation. Sparse classification of group studies can identify anatomies that are discriminative, sparse, compact, and allows model evaluation (23).

The objective of this study was to identify spatial distributions of iron accumulation and demyelination patterns in MS patients according to their clinical phenotype, identified as CIS, RRMS, SPMS and Primary Progressive (PP) MS..

4.2.Materials and Methods

4.2.1.Study Design

We prospectively consecutively enrolled 16 CIS subjects, 94 MS subjects (41 RRMS, 40 SPMS, 13 PPMS), and 75 healthy control subjects. Patient phenotypes were defined using the 2010 MacDonald criteria (24), and subjects were included provided that they had no other neurological diseases and had no contraindications to MRI. Written informed consent was obtained from all participants after the internal institutional review board approved the study design. To account for significant correlation of DGM iron with healthy aging (25), control and patient datasets were retrospectively selected to optimize age matching (**Table 4.1**). Although age-matching achieved a reasonable balance of subject sex, sex-matching was not considered because aging is the strongest predictor of MS DGM MRI changes (11). All RRMS patients were utilizing Disease Modifying Therapy (DMT), while no CIS, SPMS or PPMS were on DMT at the time of the MRI study. An MS neurologist (G.B., with 11 years of experience) measured the Kurtzke Extended Disability Status Scale (EDSS) value in each MS patient close in time to the MRI acquisition, provided that the patient did not experience a relapse within the prior 4 months. EDSS values were used to calculate MS Severity Score (MSSS) using the MSSS test program (26), after taking into account disease duration.

4.2.2.Imaging Protocol

Whole brain imaging was performed on a 4.7 T system using a 4-channel phased array receiver coil. Three dimensional multi-echo gradient echo acquisitions were carried out using repetition

time = 44 ms, number of echoes = 10, time to first echo = 2.93 ms, echo spacing = 4.1 ms, monopolar readout, flip angle = 10°, number of contiguous sections = 80, field of view = 160 x 256 x 160 mm, voxel size = 1 x 1 x 2 mm^3, and acquisition time = 9.4 mins. 3D T1w magnetization-prepared rapid gradient-echo acquisitions were also obtained to create a registration atlas using flip angle = 10°, TE/TR = 4.5/8.5 ms, inversion time = 300 ms, number of slices = 84, slice thickness = 2 mm, FOV = 256 x 200 x 168 mm, voxel size = 0.9 x 0.9 x 2 mm^3, and acquisition time = 4.8 mins.

Table 4.1 Demographic information of age-matched ($p \leq 0.05$) patient and control groups. [i]

Patient Group (n)	**Age at MRI study (mean ± SD, yrs)**		**Sex (M/F)**		**EDSS (mean ± SD)**	**Dis. Dur. (mean ± SD, yrs)**
	Patients	Controls	Patients	Controls		
CIS (16)	37.3 ± 9.2	37.2 ± 9.2	5/11	6/9	1.7 ± 1.4	
RR (40)	39.0 ± 10.0	38.9 ± 9.7	7/33	10/30	2.3 ± 1.0	6.2 ± 4.0
SP (33)	50.3 ± 8.9	50.0 ± 8.6	14/19	11/22	5.9 ± 1.3	18.8 ± 8.1
PP (13)	58.0 ± 5.7	56.9 ± 4.0	6/7	7/6	6.6 ± 1.2	16.7 ± 8.6

[i] CIS=Clinically Isolated Syndrome; RR=Relapsing Remitting MS; SP=Secondary Progressive MS; PP=Primary Progressive MS; EDSS=Expanded Disability Status Scale; Dis. Dur.=Disease Duration.

4.2.3. Image Processing

R2* and QS maps were calculated from the multi-echo gradient echo acquisition. R2* maps were computed by fitting magnitude images to a mono-exponential temporal signal model after accounting for intra-voxel background field effects (27). For QS, initial receiver phase offsets in single channel phase images were calculated using a dual-echo approach (28), and removed before coil combination using complex summation. Spatial phase unwrapping was performed for each echo time in 3D using Phase Region Expanding Labeller for Unwrapping Discrete Estimates (PRELUDE) (29) from the FMRIB Software Library (FSL). The unwrapped phase

images were further corrected for any global 2π jumps between echoes, and a field map was generated by fitting the phase images with echo times assuming linear phase evolution. A recent study has demonstrated that phase evolution may deviate from the linear model (30), while another study suggested that this non-linear effect may be caused by reconstruction errors (31). We observed robust linear fittings in DGM regions and therefore we have adopted the traditional linear model. QS maps were calculated using brain extraction using FSL Brain Extraction Tool (32), background field removal using Regularization-Enabled Sophisticated Harmonic Artifact Reduction for Phase data (RESHARP) (33), and finally magnetic field deconvolution using total variation dipole inversion (34).

Table 4.2 Legend for voxel iron / demyelination classification using combined R2* and QS maps.

MRI Parameter	Iron Accumulation (Change in MS vs. CTRL)	Demyelination (Change in MS vs. CTRL)
R2*	+	-
QS	+	+

Segmented DGM structures, ventricles, and brain masks were extracted from R2* and QS maps (**Figure 4.1**), after registering all patients and controls to a global atlas computed from QS maps and T1-weighted images (20). The specific DGM regions under study were Caudate Nucleus (CN), Putamen (PU), Thalamus (TH), and Globus Pallidus (GP). Following the method of Heckemann et al. (35), atlases were aligned with each subject using multimodal T1w, QS and R2* image datasets using non-linear registration (SyN from ANTs (36)). Aligned atlas labels were then fused to achieve optimal segmentation in subject space (20). The difference between the mean of all patient and control data was used to identify areas of positive/negative change in MS subjects compared to controls, which was then used to identify clusters of iron accumulation / demyelination according to **Table 4.2**.

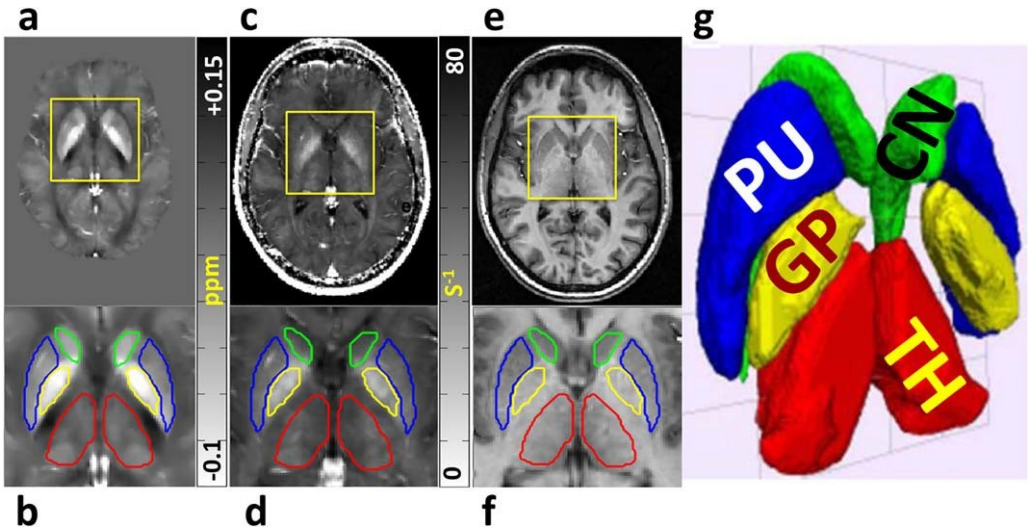

Figure 4.1 Representative QS (a,b) and R2* (c,d) maps, and T1-weighted images (e,f) from a control subject with DGM structure highlighted with a yellow box. Manual segmentation of T1-weighted and QS maps were used to automatically segment 3D DGM structures (g) of the caudate nucleus (CN), putamen (PT), thalamus (TH), and globus pallidus (GP).

4.2.4.Statistical Analysis

Sparse classification was used to identify DGM regions that are significantly different between patients and controls. Sparse formulations for regression and classification have been recently introduced in neuroimaging (37) to robustly detect compact regions of significant change in multidimensional image data (23). For group studies, sparsity and compactness are imposed through penalty terms on a logistic regression loss function:

$$\min_{x,\mathrm{b}} \sum_{i=1}^{n} \log(1+\exp(-y_i(\mathbf{a}_i\mathbf{x}+b))) + \lambda_2\|\nabla x\|_2^2 \qquad (4.1)$$

where $\mathbf{a}_i, i$=1..n are column vectors that collect voxels from the image structure of interest for every subject i. Note that all images are aligned to a common template so the dimensionality of the $\mathbf{a}_i$ vectors is the same, $\mathbf{a}_i \in \Re^m$, $\Re^m$ is the m dimensional vector space with real values, y_i are scalar indicators of the subject class (patients/controls) taking discrete values $\{-1,+1\}$. The vector $\mathbf{x} \in \Re^m$ are the unknown logistic regression coefficients estimated by the model corresponding to the image locations selected in $\mathbf{a}_{i,}$ and b is the model bias. The model has two types of penalizers on the solution coefficients $\mathbf{x}$, an l_1 term that imposes sparsity in the solution and an image regularization that encourages smoothness in the estimated coefficients. We choose

a diffusion-based (graph net) type of image penalizer that was previously used in the context of sparse classification (37) or sparse regression (23) that has the form $\|\nabla x\|_2^2$ where x are the coefficients **x** reshaped as an image and ∇x is the Laplacian operator.

Solving the optimization problem [1] is complicated due to the non-differentiability of the l_1 term. A stable and convergent projected scaled sub-gradient method (38) is employed to solve the resulting non-smooth optimization problem. This is one of the best among 14 methods tested for L1 logistic regression (38,39). The method is implemented in MATLAB based on Schmidt's functions (38,39).

The model has two parameters that we choose as $\lambda_1 = \lambda_\rho$ and $\lambda_1 = \lambda(1 - \rho)$. ρ is fixed at 0.5 while optimal values for λ are estimated using three folds cross-validation based on classification accuracy. One independent model is fitted for each type of data (QS/R2*), for each of the four types of patient-control groups. For each case, data is divided into three folds with similar age if possible. Two folds are used for fitting the model and one for testing. All three combinations of folds are tried and accuracy results are averaged. Optimal values within a range for the parameter λ are then selected. It can be shown that the sparse classification method is able to select stable regions across the folds combinations (40). Therefore, given the low number of subjects in our study, we selected the final sparse regions using all data and optimal parameters.

Finally, two forms of sparse analysis were performed on DGM: singular or combined. Singular analysis involved using only identified sparse regions on R2* or QS maps of patients versus controls. Combined sparse analysis added iron/demyelination voxel labels produced from both R2* and QS pattern changes. The intersection of identified R2* and QS sparse regions produced maps of common areas of iron/demyelination in patients compared to controls. Similar to singular sparse analysis, sparse regions identified using combined analysis was applied to R2* or QS maps. Whole structure analysis of R2* and QS was also performed.

Statistical significance (p-values) was calculated using t-test on the averaged QS/R2* values in corresponding iron / demyelination maps, including age as covariate, with significance defined at 95% confidence. The percentage of the DGM structure detected by the sparse classification method (% sparsity), effect size were also computed (**Figure 4.2**). Linear regression was applied to compute Pearson's correlation coefficient between R2*/QS DGM measures (whole structure, singular sparse, and combined sparse analysis) with ventricular volumes, MSSS, and EDSS,

which also included age as a predictor. Average computation time was 20 seconds for an average run of 6000 voxels, using a 3.5GHz quad-core Intel Core i7 computer.

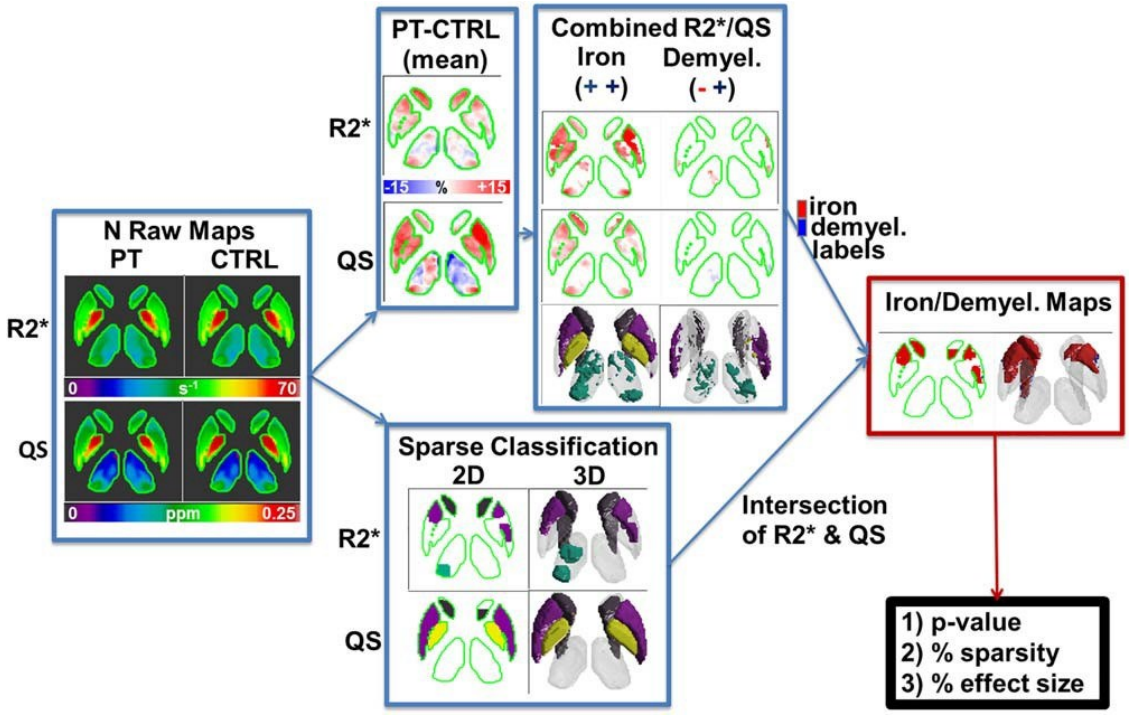

Figure 4.2 Iron/demyelination sparse classification processing pipeline shown for RRMS and control groups as an example. PT = patients; CTRL = control; Demyel. = demyelination.

4.3.Results

4.3.1.Changes in R2* and QS of patients vs. controls

Table 4.3 lists the mean and standard deviation of R2*, QS and ventricular volumes of patient and control groups using whole structure analysis. **Figure 4.3** demonstrates the mean R2* and QS differences between patients and controls, and corresponding sparse regions calculated using sparse classification. Progressive increase in iron accumulation with disease progression is qualitatively demonstrated by the increased contribution of DGM structures to MS pathology.

4.3.2. Value of Singular and Combined R2*/QS Sparse Classification

Table 4.4 demonstrates a comparison of statistical power of whole structure versus singular sparse structure analysis, and specificity of singular R2*/QS versus combined use of R2* and QSM for iron analysis. When whole structure analysis failed to detect a significant difference ($p \leq 0.5$) between patients and controls, sparse classification detected significant differences for R2* values of the Putamen (PU) and Thalamus (TH) for RRMS, Caudate Nucleus (CN) and Globus Pallidus (GP) for SPMS, and CN for PPMS (bolded /underlined values in **Table 4.4**).

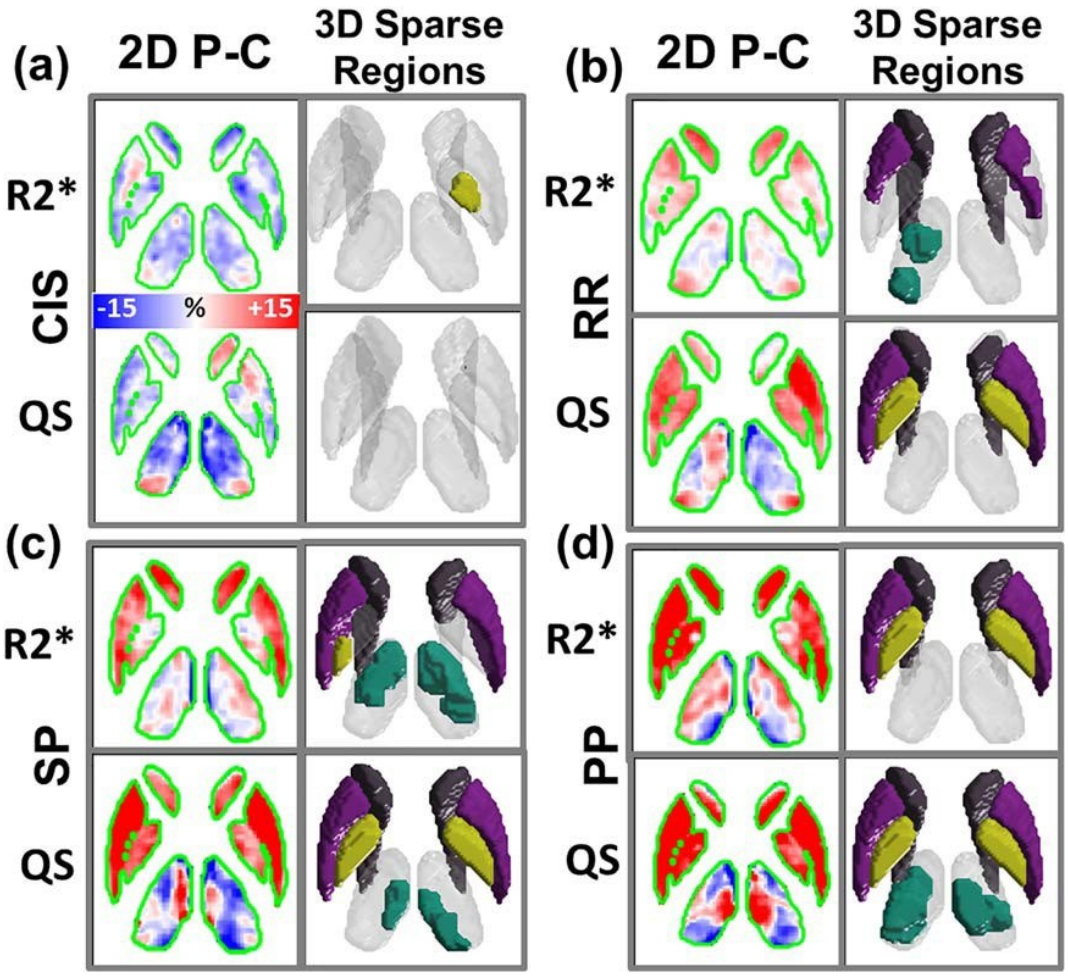

Figure 4.3 2D representative slice (left column) of mean difference between patients and controls and 3D visualization (right column) of sparse regions in patients versus controls for the segmented DGM of CIS (a), RR (b), SP (c), and PP (d) MS. CIS = clinically isolated syndrome; RR = relapsing remitting MS; SP = secondary progressive MS; PP = primary progressive MS.

Similarly, QS sparse classification detected significant differences between patients and controls when whole structure analysis failed in the CN of RRMS and the TH of PPMS. Combined sparse classification also improved the specificity of iron detection compared to singular use of R2*/QS. While significant differences between patient and controls were detected using singular sparse R2* for TH of RRMS, R2* values of voxels that have been labelled as iron accumulation using combined sparse R2*/QS were not significantly different. On the other hand, singular sparse QS detected significant differences between patients and controls for GP of RRMS and TH of PPMS when combined sparse classification did not detect significant differences (bolded/italicized values in **Table 4.4**). Sparsity decreased from combined sparse analysis compared to singular sparse analysis in all DGM structures. As for effect size, combined R2*/QS sparse analysis was typically higher, or remained the same, compared to singular significant sparse values.

4.3.3. Iron & Demyelination in MS Clinical Phenotypes

Figure 4.4 demonstrates relevant iron accumulation and demyelination DGM regions in MS patients. While DGM volumes labeled with iron accumulation clearly appear to progressively increase with advanced MS phenotypes, demyelination appears to be a highly variable process in MS DGM. **Figure 4.5** quantitatively demonstrates progressive DGM increase iron accumulation (derived from the intersection of R2* and QS increase) throughout the disease course of MS. No significant iron accumulation ($p \leq 0.05$) was found in the CIS group, and no significant demyelination ($p \leq 0.05$) in all MS groups was detected for any DGM structure using this sample size. To rule out rare DGM calcification (41), we also confirmed that voxels labels conforming to calcification (increase in R2* and decrease in QS in patients compared to controls) were insignificant in our population.

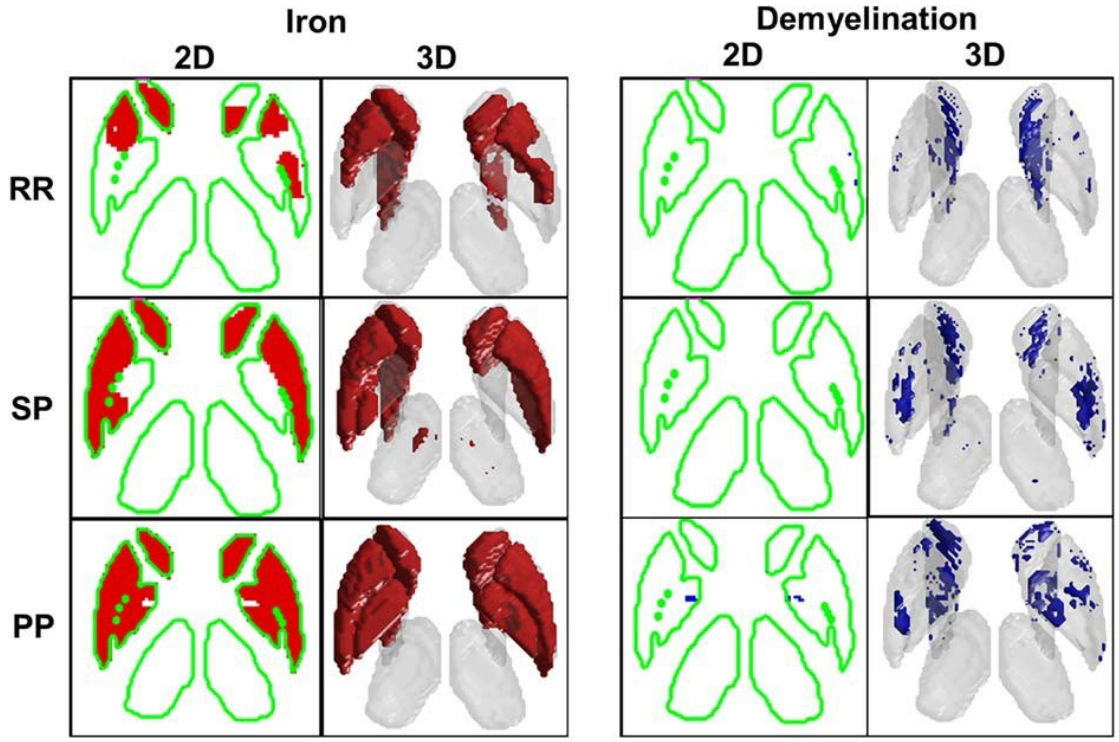

Figure 4.4 Iron accumulation (left panel) and demyelination (right panel) maps in RR, SP, and PP groups ($P < 0.05$). RR = relapsing remitting; SP = secondary progressive; PP = primary progressive.

4.3.4. Relationship with Clinical Scores and Volumes

No significant ($p \leq 0.05$) correlation was found between DGM iron accumulation and clinical scores, ventricular or DGM volumes. Significant correlation ($r = -0.53$; $p = 0.02$) was only detected for ventricular volume change in RRMS in relation to singular sparse and combined R2* sparse iron analysis in the summation of the three basal ganglia regions (CN, PU, GP).

4.4. Discussion

We have shown the progressive iron accumulation in MS using compact and sparse maps of significant iron accumulation throughout the disease course. We have also quantitatively demonstrated the progressive increase of volume suggestive of iron accumulation and increase in effect size across MS phenotypes. Furthermore, we have shown that the effect size of iron accumulation is greatest for PPMS, while the effect size of ventricular volumes is highest for progressive MS compared to RRMS.

While evaluating R2* or QS independently was utilized in previous studies to investigate MS iron accumulation in the DGM, increase in R2* or QS can be interpreted to be a paramagnetic decrease in diamagnetic myelin or an increase in paramagnetic iron. Thus, combined use of R2* and QS allowed labelling voxels as iron accumulation or demyelination. Classification using sparse logistic regression is a powerful technique that allowed identification of regions of statistical significance in MS DGM, instead of the VBA approach of evaluating voxels independently. Thus, utilization of sparse logistic regression of both QS and R2* identified sparse regions with iron accumulation that could not be identified with whole region analysis.

Although the developed technique can theoretically identify sparse demyelinating regions in MS DGM, none have been detected in the studied cohort. This may be attributed to the spatial variation of MS demyelination between individuals. For example, histological analysis of DGM demyelination indicated that benign/subclinical MS cases demonstrated very little DGM demyelination (1). Furthermore, iron accumulation might have been easier to detect because myelin has a weak negative susceptibility effect, while regions with iron accumulation have large positive susceptibility shifts.

The use of phase MRI has been suggested for investigation of DGM iron accumulation in MS (4,14-16,42). Although MRI phase is highly sensitive to iron, its non-local field effects can complicate analysis, which is remedied by using QS. On the other hand, both R2* and QS are sensitive to iron/myelin changes, but R2* is more strongly affected by inflammation and edema. This is the first application of combined R2* and QS to produce localized DGM maps of iron/demyelination in MS phenotypes relative to controls, which increases the specificity of iron detection in MS DGM. This observation from in vivo MRI confirmed previous pathological reports of progressive iron accumulation in the DGM with advanced stages of the disease (11).

Table 4.3 Mean and standard deviation of R2*, QS and ventricular volumes of patients and controls. [ii]

MS Phenotype	DGM Region	R2* (s^{-1})		QS (ppb)		Ventricular Volume (normalized with ICV/1000)	
		Patients	Controls	Patients	Controls	Patients	Controls
CIS	CN	30± 3	30±3	96±15	95±15	20±6	19±5
	PU	33± 3	35±4	94±16	96±12		
	TH	27±2	28±2	57±10	59±11		
	GP	52±5	54±6	186±19	180±19		
RR	CN	32±3	31±3	107±14	101±12	29±19*	18 ±5*
	PU	37±4.3	36±4	110±16*	102±13*		
	TH	29±3	29±2	62±12	62±09		
	GP	57±6	55±8	207±23	192±22*		
SP	CN	35±5	33±3	114±26*	103±17*	40±21*	24 ±12*
	PU	42±7*	39±5*	123±26*	105±19*		
	TH	29±4	28±2	59±14	60±10		
	GP	60±9	58±9	212±32*	195±30*		
PP	CN	35±3	33±2	119±25*	101±14*	39±24*	22 ±5*
	PU	45±8*	39±4*	130±34*	105±17*		
	TH	29±4	28±3	62±10	58±10		
	GP	66±6*	59±6*	228±32*	202±30*		

*$p \leq 0.05$, with age as a covariate. DGM=Deep Gray Matter; RR=Relapsing Remitting MS; SP=Secondary Progressive MS; PP=Primary Progressive MS. CN=Caudate Nucleus; PU=Putamen; TH=Thalamus; GP=Globus Pallidus; ICV=Intracranial Volume.

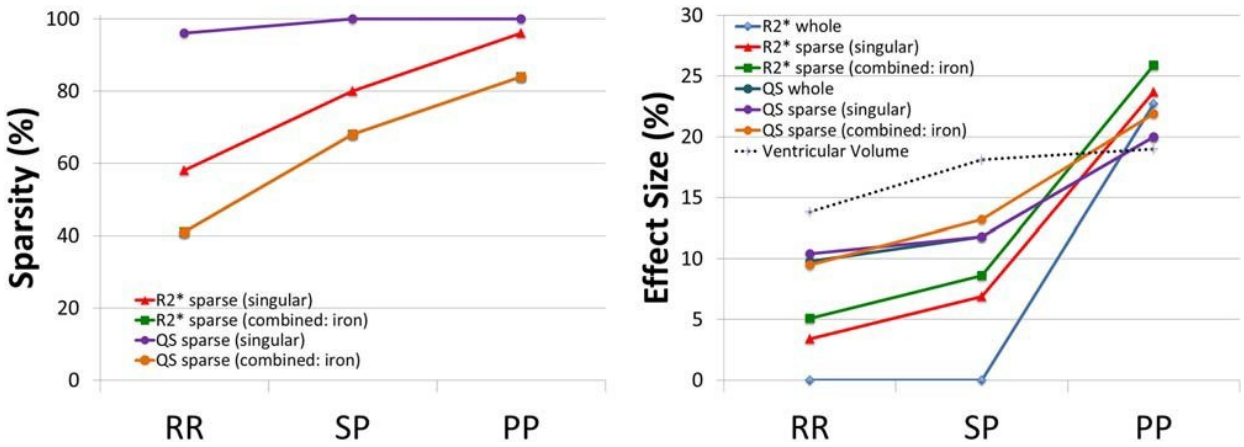

Figure 4.5 Significant (P < 0.05) regions in total DGM suggestive of iron accumulation (% Sparsity, left), and magnitude of MS effect compared to other contributing effects (% Effect Size, right) derived from iron DGM maps of MS clinical phenotypes. Total DGM is defined as the three basal ganglia structures: caudate nucleus, putamen, and globus pallidus. Note that for sparsity combined iron, the R2* and QS lines are identical. RR = relapsing remitting; SP = secondary progressive; PP = primary progressive; DGM = Deep Gray Matter; VV = Ventricular Volume.

For case control studies of CIS using R2* or QS whole structure analysis, iron accumulation in the CN (12,13,18,43), PU (13,18), GP (13,18), and total DGM (12,13) has been implicated, while for RRMS the CN (11,12,44), PU (11,12,20), GP (12,20,44), TH (20,44) and total DGM (12) was found significant. Similarly, the CN (11) and PU (11) were significantly different in patients compared to controls in SPMS and PPMS. In our study, iron accumulation measured by R2* or QS whole structure analysis reported significantly different values for R2* or QS in patient versus controls in the PU for SPMS and PPMS. The discrepancy between identified statistically significant DGM structures between various studies may be explained by several factors. In addition to being a strong contributor to iron concentrations in healthy aging (25), age was found to be the strongest predictor of MS DGM iron values measured by R2* (45,46) and QS (47). Although most studies have accounted for the correlation of aging with R2*/QSM, the interaction of aging with MS disease progression has never been accounted for in MS DGM studies, and may significantly contribute to the results. Another factor that could have contributed to discrepancies is the different methods to control for aging that have been employed in MS DGM studies, such as age-matching (12,13,18,20,44), and adjusting for the mean age of controls after fitting the data to an exponential saturation model (11). In addition,

the large variance in DGM iron concentrations in healthy controls (25) and unaccounted factors, such as alcohol consumption (48), underscore the limitations of cross-sectional MS studies.

The effect of DGM iron accumulation has been demonstrated since 1958 in healthy aging (25), and more recently it has been implicated with MS pathology (2,4,5,11-20,42,44,46,49). However, the biological significance of iron accumulation in MS remains unclear. Dysregulation of brain iron metabolism has been closely associated with the pathogenesis and progression of MS. Increased ferric iron in the vicinity of lesions in MS suggests the presence of pro-inflammatory non-phagocytizing M1 macrophages. Conversely, actively demyelinating lesions contain a high number of myelin-laden M2 anti-inflammatory macrophages, which contain small amounts of ferric iron (50). One obvious source of immune uptake of free iron in the vicinity of lesions is oligodendrocyte destruction in MS, which contain profound amounts of iron because of their role in myelin production. Detection of patchy iron presence in the center of lesions may suggest the presence of hemosiderin typical of microbleeds (51). In addition to accentuated inflammation of lesions, excess iron deposits in MS may also promote mitochondrial dysfunction and catalyze the production of toxic reactive oxygen species. Elevated iron in MS DGM may occur as a compensation mechanism for enhanced oxidative stress, which may be uptake in neurons via astrocyte end-feet processes, passage through voltage-gated calcium channels, and/or ferritin uptake through heavy chain subunit (H)-ferritin receptors. Transferrin receptor upregulation could also account for elevated iron levels in SPMS (52). However, the exact mechanism that determines the fate of iron is still unclear, which has left the question about the etiologic role of iron unanswered.

Table 4.4 Statistical results for R2* and QS in MS DGM using standard whole structure versus sparse classification for singular analysis or combined iron analysis.

Group	Parameter	p-value				Sparsity (%)				Effect Size (%)			
		CN	PU	TH	GP	CN	PU	TH	GP	CN	PU	TH	GP
RR	R2* whole	NS	NS	NS	NS	-	-	-	-	-	-	-	-
	R2* sparse (singular)	NS	**0.03**	***0.04***	NS	-	**46**	***12***	-	-	**3.4**	***5.3***	-
	R2* sparse (combined: iron)	***0.01***	0.02	NS	NS	***63***	40	-	-	***5.6***	4.2	-	-
	QS whole	NS	0.01	NS	0	-	100	-	100	-	7.7	-	10.9
	QS sparse (singular)	**0.04**	0.01	NS	***0***	**89**	100	-	***100***	**5.5**	7.7	-	***10.9***
	QS sparse (combined: iron)	0.02	0	NS	NS	63	40	-	-	6.3	11.7	-	-
SP	R2* whole	NS	0.04	NS	NS	-	100	-	-	-	6.2	-	-
	R2* sparse (singular)	**0.04**	0.04	NS	**0.05**	**84**	100	-	**13**	**6.6**	6.2	-	**6**
	R2* sparse (combined: iron)	0.02	0.02	NS	0.05	69	86	-	13	8.8	7.5	-	6
	QS whole	0.05	0	NS	0.03	100	100	-	100	100	14.9	-	6.9
	QS sparse (singular)	0.05	0	NS	0.03	100	100	-	100	100	14.9	-	6.9
	QS sparse (combined: iron)	0.04	0	NS	0.04	69	86	-	13	6.8	16.2	-	6.7
PP	R2* whole	NS	0.04	NS	0.02	-	100	-	100	-	19.1	-	26.7
	R2* sparse (singular)	**0.04**	0.04	NS	0.01	**88**	100	-	100	**21.3**	19.1	-	26.7
	R2* sparse (combined: iron)	0.01	0.04	NS	0.01	73	92	-	91	27.8	19.9	-	30.1
	QS whole	0.02	0.02	NS	0.02	100	100	-	100	25.2	23.1	-	23.9
	QS sparse (singular)	0.02	0.02	***0.04***	0.02	100	100	***43***	100	25.2	23.1	***20.6***	23.9
	QS sparse (combined: iron)	0.01	0.02	NS	0.01	73	92	-	91	28.6	23.6	-	26.2

[ii] * Significant ($p \leq 0.05$) results in singular sparse analysis that were not significant in whole analysis are underlined/bolded, and significant results in combined R2*/QS compared to singular R2*/QS (or vice versa) are italicized/bolded. RR=Relapsing Remitting MS; SP=Secondary Progressive MS; PP=Primary Progressive MS. CN=Caudate Nucleus; PU=Putamen; TH=Thalamus; GP=Globus Pallidus

Although other effects, such as chemical exchange and compartmentalization of magnetic susceptibility inclusions, can contribute to R2* and QS observed changes, the interpretation of R2* (5) and QS (53) increase as iron accumulation has been validated in MS DGM. Similarly, the interpretation of QS decrease as demyelination has been histochemically validated in MS lesions (54). As for the unaccounted effect of fiber orientation, the minor amount of WM fibers in most of the DGM would limit the effect of fiber orientation on DGM R2* and QS. In addition, head position was controlled by the closely-fitting receiver head coil, leading to similar orientations between subjects. Nonetheless, the developed framework can be extended to full brain studies after using models correcting for fiber orientation (8). Finally, a postmortem histochemical analysis of iron accumulation and demyelination could offer a validation for the technique developed herein, which was beyond the scope of this study. The findings of our study are also limited by its relatively small sample size, especially for the CIS and PPMS groups. However, the main contribution of this study is the demonstration of combined use of R2* and QS for group analysis of MS DGM. Application of the developed technique to a larger cohort of MS patients would be required to produce more reliable results.

4.5. Conclusions

In conclusion, a localized technique for identifying sparse regions indicative of iron or myelin in the DGM was developed. Extensive and statistically significant iron accumulation was observed in MS DGM. Progressive iron accumulation with advanced MS phenotypes was demonstrated, as indicated by iron-associated sparsity and effect size.

References

1. Haider L, Simeonidou C, Steinberger G, et al. Multiple sclerosis deep grey matter: the relation between demyelination, neurodegeneration, inflammation and iron. J Neurol Neurosurg Psychiatry 2014:85:1386-1395.
2. Walsh AJ, Blevins G, Lebel RM, Seres P, Emery DJ & Wilman AH. Longitudinal MR imaging of iron in multiple sclerosis: an imaging marker of disease. Radiology 2014:270:186-196.
3. Uddin MN, Lebel RM, Seres P, Blevins G & Wilman AH. Spin echo transverse relaxation and atrophy in multiple sclerosis deep gray matter: A two-year longitudinal study. Mult Scler 2015.
4. Hagemeier J, Weinstock-Guttman B, Heininen-Brown M, et al. Gray matter SWI-filtered phase and atrophy are linked to disability in MS. Front Biosci (Elite Ed) 2013:5:525-532.

5. Walsh AJ, Lebel RM, Eissa A, et al. Multiple sclerosis: validation of MR imaging for quantification and detection of iron. Radiology 2013:267:531-542.
6. de Rochefort L, Liu T, Kressler B, et al. Quantitative susceptibility map reconstruction from MR phase data using bayesian regularization: validation and application to brain imaging. Magn Reson Med 2010:63:194-206.
7. Langkammer C, Krebs N, Goessler W, et al. Susceptibility induced gray-white matter MRI contrast in the human brain. Neuroimage 2012:59:1413-1419.
8. F. Schweser, A. Deistung, K. Sommer and J. R. Reichenbach. Disentangling contributions from iron and myelin architecture to brain tissue magnetic susceptibility by using Quantitative Susceptibility Mapping (QSM). In: Proc. Int. Soc. Magn. Reson. Med. , 2012. (Volume 20, p. 409).
9. Stuber C, Morawski M, Schafer A, et al. Myelin and iron concentration in the human brain: a quantitative study of MRI contrast. Neuroimage 2014:93 Pt 1:95-106.
10. Lobel U, Schweser F, Nickel M, et al. Brain iron quantification by MRI in mitochondrial membrane protein-associated neurodegeneration under iron-chelating therapy. Ann Clin Transl Neurol 2014:1:1041-1046.
11. Ropele S, Kilsdonk ID, Wattjes MP, et al. Determinants of iron accumulation in deep grey matter of multiple sclerosis patients. Mult Scler 2014:20:1692-1698.
12. Khalil M, Langkammer C, Ropele S, et al. Determinants of brain iron in multiple sclerosis: a quantitative 3T MRI study. Neurology 2011:77:1691-1697.
13. Langkammer C, Liu T, Khalil M, et al. Quantitative susceptibility mapping in multiple sclerosis. Radiology 2013:267:551-559.
14. Zivadinov R, Heininen-Brown M, Schirda CV, et al. Abnormal subcortical deep-gray matter susceptibility-weighted imaging filtered phase measurements in patients with multiple sclerosis: a case-control study. Neuroimage 2012:59:331-339.
15. Hagemeier J, Weinstock-Guttman B, Bergsland N, et al. Iron deposition on SWI-filtered phase in the subcortical deep gray matter of patients with clinically isolated syndrome may precede structure-specific atrophy. AJNR Am J Neuroradiol 2012:33:1596-1601.
16. Hagemeier J, Yeh EA, Brown MH, et al. Iron content of the pulvinar nucleus of the thalamus is increased in adolescent multiple sclerosis. Mult Scler 2013:19:567-576.
17. Quinn MP, Gati JS, Klassen ML, Lee DH, Kremenchutzky M & Menon RS. Increased deep gray matter iron is present in clinically isolated syndromes. Mult Scler Relat Disord 2014:3:194-202.
18. Al-Radaideh AM, Wharton SJ, Lim SY, et al. Increased iron accumulation occurs in the earliest stages of demyelinating disease: an ultra-high field susceptibility mapping study in Clinically Isolated Syndrome. Mult Scler 2013:19:896-903.
19. Rudko DA, Solovey I, Gati JS, Kremenchutzky M & Menon RS. Multiple sclerosis: improved identification of disease-relevant changes in gray and white matter by using susceptibility-based MR imaging. Radiology 2014:272:851-864.
20. Cobzas D, Sun H, Walsh AJ, Lebel RM, Blevins G & Wilman AH. Subcortical gray matter segmentation and voxel-based analysis using transverse relaxation and quantitative susceptibility mapping with application to multiple sclerosis. J Magn Reson Imaging 2015:42:1601-10.
21. Ashburner J & Friston KJ. Voxel-based morphometry--the methods. Neuroimage 2000:11:805-821.
22. Worsley K, Andermann M, Koulis T, MacDonald D & Evans A. Detecting changes in nonisotropic images. Hum Brain Mapp 1999:8:98-101.

23. Kandel BM, Wolk DA, Gee JC & Avants B. Predicting cognitive data from medical images using sparse linear regression. Inf Process Med Imaging 2013:23:86-97.
24. Polman CH, Reingold SC, Banwell B, et al. Diagnostic criteria for multiple sclerosis: 2010 Revisions to the McDonald criteria. Ann Neurol 2011:69:292-302.
25. Hallgren B & Sourander P. The effect of age on the non-haemin iron in the human brain. J Neurochem 1958:3:41-51.
26. Roxburgh RH, Seaman SR, Masterman T, et al. Multiple Sclerosis Severity Score: using disability and disease duration to rate disease severity. Neurology 2005:64:1144-1151.
27. Du YP, Jin Z, Hu Y & Tanabe J. Multi-echo acquisition of MR angiography and venography of the brain at 3 Tesla. J Magn Reson Imaging 2009:30:449-454.
28. H. Sun, M. E. MacDonald and G. B. Pike. Phase Correction of a Bipolar Gradient-Echo Acquisition for Quantitative Susceptibility Mapping. In: 24th ISMRM Scientific Meeting, Singapore City, Republic of Singapore, 2015.
29. Jenkinson M. Fast, automated, N-dimensional phase-unwrapping algorithm. Magn Reson Med 2003:49:193-197.
30. Sood S, Urriola J, Reutens D, et al. Echo time-dependent quantitative susceptibility mapping contains information on tissue properties. Magn Reson Med 2016.
31. Cronin MJ, Wang N, Decker KS, Wei H, Zhu WZ & Liu C. Exploring the origins of TE-dependent QSM measurements in healthy tissue and cerebral microbleeds. Neuroimage 2017.
32. Smith SM. Fast robust automated brain extraction. Hum Brain Mapp 2002:17:143-155.
33. Sun H & Wilman AH. Background field removal using spherical mean value filtering and Tikhonov regularization. Magn Reson Med 2013:71:1151-7.
34. Bilgic B, Pfefferbaum A, Rohlfing T, Sullivan EV & Adalsteinsson E. MRI estimates of brain iron concentration in normal aging using quantitative susceptibility mapping. Neuroimage 2012:59:2625-2635.
35. Heckemann RA, Hajnal JV, Aljabar P, Rueckert D & Hammers A. Automatic anatomical brain MRI segmentation combining label propagation and decision fusion. Neuroimage 2006:33:115-126.
36. Avants BB, Tustison NJ, Song G, Cook PA, Klein A & Gee JC. A reproducible evaluation of ANTs similarity metric performance in brain image registration. Neuroimage 2011:54:2033-2044.
37. Grosenick L, Klingenberg B, Katovich K, Knutson B & Taylor JE. Interpretable whole-brain prediction analysis with GraphNet. Neuroimage 2013:72:304-321.
38. Mark Schmidt, Glenn Fung and Rmer Rosales. Fast optimization methods for l1 regularization: A comparative study and two new approaches. In: European Conference on Machine Learning, 2007.
39. Schmidt M, Fung G & Rosales R. Optimization methods for l1-regularization. University of British Columbia, Technical Report TR-2009 2009:19.
40. Cobzas D & Wilman A. unpublished data.
41. Koller WC, Cochran JW & Klawans HL. Calcification of the basal ganglia: computerized tomography and clinical correlation. Neurology 1979:29:328-333.
42. Zivadinov R, Weinstock-Guttman B & Pirko I. Iron deposition and inflammation in multiple sclerosis. Which one comes first? BMC Neurosci 2011:12:60-2202-12-60.
43. F. Schweser, J. Hagemeier, P. Polak, et al. Quantitative Susceptibility Mapping (QSM) in patients with clinically isolated syndrome (CIS) and multiple sclerosis (MS) - a large cohort

study. In: Proceedings of the 22nd Joint Annual Meeting of ISMRM-ESMRB, Milan, Italy, 2016. (abstract 0895).
44. Lebel RM, Eissa A, Seres P, Blevins G & Wilman AH. Quantitative high-field imaging of sub-cortical gray matter in multiple sclerosis. Mult Scler 2012:18:433-441.
45. Khalil M, Enzinger C, Langkammer C, et al. Quantitative assessment of brain iron by R(2)* relaxometry in patients with clinically isolated syndrome and relapsing-remitting multiple sclerosis. Mult Scler 2009:15:1048-1054.
46. Khalil M, Langkammer C, Pichler A, et al. Dynamics of brain iron levels in multiple sclerosis: A longitudinal 3T MRI study. Neurology 2015:84:2396-2402.
47. Langkammer C, Schweser F, Krebs N, et al. Quantitative susceptibility mapping (QSM) as a means to measure brain iron? A post mortem validation study. Neuroimage 2012:62:1593-1599.
48. Foster M, Zivadinov R, Weinstock-Guttman B, et al. Associations of moderate alcohol consumption with clinical and MRI measures in multiple sclerosis. J Neuroimmunol 2012:243:61-68.
49. Vercellino M, Masera S, Lorenzatti M, et al. Demyelination, inflammation, and neurodegeneration in multiple sclerosis deep gray matter. J Neuropathol Exp Neurol 2009:68:489-502.
50. Mehta V, Pei W, Yang G, et al. Iron is a sensitive biomarker for inflammation in multiple sclerosis lesions. PLoS One 2013:8:e57573.
51. Bagnato F, Hametner S, Yao B, et al. Tracking iron in multiple sclerosis: a combined imaging and histopathological study at 7 Tesla. Brain 2011:134:3602-3615.
52. Williams R, Buchheit CL, Berman NE & LeVine SM. Pathogenic implications of iron accumulation in multiple sclerosis. J Neurochem 2012:120:7-25.
53. Sun H, Walsh AJ, Lebel RM, et al. Validation of quantitative susceptibility mapping with Perls' iron staining for subcortical gray matter. Neuroimage 2015:105:486-492.
54. Wisnieff C, Ramanan S, Olesik J, Gauthier S, Wang Y & Pitt D. Quantitative susceptibility mapping (QSM) of white matter multiple sclerosis lesions: Interpreting positive susceptibility and the presence of iron. Magn Reson Med 2014.

Chapter 5: Discriminative Analysis of Regional Evolution of Iron and Myelin/Calcium in Deep Gray Matter of Multiple Sclerosis and Healthy Subjects [4]

Abstract

Background: Combined R2* and Quantitative Susceptibility (QS) has been previously used in cross-sectional Multiple Sclerosis (MS) studies to distinguish Deep Gray Matter (DGM) iron accumulation and demyelination.

Purpose: We propose and apply Discriminative Analysis of Regional Evolution (DARE) to define specific changes in MS and healthy DGM.

Study Type: Longitudinal (baseline and 2-year follow-up) retrospective study.

Subjects: 27 Relapsing-Remitting MS (RRMS), 17 Progressive MS (PMS), and corresponding age-matched healthy subjects.

Field Strength/Sequence: 4.7T 10-echo gradient-echo acquisition.

Assessment: Automatically segmented Caudate Nucleus (CN), Thalamus (TH), Putamen (PU), globus pallidus, Red Nucleus (RN), substantia nigra, and dentate nucleus were retrospectively analyzed to quantify regional volumes, bulk mean R2* and QS. DARE utilized combined R2* & QS changes to compute spatial extent, mean intensity, and total changes of DGM iron and myelin/calcium over 2 years.

Statistical Tests: We used mixed factorial analysis for bulk analysis, non-parametric tests for DARE (α=0.05), and multiple regression analysis using backward elimination of DGM structures (α=0.05, P=0.1) to regress bulk and DARE measures with follow-up Multiple Sclerosis Severity Scale (MSSS). False detection rate correction was applied to all tests.

Results: Bulk analysis only detected significant ($Q \leq 0.05$) interaction effects in RRMS CN QS (η=0.45; Q=0.004) and PU volume (η=0.38; Q=0.034). DARE demonstrated significant group

[4] A version of this chapter has been published: *Elkady AM, Cobzas D, Sun H, Blevins G & Wilman AH. Discriminative analysis of regional evolution of iron and myelin/calcium in deep gray matter of multiple sclerosis and healthy subjects. Journal of Magnetic Resonance Imaging 2018.*

differences in all RRMS structures, and in all PMS structures except the RN. The largest RRMS effect size was CN total QS iron decrease (r=0.74; Q=0.00002), and TH total QS myelin/calcium decrease for PMS (r=0.70; Q=0.002). DARE CN iron increase using total QS demonstrated the highest correlation with MSSS (r=0.68; Q=0.0005).

Data Conclusion: DARE enabled discriminative assessment of specific DGM changes over 2 years, where iron and myelin/calcium changes were the primary drivers in RRMS and PMS compared to age-matched controls, respectively. Specific DARE measures of MS DGM correlated with follow-up MSSS, and may reflect complex disease pathology.

5.1. Introduction

Multiple Sclerosis (MS) is a disease of the central nervous system that causes inflammation, demyelinating lesions, and neuronal/axonal loss in the brain's deep gray matter (DGM) (1). Apart from iron accumulation due to healthy aging (2), MS DGM also suffers from profound oxidative stress that is associated with oligodendrocyte destruction (1). Furthermore, iron overload in demyelinating lesions hinders repair and promotes pro-inflammatory M1 macrophages activity (3).

While many MRI methods are available to examine myelin, the simultaneous in vivo monitoring of MS DGM iron and myelin changes would aid in understanding the role of iron in MS pathology and enable non-invasive evaluation of novel treatments for MS iron dysregulation. Previous MRI studies have implicated increased DGM iron levels using transverse relaxation R2* mapping cross-sectionally (4) and longitudinally (5). Likewise, Quantitative Susceptibility (QS) mapping has demonstrated increased MS iron using cross-sectional (4) and longitudinal (6) studies.

Combined use of R2* and QS mapping may be used to distinguish brain iron and myelin changes in MS (7,8). An iron increase would cause an increase in R2* and QS due to accentuated signal loss caused by stronger field perturbations and the paramagnetic effect of iron. An increase in DGM myelin would increase R2* because of myelin lipid content, but it would also decrease QS as a result of lipid diamagnetism. Conversely, a decrease in DGM iron and myelin would have opposite effects to their increase. Calcium also behaves similar to myelin in terms of MRI gradient-echo contrast (9), and thus cannot be easily separated from myelin in R2* and QS maps.

Recently, sparse logistic regression of combined R2* and QS maps has been introduced in the context of delineating iron and myelin localized changes in MS cross-sectional studies (7). While indicating increased iron accumulation across MS phenotypes, that study was limited by individual variations typical of cross-sectional studies, and failed to detect significant MS DGM demyelination. Combined R2* and QS has also been used to elucidate MS myelin and iron changes in lesions at various gadolinium-enhanced stages (8).

Using longitudinal changes in R2* and QS over 2 years, we propose Discriminative Analysis of Regional Evolution (DARE) of iron and myelin/calcium in MS DGM. The purpose of this study was to leverage the increased specificity offered by longitudinal data to elucidate DGM iron and myelin changes in MS phenotypes, and to explore the correlation of DARE biomarkers with clinical severity measures.

5.2.Methods

5.2.1.Study Design

Twenty-seven relapsing-remitting MS (RRMS), 17 (15 secondary and 2 primary) progressive MS (PMS), and healthy control (CTRL) subjects were retrospectively selected to create RRMS, PMS and age-matched control groups (CTRL-R and CTRL-P, respectively). Note that age matching is necessary to account for DGM iron accumulation in healthy aging (2). Inclusion criterion was an MS diagnosis according to the 2010 MacDonald criteria and the presence of a 2-year follow-up MRI acquisition for the subject, while exclusion criteria included being diagnosed with other neurological diseases. Written informed consent was obtained from all subjects after the internal institutional review board approved the study design. Extended Disability Status Scale (EDSS) was evaluated by an MS neurologist (G.B., with 11 years of experience) close in time to the MRI acquisition, while Multiple Sclerosis Severity Score (MSSS) was calculated from EDSS and disease durations using MSSStest software (10).

5.2.2.MRI Acquisitions

MRI acquisitions were carried out on all control and MS subjects at baseline and two-year followup using a 4.7T MRI system. Briefly, a 10-echo gradient-echo acquisition was used with field of view (FOV) = 160 x 256 x 160 mm, voxel size = 1 x 1 x 2 mm3, and acquisition time = 9.4 mins. Additionally, 3D anatomical T1-weighted Magnetization-Prepared Rapid Gradient-Echo (MPRAGE) acquisitions were conducted with FOV = 256 x 200 x 168 mm, voxel size = 0.9 x 0.9 x 2 mm3, and acquisition time = 4.8 mins.

5.2.3. Quantitative MRI Maps

R2* and QS maps were computed from the multiple gradient echoes. R2* mapping used a mono-exponential fit of magnitude signal after sinc-correction of intra-voxel linear susceptibility-induced magnetic fields (11). QS maps were computed using brain extraction with FSL Brain Extraction Tool (12), Phase Region Expanding Labeller for Unwrapping Discrete Estimates (PRELUDE) (13), background field removal using Regularization-Enabled Sophisticated Harmonic Artifact Reduction for Phase data (RESHARP) (14), and finally magnetic field deconvolution using total variation dipole inversion (15). Since zero susceptibility is inherently undefined for QS mapping, all QS values were referenced to the susceptibility of the internal capsule.

5.2.4. Image Processing

5.2.4.1. Registration

Bias field intensity normalization for MPRAGE images was performed using the N4 method (16) as part of the Advanced Normalization Tools package (stnava.github.io/ANTs/). Volumetric MPRAGE data from each participant were then rigidly aligned with R2* and QS maps and interpolated to the same map resolution (1 x 1 x 2 mm3).

5.2.4.2. DGM Segmentation

Whole brain, and seven DGM nuclei (**Figure 5.1**) Caudate Nucleus (CN), PUtamen (PU), THalamus (TH), Globus Pallidus (GP), Red Nucleus (RN), Substantia Nigra (SN), and Dentate Nucleus (DN) - were automatically segmented using a multi-atlas segmentation method based on both MPRAGE and QS images, taking advantage of the high DGM contrast available in QS maps (4). Ten manually segmented volumes from healthy controls were used as atlases. Following a standard multi-atlas segmentation method (17), the atlases from the ten healthy controls were propagated to each individual using automatic nonlinear registration on

multimodal MPRAGE, R2* and QS data (18). The registered anatomical labels propagated from the ten atlases were fused from MPRAGE and QS labels using a probabilistic method (19) to produce optimal segmentation of each dataset. Segmentations of all patients were manually checked on Insight Toolkit Snake Automatic Partitioning (ITK-SNAP) software to verify that they were error-free.

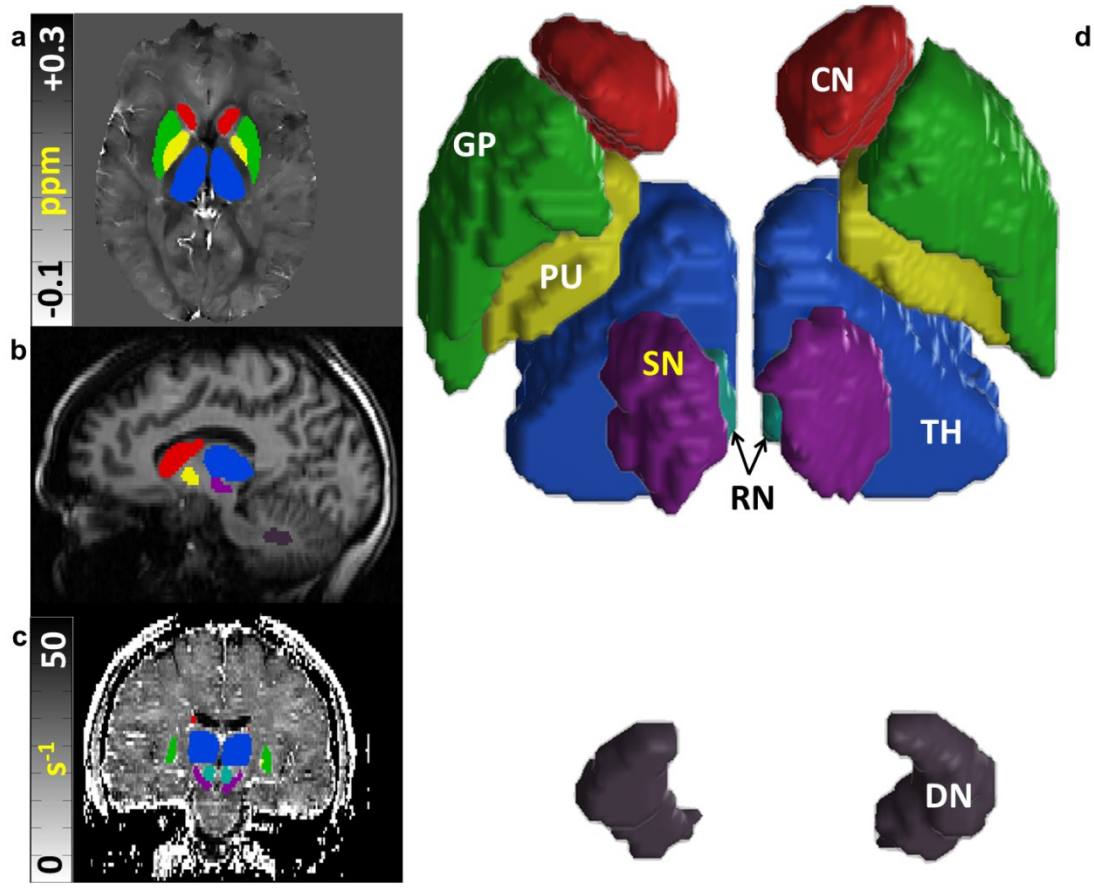

Figure 5.1 Representative images from a 33 year-old RRMS female patient showing (a) QS axial, (b) T1-weighted sagittal, and (c) R2* coronal slice. The segmented DGM structures are shown in (a), (b), (c) and (d), including Caudate Nucleus (CN), PUtamen (PU), THalamus (TH), and Globus Pallidus (GP), Red Nucleus (RN), Substantia Nigra (SN), and the Dentate Nucleus (DN).

5.2.4.3. Bulk Analysis

For bulk analysis, anatomical segmentation labels were used to compute mean R2*, mean QS and volumes of bilateral segmented DGM structures for baseline and follow-up. DGM volumes were first normalized to baseline whole brain volumes.

5.2.4.4. Discriminative Analysis of Regional Evolution (DARE)

For DARE, follow-up datasets were registered to baseline using rigid and then nonlinear registration (206) to identify DARE regions in baseline space. DARE regions were then labelled according to iron and myelin/calcium longitudinal increase or decrease (**Figure 5.2**). Positive R2* & positive QS and negative R2* & negative QS longitudinal changes were labelled as iron increase and decrease respectively, while positive R2* & negative QS and negative R2* & positive QS indicated myelin/calcium increase and decrease respectively (159). Bilateral DGM spatial extent of longitudinal changes in iron and myelin/calcium was computed using a voxel count of DARE regions, while average and total longitudinal changes in iron and myelin/calcium were quantified by taking the mean and sum of R2* and QS values in identified DARE regions. All DARE computed parameters were normalized to the baseline volume of the DGM structure to account for individual variations in structure size.

5.2.5. Statistical Analysis

Separate mixed factorial analyses of mean R2*, mean QS, and regional volumes of segmented structures were carried out for bulk analysis using longitudinal acquisitions as within subject variables, and RRMS and PMS versus control groups as between subject variables. The objective was to test if there were longitudinal effects for aging, group differences between patients and controls, and a longitudinal*group interaction that reflects the effect of diseased versus healthy aging. Normality was tested using Shapiro-Wilk tests and Q-Q plots. Due to violation of normality assumptions for follow-up PMS data, PMS TH volume was excluded from analysis of

variance (ANOVA). Independent t-tests were used to test for TH volume group effects at baseline, Mann-Whitney U tests were used to test specific group effects at follow-up and for follow-up-baseline, paired t-tests were used to test for longitudinal effects for CTRL-P, and Wilcoxon rank sum tests were used to test for specific longitudinal effects for PMS. Two-one-sided-tests (TOST) of followup-baseline bulk measures were also performed using XLStat (Addinsoft, NY) and Microsoft Excel, to probe whether non-significant ANOVA interaction results have been caused by the study's small sample size.

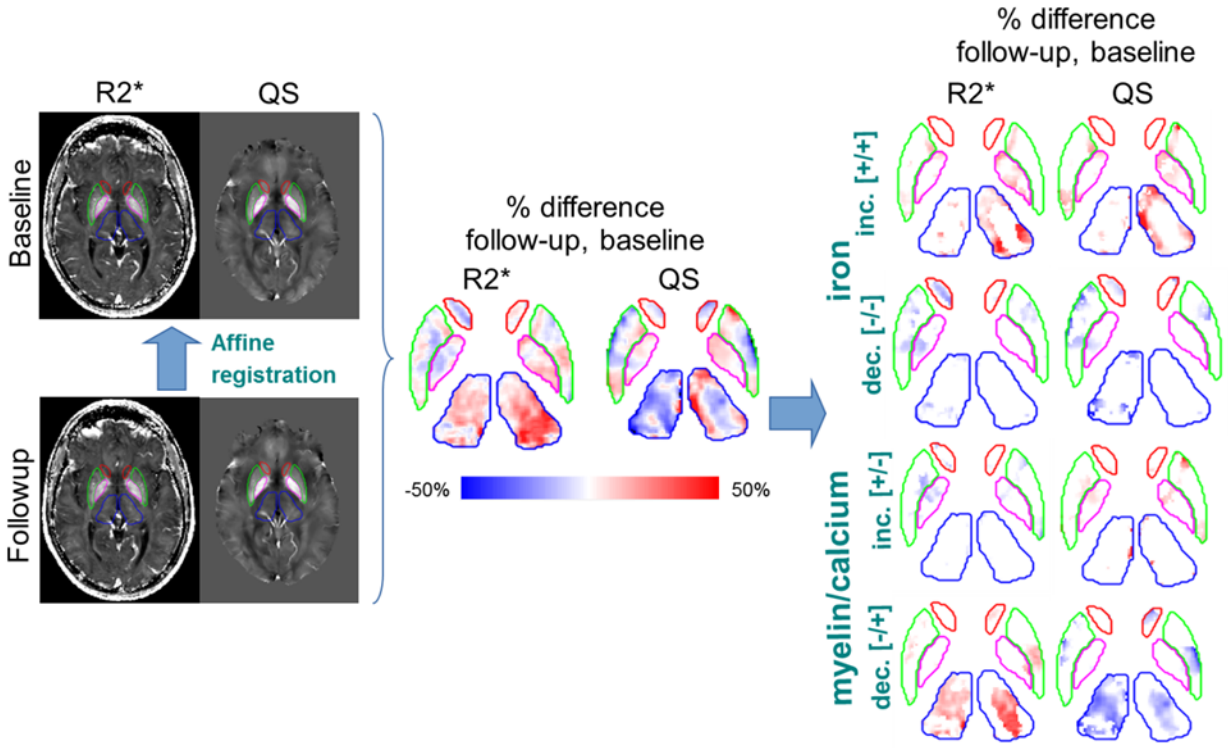

Figure 5.2 Algorithm for DARE image processing for patient shown in **Figure 5.1**, where followup R2* & QS were registered to baseline (left), then the percent difference of segmented structures R2* & QS (middle) was used to distinguish DGM iron increase (positive R2* & positive QS longitudinal changes), iron decrease (negative R2* & negative QS longitudinal changes), myelin/calcium increase (positive R2* & negative QS longitudinal changes), and myelin/calcium decrease (negative R2* & positive QS longitudinal changes) (right). inc.=increase; dec.=decrease.

Since DARE mostly exhibited non-normal distributions, Mann-Whitney U tests were used to test the hypotheses that iron increase/decrease and myelin/calcium increase/decrease in DGM structures were different between RRMS and PMS versus age-matched controls. η was used to measure effect sizes of parametric tests in bulk analysis, while rank biserial correlation was used for non-parametric tests in DARE and bulk analysis.

Multiple regression analysis using a backward elimination model (α=0.05, P=0.1) of DGM structures was used to regress bulk followup-baseline MRI and DARE measures with followup MSSS to estimate the most appropriate measure for MS severity prediction. The regression model included age as a regressor to account for its effect on disability progression, and grouped all RRMS and PMS patients into a large MS group. Assumptions of linearity and homoscedasticity were confirmed using plots of predicted residuals versus error residuals. Normality of residuals was confirmed using residual histograms and Q-Q plots, while histograms also confirmed absence of outliers. Data was confirmed to be free of multi-collinearity violations by checking Variance Inflation Factor values. Finally, independence of errors was confirmed after checking plots of residual autocorrelations and the Durbin-Watson statistic.

Unless otherwise stated, all statistical analyses were performed in SPSS (IBM, Armonk, NY) and MATLAB using α=0.05 and False Detection Rate (FDR) correction, with FDR-corrected P-values referred to as Q-values. Non-corrected P-values for bulk analysis were also reported for comparison with appropriate literature values.

5.3.Results

5.3.1.Study Design

Table 5.1 describes demographic information of retrospectively selected age-matched groups. Age-matching was confirmed using t-tests indicating that there were no significant ($P \leq 0.05$) differences between ages of RRMS and CTRL-R groups, and between ages of PMS and CTRL-P groups.

5.3.2.Bulk Analysis of MRI data

Table 5.2 lists median and interquartile range of bulk mean R2*, bulk mean QS, and regional volumes of segmented DGM structures, along with the FDR-corrected effect sizes of DGM ANOVA and specific parametric and non-parametric statistical tests of PMS TH. Significant effects ($Q \leq 0.05$) were only found for group effects using TH volume in RRMS ($Q=0.0032$) and PMS ($Q=0.000021$ at baseline and $Q=0.000006$ at followup). Significant longitudinal effects were found using R2* in CN for RRMS ($Q=0.00058$) and PMS ($Q=0.02$), PU for RRMS ($Q=0.00038$) and PMS ($Q=0.013$), RRMS GP ($Q=0.0046$), and RRMS RN ($Q=0.012$), and using volumes in RRMS PU ($Q=0.0076$) and RRMS DN ($Q=0.0017$). Significant longitudinal*group interaction effects were only found in RRMS CN QS ($Q=0.004$) and RRMS PU volume ($Q=0.034$). No outliers were present in any of the tested data, except for follow-up TH QS and follow-up DN volume. However, the presence/absence of these outliers did not affect the results, which was revealed by repeating analyses without the outliers.

Table 5.1 Demographic information of RRMS ($P=0.98$) and PMS ($P=0.3$) and age-matched control groups. The number of patients without relapses since diagnosis prior to the study, compared to during the study period is also shown for RRMS. [i]

Patient Group (n)	EDSS (mean ± SD)		relapse-free		DMT	Disease Duration	Baseline Age	Followup period	Sex (M/F)
	baseline	follow-up	before	during		(mean ± SD, yrs)			
CTRL-R (27)							38.5±8.8	2.0±0.2	8/19
RRMS (27)	2.4±1.2	2.5±0.9	3	14	27	7.7±4.0	38.6±8.7	2.0±0.3	4/23
CTRL-P (17)							45.1±6.8	2.1±0.9	4/13
PMS (17)	6.2±0.3	6.3±0.3			5	16.6±8.6	49.6±8.7	1.9±0.4	8/9

[1] CTRL-R = control group age matched to RRMS group; RRMS = relapsing-remitting MS; CTRL-P = control group age matched to PMS group; PMS = Progressive MS; DMT = Disease Modifying Therapy.

For non-corrected ANOVA, significant group differences between RRMS and CTRL-R were also detected using R2* CN ($P=0.02$), PU QS ($P=0.04$), and GP QS ($P=0.04$), while significant

group differences were detected between PMS and CTRL-P in RN volume (P=0.04) and DN volume (P=0.04). Significant (non-corrected) longitudinal effects were also detected for RRMS TH QS (P=0.03) and TH volume (P=0.03), while longitudinal effects were detected for RN QS (P=0.03) and SN QS (P=0.05). For non-corrected interaction effects, significant group differences were also detected in RRMS TH volume (P=0.05). Finally, TOST revealed that all non-significant ANOVA interaction effects were non-equivalent using a confidence interval of 95%.

5.3.3. DARE of Iron & Myelin/Calcium

Histograms of R2* and QS longitudinal differences for patient and control groups DGM voxels are shown in **Figure 5.3**. For R2*, CTRL-R DGM shows a distinct concentration of longitudinal differences at zero percent change, which was not found in RRMS. Similarly, both CTRL-P and PMS groups demonstrated this effect, although it was more pronounced for CTRL-P. The majority of R2* values ranged between ±30% longitudinal changes. For QS, normal distributions were observed for all groups, with the majority of values ranging between ±2.5% longitudinal changes. The area under the curve for MS patients' histograms was less than that for controls because of DGM atrophy.

For visual illustration of DARE parameters, **Figure 5.4** displays surface maps of RRMS and PMS compared to age-matched control groups. Surface maps show the first regional surface encountered through a 3D volume at a given orientation, but does not provide information about regions behind this surface. Colored regions indicate the most frequent DARE label in each group, i.e. DGM iron increase, decrease, and myelin/calcium increase, or decrease. Only CN, PU, TH, and GP structures are shown to avoid visual overlap with the RN, SN, and DN. To further improve visualization of DARE regions in **Figure 5.4**, a threshold of one percent longitudinal difference was implemented in the figure.

5.3.3.1. Size of DARE Regions

Figure 5.5 demonstrates the size of regions labeled as iron or myelin/calcium changes for patients versus controls. Statistically significant differences between RRMS and CTRL-R groups were only detected for iron increase (Q=0.004) and iron decrease (Q=0.0003) in the CN, with RRMS demonstrating smaller regions of iron increase and larger regions of iron decrease compared to CTRL-R. Significant differences between PMS and CTRL-P were only detected for GP myelin/calcium increase (Q=0.03), with CTRL-P demonstrating larger regions than the PMS group.

Table 5.2 Median [interquartile range] of DGM R2*, QS, and regional volumes with their longitudinal, group, and longitudinal*group interaction effect sizes; Significant FDR-corrected effect sizes (Q≤0.05) are bolded, while significant (P≤0.05) non-corrected P-values are italicized. E.S. = effect size, * = Q≤0.05, ** = Q≤0.01, *** = Q≤0.001, ***** = Q≤0.00001, ****** = Q≤0.000001.

		R2* (s^{-1})			QS (ppb)			Volume (mm^3 $x10^3$)		
		baseline	followup	E.S.	baseline	followup	E.S.	baseline	followup	E.S.
CN	CTRL-R	29.7 [28.2-33.8]	32.1 [30.4-34.6]	0.49 *** [b]	101.1 [88.1-110.4]	99.9 [91.7-114.4]	NS [b]	5.99 [5.67-6.31]	6.15 [5.70-6.51]	NS [b]
	RRMS	33.3 [30.9-35.6]	34.0 [31.6-35.9]		113.4 [98.1-119.8]	111.2 [92.6-121.7]		5.76 [5.42-6.32]	5.73 [5.33-6.20]	
	E.S.	NS (0.02) [a]		NS [c]	NS [a]		0.45** [c]	NS [a]		NS [c]
	CTRL-P	33.4 [30.1-34.0]	33.5 [32.1-34.8]	0.47 * [b]	106.8 [98.5-118.2]	110.0 [89.1-116.7]	NS [b]	6.06 [5.73-6.40]	6.24 [5.82-6.44]	NS [b]
	PMS	34.3 [30.4-37.4]	34.7 [30.6-39.2]		94.3 [85.4-122.3]	99.9 [82.9-130.3]		5.81 [5.40-6.25]	5.96 [5.29-6.57]	
	E.S.	NS [a]		NS [c]	NS [a]		NS [c]	NS [a]		NS [c]
PU	CTRL-R	34.7 [30.8-37.3]	36.6 [32.4-38.7]	0.52 *** [b]	95.1 [86.0-112.4]	99.7 [85.2-107.2]	NS [b]	9.16 [8.73-9.68]	9.20 [8.77-9.64]	0.41** [b]
	RRMS	35.9 [33.0-41.1]	36.2 [34.7-41.5]		105.5 [97.7-130.1]	100.0 [87.4-124.4]		9.10 [8.45-9.80]	9.07 [8.34-9.62]	
	E.S.	NS [a]		NS [c]	NS [a] (0.04)		NS [c]	NS [a]		0.38* [c]
	CTRL-P	37.0 [34.4-39.3]	37.6 [35.4-39.8]	0.43 * [b]	102.2 [89.8-110.6]	103.2 [90.6-111.9]	NS [b]	9.21 [8.83-9.48]	9.20 [8.80-9.72]	NS [b]
	PMS	38.7 [33.6-43.0]	39.6 [35.7-43.7]		100.7 [84.1-126.0]	103.2 [82.3-130.8]		8.73 [8.06-9.33]	8.60 [7.92-9.22]	
	E.S.	NS [a]		NS [c]	NS [a]		NS [c]	NS [a]		NS (0.04) [c]
TH	CTRL-R	27.5 [26.3-28.3]	27.8 [26.4-29.0]	NS [b]	60.8 [54.3-64.8]	61.5 [55.2-67.4]	NS [b]	13.8 [13.2-14.9]	14.0 [13.3-14.8]	NS (0.03) [b]
	RRMS	28.2 [25.8-31.7]	28.8 [26.7-31.2]		61.0 [55.6-73.8]	63.0 [49.8-73.4]		13.0 [12.0-13.4]	12.7 [12.0-12.9]	
	E.S.	NS [a]		NS [c]	NS [a]		NS [c]	0.46** [a]		NS (0.05) [c]

	CTRL-P	27.3 [26.4-28.6]	28.8 [26.2-28.9]	NS [b]	63.8 [56.7-69.3]	58.4 [53.2-68.5]	NS [b]	13.8 [13.2-14.7]	13.8 [13.0-14.3]	NS [f]
	PMS	26.7 [24.4-28.4]	27.0 [24.2-28.2]		52.9 [44.7-63.6]	52.6 [41.0-60.1]		11.0 [9.51-12.7]	10.6 [8.81-11.8]	NS [g]
	E.S.	NS [a]		NS [c]	NS [a] (0.04)		NS [c]	0.71 [d] *****	0.88 [e] ******	NS [h]
GP	CTRL-R	54.4 [51.2-59.8]	56.2 [53.1-60.6]	0.41 ** [b]	197.2 [177.1-213.8]	191.1 [169.3-211.5]	NS [b]	3.47 [3.33-3.57]	3.45 [3.27-3.58]	NS [b]
	RRMS	59.0 [54.3-62.6]	62.1 [55.6-66.1]		216.3 [192.9-227.3]	212.5 [185.3-218.5]		3.47 [3.23-3.75]	3.39 [3.25-3.65]	
	E.S.	NS [a]		NS [c]	NS [a] (0.04)		NS [c]	NS [a]		NS [c]
	CTRL-P	56.1 [52.3-63.9]	59.8 [54.7-64.5]	NS [b]	204.6 [180.9-221.4]	204.4 [172.6-216.2]	NS [b]	3.52 [3.33-3.64]	3.50 [3.37-3.65]	NS [b]
	PMS	58.3 [53.4-66.7]	60.4 [52.5-64.6]		196.6 [182.8-236.2]	211.7 [175.9-244.4]		3.42 [3.13-3.72]	3.39 [3.04-3.64]	
	E.S.	NS [a]		NS [c]	NS [a]		NS [c]	NS [a]		NS [c]
RN	CTRL-R	44.2 [40.4-48.6]	45.6 [41.0-48.3]	0.36 * [b]	128.7 [119.6-158.7]	133.7 [116.0-163.0]	NS [b]	0.63 [0.60-0.70]	0.62 [0.59-0.69]	NS [b]
	RRMS	44.0 [40.0-48.5]	46.2 [41.4-50.2]		144.1 [126.6-156.9]	146.1 [128.2-166.7]		0.59 [0.56-0.64]	0.61 [0.56-0.65]	
	E.S.	NS [a]		NS [c]	NS [a]		NS [c]	NS [a]		NS [c]
	CTRL-P	47.4 [43.2-52.0]	46.7 [41.8-52.6]	NS [b]	149.4 [127.1-170.6]	146.6 [12.7-172.0]	NS [b] (0.03)	0.64 [0.62-0.71]	0.63 [0.60-0.69]	NS [b]
	PMS	47.0 [40.1-51.8]	47.5 [40.1-52.3]		154.4 [135.5-183.5]	157.3 [118.8-184.0]		0.59 [0.58-0.65]	0.59 [0.56-0.65]	
	E.S.	NS [a]		NS [c]	NS [a]		NS [c]	NS [a] (0.04)		NS [c]
SN	CTRL-R	47.9 [43.5-53.2]	47.7 [44.0-52.1]	NS [b]	170.7 [147.9-188.0]	170.4 [158.2-186.2]	NS [b]	1.46 [1.34-1.51]	1.44 [1.35-1.52]	NS [b]
	RRMS	48.3 [43.9-53.9]	49.0 [44.2-55.0]		178.9 [153.6-194.6]	178.9 [153.8-195.8]		1.39 [1.31-1.55]	1.36 [1.30-1.54]	
	E.S.	NS [a]		NS [c]	NS [a]		NS [c]	NS [a]		NS [c]
	CTRL-P	49.2 [46.1-56.9]	49.9 [46.9-56.8]	NS [b]	176.3 [160.5-193.3]	178.5 [155.2-194.2]	NS [b] (0.05	1.45 [1.36-1.52]	1.46 [1.36-1.55]	NS [b]

	PMS	49.4 [42.0-59.0]	52.7 [42.3-55.6]		180.5 [135.4-209.8]	187.1 [129.1-238.8]	)	1.31 [1.23-1.50]	1.40 [1.20-1.53]	
	E.S.	NS [a]		NS [c]	NS [a]		NS [c]	NS [a]		NS [c]
	CTRL-R	40.4 [36.9-45.2]	40.1 [35.8-48.5]	NS [b]	124.5 [110.6-149.0]	130.5 [117.5-158.5]	NS [b]	1.69 [1.47-1.83]	1.59 [1.40-1.77]	0.48** [b]
	RRMS	43.5 [36.4-48.2]	43.3 [39.2-53.9]		141.7 [127.2-150.8]	147.2 [113.5-157.3]		1.71 [1.45-2.00]	1.62 [1.44-1.77]	
DN	E.S.	NS [a]		NS [c]	NS [a]		NS [c]	NS [a]		NS [c]
	CTRL-P	39.3 [36.9-44.0]	42.6 [37.8-50.5]	NS [b]	138.3 [115.5-154.3]	134.8 [121.9-134.8]	NS [c]	1.73 [1.50-1.97]	1.66 [1.57-1.89]	NS [c]
	PMS	40.5 [34.0-49.1]	41.1 [35.6-47.4]		124.4 [105.3-156.7]	144.5 [108.1-187.0]	NS [b]	1.46 [1.22-1.75]	1.52 [1.18-1.72]	NS [b]
	E.S.	NS [a]		NS [c]	NS [a]		NS [c]	NS [a] (0.04)		NS [c]

RRMS = Relapsing-remitting Multiple Sclerosis; PMS. = Progressive Multiple Sclerosis, CTRL-R = control group age-matched to RRMS, CTRL-P = control group age-matched to PMS, E.S. = Effect Size; NS = Not Significant; QS = Quantitative Susceptibility; CN = Caudate Nucleus, PU = Putamen, TH = Thalamus; GP = Globus Pallidus; RN = Red Nucleus; SN = Substantia Nigra; DN = Dentate Nucleus.

[a] group effect size (η) for mixed factorial ANOVA
[b] longitudinal effect size (η) for mixed factorial ANOVA
[c] interaction effect size (η) for mixed factorial ANOVA
[d] group effect size (η) for independent t-test at baseline
[e] effect size (rank biserial correlation) for Mann-Whitney U test for group tests at followup due to non-normality of data
[f] longitudinal effect size (η) for paired t-test between baseline and followup for CTRL-P group
[g] longitudinal effect size (matched-pairs rank-biserial correlation) for Wilcoxon rank sum for between baseline and followup for PMS group due to non-normality of data
[h] disease effect size (rank biserial correlation) for Mann-Whitney U test for group tests of followup-baseline due to non-normality of data

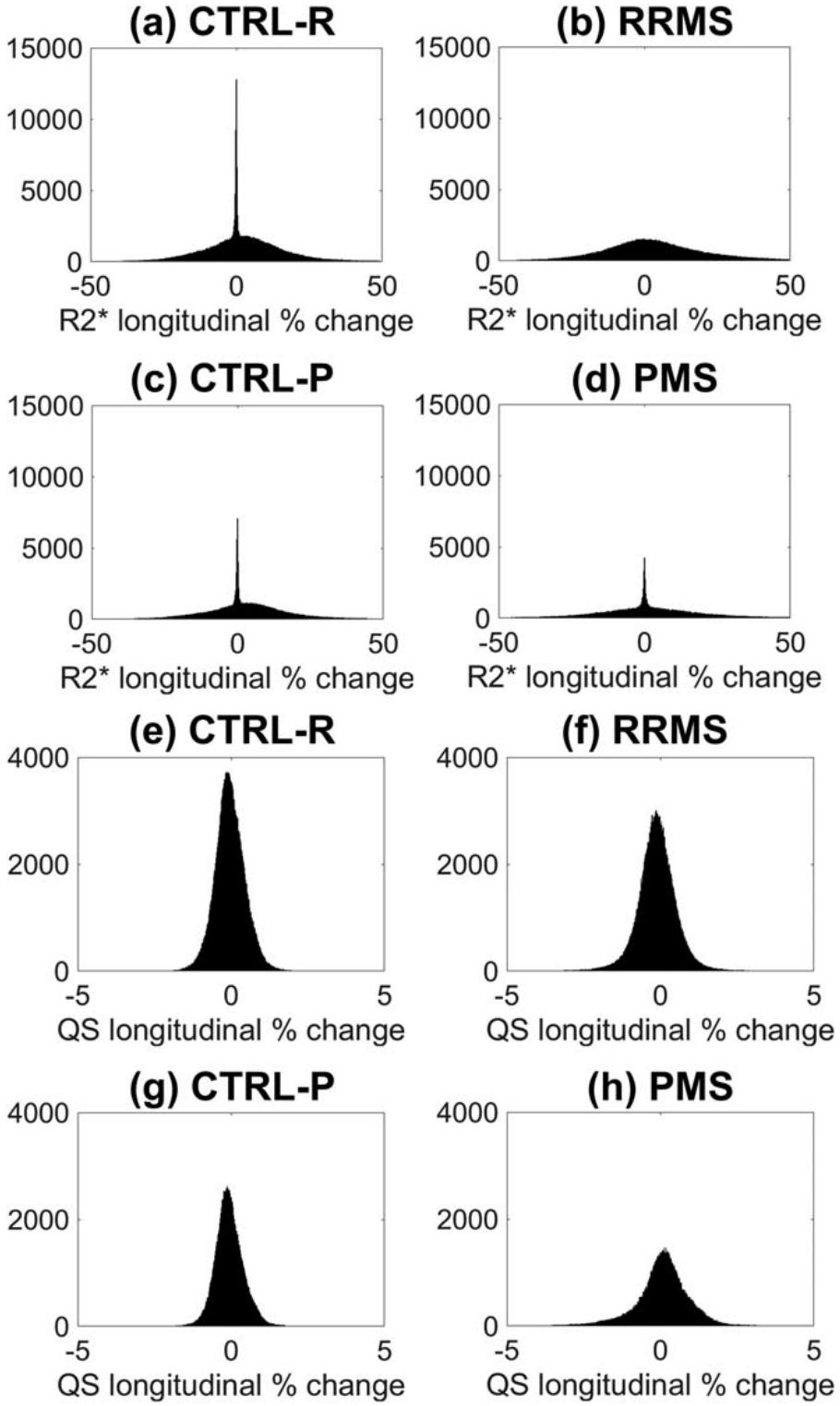

Figure 5.3 Histograms of R2* (**a**-**d**) and QS (**e**-**h**) longitudinal differences for CTRL-R (**a**,**e**) vs. RRMS (**b**,**f**) and CTRL-P (**c**,**g**) vs. PMS (**d**,**h**). Note the different axis scales for R2* (**a**-**d**) and QS (**e**-**h**) plots.

5.3.3.2. Mean Intensity of DARE Regions

Mean R2* and QS longitudinal intensity changes of DARE regions is displayed in **Figure 5.6**, which represents the average longitudinal change in iron and myelin/calcium in RRMS and PMS DGM compared to CTRL-R and CTRL-P, respectively. Compared to QS, R2* demonstrated increased sensitivity to detect significant changes in iron and myelin/calcium between RRMS and CTRL-R, whereas R2* and QS performed similarly for detecting significant group differences between PMS and CTRL-P.

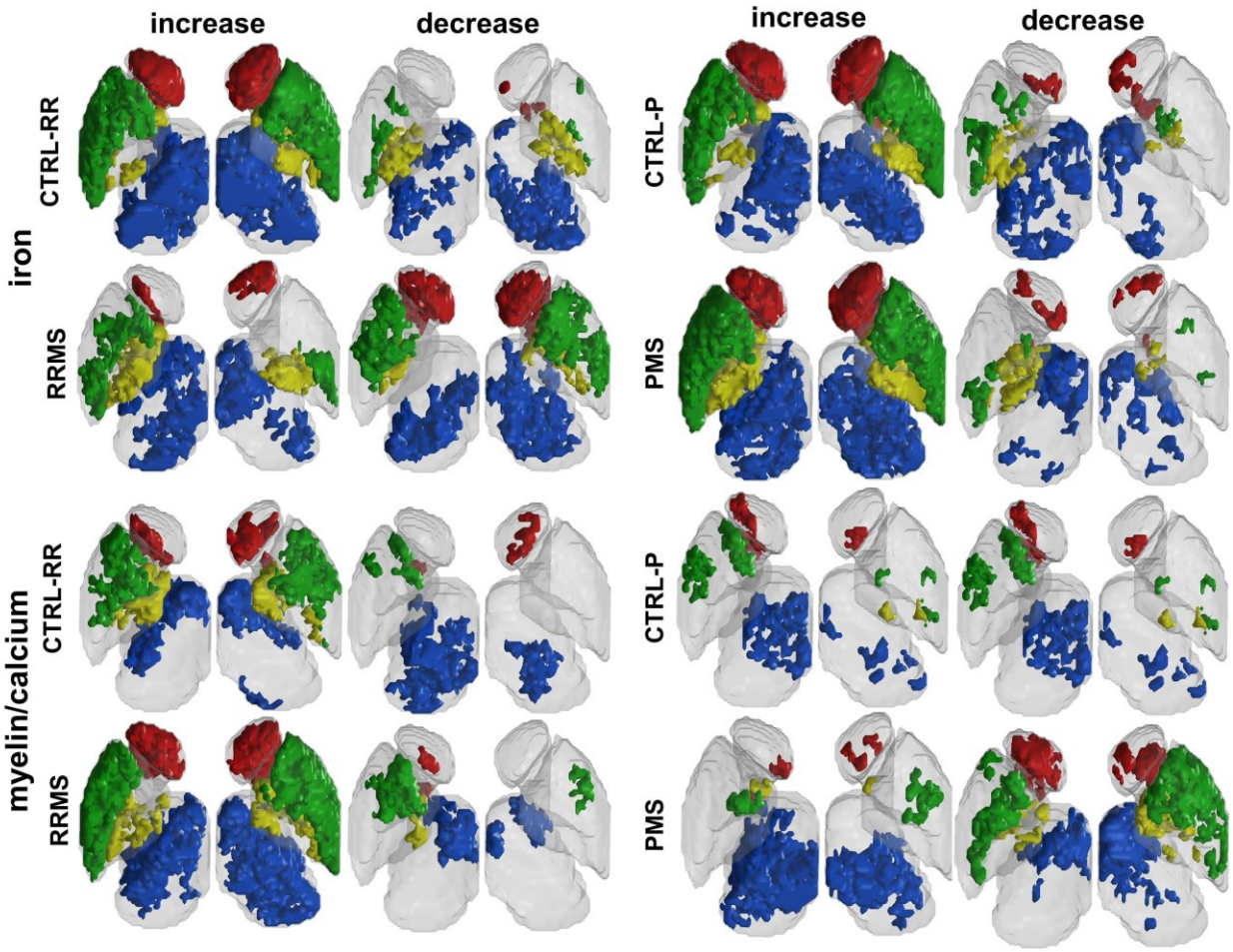

Figure 5.4 Maps of DARE regions' surfaces shown within 3D structures for CN, PU, GP, and TH, where displayed structures were colored according to the color scheme shown in **Figure 5.1** for distinction.

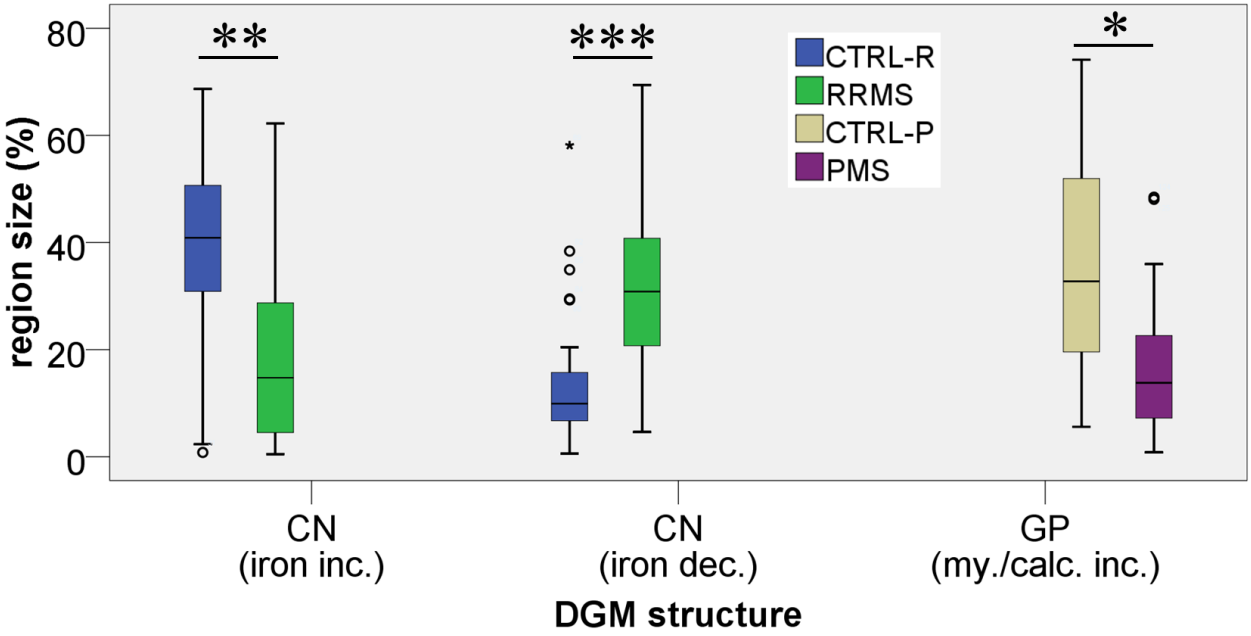

Figure 5.5 Size of DARE regions labelled with iron and myelin/calcium increase/decrease of RRMS (green) and PMS (purple) compared to age-matched controls. Only values significantly different between patients and controls are shown; * = Q≤0.05, ** = Q≤0.01, *** = Q≤0.001. Inc. = Increase; Dec. = Decrease; My. = Myelin; Calc. = Calcium.

Using mean R2*, significant longitudinal changes between RRMS vs. CTRL-R were found: for iron increase in TH (Q=0.007), GP (Q=0.004), RN (Q=0.03), SN (Q=0.03); for iron decrease in CN (Q=0.01), TH (Q=0.02), GP (Q=0.008); for myelin/calcium increase in PU (Q=0.02), TH (Q=0.003), GP (Q=0.02), RN (Q=0.05), SN (Q=0.02), DN (Q=0.02); and for myelin/calcium decrease in CN (Q=0.002), PU (Q=0.001), TH (Q=0.01), and GP (Q=0.005). In contrast, mean QS detected significant longitudinal changes for iron increase in SN (Q=0.02); for iron decrease in in CN (Q=0.0002), PU (Q=0.04), and TH (Q=0.02); and for myelin/calcium increase in CN (Q=0.004), PU (Q=0.007), and TH (Q=0.04).

For PMS, significant longitudinal changes in mean R2* between PMS vs. CTRL-P were found: for calcium/myelin increase in CN (Q=0.04), PU (Q=0.04), TH (Q=0.04), and SN (Q=0.04); and in mean QS for calcium/myelin decrease for CN (Q=0.03), PU (Q=0.007), TH (Q=0.002), SN (Q=0.03), and DN (Q=0.007).

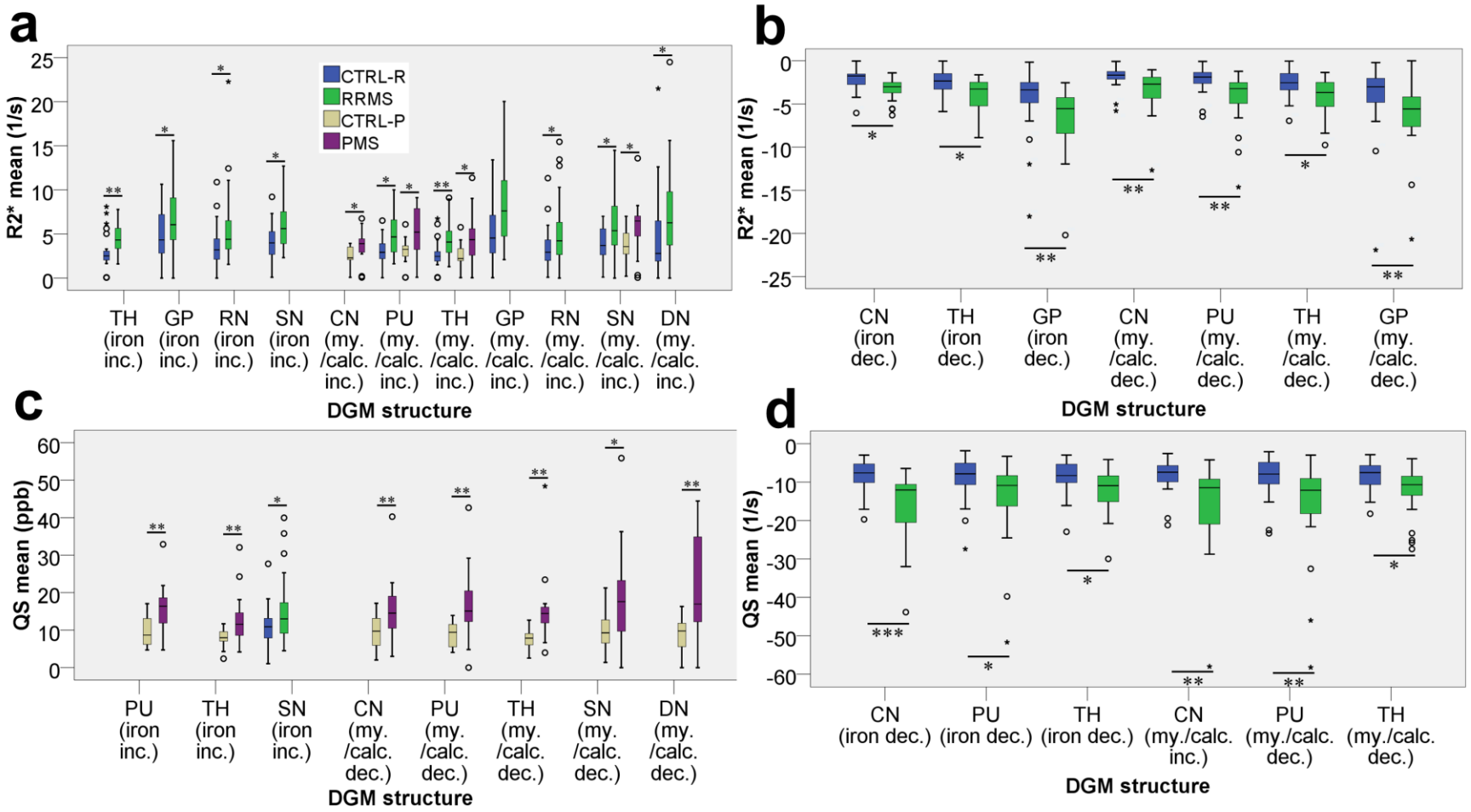

Figure 5.6 Positive (**a**,**c**) and negative (**b**,**d**) longitudinal changes in mean R2* (**a**,**b**) and QS (**c**,**d**) of DARE regions for iron and myelin/calcium increase/decrease of RRMS (green) and PMS (purple) compared to age-matched controls. Only values significantly different between patients and controls are shown; * = Q≤0.05, ** = Q≤0.01, *** = Q≤0.001. Inc. = Increase; Dec. = Decrease; My. = Myelin; Calc. = Calcium.

5.3.3.3. Total Changes in DARE Regions

The sum of R2* and QS values of DARE regions are presented in **Figure 5.7**, which represent the total longitudinal DGM changes of iron and myelin/calcium after taking into account both size (iron and myelin spatial extent) and average intensity changes (average iron and myelin concentration changes) of DARE regions. Significant changes were detected between RRMS and CTRL-R using total R2* values of DARE regions for iron decrease in CN (Q=0.00002) and PU (Q=0.02); and for myelin/calcium increase in PU (Q=0.03) and TH (Q=0.03). For QS mapping, total DARE significant changes between RRMS and CTRL-R were detected in CN for iron increase (Q=0.02) and decrease (Q=0.00006), and myelin/calcium increase (Q=0.03). Significant total longitudinal changes between PMS and CTRL-P were detected only for QS PU (Q=0.05).

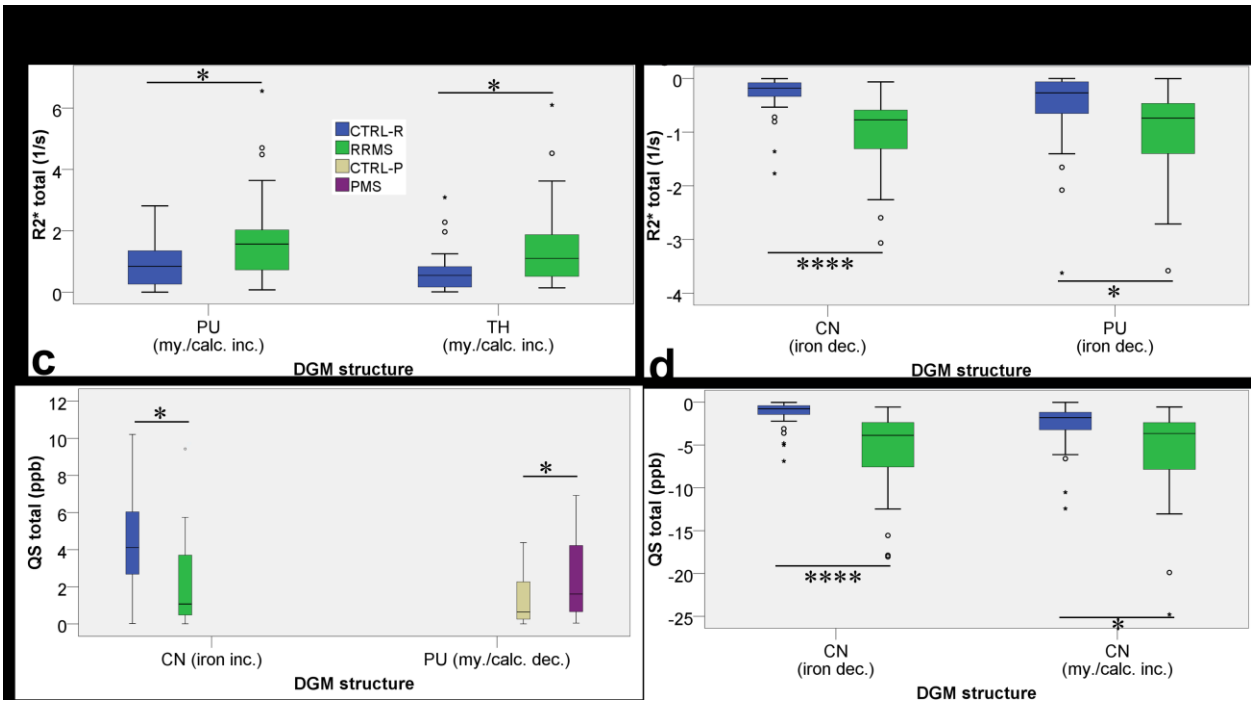

Figure 5.7 Positive (**a**,**c**) and negative (**b**,**d**) longitudinal changes in total R2* (**a**,**b**) and QS (**c**,**d**) of DARE regions for iron and myelin/calcium increase/decrease of RRMS (green) and PMS (purple) compared to age-matched controls; The total longitudinal change is defined as the number of voxels within a region multiplied by the sum of R2* or QS intensity within the region. Only values significantly different between patients and controls are shown * = Q≤0.05, **** = Q≤0.0001. Inc. = Increase; Dec. = Decrease; My. = Myelin; Calc. = Calcium.

5.3.3.4. Effect Size of DARE Regions

The effect sizes of significant differences between controls and patients using DARE are presented in **Table 5.3**. Apparently, the CN was the most common DGM structure that demonstrated longitudinal regional iron changes in RRMS versus CTRL-R. Additionally, the CN demonstrated the highest effect size for DGM changes using total R2* (r=0.74; Q=0.00002) and total QS (r=0.71; P=0.00006). On the other hand, iron increase in the PU(r=0.62; Q=0.007) and TH (r=0.61; Q=0.007) using mean QS were the observed significant differences between PMS and CTRL-P, with higher effect sizes than corresponding RRMS values.

For calcium/myelin changes, the most affected structures for RRMS versus CTRL-R the PU and TH, where the highest effect sizes were observed for PU myelin/calcium decrease using mean R2* (r=0.59; Q=0.001), and TH calcium/myelin increase (r=0.56; Q=0.003). Similarly, the most affected structure for calcium/myelin changes in PMS versus CTRL-P were the PU and TH, with the highest effect sizes recorded for TH myelin/calcium decrease using mean QS (r=0.7; Q=0.002) and PU calcium/myelin decrease using mean QS (r=0.59; Q=0.007),

5.3.4. Regression With Disease Severity

Standardized regression coefficients of followup MSSS with bulk analysis and DARE measures are displayed in **Table 5.4**, with the models with the highest Person's correlation in bulk analysis, DARE iron increase, iron decrease myelin/calcium increase, and myelin/calcium decrease displayed in **Figure 5.8**. DARE clearly demonstrated improved correlation with disease severity compared to followup-baseline R2*, QS and volume bulk analysis, after accounting for the effect of age.

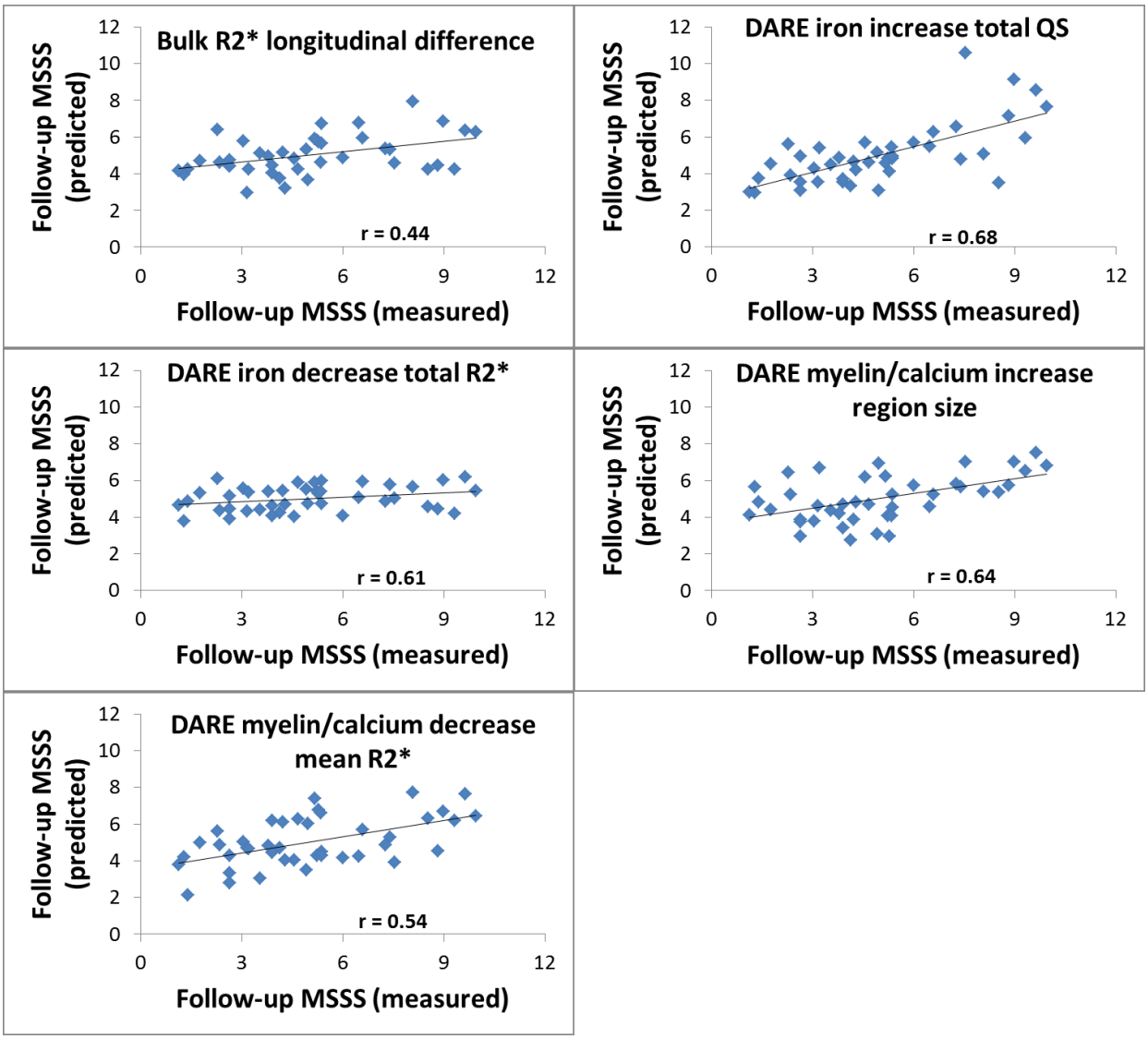

Figure 5.8 Correlation plots of predicted follow-up Multiple Sclerosis Severity Scale (MSSS) with the measured follow-up MSSS for the models with the highest Pearson's correlation coefficients in Table 5.4. Structures in cluded in the model of bulk R2* are CN and DN; of DARE iron increase total QS are RN and SN; of DARE iron decrease total R2* are PU and SN; of DARE myelin/calcium increase regin size are CN and GPl of DARE myelin/calcium decrease mean R2* are GP, RN and SN.

Table 5.3 Effect sizes for iron and myelin/calcium changes of control and MS group differences of DARE region size, mean R2*, total R2*, mean QS, and total QS. Only significant (Q≤0.05) effects are shown, and the RN PMS column is not shown because it did not contain any significant values.

		CN		PU		TH		GP		RN	SN		DN	
		RR	**PMS**	**RR**	**PMS**	**RR**	**PMS**	**RR**	**PMS**	**RR**	**RR**	**PMS**	**RR**	**PMS**
iron inc.	Size	**0.54 ($4x10^{-3}$)**												
	$R2^*_m$					**0.52 ($7x10^{-3}$)**		**0.36 ($4x10^{-2}$)**		**0.39 ($3x10^{-2}$)**	**0.41 ($3x10^{-2}$)**			
	QS_m				**0.62 ($7x10^{-3}$)**		**0.61 ($7x10^{-3}$)**				**0.54 ($2x10^{-2}$)**			
	$R2^*_t$													
	QS_t	**0.47 ($2x10^{-2}$)**												
iron dec.	Size	**0.65 ($3x10^{-4}$)**												
	$R2^*_m$	**0.47 ($1x10^{-2}$)**				**0.43 ($2x10^{-2}$)**		**0.51 ($8x10^{-3}$)**						
	QS_m	**0.66 ($2x10^{-4}$)**		**0.39 ($4x10^{-2}$)**		**0.40 ($4x10^{-2}$)**								
	$R2^*_t$	**0.74 ($2x10^{-5}$)**		**0.44 ($2x10^{-2}$)**										
	QS_t	**0.71 ($6x10^{-5}$)**												
My./Calc. inc.	Size								**0.56 ($3x10^{-2}$)**					
	$R2^*_m$		**0.52 ($4x10^{-2}$)**	**0.45 ($2x10^{-2}$)**	**0.51 ($4x10^{-2}$)**	**0.56 ($3x10^{-3}$)**	**0.45 ($4x10^{-2}$)**	**0.42 ($2x10^{-2}$)**		**0.32 ($5x10^{-2}$)**	**0.42 ($2x10^{-2}$)**	**0.47 ($4x10^{-2}$)**	**0.39 ($2x10^{-2}$)**	
	QS_m	**0.55 ($4x10^{-3}$)**		**0.49 ($7x10^{-3}$)**		**0.37 ($4x10^{-2}$)**								
	$R2^*_t$			**0.42 ($3x10^{-2}$)**		**0.42 ($3x10^{-2}$)**								
	QS_t	**0.46**												

		($3x10^{-2}$)													
My./Calc. dec.	Size														
	$R2^*_m$	**0.53 ($2x10^{-3}$)**		**0.59 ($1x10^{-3}$)**		**0.42 ($1x10^{-2}$)**		**0.48 ($5x10^{-3}$)**							
	QS_m		**0.45 ($3x10^{-3}$)**		**0.59 ($7x10^{-3}$)**		**0.70 ($2x10^{-3}$)**					**0.46 ($3x10^{-2}$)**		**0.58 ($7x10^{-3}$)**	
	$R2^*_t$														
	QS_t				**0.53 ($5x10^{-2}$)**										

DARE = Discriminative Analysis of Regional Evolution; Inc. = Increase; Dec. = Decrease; My. = Myelin; Calc. = Calcium; Size = Region Size; QS = Quantitative Susceptibility; $R2^*_m$ = R2* mean; $R2^*_t$ = R2* total; QS_m = QS mean; QS_t = QS mean; CN = Caudate Nucleus, PU = Putamen, TH = Thalamus; GP = Globus Pallidus; RN = Red Nucleus; SN = Substantia Nigra; DN = Dentate Nucleus.

Table 5.4 Standardized coefficients of followup MSSS with DGM bulk measures (mean R2*, QS and volumes), and DARE measures (size, mean intensity, and total intensity of R2* and QS of identified regions). Multiple regression was implemented using backward elimination (α=0.05, P=0.1) of DGM structures and baseline age. Only predictors included in the model are shown, and FDR-corrected Q-values are shown between brackets.

		Model	Standardized Coefficients (Q)							
		r (Q)	age	CN	PU	TH	GP	RN	SN	DN
MRI Followup -Baseline	R2* mean	**0.44 ($5x10^{-2}$)**	0.29 ($8x10^{-2}$)	0.29 ($6x10^{-2}$)						-0.26 ($1x10^{-1}$)
	QS mean	**0.43 ($6x10^{-2}$)**	0.32 ($8x10^{-2}$)			-0.57 ($5x10^{-2}$)			0.59 ($4x10^{-2}$)	
	Volume	**0.42 ($3x10^{-2}$)**	0.40 ($4x10^{-2}$)			-0.33 ($5x10^{-2}$)				
	Size	**0.62 ($8x10^{-4}$)**	0.34 ($7x10^{-2}$)					-0.36 ($4x10^{-2}$)	0.78 ($2x10^{-4}$)	
DARE Iron Increase	R2* mean	**0.54 ($2x10^{-2}$)**	0.25 ($9x10^{-2}$)				0.56 ($2x10^{-2}$)	0.48 ($2x10^{-2}$)	-0.49 ($3x10^{-2}$)	
	QS mean	**0.52 ($1x10^{-2}$)**				0.28 ($5x10^{-2}$)				0.43 ($6x10^{-3}$)
	R2* total	**0.54 ($5x10^{-3}$)**	0.26 ($8x10^{-2}$)						0.46 ($3x10^{-3}$)	
	QS total	**0.68 ($5x10^{-4}$)**	0.24 ($8x10^{-2}$)					-0.33 ($4x10^{-2}$)	0.49 ($8x10^{-5}$)	
DARE Iron Decrease	Size	**0.40 ($2x10^{-2}$)**	0.40 ($4x10^{-2}$)							
	R2* mean	**0.28 ($7x10^{-2}$)**	0.28 ($8x10^{-2}$)							
	QS mean	**0.28 ($7x10^{-2}$)**	0.28 ($8x10^{-2}$)							
	R2* total	**0.61 ($3x10^{-3}$)**	0.58 ($2x10^{-3}$)		0.39 ($3x10^{-2}$)				-0.43 ($2x10^{-2}$)	
	QS total	**0.39 ($5x10^{-2}$)**		1.4 ($3x10^{-2}$)	-1.5 ($3x10^{-2}$)					

	Size	**0.64 ($8x10^{-4}$)**	0.42 ($2x10^{-2}$)	-0.27 ($6x10^{-2}$)			-0.25 ($8x10^{-2}$)			
	R2*	**0.39**				0.32				-0.34
DARE	mean	**($5x10^{-2}$)**				($5x10^{-2}$)				($4x10^{-2}$)
Myelin/	QS	**0.28**	0.28							
Calcium	mean	**($7x10^{-2}$)**	($8x10^{-2}$)							
Increase	R2*	**0.43**	0.26				-0.32			
	total	**($3x10^{-2}$)**	($8x10^{-2}$)				($4x10^{-2}$)			
	QS	**0.49**	0.32					-0.64	0.71	
	total	**($3x10^{-2}$)**	($8x10^{-2}$)					($3x10^{-2}$)	($1x10^{-2}$)	
	Size	**0.38 ($2x10^{-2}$)**		0.38 ($3x10^{-2}$)						
	R2*	**0.54**	0.25				0.56	0.48	-0.49	
DARE	mean	**($2x10^{-2}$)**	($9x10^{-2}$)				($2x10^{-2}$)	($2x10^{-2}$)	($3x10^{-2}$)	
Myelin/	QS	**0.28**	**0.28**							
Calcium	mean	**($7x10^{-2}$)**	($8x10^{-2}$)							
Decrease	R2*	**0.40**		-0.70	0.54					
	total	**($5x10^{-2}$)**		($3x10^{-2}$)	($4x10^{-2}$)					
	QS	**0.47**								0.47
	total	**($1x10^{-2}$)**								($6x10^{-3}$)

DARE = Discriminative Analysis of Regional Evolution; diff. = difference between followup and baseline, QS = Quantitative Susceptibility; CN = Caudate Nucleus, PU = Putamen, TH = Thalamus; GP = Globus Pallidus; RN = Red Nucleus; SN = Substantia Nigra; DN = Dentate Nucleus.

For bulk analysis, CN (β=0.29, Q=0.06) and DN (β=0.26, Q=0.01) were the only DGM structures included in the R2* regression model (r=0.44; Q=0.05); TH (β=-0.57, Q=0.05) and SN (β=0.59; Q=0.04) for the QS model (r=0.42; Q=0.06); and TH (β=-0.33, Q=0.05) for the regional volume model (r=0.42; Q=0.03). Conversely, DARE allowed correlating MSSS with specific iron and myelin/calcium longitudinal changes, which generally produced higher correlation coefficients for the regression models.

Although both QS bulk analysis (β=0.59; Q=0.0) and DARE QS total (β=0.71; Q=0.01) detected that the strongest MSSS predictor for QS was the SN, the use of combined R2* and QS in DARE QS total revealed that longitudinal QS changes in the SN were driven by both iron increase and myelin/calcium increase. Similarly, DARE R2* total revealed that the driver of MSSS correlation with bulk R2* in the CN was a negative correlation with myelin/calcium decrease, while DARE R2* mean revealed that the driver of observed negative MSSS correlation in the DN with bulk R2* was a negative correlation with myelin/calcium increase. Furthermore, DARE revealed that PU total longitudinal changes (β=-1.5; Q=0.03) and CN total QS changes (β=1.4; Q=0.03) were the strongest MSSS DARE predictors.

Although MSSS correlated negatively with both TH QS (β=-0.57; Q=0.05) and volume (β=-0.33; Q=0.05) bulk longitudinal changes, DARE revealed an effect for TH iron increase using QS mean (β=0.28; Q=0.05) and an effect for myelin calcium/myelin increase using R2* mean (β=0.59; Q=0.05). These results suggest that although the TH is experiencing atrophy which negatively correlates with disease severity, parts of the TH may actually be experiencing increased paramagnetic iron and diamagnetic myelin/calcium levels that correlate positively with MSSS. DARE's specificity also revealed that all studied DGM structures correlated with MSSS, but each structure correlated differently depending on observed longitudinal iron and myelin/calcium specific changes.

5.4.Discussion

The current study has demonstrated the use of combined R2* and QS for discriminating iron and myelin/calcium longitudinal regional changes in DGM, and compared DARE to conventional

bulk analysis. Unlike the recently introduced framework for combined R2* and QS cross-sectional analysis (7), DARE leveraged the use of longitudinal data to account for individual variation in group studies. Furthermore, we demonstrated that the specificity of DARE to longitudinal changes in DGM iron and myelin/calcium offers superior correlation with disease severity measures.

Although bulk analysis of R2* (21) and QS (22) of the MS DGM has been histochemically validated to correlate with iron concentration, these studies have not taken into account the complex nature of the disease. MS DGM is plagued by the formation of focal demyelination lesions and diffuse degeneration (1). In contrast to QS, R2* is sensitive to processes that affect tissue water content, such as inflammation and neurodegeneration., On the other hand, QS would be more sensitive to changes of DGM iron (15), myelin (23), and calcium content. Thus, it is expected that R2* would be more sensitive to biological changes in MS DGM, because it has added sensitivity to damage and repair processes in MS, which has been observed throughout this study. Moreover, it has been shown that the R2* and QS contrast of white matter in MS lesions evolves during different activity stages (8). Furthermore, the complex sensitivities of R2* (24) and MRI phase (25,26) to tissue micro-architecture has yielded different healthy aging patterns for cross-sectional R2* and QS analysis of the GP, despite having been computed using the same MRI acquisitions (27).

This complex biosensitivity of R2* and QS in MS, combined with differences in study design and limitations of sample size, may explain discrepancies between different DGM MS studies. While a recent QS study over a 2-year time period (6) has detected significant longitudinal QS effects between MS patients and controls in the CN, and significant group effects in the CN, TH, and GP, we could not confirm these findings using bulk analysis. However, non-corrected P-values found significant QS group effects between RRMS and CTRL-R in the PU and TH, suggesting that deviation of our results from (6) may have been partially caused by the smaller sample size and larger number of comparisons in our study. Also, we have detected a significant CN QS interaction effect in RRMS that was not found in (6). This suggests that the increased specificity offered by the more homogenous comparison of RRMS and PMS to age-matched

groups, rather than comparing a large MS group to age-matched controls, may also explain discrepancies with results from (6). For R2*, a previous 2-year RRMS longitudinal study (5) detected significant (uncorrected) group and longitudinal effects in the GP and SN, in addition to significant (uncorrected) group differences in the TH. In partial confirmation of these results, we also found significant longitudinal effects between RRMS and CTRL-R in the GP. Our study also confirmed the pathological relevance of regional atrophy that occurs in the PU (6) and TH (28) of MS patients.

Although bulk longitudinal analysis of R2* and QS has the unique advantage of separating longitudinal, group, and group*longitudinal interaction effects, DARE utilizes combined R2* and QS longitudinal differences to increase specificity to iron and myelin/calcium DGM changes. Compared to bulk analysis group*longitudinal interaction effects of patients versus controls, DARE's specificity enabled identification of more significantly different structures between patients and controls. Furthermore, bulk analysis only indicates the increased mean bulk intensity of R2* and QS of MS DGM compared to controls. Increased R2* in MS compared to controls has been previously interpreted as iron accumulation (5), even though both iron and myelin changes have been shown to contribute to MS DGM changes (1). Conversely, DARE has allowed identification of regional changes in size, mean and total R2* intensities of iron and myelin/calcium within DGM structures. These additional quantitative parameters may provide useful information for non-invasive gradient-echo MRI therapeutic studies monitoring brain iron (29) and myelin (30) changes.

Cross-sectional (4) and longitudinal (5) studies have associated increased bulk R2* and QS of MS DGM with increased iron accumulation. However, histologic assessment of the disease suggests that MS brain iron is actually being redistributed during the processes of demyelination and inflammation (1). Furthermore, upon demyelination, iron, which is normally found in oligodendrocytes and myelin, was found in microglial cells found at the rim of active white matter lesions (31). Moreover, iron decrease in normal appearing white matter was shown to be driven by oligodendrocyte death, and associated with an increase in upregulation of iron-exporting ferroxidases and iron uptake into microglia and macrophages (32). The effect of the size, mean and total change of regions with iron decrease in RRMS compared to controls was larger than the effect of iron increase in RRMS. Moreover, our finding that the CN is the most

prominent pathological target in RRMS confirms a previous histological (1) and QS (6) study. TH DARE results indicating heterogeneous longitudinal changes also agree with a recent study that found reduced QS in TH subregions over 2 years (33), while cross-sectional studies reported an increase in bulk TH QS (7).

The studied RRMS patient population is expected to have increased myelination and repair processes because of their low and stable MSSS values, an increase in the number of patients without relapses during compared to prior to the study, and use of disease modifying therapy throughout the two-year study. This effect has been observed in DARE regions, where significant myelin/calcium increase was observed in all DGM structures using at least one DARE parameter. The relatively higher myelin content of the TH compared to other DGM structures may explain the demonstrated higher myelin/calcium increase correlation coefficients in RRMS compared to other structures. On the other hand, PMS patients are expected to have less repair processes, given their relatively high disease severity. This may explain the observation that for myelin/calcium decrease more PMS DGM structures were significantly different than age-matched controls compared to RRMS.

Demonstrated DGM iron decrease may indicate release of iron upon oligodendrocyte destruction, while DGM iron increase may indicate accumulation of iron in neuronal and glial cells (1). Conversely, no iron decrease was observed when comparing PMS and CTRL-P, while iron increase was only observed in the PU and TH. This suggests that later progressive stages of the disease are dominated by demyelination and, to a lesser extent, remyelination (34), while remyelination (35) and iron-associated oligodendrocyte destruction (36) dominates the earlier relapsing-remitting stages of the disease.

In extension of a previous study demonstrating that R2* change is a predictor of disease severity in RRMS (5), the current study demonstrated that DARE provides better correlation with MS disease severity compared to bulk analysis change in R2*, QS and volume. Furthermore, this study confirms a previous iron densitometry study that demonstrated the correlation of disease progression with iron decrease in the MS brain (32), and also confirms a recent study demonstrating association of MS disease duration with QS reduction in TH subregions (33). Thus, DARE may be used for correlating changes in DGM iron and myelin/calcium in MS with

disease severity, which can benefit from restricted field-of-view QS mapping (37) to reduce motion artifacts associated with longer MRI scans. Additionally, DARE may be beneficial for monitoring the effect of therapies targeting brain iron and myelin/calcium changes in MS clinical trials.

Given the large number of non-significant results demonstrated in this study, it is understandable that type II errors may be a valid concern. TOST revealed that small sample sizes may indeed have been a reason for the observed non-significant results. However, this is a general limitation of longitudinal MS studies because of the difficulty in tracking committed MS volunteers over a long period. A power analysis by Hagemeier et al. (6) for a larger MS cohort estimated that sample sizes of more than 800, 2000, and 20,000 would be needed to detect susceptibility changes over 2 years in the PU, CN, and GP, respectively, assuming the standard deviations in their cohort were representative of the MS population. That said, longitudinal studies using DARE increases statistical power and allows better comparison between studies because it monitors specific changes in individuals, rather than bulk group changes.

Additionally, absence of sex-matching for control groups is a limitation of the study design. However, there were no significant effect for sex was found when studying DGM using susceptibility-sensitive phase MRI (38) and R2* mapping (39). Thus, absence of sex-matching should not have biased the results. The increased representation of male MS patients in this study compared to the general MS population is another limitation. Although no significant ($P \leq 0.05$) histochemical differences between sexes were found in the extent of DGM demyelination, female MS patients displayed higher iron density in DGM lesions (1). However, correlation bulk analysis found no significant effect for sex on R2* values of MS DGM (40). Consequently, iron density in DGM lesions may be accentuated in the general MS population compared to the sample used in this study, but may have not affected MRI bulk analysis.

Another limitation of DARE is the possibility that detected changes in iron and myelin/calcium had been affected by longitudinal registration errors. A scan-rescan reliability test for DGM voxel registration revealed that the maximum DGM percent error was 5.8% and 0.9% for R2* and QSM, respectively (4). Nonetheless, statistical group testing should have identified significant disease related effects, and thus filtered out other effects.

Another inherent DARE limitation is partial volume effects. Although several effects or tissues may occupy a voxel, DARE would only identify the dominant effect. Additionally, DARE is unable to discriminate inflammation, which translates as an R2* decrease. That said, the effect of DGM iron decrease and myelin/calcium decrease in DARE regions may have been amplified by ongoing inflammation. Moreover, DARE cannot distinguish myelin and calcium changes because of their similar magnetism; although it is probably myelin changes that dominate in the MS brain. Furthermore, DARE has only considered demyelination in the case of a decrease in R2* accompanied with an increase in QS, which corresponds to degradation of myelin within macrophages (8). Another limitation of DARE is iron overload in demyelinating lesions (3) that may mask other iron/myelin changes.

5.5. Conclusions

In conclusion, we have developed quantitative *in vivo* DARE measures specific to brain longitudinal iron and myelin/calcium changes. DARE measures have successfully detected significant group differences over 2 years in more DGM structures compared to bulk analysis, and revealed that CN iron decrease and TH myelin/calcium decrease were the primary drivers of RRMS and PMS DGM longitudinal changes compared to age-matched healthy controls, respectively. However, given the limitations of DARE, the results of this study needs to be further validated histochemically. DARE has also shown superior correlation with disease severity in MS compared to bulk analysis.

References

1. Haider L, Simeonidou C, Steinberger G, et al. Multiple sclerosis deep grey matter: the relation between demyelination, neurodegeneration, inflammation and iron. J Neurol Neurosurg Psychiatry 2014:85:1386-1395.
2. Hallgren B & Sourander P. The effect of age on the non-haemin iron in the human brain. J Neurochem 1958:3:41-51.
3. Stephenson E, Nathoo N, Mahjoub Y, Dunn JF & Yong VW. Iron in multiple sclerosis: roles in neurodegeneration and repair. Nat Rev Neurol 2014:10:459-468.

4. Cobzas D, Sun H, Walsh AJ, Lebel RM, Blevins G & Wilman AH. Subcortical gray matter segmentation and voxel-based analysis using transverse relaxation and quantitative susceptibility mapping with application to multiple sclerosis. J Magn Reson Imaging 2015:42:1601-10.
5. Walsh AJ, Blevins G, Lebel RM, Seres P, Emery DJ & Wilman AH. Longitudinal MR imaging of iron in multiple sclerosis: an imaging marker of disease. Radiology 2014:270:186-196.
6. Hagemeier J, Zivadinov R, Dwyer MG, et al. Changes of deep gray matter magnetic susceptibility over 2years in multiple sclerosis and healthy control brain. NeuroImage: Clinical 2017.
7. Elkady AM, Cobzas D, Sun H, Blevins G & Wilman AH. Progressive iron accumulation across multiple sclerosis phenotypes revealed by sparse classification of deep gray matter. J Magn Reson Imaging 2017.
8. Zhang Y, Gauthier SA, Gupta A, et al. Quantitative Susceptibility Mapping and R2* Measured Changes during White Matter Lesion Development in Multiple Sclerosis: Myelin Breakdown, Myelin Debris Degradation and Removal, and Iron Accumulation. AJNR Am J Neuroradiol 2016:37:1629-1635.
9. Yamada N, Imakita S, Sakuma T & Takamiya M. Intracranial calcification on gradient-echo phase image: depiction of diamagnetic susceptibility. Radiology 1996:198:171-178.
10. Roxburgh RH, Seaman SR, Masterman T, et al. Multiple Sclerosis Severity Score: using disability and disease duration to rate disease severity. Neurology 2005:64:1144-1151.
11. Du YP, Jin Z, Hu Y & Tanabe J. Multi-echo acquisition of MR angiography and venography of the brain at 3 Tesla. J Magn Reson Imaging 2009:30:449-454.
12. Smith SM. Fast robust automated brain extraction. Hum Brain Mapp 2002:17:143-155.
13. Jenkinson M. Fast, automated, N-dimensional phase-unwrapping algorithm. Magn Reson Med 2003:49:193-197.
14. Sun H & Wilman AH. Background field removal using spherical mean value filtering and Tikhonov regularization. Magn Reson Med 2013:71:1151-7.
15. Bilgic B, Pfefferbaum A, Rohlfing T, Sullivan EV & Adalsteinsson E. MRI estimates of brain iron concentration in normal aging using quantitative susceptibility mapping. Neuroimage 2012:59:2625-2635.
16. Tustison NJ, Avants BB, Cook PA, et al. N4ITK: improved N3 bias correction. IEEE Trans Med Imaging 2010:29:1310-1320.
17. Heckemann RA, Hajnal JV, Aljabar P, Rueckert D & Hammers A. Automatic anatomical brain MRI segmentation combining label propagation and decision fusion. Neuroimage 2006:33:115-126.
18. Avants BB, Tustison NJ, Song G, Cook PA, Klein A & Gee JC. A reproducible evaluation of ANTs similarity metric performance in brain image registration. Neuroimage 2011:54:2033-2044.
19. Wang H, Suh JW, Das SR, Pluta JB, Craige C & Yushkevich PA. Multi-atlas segmentation with joint label fusion. IEEE Trans Pattern Anal Mach Intell 2013:35:611-623.
20. Langkammer C, Krebs N, Goessler W, et al. Susceptibility induced gray-white matter MRI contrast in the human brain. Neuroimage 2012:59:1413-1419.
21. Walsh AJ, Lebel RM, Eissa A, et al. Multiple sclerosis: validation of MR imaging for quantification and detection of iron. Radiology 2013:267:531-542.
22. Sun H, Walsh AJ, Lebel RM, et al. Validation of quantitative susceptibility mapping with Perls' iron staining for subcortical gray matter. Neuroimage 2015:105:486-492.

23. Langkammer C, Schweser F, Krebs N, et al. Quantitative susceptibility mapping (QSM) as a means to measure brain iron? A post mortem validation study. Neuroimage 2012:62:1593-1599.
24. Cohen-Adad J, Polimeni JR, Helmer KG, et al. T 2* mapping and B 0 orientation-dependence at 7T reveal cyto-and myeloarchitecture organization of the human cortex. Neuroimage 2012:60:1006-1014.
25. He X & Yablonskiy DA. Biophysical mechanisms of phase contrast in gradient echo MRI. Proc Natl Acad Sci U S A 2009:106:13558-13563.
26. Yablonskiy DA, Luo J, Sukstanskii AL, Iyer A & Cross AH. Biophysical mechanisms of MRI signal frequency contrast in multiple sclerosis. Proc Natl Acad Sci U S A 2012:109:14212-14217.
27. Betts MJ, Acosta-Cabronero J, Cardenas-Blanco A, Nestor PJ & Düzel E. High-resolution characterisation of the aging brain using simultaneous quantitative susceptibility mapping (QSM) and R 2* measurements at 7T. Neuroimage 2016:138:43-63.
28. Zivadinov R, Havrdová E, Bergsland N, et al. Thalamic atrophy is associated with development of clinically definite multiple sclerosis. Radiology 2013:268:831-841.
29. Zivadinov R, Dwyer M, Markovic-Plese S, et al. A pilot, longitudinal, 24-week study to evaluate the effect of interferon beta-1a subcutaneous on changes in susceptibility-weighted imaging-filtered phase assessment of lesions and subcortical deep-gray matter in relapsing–remitting multiple sclerosis. Therapeutic advances in neurological disorders 2015:8:59-70.
30. Ziser L, Meyer-Schell N, Kurniawan ND, et al. Utility of gradient recalled echo magnetic resonance imaging for the study of myelination in cuprizone mice treated with fingolimod. NMR Biomed 2017.
31. Bagnato F, Hametner S, Yao B, et al. Tracking iron in multiple sclerosis: a combined imaging and histopathological study at 7 Tesla. Brain 2011:134:3602-3615.
32. Hametner S, Wimmer I, Haider L, Pfeifenbring S, Bruck W & Lassmann H. Iron and neurodegeneration in the multiple sclerosis brain. Ann Neurol 2013:74:848-861.
33. Schweser F, Martins, Ana Luiza Raffaini Duarte, Hagemeier J, et al. Mapping of thalamic magnetic susceptibility in multiple sclerosis indicates decreasing iron with disease duration: A proposed mechanistic relationship between inflammation and oligodendrocyte vitality. Neuroimage 2017.
34. Bramow S, Frischer JM, Lassmann H, et al. Demyelination versus remyelination in progressive multiple sclerosis. Brain 2010:133:2983-2998.
35. Patrikios P, Stadelmann C, Kutzelnigg A, et al. Remyelination is extensive in a subset of multiple sclerosis patients. Brain 2006:129:3165-3172.
36. Barnett MH & Prineas JW. Relapsing and remitting multiple sclerosis: pathology of the newly forming lesion. Ann Neurol 2004:55:458-468.
37. Elkady AM, Sun H & Wilman AH. Importance of extended spatial coverage for quantitative susceptibility mapping of iron-rich deep gray matter. Magn Reson Imaging 2016:34:574-578.
38. Xu X, Wang Q & Zhang M. Age, gender, and hemispheric differences in iron deposition in the human brain: an in vivo MRI study. Neuroimage 2008:40:35-42.
39. Pirpamer L, Hofer E, Gesierich B, et al. Determinants of iron accumulation in the normal aging brain. Neurobiol Aging 2016:43:149-155.
40. Ropele S, Kilsdonk ID, Wattjes MP, et al. Determinants of iron accumulation in deep grey matter of multiple sclerosis patients. Mult Scler 2014:20:1692-1698.

Chapter 6: Five-year Deep Gray Matter Changes of Iron and Myelin in Relapsing Remitting Multiple Sclerosis and Healthy Subjects

Abstract

Introduction: Quantitative Magnetic Resonance Imaging (MRI) using combined R2* and Quantitative Susceptibility (QS) mapping has been recently proposed for Discriminative Analysis of Regional Evolution (DARE) of iron and myelin longitudinal changes in Multiple Sclerosis (MS) Deep Gray Matter (DGM). We apply DARE to analyze 5-year DGM changes in Relapsing-Remitting MS (RRMS).

Methods: A 10-minute 4.7T 10-echo gradient-echo acquisition was used to compute R2* and QS in 22 RRMS and 22 age/sex-matched (P=0.45; P=0.3) control subjects for baseline and 5-year follow-up. Automatic segmentation of the Caudate Nucleus (CN), PUtamen (PU), THalamus (TH), Globus Pallidus (GP), Red Nucleus (RN), Substantia Nigra (SN), and Dentate Nucleus (DN) were used to quantify mean R2*/QS and normalized DGM regional volumes. Parametric mixed factorial analysis (α=0.05) of bulk DGM structures was implemented to investigate longitudinal, group and interaction effects, while DARE employed non-parametric analysis of RRMS compared to control group effects. Depending on data distribution, Pearson's regression or Spearman's correlation were performed between all significant bulk interaction and DARE results with disease duration and MS Severity Scale (MSSS).

Results: Significant interaction was only found for TH volume (Q = 0.0009; η^2 = 0.24). Specific paired t-tests indicated that there were no longitudinal effects for the control group, while 46% of the variance in the data was explained by longitudinal effects of the MS group for TH volume (Q = 0.001; η^2 = 0.46). Significant DARE results were demonstrated in several DGM regions, with the highest effect sizes reported for mean QS of TH myelin increase regions (Q = 0.0004; η^2 = 0.40) and TH iron decrease regions (Q = 0.0004; η^2 =0.29). Regression analysis revealed a signifcant linear relationship between mean R2* of CN iron decrease regions with MSSS (r =

0.64; Q = 0.03), and mean R2* of SN myelin increase regions with disease duration (r = 0.49; Q = 0.008).

Conclusion: Longitudinal decrease in DGM iron levels and thalamic atrophy are a pathologic feature in RRMS over a period of 5 years. DGM iron decrease and myelin increase correlate with disease duration and severity, possibly due to depletion of iron from oligodendrocytes that are normally abundant in the DGM and remyelination repair processes, respectively.

6.1. Introduction

Deep Gray Matter (DGM) pathology in Multiple Sclerosis (MS) has been shown histologically to manifest as demyelinating inflammatory lesions and neurodegenerative changes (1,2), which were associated with oxidative injury in the DGM (1). A five-year serial MRI evaluation of DGM volumes demonstrated that DGM experiences accelerated volume loss (3). More recently, atrophy of the DGM has been recently shown to be to be faster than cortical brain regions, and is a main driver of disability progression in MS (4).

Several cross-sectional MRI studies have demonstrated increased quantitative MRI measures suggestive of increased iron accumulation in MS DGM compared to age matched controls. R2* mapping is a quantitative assessment of the transverse relaxation rate of the MRI signal, and it is linearly related to DGM iron concentrations (5). Mean DGM R2* values have been shown to be accentuated in MS compared to age-matched controls (6,7), and was associated with disease duration, brain atrophy (8), cortical gray matter atrophy, age, and lesion load (9). Quantitative Susceptibility (QS) mapping is another quantitative MRI measure that has been validated to correlate with DGM iron (10). Cross-sectional evaluation of DGM QS (11) has also confirmed earlier R2* results suggestive of DGM iron increase. Furthermore, combined use of R2* and QS mapping have demonstrate progressive iron accumulation occurs with advanced MS phenotypes (12).

Compared to cross-sectional studies, longitudinal assessment of MS DGM changes provides a more accurate depiction of MS pathology because of the high individual variability of DGM iron levels (13). Except for the CN (15), two-year R2* (14,15) and QS (15,16) studies evaluating longitudinal changes in MS compared to age-matched control groups failed to demonstrate a significant interaction effect reflecting the pathological DGM iron accumulation in MS patients compared to iron accumulation associated with healthy aging. Another longitudinal R2* study

(17) which evaluated changes in MS compared to Clinically Isolated Syndrome over a median period of 2.9 years demonstrated cross-sectional increases in R2* of MS DGM compared to CIS, but significant longitudinal effects of R2* increase was only found in the MS GP, no significant longitudinal changes were found in the CN and PU, and a significant longitudinal R2* decrease was found in the TH. Thus, longitudinal studies have mostly failed to confirm cross-sectional findings of increased rate of iron accumulation in MS compared to controls. Furthermore, the QS longitudinal 2-year study demonstrated that simulations indicate that the expected increase of the CN QS exceeds the observed longitudinal QS increase in that study (16). Additionally, a recent high-resolution cross-sectional assessment found reduced QS suggestive of iron decrease in focal subregions of the thalamus (18). Moreover, cross-sectional analysis of DGM R2* combined with volumetric measurements to produce a total voxel iron measure indicated that total iron is actually less in MS DGM compared to age-matched controls (19).

Discriminative Analysis of Regional Evolution (DARE) of DGM regions has been recently introduced to combine R2* and QS longitudinal changes to gain greater specificity to iron and myelin/calcium changes, and was applied to changes in MS DGM over a period of 2 years (15). DARE utilizes the opposite sensitivity of R2* and QS to myelin/calcium changes to discriminate iron and myelin changes in the DGM. While that study revealed that the RRMS exhibited significant longitudinal iron increase/decrease and myelin/calcium increase/decrease changes over a 2 year period compared to age-matched controls, it is still unknown how these changes behave when observed over longer periods. Although DARE cannot discriminate myelin from calcium changes because of their similar diamagnetism, there has been no reports of different calcium levels in MS DGM. Thus, detected pathological changes in MS DGM compared to controls are assumed to be myelin changes, which are expected in MS due to recurrent demyelination and repair processes inherent to the disease. The purpose of this study was to apply DARE to determine changes in DGM iron and myelin in Relapsing-Remitting MS (RRMS) over a 5-year period, and investigate the relationship of these changes with disease duration and severity.

6.2.Methods

6.2.1.Study Design

We prospectively enrolled 35 RRMS patients and 31 control subjects for a 5-year longitudinal MRI study. Written informed consent was obtained from all participants after the internal institutional review board approved the study design. Exclusion criteria were pregnancy and any neurological condition. MS patients were diagnosed with 2010 revised McDonald Criteria, and an MS neurologist (G.B., with 11 years of experience) close in time to the MRI acquisition, while Multiple Sclerosis Severity Score (MSSS) was calculated from EDSS and disease durations using MSSStest software (20).

6.2.2. Image Processing

R2* and QS maps were calculated from the multi-echo gradient echo acquisition. R2* maps were computed by fitting magnitude images to a mono-exponential temporal signal model. QS maps were calculated from phase images after phase unwrapping using PRELUDE/FSL, brain extraction using FSL Brain Extraction Tool, background field removal using Regularization-Enabled Sophisticated Harmonic Artifact Reduction for Phase data (RESHARP) (21), and finally magnetic field deconvolution using total variation dipole inversion (22). Segmented DGM structures were extracted from R2* and QS maps, after registering all patients and controls to a global atlas computed from QS maps and T1-weighted images (6). The difference between the follow-up and baseline data was used to identify regions of iron and myelin changes in MS and control groups (15).

6.2.3. Statistical Analysis

6.2.3.1. Bulk Analysis

Mixed factorial analysis ($\alpha<0.05$) was carried out separately for DGM structures using Analysis of Variance (ANOVA) with control and RRMS groups as the between-subjects variable and baseline and follow-up mean R2*, mean QS, and regional volumes of DGM segmented structures as the within-subjects variable. Assumptions of normality were confirmed using Shapiro-Wilk tests and Q-Q plots, and box plots were used to assess outliers. False Detection Rate (FDR) correction was performed for all tests to account for inflated type I errors during

multiple comparisons. Non-corrected values are reported as P-values and analyzed as significant ($P<0.05$) trends, while FDR-corrected P-values are reported as Q-values and analyzed as significant ($Q<0.05$) results. Group, longitudinal and interaction effect sizes of ANOVA were reported as partial η^2, and further independent and paired t-tests were performed on group and longitudinal data when a significant ($Q<0.05$) interaction was found.

6.2.3.2. DARE

To account for non-normal data distribution, Mann-Whitney U tests were applied to test differences between RRMS and controls for volumes, mean R2*, total R2*, mean QS, and total QS of iron increase/decrease and myelin increase/decrease DARE regions. The presence of outliers and the non-normal distribution of data may be explained by the heterogeneous nature of MS, which is expected to be amplified over a period of 5 years, where effect sizes were reported as partial η^2. Similar to bulk analysis, significant ($Q<0.05$) FDR-corrected results were reported as Q-values, while significant ($P<0.05$) non-corrected trends were reported as P-values.

6.2.3.3. Regression

Depending on data distribution, Pearson's regression and Spearman's correlation were performed between disease duration and baseline MSSS with all significant bulk interaction and DARE results with disease duration and MSSS. The objective of the regression was identifying results that correlate with clinical MS measures, and to define the relationship that describes the correlation for linear regression. Normality of residuals was confirmed using Shapiro-Wilk test and Q-Q plots, while box plots confirmed absence of outliers. In the case of the presence of outliers, repeating the regression analysis without the outlier was conducted to ensure the linear relationship remained significant without the outlier.

6.3. Results

6.3.1. Study Design

One RRMS patients was excluded from the study due to pregnancy at the time of the follow-up scan, and one control subject was excluded due to poor quality MPRAGE data which caused failed segmentation. Only 21 control subjects returned for a follow-up scan and they were generally younger than the patient group, thus only 21 RRMS subjects were included in the study to optimize age matching and account for significant correlation of DGM iron with healthy aging (13). **Table 6.1** describes demographic information of age/sex-matched RRMS and control

groups. Age-matching were confirmed using independent t-tests (P = 0.49). The patients' female to male sex ratio was approximately 4, close to the average sex incidence ratio of the North American MS population (23).

Table 6.1 Demographic information of RRMS and age-matched control groups.

Patient Group (n)	EDSS (mean ± SD)		Disease Duration	Baseline Age	Followup period	Sex (M/F)
	baseline	follow-up(mean ± SD, yrs)				
CTRL (21)				34.1±9.1	5.1±0.1	7/14
RRMS (21)	2.4±1.2	2.4±1.6	10.2±4.3	35.2±7.8	5.2±0.5	4/17

CTRL = control subjects; RRMS = relapsing-remitting MS subjects;

6.3.2.Bulk Analysis

Table 6.2 lists median and interquartile range of bulk mean R2*, bulk mean QS, and regional volumes of segmented DGM structures. Also displayed in the table are FDR-corrected effect sizes, effect sizes of non-corrected trends, and effect sizes of specific group and longitudinal t-tests for TH volume.

Significant ($Q<0.05$) group effects were only found for TH volume ($Q = 0.008$; $\eta^2 = 0.25$). Significant time effects were found for R2* in the CN ($Q = 0.0003$; $\eta^2 = 0.32$), PU ($Q = 0.00002$; $\eta^2 = 0.43$), GP ($Q = 0.006$; $\eta^2 = 0.21$); for QS in the RN ($Q = 0.05$; $\eta^2 = 0.14$), DN ($Q = 0.03$; $\eta^2 = 0.19$); for volume in the PU ($Q = 0.01$; $\eta^2 = 0.20$), TH ($Q = 0.004$; $\eta^2 = 0.26$), RN ($Q = 0.02$; $\eta^2 = 0.15$), SN ($Q = 0.02$; $\eta^2 = 0.16$).

Significant interaction was only found for TH volume ($Q = 0.0009$; $\eta^2 = 0.24$). Specific independent t-tests revealed significant group effects at baseline ($Q = 0.003$; $\eta^2 = 0.21$) and follow-up ($Q = 0.0002$; $\eta^2 = 0.34$). Specific paired t-tests indicated that there were no longitudinal effects for the control group, while 46% of the variance in the data was explained by longitudinal effects of the MS group for TH volume ($Q = 0.001$; $\eta^2 = 0.46$).

Significant (P<0.05) group trends were only demonstrated for RN R2* (P = 0.01; η^2 = 0.16) and QS GP (P = 0.02; η^2 =0.15). Significant longitudinal trends were only demonstrated for RN R2* (P = 0.04; η^2 = 0.11) and QS GP (P = 0.02; η^2 = 0.12). No significant interaction trends were detected.

Figures 6.1, **6.2** and **6.3** demonstrate longitudinal trajectories of DGM R2* and QS, and regional volumes for RRMS and control subjects with the average group trajectory overlaid, respectively.

6.3.3.DARE

Table 6.3 lists median and interquartile range, FDR-corrected effect sizes, and effect sizes of non-corrected trends of DARE parameters which displayed significant differences (Q<0.05) and trends (P<0.05) between RRMS and control groups. Significant results were demonstrated in the CN for iron decrease regions using mean R2* (Q = 3E-2; η^2 = 0.12), mean QS (Q = 1E-2; η^2 = 0.15), and total QS (Q = 3E-2; η^2 = 0.14), and for myelin increase using mean QS (Q = 4E-2; η^2 = 0.26) and myelin decrease using mean R2* (Q = 2E-2; η^2 = 0.14); in the TH for iron increase mean R2* (Q = 5E-2; η^2 = 0.15), iron decrease mean R2* (Q = 5E-4; η^2 = 0.28), iron decrease total QS (Q = 4E-3; η^2 = 0.29), myelin increase mean QS (Q = 4E-4; η^2 = 0.40), myelin increase total QS (Q = 8E-3; η^2 = 0.26), myelin decrease mean R2* (Q = 3E-2; η^2 = 0.20); in th GP for iron decrease mean R2* (Q = 2E-2; η^2 = 0.17); in the RN for iron increase mean R2* (Q = 5E-2; η^2 = 0.16), iron decrease mean R2* (Q = 4E-2; η^2 = 0.12), iron decrease mean QS (Q = 4E-3; η^2 = 0.25), myelin increase mean QS (Q = 1E-2; η^2 = 0.18); in the SN for iron decrease mean R2* (Q = 7E-3; η^2 = 0.23), iron decrease mean QS (Q = 5E-2; η^2 = 0.11), myelin increase mean R2* (Q = 2E-2; η^2 = 0.22); in the DN for iron decrease mean QS (Q = 3E-2; η^2 = 0.14), myelin increasw mean QS (Q = 4E-3; η^2 = 0.24).

Significant trends (P<0.05) were demonstrated for iron increase in CN total QS (Q = 2E-2; η^2 = 0.14); in PU myelin increase mean R2* (Q = 5E-2; η^2 = 0.10) and myelin decrease mean R2* (Q = 4E-2; η^2 = 0.10); in the TH for iron decrease total R2* (Q = 1E-2; η^2 = 0.15), iron decrease total QS (Q = 3E-2; η^2 = 0.12), myelin increase total R2* (Q = 3E-2; η^2 = 0.12); in the GP for

myelin decrease mean R2* (Q = 3E-2; $\eta^2 = 0.12$); in the RN for iron decrease total QS (Q = 3E-2; $\eta^2 = 0.12$); in the SN for myelin increase mean QS (Q = 4E-2; $\eta^2 = 0.10$).

Table 6.2 Median [Lower Inter-Quartile Range (LIQR), Upper Inter-Quartile Range (UIQR)] of bulk R2*, QS and volumes of DGM segmented structures. Also listed are Group Effect Size (GES), Time Effect Size (TES), and Specific Group Effect Size (S.G.E.S) for significant FDR-corrected Q-values and P-values. Significant (Q<0.05) FDR-corrected tests are bolded and display associated Q values between brackets, while significant trends (P<0.05) are not bolded and display P-values between brackets. Statistical analyses were performed using a mixed design using ANOVA, where effect sizes are reported as partial η^2 of group, time, and time*group.

		R2* (1/s)			QS (ppb)			Volume*1000 (mm^3)			
		Median [LIQR,UIQR]		GES (Q or P)	Median [LIQR,UIQR]		GES (Q or P)	Median [LIQR,UIQR]		GES (Q or P)	SGES (Q or P)
		CTRL	MS		CTRL	MS		CTRL	MS		
CN	B.	**29.8 [27.8,31.9]**	**31.8 [30.2,34.2]**		**97.3 [87.3,110.5]**	**115.2 [103.1,123.2]**	0.16 [a,f] (1E-2)	6.3 [5.7,6.7]	5.8 [5.5,6.3]		
	F.	**31.5 [29.4,33.3]**	**34.7 [30.8,38.5]**		**99.2 [89.3,112.9]**	**112.2 [100.5,129.8]**		6.2 [5.6,6.6]	5.9 [5.5,6.2]		
	TES. (Q or P)		**0.32 [b] (3E-4)**								
PU	B.	**33.0 [31.7,35.8]**	**35.4 [32.6,37.9]**		93.3 [85.6,103.7]	109.3 [95.0,128.9]	-	**9.3 [8.7,10.3]**	**9.0 [8.5,10.1]**		
	F.	**36.6 [32.8,38.4]**	**38.2 [34.1,43.8]**		99.0 [84.6,102.8]	110.6 [92.1,124.8]		**9.4 [8.7,10.2]**	**9.0 [8.4,9.8]**		
	TES. (Q or P)		**0.43 [b] (2E-5)**						**0.20 [b] (1E-2)**		
TH	B.	27.6 [25.9,28.2]	28.3 [26.2,30.7]		59.8 [54.3,65.0]	69.3 [55.7,74.3]		**14.1 [13.2,14.9]**	**12.9 [12.1,13.4]**	**0.25 [a] (8E-3)**	**0.21 [d] (3E-3)**
	F.	27.5 [26.0,28.7]	28.8 [26.0,33.1]		60.5 [54.5,69.5]	60.3 [50.3,77.5]		**14.4 [13.3,14.9]**	**12.2 [11.0,13.0]**		**0.34 [d] (2E-4)**
	TES. (Q or P)								**0.26 [b] (4E-3)**	**0.24 [c] (9E-4)**	
	STES. (Q or P)						-		**0.46 [e] (1E-3)**		

			58.5					
		54.6		194.8	214.1	3.5	3.4	
	B.	**[51.7,57.0]**	**[54.8,62.6]**	[177.4,205.4]	[195.8,224.4]	[3.3,3.7]	[3.2,3.7]	
GP			**61.1**					
		57.8		185.6	207.7	3.4	3.4	
	F.	**[53.5,61.7]**	**[55.9,64.1]**	[164.4,203.3]	[187.5,223.9]	[3.3,3.7]	[3.2,3.6]	
	TES. (Q or P)	**0.21** [b] **(6E-3)**		0.12 [b,f] (5E-2)				
			44.3					
		41.2		**127.5**	**143.1**	**0.6**	**0.6**	
	B.	[39.9,47.4]	[40.8,49.1]	**[117.4,141.0]**	**[125.7,161.1]**	**[0.6,0.7]**	**[0.6,0.7]**	
RN			48.1					
		45.2		**132.3**	**151.6**	**0.6**	**0.7**	
	F.	[39.9,46.8]	[42.4,51.8]	**[109.9,151.1]**	**[125.1,168.1]**	**[0.6,0.7]**	**[0.6,0.7]**	
	TES. (Q or P)	0.11 [b,f] (4E-2)		**0.14** [b] **(5E-2)**		**0.15** [b] **(2E-2)**		
			47.7					
		46.9		**167.8**	**181.9**	**1.4**	**1.4**	
	B.	[43.6,49.6]	[43.9,54.1]	**[143.8,175.8]**	**[156.2,204.6]**	**[1.3,1.5]**	**[1.3,1.6]**	
SN			50.8					
		47.9		**157.8**	**178.7**	**1.4**	**1.4**	
	F.	[45.1,50.9]	[46.3,55.7]	**[133.6,173.1]**	**[153.8,196.7]**	**[1.3,1.5]**	**[1.4,1.5]**	
	TES. (Q or P)					**0.15** [b] **(2E-2)**		
			43.4					
		40.6		**119.5**	**140.7**	1.6	1.9	
	B.	[35.9,45.5]	[35.2,46.8]	**[106.6,136.3]**	**[128.8,151.8]**	[1.4,1.8]	[1.6,2.0]	0.15 [a,f] (2E-2)
DN			41.3					
		42.1		**129.9**	**127.4**	1.6	1.8	
	F.	[38.2,47.1]	[35.8,48.8]	**[110.2,146.3]**	**[116.1,167.3]**	[1.3,1.7]	[1.5,1.9]	
	TES. (Q or P)			**0.19** [b] **(3E-2)**				

[a] Group Effect Size (GES) for mixed factorial ANOVA (η^2)
[b] Time Effect Size (TES.) for mixed factorial ANOVA (η^2)

[c] Interaction effect size for mixed factorial ANOVA (η^2)
[d] Specific GES (SGES) for independent t-tests (η^2)
[e] Specific GES (SGES) for paired t-tests (η^2)
[f] significant trend ($P<0.05$)
CTRL = Controls; RRMS = Relapsing Remitting Multiple Sclerosis; CN = Caudate Nucleus; PU = Putamen; TH = Thalamus; GP = Globus Pallidus; RN = Red Nucleus; SN = Substantia Nigra; DN = Dentate Nucleus; B. = Baseline; F. = Follow-up; TES = Time Effect Size; G.E.S = Group Effect Size; STES = Specific Time Effect Size; SGES = Specific Group Effect Size.

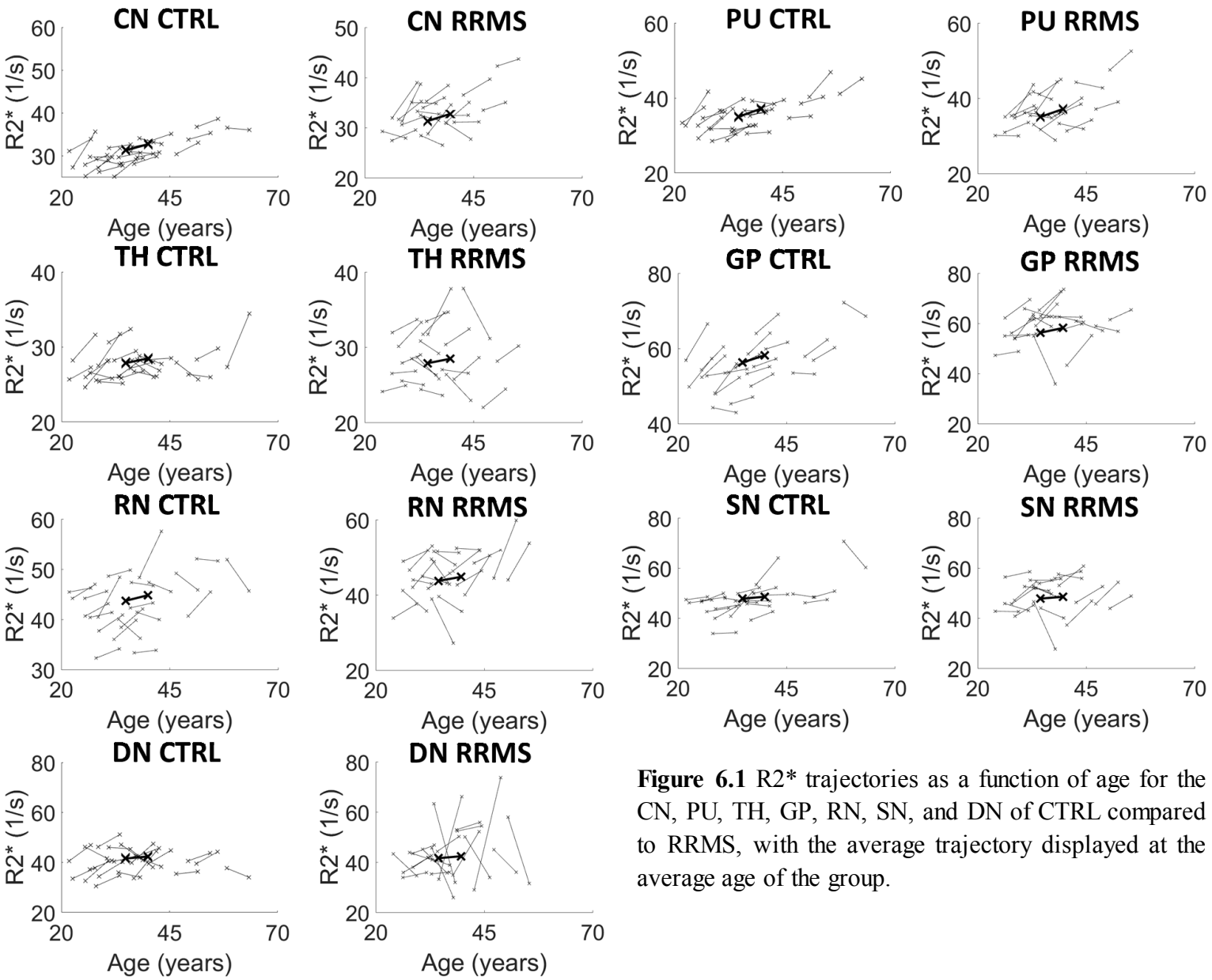

Figure 6.1 R2* trajectories as a function of age for the CN, PU, TH, GP, RN, SN, and DN of CTRL compared to RRMS, with the average trajectory displayed at the average age of the group.

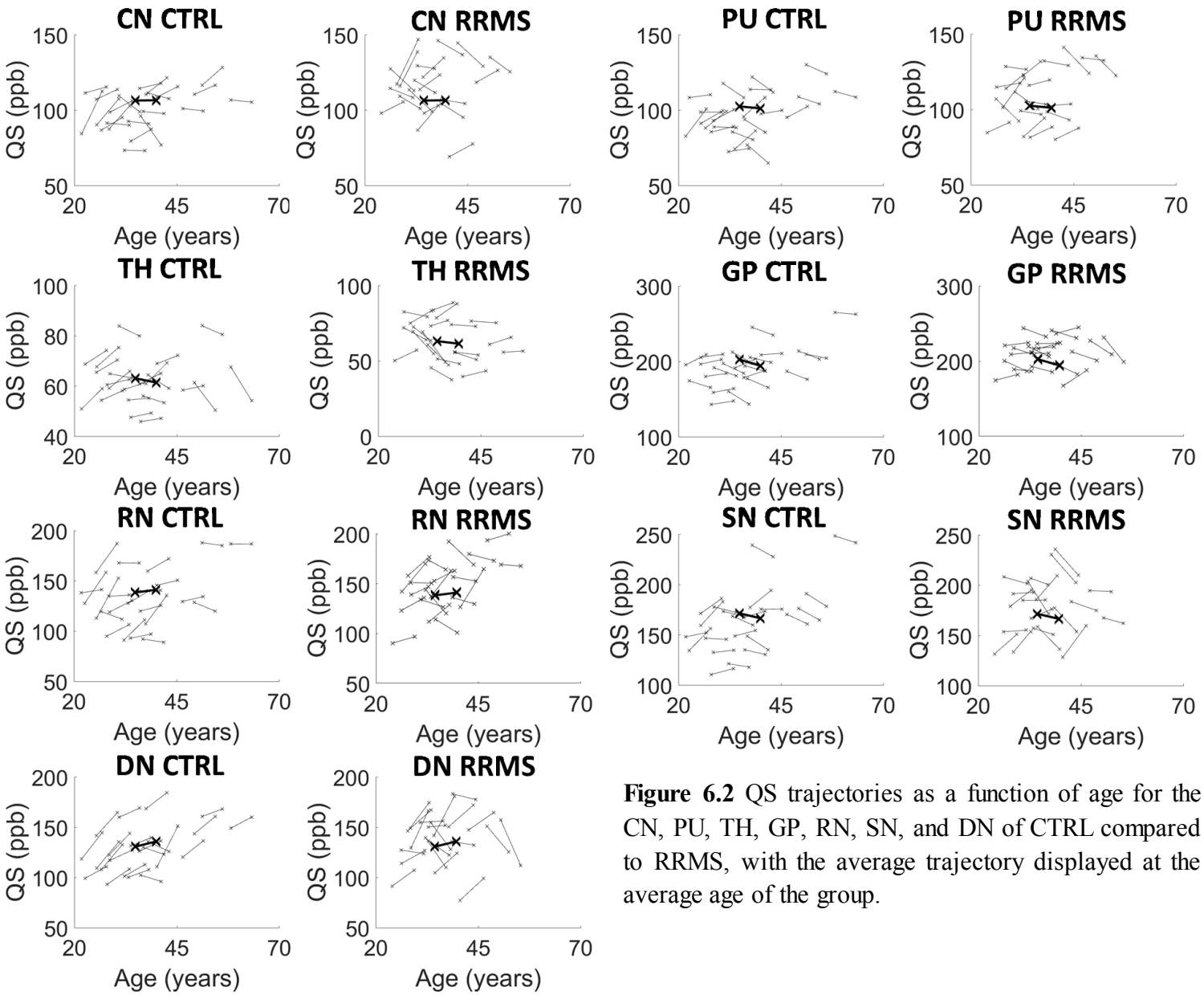

Figure 6.2 QS trajectories as a function of age for the CN, PU, TH, GP, RN, SN, and DN of CTRL compared to RRMS, with the average trajectory displayed at the average age of the group.

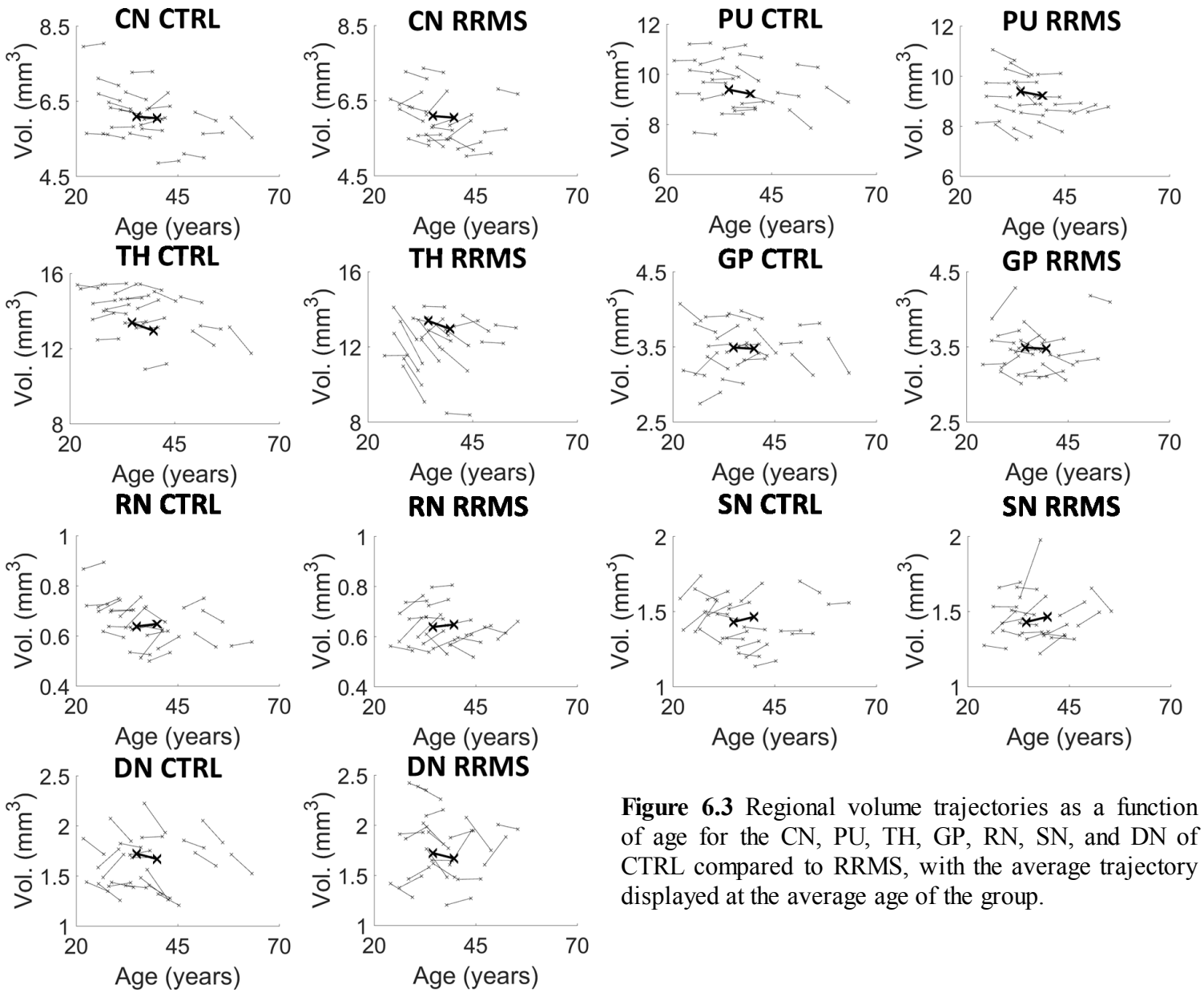

Figure 6.3 Regional volume trajectories as a function of age for the CN, PU, TH, GP, RN, SN, and DN of CTRL compared to RRMS, with the average trajectory displayed at the average age of the group.

Table 6.3 Median [Lower Inter-Quartile Range (LIQR), Upper Inter-Quartile Range (UIQR)] of DARE of DGM segmented structures. Also listed is Effect Size (E.S.) for significant FDR-corrected Q-values and P-values. Significant (Q<0.05) FDR-corrected tests are bolded and display associated Q values between brackets, while significant trends (P<0.05) are not bolded and display P-values between brackets. Statistical analyses were performed using Mann Whitney U tests, where effect sizes are reported as partial η2 in both cases.

		CTRL	RRMS	E.S. (P or Q)
CN	**iron decrease mean R2***	**-3.5 [-4.6,-2.6]**	**-4.7 [-6.9,-3.6]**	**0.12 (3E-2)**
	iron decrease mean QS	**-34.4 [-79.6,-18.0]**	**-92.7 [-179.6,-36.3]**	**0.15 (1E-2)**
	iron decrease total QS	-8.7 [-12.6,-5.1]	-14.3 [-28.2,-9.8]	**0.14 (3E-2)**
	myelin increase mean QS	**-6.4 [-10.0,-4.5]**	**-12.4 [-20.1,-11.4]**	**0.26 (4E-3)**
	myelin increase total QS	-1.3 [-4.7,-0.6]	-4.3 [-7.4,-1.7]	0.14 (2E-2)
	myelin decrease mean R2*	**-1.8 [-2.5,-1.5]**	**-3.0 [-4.3,-2.2]**	**0.14 (2E-2)**
PU	myelin increase mean R2*	3.5 [2.5,5.0]	5.0 [3.1,7.1]	0.10 (5E-2)
	myelin decrease mean R2*	-2.0 [-2.8,-1.8]	-2.8 [-3.4,-2.2]	0.10 (4E-2)
TH	**iron increase mean R2***	**2.9 [2.3,3.9]**	**4.2 [3.3,5.0]**	**0.15 (5E-2)**
	iron decrease mean R2*	**-2.1 [-3.1,-1.8]**	**-3.7 [-4.3,-2.6]**	**0.28 (5E-3)**
	iron decrease total R2*	-0.3 [-0.8,-0.2]	-0.9 [-1.8,-0.4]	0.15 (1E-2)
	iron decrease mean QS	**-7.6 [-9.2,-6.2]**	**-11.3 [-17.4,-9.0]**	**0.29 (4E-3)**
	iron decrease total QS	-1.2 [-2.1,-0.9]	-3.2 [-6.9,-1.2]	0.12 (3E-2)
	myelin increase total R2*	0.6 [0.3,1.0]	1.0 [0.5,1.6]	0.12 (3E-2)
	myelin increase mean QS	**-6.9 [-9.1,-5.3]**	**-11.6 [-15.2,-9.3]**	**0.40 (4E-4)**
	myelin increase total QS	**-1.5 [-2.8,-0.9]**	**-3.3 [-4.6,-2.1]**	**0.26 (8E-3)**
	myelin decrease mean R2*	**-2.0 [-3.4,-1.7]**	**-3.4 [-4.5,-2.6]**	**0.20 (3E-2)**
GP	**iron decrease mean R2***	**-3.1 [-4.9,0.0]**	**-6.0 [-8.0,-3.2]**	**0.17 (2E-2)**
	myelin decrease mean R2*	-3.5 [-4.6,-2.6]	-4.7 [-6.9,-3.6]	0.12 (3E-2)
RN	**iron increase mean R2***	**3.4 [2.8,4.6]**	**4.9 [4.3,6.9]**	**0.16 (5E-2)**
	iron decrease mean R2*	**-2.4 [-4.9,-1.1]**	**-4.7 [-6.2,-2.5]**	**0.12 (4E-2)**
	iron decrease mean QS	**-6.1 [-2.5,-0.1]**	**-14.6 [-5.8,-0.5]**	**0.25 (4E-3)**
	iron decrease total QS	-0.4 [-2.5,-0.1]	-3.3 [-5.8,-0.5]	0.12 (2E-2)
	myelin increase mean QS	**-6.8 [-10.1,-3.1]**	**-13.8 [-16.0,-7.7]**	**0.18 (1E-2)**
SN	**iron decrease mean R2***	**-4.0 [-5.2,-3.1]**	**-6.8 [-8.7,-5.2]**	**0.23 (7E-3)**
	iron decrease mean QS	**-12.6 [-18.5,-8.9]**	**-20.0 [-38.7,-2.1]**	**0.11 (5E-2)**
	myelin increase mean R2*	**4.2 [3.2,5.7]**	**6.1 [5.0,8.1]**	**0.22 (2E-2)**
	myelin increase mean QS	-10.3 [-17.5,-8.4]	-18.1 [-25.1,-11.5]	0.10 (4E-2)
DN	**iron decrease mean QS**	**-8.7 [-12.6,-5.1]**	**-14.3 [-28.2,-9.8]**	**0.14 (3E-2)**
	myelin increase mean QS	**-5.8 [-9.3,-4.3]**	**-10.0 [-23.2,-7.7]**	**0.24 (4E-3)**

Figure 6.4 demonstrates DGM surface maps of RRMS compared to controls. Surface maps provide a visual illustration of the frequency of DARE effects within displayed 3D DGM structures, where colored regions correspond to the first regional surface that exhibits the highest frequency of the DARE effect across subjects. A threshold of one percent longitudinal difference was implemented to improve visual clarity. Iron increase is appears similar in the DGM of controls compared to RRMS, while iron decrease is more prominent in RRMS compared to controls. Myelin decrease appears qualitatively similar in both RRMS and controls, but myelin increase seems to be more prominent in RRMS.

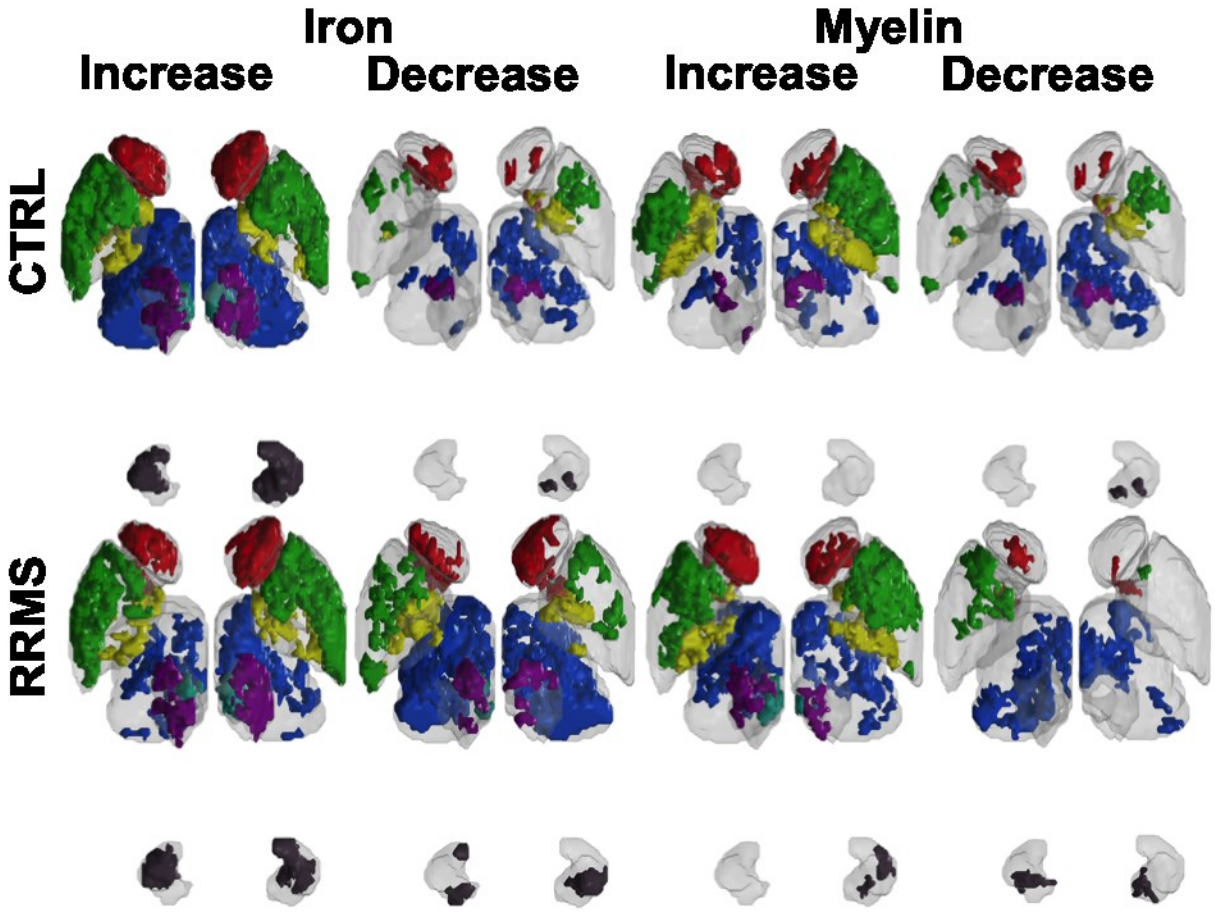

Figure 6.4 Maps of DARE regions' surfaces shown within 3D structures for CN, PU, TH, GP, RN, and SN, where displayed structures were colored according to the color scheme shown in Figure 1 in Chapter 5 for distinction.

Figure 6.5 shows box plots of significant R2* and QS DARE results. Since iron concentration is linearly related to R2* (5) and QS (10), increased iron decrease in RRMS is demonstrated as less R2* values compared to controls. Additionally, lesser susceptibility values of RRMS myelin increase regions compared to controls can be explained by the diamagnetic susceptibility of myelin. Thus, RRMS DARE regions that exhibit more myelin increase compared to controls have lower susceptibilities.

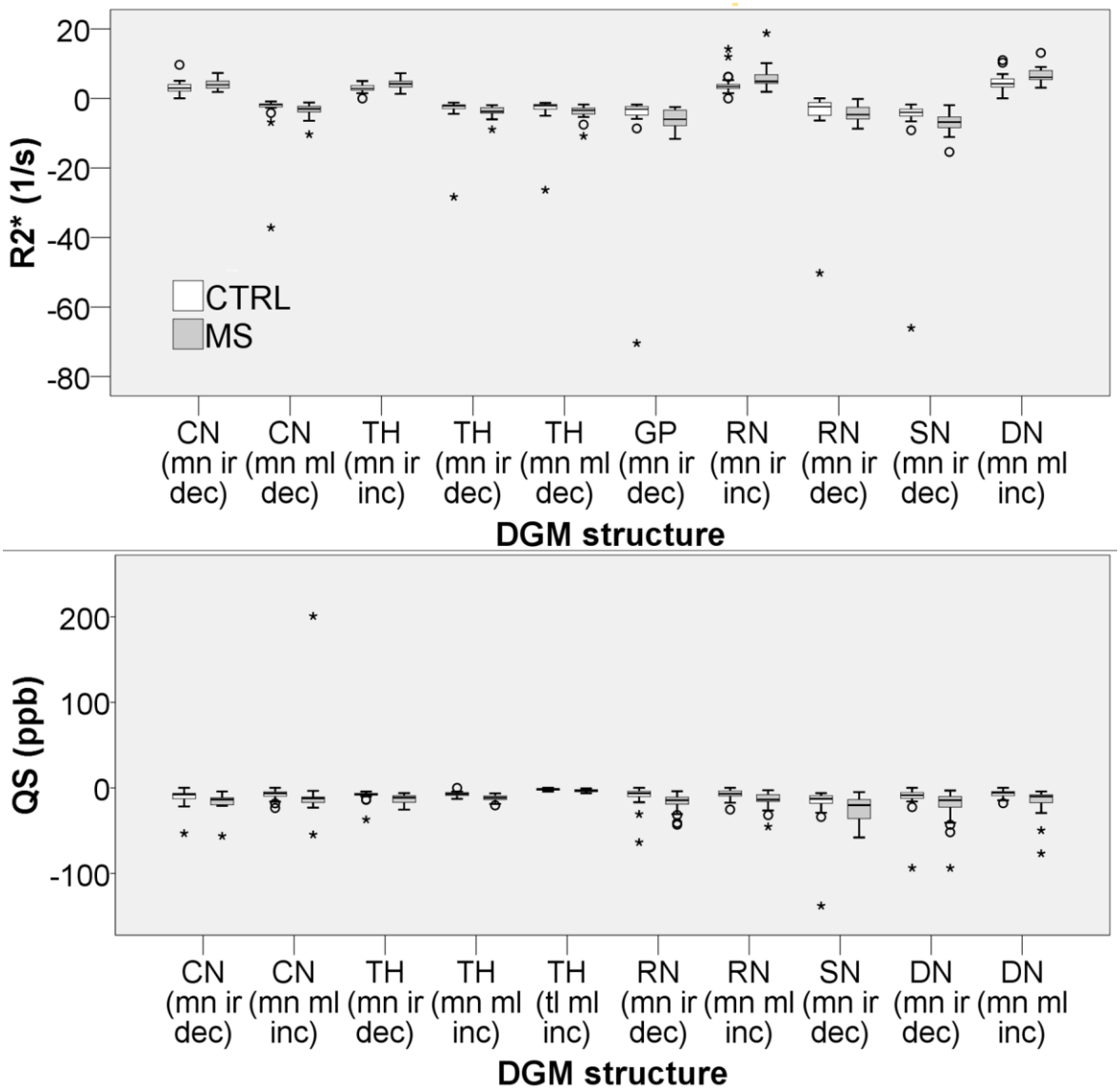

Figure 6.5 Box plots of R2* (top) and QS (bottom) of DARE regions for DGM structures that were found to be significantly different ($Q<0.05$) between CTRL (left) and RRMS (right) groups. mn = mean; tl = total; ir = iron; ml = myelin; inc = increase; dec = decrease.

6.3.4.Regression Analysis

Figure 6.6 shows Pearson's linear regression of MSSS with mean R2* of CN iron decrease regions (r = 0.64; Q = 0.03), and disease duration with mean R2* of SN myelin increase regions (r = 0.49; Q = 0.008). No significant (Q < 0.05) linear relationships were found for regression of MSSS or disease duration with TH bulk regional volume longitudinal change (for both RRMS and controls). For non-normal residuals, significant Spearman's correlation was found between disease duration and mean R2* of GP iron decrease regions (r = -0.56; Q = 0.02) and between MSSS and mean QS of DN myelin increase regions (r = -0.51; Q = 0.02). No other significant correlations were found for other DARE regions that were found significantly different between RRMS and controls.

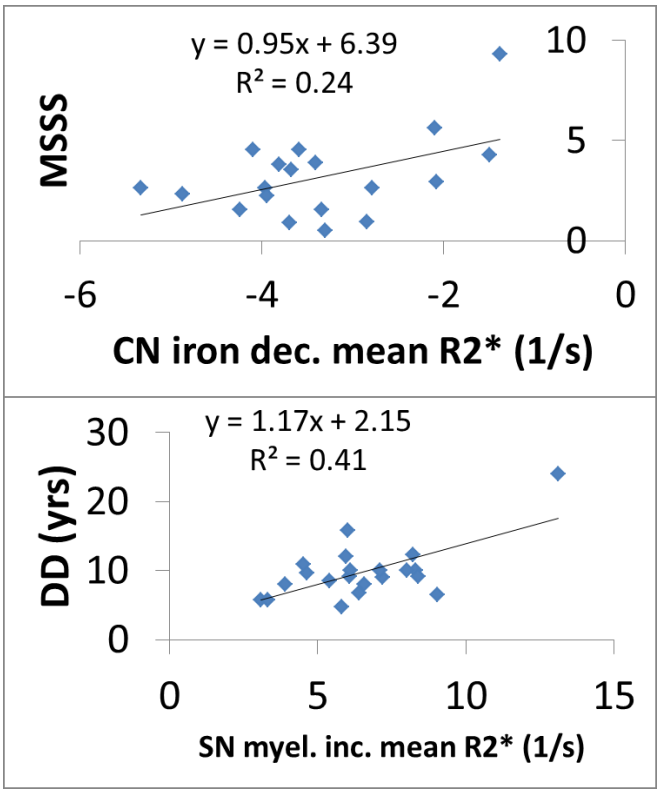

Figure 6.6 Linear regression for mean R2* of CN iron decrease DARE regions with Multiple Sclerosis Disease Severity Scale (MSSS) (top), and mean R2* of SN iron decrease DARE regions with Disease Duration (DD) (bottom). Note that R2* is negative in the top figure because these values represent the R2* longitudinal differences of regions which exhibit iron decrease.

6.4.Discussion

The current study evaluates MS and age-matched control longitudinal changes in iron/myelin-sensitive quantitative MRI of the DGM over 5 years. We have used a recently introduced analysis framework (15) that uses combined R2* and QS for DARE to identify regions of iron and myelin change. This technique provides a parameter indicating the volume of these regions relative to the volume of the DGM structure, a parameter indicating the average normalized iron/myelin concentration change in the DGM structure as measured by R2* or QS, and a parameter indicating the normalized total iron/myelin concentration change in the DGM structure as measured by R2* or QS.

Histological assessment of MS DGM revealed extensive inflammation, neurodegenerative damage, demyelination, increase microglial activation, and accentuated influx of iron-laden macrophages (1,2). Furthermore, the extent of oxidative injury and axonal injury partially due to increased iron levels significantly increased with age in control DGM and normal appear MS DGM brain samples, but histochemical iron loading significantly increased in DGM age only in DGM of controls (1). However, histological and histochemical analysis of brain samples do not capture the full complexity of the disease, which includes both damage and repair processes.

Cross-sectional studies have consistently demonstrated increased R2* (6,7) and QS (6,11,24) values in MS compared to controls, which have been traditionally interpreted as increased iron accumulation in MS. However, longitudinal studies using R2* (14,15,17) and QS (15,16) indicate that iron deposition is occurring at a similar rate to normal DGM iron deposition during healthy aging (13), except of the CN (15). This implies that DGM iron accumulation may indeed be a feature of MS, but not iron deposition (18). This is supported by the detection of significant differences between patients compared to controls over 5 years in this study and over 2 years in a previous study (15) for many DGM structures using DARE mean R2*/QS, but much less significant structures were found using total DARE R2*/QS. The former represents mean DGM iron concenctration, which is inidcative of iron accumulation, while the latter represents total DGM iron concentration, which is reflective of iron deposition.

The development of DARE enabled more specific and sensitive *in vivo* analysis of longitudinal data that accounts for individual variations. Two-year DARE of RR and progressive MS DGM

(15) revealed significantly different iron increase/decrease and myelin increase/decrease longitudinal changes compared to different healthy controls. In that study, significantly different iron increase compared to controls was the most frequently observed iron change only in the RN and SN. Conversely, iron decrease was most frequently observed in the CN, PU, and TH. Both iron increase and iron decrease were observed in the GP, but iron decrease demonstrated a higher effect size. Two-year myelin increase was the most frequent myelin change in the CN, PU, TH, RN, and SN, while myelin increase and decrease were equally observed in the GP (15).

In contrast, the current study found significant 5-year iron increase only in TH and RN. We have also demonstrated that iron decrease is the only iron change that registered significantly different longitudinal differences in RRMS compared to age-matched controls over a period of 5 years in the CN, GP, SN, and DN, while significant trends were also found in the PU. Five-year significant myelin increase over 5 years was observed for the CN, TH, RN, SN, and DN, while significant myelin decrease was detected in the CN and TH. Similar to the 2-year DARE study (15), the increased prominence of DGM myelin increase compared to myelin decrease may be a reflection of the relatively stable EDSS of the patients over the study period.

In a study by Schweser et al. (18), iron decrease in thalamic subnuclei was a consistent finding in RRMS and secondary progressive MS, but not in CIS. The authors explained the inconsistency of these results with earlier cross-sectional studies by an "early-rise late-decline" mechanism that would have caused patient groups with an average age of less than 40 years to exhibit iron increase, while older groups with older mean age would exhibit an iron decrease. Inline with this hypothesis, iron decrease was most frequently observed in the TH of RRMS over 5 years in this study, and over 2 years in a previous study (15). In both cases, the mean group age was close to 40 (35.6±8.0 and 35.2±7.8, respectively). However, this hypothesis does not explain the observed DARE iron decrease over 5 years observed in other DGM structures in the current study, and over 2 years in a previous study (15). It also does not fully explain the discrepancy between significant group effects for iron accumulation, but the inability of longitudinal studies to demonstrate interaction effect for iron accumulation at a rate different than healthy aging.

Furthermore, the same study by Schweser et al. (18) demonstrated a positive correlation between structural volumes and magnetic susceptibility, which was hypothesized as a result of the iron

depleting secondary to oligodendrocyte death. This hypothesis may indeed explain the significant interaction observed in bulk analysis of TH volume and significant iron decrease observed using DARE. A similar hypothesis was proposed by the same group for the CN by longitudinal changes in susceptibility and volume compared to expected changes estimated using theoretical simulations (16). Using DARE, the current study confirms that iron decrease is indeed a feature of the CN over 5 years, and has also been demonstrated previously over a period of 2 years (15). We have also further demonstrated that iron decrease over 5 years is significantly different than controls in the GP and SN, while a previous study has demonstrated significant iron decrease over 2 years in the CN, PU, TH, and GP.

Another possible hypothesis that may explain the discrepancy between cross-sectional studies and longitudinal studies is the effect of compartmentalization of iron in scavenging macrophages upon oligodendrocyte death. Bowen et al. (25) demonstrated that the compartmentalization of iron in phagocytic THP-1 cells increases R2* relaxivity because the perturber strength has become large enough to fulfil the static dephasing regime. Thus, compartmentalized iron causes transverse relaxation to be enhanced because diffusion has a minimal effect on signal decay (26). It has been shown that magnetic susceptibility of lesions sharply increases upon the formation of a new lesion as it changes from enhanced to non-enhanced in its initial years, but decreases as it ages (at approximately 4 years) (27). According to this proposed hypothesis, susceptibility increases rapidly in a new lesion due to relocation of iron from its diffuse distribution in oligodendrocytes to scavenging macrophages. Since this pathological process is prominent in MS DGM (1), a cross-sectional study of the DGM may capture a large number of iron-laden macrophages. Conversely, longitudinal MRI studies do not capture this transient view of iron, and are better reflected by the total longitudinal changes in DGM iron levels. This hypothesis is supported by the fact the significant DGM DARE iron increase was observed over 2 years (15), but limited iron increase over 5 years.

While demyelination, increases in macrophage presence, and tissue restructuring may partially explain observed increases in frequency upon new lesion formation (28), this hypothesis does not take into account the increased DGM presence of iron-laden cells shown by histological studies (1,2). Combined R2* and QS analysis of MS lesions with different enhancing patterns (29) indicated that early active lesions display R2*/QS contrast consistent with demyelination (i.e.

R2* decrease with no change in QS), while late active lesions demonstrate R2* and QS contrast consist with myelin removal/degradation. A limitation of the current study is that it has only considered the latter case of myelin removal/degradation.

DGM atrophy has been shown to be explained by White Matter (WM) atrophy and lesion volume (30), however the link between DGM atrophy and iron/myelin changes is still unknown. We have demonstrated significant atrophy in TH over 5 years in this study, and the PU over 2 years (15), significant group*longitudinal interaction of atrophy in the TH over 5 years in this study, and in the PU over 2 years in a previous study (15), significant atrophy trends in the PU over 5 years and in the TH over 2 years (15), and significant interaction trends in the PU over 5 years and TH over 2 years (15). Combined with iron decrease DARE results in both studies, these observations are in agreement with a hypothesis proposed by Schweser et al. (18) for the role of "bystander damage of chronic inflammation" on the local DGM availability of iron, providing a partial explanation of the slow transition between inflammatory changes dominant in RRMS and neurodegenerative changes dominant in secondary progressive MS.

In comparison to the previous 2-year study that identified significant differences between RRMS and controls in all DGM structures, the current study only identified significant differences in a select number of structures for iron decrease, myelin increase, and limited iron increase. Thus, the objective of regression analysis in this study was to investigate the relationship between identified significant parameters and disease duration and severity. A negative correlation was identified between disease duration and mean R2* of GP iron decrease regions, while a positive linear relationship was found between MSSS and mean R2* of CN iron decrease regions. These observations suggest that more iron decrease occurs with longer disease duration in the GP, but less iron decrease occurs with severe MS symptoms in the CN. This may be explained by the accumulated loss of oligodendrocytes which occurs over longer disease durations, and the role of oxidative damage caused by increased DGM iron levels on disease severity. The negative correlation between disease duration and R2* of iron decrease regions in the GP are in agreement with Schweser's study (18), who found significant negative association of the right TH susceptibility and the natural logarithm of disease duration. The non-linear relationship observed in their study of the TH, compared to the linear relationship observed in this study in the GP may be explained by the complex trajectory of iron accumulation in the TH, which

increases before decreasing after age of 40 (13). The positive relationship between MSSS and CN R2* iron decrease is in agreement with an earlier 4-year longitudinal study (31) that found higher R2 values indicative of increase iron levels at baseline as directly proportional to Extended Disability Status Score. Additionally, a positive correlation was identified between MSSS and mean QS of DN myelin increase regions and a positive linear relationship was found between disease duration and mean R2* of SN myelin increase regions. Since increased myelination would cause lower QS and higher R2* values, thus more myelination is observed with less disease severity and longer disease durations (for the studied group with a relatively stable disease course). This underscores the relationship between DGM damage/repair processes and disease severity and duration. Alternatively, the correlation between between MSSS and mean QS of DN myelin increase regions may reflect the accumulation of Gadolinium contrast agent in the DN of MS patients (32).

6.5.Conclusions

In conclusion, we have demonstrated 5-year changes in bulk and DARE measures and compared these changes to earlier 2-year DGM changes reported earlier. While iron/myelin increase and decrease were observed over 2 years using DARE, DGM iron decrease and myelin increase were the most prominent significant changes observed over 5 years compared to controls in this group of RRMS patients with a relatively stable disease course. DGM Iron decrease over 5 years in the GP was shown to exhibit an inversely proportionally relationship with disease duration, and a directly proportional relationship with disease severity in the CN, possibly due to depletion of iron. Myelination in the DN and SN also correlated with disease duration and severity, with more myelination observed in the DN and SN with less disease severity and longer disease durations, respectively. Thus, the results of this study confirm the pathological role of DGM iron depletion and re-myelination, which may be caused by oligodendrocytes death.

References

1. Haider L, Simeonidou C, Steinberger G, et al. Multiple sclerosis deep grey matter: the relation between demyelination, neurodegeneration, inflammation and iron. J Neurol Neurosurg Psychiatry 2014:85:1386-1395.
2. Vercellino M, Masera S, Lorenzatti M, et al. Demyelination, inflammation, and neurodegeneration in multiple sclerosis deep gray matter. J Neuropathol Exp Neurol 2009:68:489-502.
3. Niels Bergsland, Dana Horakova, Michael G. Dwyer, et al. A five-year serial longitudinal study of deep gray matter atrophy in patients with multiple sclerosis. In: Neurology, 2010.
4. Eshaghi A, Prados F, Brownlee W, et al. Deep grey matter volume loss drives disability worsening in multiple sclerosis. Ann Neurol 2017.
5. Walsh AJ, Lebel RM, Eissa A, et al. Multiple sclerosis: validation of MR imaging for quantification and detection of iron. Radiology 2013:267:531-542.
6. Cobzas D, Sun H, Walsh AJ, Lebel RM, Blevins G & Wilman AH. Subcortical gray matter segmentation and voxel-based analysis using transverse relaxation and quantitative susceptibility mapping with application to multiple sclerosis. J Magn Reson Imaging 2015:42:1601-10.
7. Ropele S, Kilsdonk ID, Wattjes MP, et al. Determinants of iron accumulation in deep grey matter of multiple sclerosis patients. Mult Scler 2014:20:1692-1698.
8. Khalil M, Enzinger C, Langkammer C, et al. Quantitative assessment of brain iron by R(2)* relaxometry in patients with clinically isolated syndrome and relapsing-remitting multiple sclerosis. Mult Scler 2009:15:1048-1054.
9. Khalil M, Langkammer C, Ropele S, et al. Determinants of brain iron in multiple sclerosis: a quantitative 3T MRI study. Neurology 2011:77:1691-1697.
10. Sun H, Walsh AJ, Lebel RM, et al. Validation of quantitative susceptibility mapping with Perls' iron staining for subcortical gray matter. Neuroimage 2015:105:486-492.
11. Hagemeier J, Ferdinand S, Dwyer M, et al. Quantitative Susceptibility Mapping Study of Deep Gray Matter Iron at 3T in Large Cohort of Multiple Sclerosis Patients (P4. 162). Neurology 2016:86:P4. 162.
12. Elkady AM, Cobzas D, Sun H, Blevins G & Wilman AH. Progressive iron accumulation across multiple sclerosis phenotypes revealed by sparse classification of deep gray matter. J Magn Reson Imaging 2017.
13. Hallgren B & Sourander P. The effect of age on the non-haemin iron in the human brain. J Neurochem 1958:3:41-51.
14. Walsh AJ, Blevins G, Lebel RM, Seres P, Emery DJ & Wilman AH. Longitudinal MR imaging of iron in multiple sclerosis: an imaging marker of disease. Radiology 2014:270:186-196.
15. Elkady AM, Cobzas D, Sun H, Blevins G & Wilman AH. Discriminative analysis of regional evolution of iron and myelin/calcium in deep gray matter of multiple sclerosis and healthy subjects. Journal of Magnetic Resonance Imaging 2018.
16. Hagemeier J, Zivadinov R, Dwyer MG, et al. Changes of deep gray matter magnetic susceptibility over 2years in multiple sclerosis and healthy control brain. NeuroImage: Clinical 2017.
17. Khalil M, Langkammer C, Pichler A, et al. Dynamics of brain iron levels in multiple sclerosis: A longitudinal 3T MRI study. Neurology 2015:84:2396-2402.
18. Schweser F, Martins, Ana Luiza Raffaini Duarte, Hagemeier J, et al. Mapping of thalamic magnetic susceptibility in multiple sclerosis indicates decreasing iron with disease duration: A

proposed mechanistic relationship between inflammation and oligodendrocyte vitality. Neuroimage 2017.
19. E. Hernández-Torres, V. Wiggermann, D. K. Li, et al. Iron loss occurs in the deep gray matter of multiple sclerosis patients. In: Proc. Intl Soc. Mag. Reson Med. Hawaii, .
20. Roxburgh RH, Seaman SR, Masterman T, et al. Multiple Sclerosis Severity Score: using disability and disease duration to rate disease severity. Neurology 2005:64:1144-1151.
21. Sun H & Wilman AH. Background field removal using spherical mean value filtering and Tikhonov regularization. Magn Reson Med 2013:71:1151-7.
22. Wu B, Li W, Guidon A & Liu C. Whole brain susceptibility mapping using compressed sensing. Magn Reson Med 2012:67:137-147.
23. Trojano M, Lucchese G, Graziano G, et al. Geographical variations in sex ratio trends over time in multiple sclerosis. PLOS one 2012:7:e48078.
24. Langkammer C, Liu T, Khalil M, et al. Quantitative susceptibility mapping in multiple sclerosis. Radiology 2013:267:551-559.
25. Bowen CV, Zhang X, Saab G, Gareau PJ & Rutt BK. Application of the static dephasing regime theory to superparamagnetic iron-oxide loaded cells. Magnetic Resonance in Medicine 2002:48:52-61.
26. Yablonskiy DA & Haacke EM. Theory of NMR signal behavior in magnetically inhomogeneous tissues: the static dephasing regime. Magnetic resonance in medicine 1994:32:749-763.
27. Chen W, Gauthier SA, Gupta A, et al. Quantitative susceptibility mapping of multiple sclerosis lesions at various ages. Radiology 2014:271:183-192.
28. Wiggermann V, Hernandez Torres E, Vavasour IM, et al. Magnetic resonance frequency shifts during acute MS lesion formation. Neurology 2013:81:211-218.
29. Zhang Y, Gauthier SA, Gupta A, et al. Quantitative Susceptibility Mapping and R2* Measured Changes during White Matter Lesion Development in Multiple Sclerosis: Myelin Breakdown, Myelin Debris Degradation and Removal, and Iron Accumulation. AJNR Am J Neuroradiol 2016:37:1629-1635.
30. Steenwijk MD, Daams M, Pouwels PJ, et al. What explains gray matter atrophy in long-standing multiple sclerosis? Radiology 2014:272:832-842.
31. Neema M, Arora A, Healy BC, et al. Deep gray matter involvement on brain MRI scans is associated with clinical progression in multiple sclerosis. Journal of Neuroimaging 2009:19:3-8.
32. Schlemm L, Chien C, Bellmann-Strobl J, et al. Gadopentetate but not gadobutrol accumulates in the dentate nucleus of multiple sclerosis patients. Multiple Sclerosis Journal 2017:23:963-972.

Chapter 7: Conclusions and Future Work

7.1. Concluding Remarks

The main goals of this thesis were to develop technical MRI innovations and to study research applications to further the field of quantitative gradient-echo MRI of MS. We have hypothesized that quantitative gradient-echo MRI methods may serve as a biomarker of disease progression in MS.

7.1.1. Lesions in MS

We have confirmed the presence of the characteristic dipole signature indicative of iron in LFS maps for one *postmortem* lesion. However, dipole patterns were not observed in other iron-positive lesions. Similarly, dipole patterns were only visible in a small fraction of *in vivo* lesions. Simulations indicated that the dipole visualization of iron-positive lesions is a function of the size of the lesion, the strength of the magnetic perturber (i.e. the amount of iron present in the lesion), the signal to noise ratio, and the 2D view orientation. As for QS, *post-mortem* iron-positive lesions and *in vivo* lesions demonstrated various core and rim contrast, with QS hyper-intense core and iso-intense rim contrast the most common appearance of *in vivo* lesions. Approximately half of lesions visible on T2-weighted images were not visible on LFS and QS maps. Thus, the use of LFS and QS lesion contrast for detection is sensitive, but not sufficiently specific for lesion iron detection, while the use of lesion dipole signature is specific but not sensitive (1). The presence of positive rim contrast in lesions may indicate their chronic active status with increased myelin damage and presence of iron-laden macrophages (2).

7.1.2. FOV-restricted QSM

By studying the effect of FOV reduction in theoretical simulations and *in vivo* data, we have found that the QSM accuracy decreases with FOV restriction, especially with FOV reduction in the main magnetic field direction. The unique requirement for an extended, non-local FOV leads

to a strong dependence of QSM on FOV choice. An axial gradient-echo acquisition with a FOV centered on the globus pallidus should encompass at least five-fold the coronal physical dimension of the globus pallidus to ensure 95% QSM accuracy. Thus, to preserve QSM accuracy, FOV-restricted acquisitions are not recommended (3).

7.1.3. Cross-sectional Deep Gray Matter Iron and Myelin Changes in MS

Using combined R2* and QS maps of MS patients compared to controls, we have developed a sparse logistic regression technique for localized cross-sectional analysis of sparse regions indicative of DGM pathological iron and myelin. The developed technique demonstrated improved statistical power compared to conventional singular R2* and QS analysis, and revealed progressive iron accumulation that increases progressively with MS disease phenotype (4).

7.1.4. Longitudinal Deep Gray Matter Iron and Myelin Changes in MS

In Chapter 5, we have presented a novel sparse analysis technique using combined R2* and QS maps for discriminative analysis of regional evolution of iron and myelin/calcium in longitudinal MS data compared to controls. By applying this technique to 2-year data in RRMS and PMS in 5 year RRMS data, we have demonstrated that the DGM exhibits a wide repertoire of increase and decrease in DGM iron and myelin over a period of 2 years (5), but only iron decrease and myelin increase is observed over 5 years (Chapter 6). We have also shown that iron changes are more prominent over 2 years in RRMS, whereas myelin changes are more prominent in PMS compared to age-matched controls for the same period. We have also demonstrated that longitudinal changes in quantitative MRI of identified DGM iron/myelin regions significantly correlate with clinical measures over 2 (5) and 5 (Chapter 6) years.

These results reveal important features of MS DGM pathology, however, more studies are needed to validate the results of the conducted research in this thesis. The tools developed to perform these studies are a valuable addition to the available set of analysis tools used to study the MS brain, and can help improve understanding of the complex MS DGM pathology.

7.2.Limitations

The technical innovations presented in this thesis have several limitations. First, lesions were defined as those conspicuous on T2 and T1-weighted MRI. This lesion definition does not account for lesions exhibiting iron-laden macrophages that may be more easily conspicuous on gradient-echo MRI (6,7). We have also not included in our protocol Gd-enhanced T1-weighted acquisitions to estimate lesion age and relate to conspicuity findings. Regarding *postmortem* studies, we have only corroborated phase and susceptibility appearance of iron-positive lesion, but did not account for changes in myelin. Validating myelin contrast in the presence of lesion iron has been previously demonstrated (8), but investigating these results in *postmortem* data would have provided further verification. Additionally, we have not accounted for white matter fiber orientation and microarchitecture. Although this contribution may have been less significant for focal demyelinated lesions, normal appearing white matter needs to be corrected for these effects. Another limitation is that Perls' iron stain only is a qualitative measure of iron. Quantitative iron techniques, such as laser ablation inductively coupled mass spectroscopy (8), can help improved understanding of correlation of lesion iron concentration with susceptibility and gradient-echo phase contrast.

Investigations of FOV effects on QSM accuracy were limited by only evaluating the globus pallidus. Since shape and orientation are important contributors to QSM contrast, further studies need to evaluate FOV effects for acquisitions centered on other DGM structures. However, such studies should exhibit similar results demonstrating the sensitivity of QSM accuracy to FOV reductions, especially parallel to the static field. Although no FOV effect was observed on the employed RESHARP background removal technique, further studies are needed to evaluate other background removal techniques. Similarly, the performance of other field inversion techniques in the case of reduced FOV needs to be investigated. Erosion of brain edges by RESHARP was also not accounted for, which can be remedied using extended-SHARP (9) and Laplacian boundary value (10).

A limitation of all cross-sectional DGM MS studies, including ours, is the large variance in DGM iron concentrations in healthy controls (11) and unaccounted factors, such as alcohol

consumption (12), that result in many discrepancies when comparing to other studies. Another limitation of our study was we have ignored diffusion and microstructure effects. However, the interpretation of R2* (13) and QS (14) as iron increase have been validated in *postmortem* MS DGM.

Common limitations for both techniques that we have developed (i.e. sparse logistic regression and DARE) are that we have not accounted for fiber orientation and head orientation. Although the effect of fiber orientation may be minimal in the DGM, application of these techniques to the white matter would require some form of correction (15). The closely-fitting receiver head coil utilized throughout this thesis may have reduced the effect of head orientation, but other coil settings would require careful consideration of head position/orientation. Common limitations for all cross-sectional and longitudinal studies conducted in this thesis are their relatively small sample sizes, and thus further studies in larger cohorts are needed to corroborate findings. That said, the developed cross-sectional and longitudinal analysis techniques increase statistical power, which should partially remedy the effect of small group sizes.

Another common limitation is the reliability of R2* and QS measurements from one scan to another, and the associated segmentation/registration reliability. The maximum scan-rescan percent error in DGM quantification was 5.8% and 0.9% for R2* and QSM, respectively (16). Nonetheless, the developed sparse-logistic regression and DARE techniques compare to age-matched controls, which is included as a filtering step to identify significant disease related effects only, and thus filtered out other systemic effects that exist in both groups. Furthermore, DARE is limited by noise that may occur between repeated acquisitions. Future improvements to DARE will be performed by evaluating its performance for test-retest acquisitions, and using a threshold to filter out noise that occurs within the inherent variability of DARE as measured by the test-retest scans.

A further common limitation of these techniques is that it only considers the dominant effect in a voxel, and does not reveal information about other effects that may be also occurring. Moreover, these techniques cannot discriminate inflammation and calcium effects, which may have influenced the results. Lastly, we have only considered demyelination in the case of degradation of myelin within macrophages, and have not considered myelin breakdown with associated

debris present in macrophages (17). This limitation implies that there may have been demyelinated regions in chronic active lesions that have not been detected by these techniques.

7.3. Future Directions

Since the focus of this thesis was on MS DGM, the relationship of pathological processes occurring in the white matter (WM) with DGM were not considered. As detailed earlier in **Section 1.4.1**, the DGM is connected to the cortex via five major feedback loops. A major focus of future research will be exploring the relationship between DGM and WM pathology.

7.3.1. Relationship between DGM iron/myelin and WM lesions

Myelin water imaging (18,19) is an important spin-echo MRI technique that has been validated to correlate with myelin content of white matter. Using this technique, a recent study (2) has evaluated the myelin water fraction of MS lesions that exhibit a hyper-intense susceptibility rim. The study has found that these chronic active lesions had higher susceptibilities and lower myelin water fraction than lesions without hyper-intense rims. In the future, we would like to investigate the relationship between myelin water fraction of MS lesions and normal appearing white matter and DGM DARE parameters.

Gradient-echo myelin water imaging has also been demonstrated as a measure of white matter content (20). As a preliminary pilot study, we have acquired a multi-echo gradient acquisition of an MS subject with short echo spacing (**Figure 1.9**). Future work will focus on developing a fitting routine to a three compartment model containing a short myelin water component, an intermediate component for myelinated axon, and a long component for mixed water-pool (21). We will also investigate including compartmental frequency in the model (22,23), and the use of ΔB_o correction to alleviate errors due to field inhomogeneity (24). Quantitative magnetization transfer myelin water imaging (25) may also be an avenue that we may explore for estimation of myelin volume in the MS brain.

7.3.2. Relationship between DGM iron/myelin and Fiber Tract Integrity

Fractional Anisotropy (FA) is an important biomarker of fiber integrity that can be measured using diffusion MRI. Studying the relationship between fiber integrity and DGM iron/myelin in MS may help elucidate on the process of retrograde degeneration in MS, where the degeneration moves backward towards the neuronal cell body due to damage in the connecting axon (26). We have acquired preliminary DTI data for a RRMS subject (**Figure 7.1**) in conjunction with multi-echo gradient echo data using a 3T Siemens PRISMA system. Future research will explore correlation of fractional anisotropy changes of white matter fibers with DARE changes in deep gray matter structures, and also sparse logistic regression of deep gray matter cross-sectional changes with fractional anisotropy of white matter fibers.

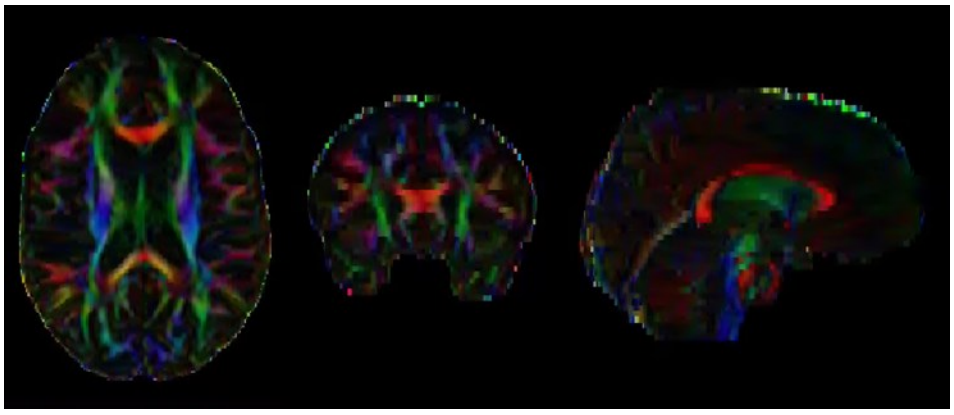

Figure 7.1 Fractional anisotropy (FA) maps in axial (left), coronal (middle), and sagittal (right) view reconstructed using FSL for a 32-year old MS subject. Regions with low FA (such as cerebrospinal fluid) are dull, while tissues with extreme FA (i.e. fiber tracts) are bright. Red indicates left-right orientation, green is front to back, and blue is head to foot. Slice thickness = 3mm; number of slices = 43; repetition time = 4.4 s; echo time = 66 ms; echo train length = 63; 12 diffusion directions with b = 1000 s/mm^2; FOV = 1680*1680*105 mm^3; voxel size = 0.94 x 0.94 x 3.00 mm^3.

7.3.3. Correlation of DARE Deep Grey Matter & DARE White Matter

As a preliminary pilot study, we have applied DARE to 17 WM structures that were segmented using John Hopkins Eve atlas (27) (**Figure 1.7**) for 2-year longitudinal data of 37 MS patients and age-matched controls, then correlated DARE region sizes of WM fibers and DGM structures

using Pearson's correlation. As expected, there was almost no significant correlation in controls. However, many significant ($Q<0.05$) correlations were found in MS patients, indicating that there is a pathological link between WM fiber tracts and DGM in MS. To quantitatively assess correlation group differences, we also applied Fischer's r to z transformation to test whether there were significant ($Q<0.05$) differences between the correlation coefficient of the groups. Preliminary analysis of the results indicated that there were significant differences between correlation of DARE DGM and WM fiber region size in MS compared to age-matched controls. Further research will focus on investigating the nature of the link between DGM and WM iron/myelin longitudinal changes in MS.

7.3.4. General Outlook of Future Directions

Until recently, MS has been considered solely a demyelinating white matter disease. However, gray matter neurodegeneration has been implicated in the disease's pathology. The general outlook of future research is to develop and apply quantitative gradient-echo MRI techniques to both gray matter and white matter to elucidate the relationship between demyelination and neurodegeneration in MS.

References

1. A. M. Elkady, H. Sun, A. J. Walsh, G. Blevins, D. Zhuozi and A. H. Wilman. Quantitative Susceptibility Mapping of Lesions in Multiple Sclerosis. In: ISMRM 23rd Annual Meeting & Exhibition, Toronto, Canada, 2015.
2. Yao Y, Nguyen TD, Pandya S, et al. Combining Quantitative Susceptibility Mapping with Automatic Zero Reference (QSM0) and Myelin Water Fraction Imaging to Quantify Iron-Related Myelin Damage in Chronic Active MS Lesions. AJNR Am J Neuroradiol 2018:39:303-310.
3. Elkady AM, Sun H & Wilman AH. Importance of extended spatial coverage for quantitative susceptibility mapping of iron-rich deep gray matter. Magn Reson Imaging 2016:34:574-578.
4. Elkady AM, Cobzas D, Sun H, Blevins G & Wilman AH. Progressive iron accumulation across multiple sclerosis phenotypes revealed by sparse classification of deep gray matter. J Magn Reson Imaging 2017.
5. Elkady AM, Cobzas D, Sun H, Blevins G & Wilman AH. Discriminative analysis of regional evolution of iron and myelin/calcium in deep gray matter of multiple sclerosis and healthy subjects. Journal of Magnetic Resonance Imaging 2018.
6. Haacke EM, Makki M, Ge Y, et al. Characterizing iron deposition in multiple sclerosis lesions using susceptibility weighted imaging. J Magn Reson Imaging 2009:29:537-544.

7. Eissa A, Lebel RM, Korzan JR, et al. Detecting lesions in multiple sclerosis at 4.7 tesla using phase susceptibility-weighting and T2-weighting. J Magn Reson Imaging 2009:30:737-742.
8. Wisnieff C, Ramanan S, Olesik J, Gauthier S, Wang Y & Pitt D. Quantitative susceptibility mapping (QSM) of white matter multiple sclerosis lesions: Interpreting positive susceptibility and the presence of iron. Magn Reson Med 2014.
9. Topfer R, Schweser F, Deistung A, Reichenbach JR & Wilman AH. SHARP edges: recovering cortical phase contrast through harmonic extension. Magn Reson Med 2015:73:851-856.
10. Zhou D, Liu T, Spincemaille P & Wang Y. Background field removal by solving the Laplacian boundary value problem. NMR Biomed 2014:27:312-319.
11. Hallgren B & Sourander P. The effect of age on the non-haemin iron in the human brain. J Neurochem 1958:3:41-51.
12. Foster M, Zivadinov R, Weinstock-Guttman B, et al. Associations of moderate alcohol consumption with clinical and MRI measures in multiple sclerosis. J Neuroimmunol 2012:243:61-68.
13. Walsh AJ, Lebel RM, Eissa A, et al. Multiple sclerosis: validation of MR imaging for quantification and detection of iron. Radiology 2013:267:531-542.
14. Sun H, Walsh AJ, Lebel RM, et al. Validation of quantitative susceptibility mapping with Perls' iron staining for subcortical gray matter. Neuroimage 2015:105:486-492.
15. F. Schweser, A. Deistung, K. Sommer and J. R. Reichenbach. Disentangling contributions from iron and myelin architecture to brain tissue magnetic susceptibility by using Quantitative Susceptibility Mapping (QSM). In: Proc. Int. Soc. Magn. Reson. Med. , 2012. (Volume 20, p. 409).
16. Cobzas D, Sun H, Walsh AJ, Lebel RM, Blevins G & Wilman AH. Subcortical gray matter segmentation and voxel-based analysis using transverse relaxation and quantitative susceptibility mapping with application to multiple sclerosis. J Magn Reson Imaging 2015:42:1601-10.
17. Zhang Y, Gauthier SA, Gupta A, et al. Quantitative Susceptibility Mapping and R2* Measured Changes during White Matter Lesion Development in Multiple Sclerosis: Myelin Breakdown, Myelin Debris Degradation and Removal, and Iron Accumulation. AJNR Am J Neuroradiol 2016:37:1629-1635.
18. MacKay A, Whittall K, Adler J, Li D, Paty D & Graeb D. In vivo visualization of myelin water in brain by magnetic resonance. Magn Reson Med 1994:31:673-677.
19. Alonso-Ortiz E, Levesque IR & Pike GB. MRI-based myelin water imaging: A technical review. Magnetic resonance in medicine 2015:73:70-81.
20. Lee J, Nam Y, Choi JY, Kim EY, Oh S & Kim D. Mechanisms of T2* anisotropy and gradient echo myelin water imaging. NMR Biomed 2017:30.
21. Lancaster JL, Andrews T, Hardies LJ, Dodd S & Fox PT. Three- pool model of white matter. Journal of Magnetic Resonance Imaging 2003:17:1-10.
22. Van Gelderen P, De Zwart JA, Lee J, Sati P, Reich DS & Duyn JH. Nonexponential T2* decay in white matter. Magnetic resonance in medicine 2012:67:110-117.
23. Nam Y, Lee J, Hwang D & Kim D. Improved estimation of myelin water fraction using complex model fitting. Neuroimage 2015:116:214-221.
24. Alonso-Ortiz, E., Levesque, I.R., Paquin, R. and Pike, G.B., 2017. Field inhomogeneity correction for gradient echo myelin water fraction imaging. Magnetic resonance in medicine, 78(1), pp.49-57.

25. Stikov N, Campbell JS, Stroh T, et al. In vivo histology of the myelin g-ratio with magnetic resonance imaging. Neuroimage 2015:118:397-405.
26. Stadelmann C, Wegner C & Brück W. Inflammation, demyelination, and degeneration—recent insights from MS pathology. Biochimica et Biophysica Acta (BBA)-Molecular Basis of Disease 2011:1812:275-282.
27. Lim IAL, Faria AV, Li X, et al. Human brain atlas for automated region of interest selection in quantitative susceptibility mapping: application to determine iron content in deep gray matter structures. Neuroimage 2013:82:449-469.

Works Cited

Retrieved from https://mssociety.ca/research-news/article/breaking-news-ocrevus-ocrelizumab-is-the-first-drug-approved-by-health-canada-for-primary-progressive-ms

Acosta-Cabronero, J., Williams, G. B., Cardenas-Blanco, A., Arnold, R. J., Lupson, V., & Nestor, P. J. (2013). In vivo quantitative susceptibility mapping (QSM) in alzheimer's disease. *PloS One, 8*(11), e81093. doi:10.1371/journal.pone.0081093; 10.1371/journal.pone.0081093

Alonso-Ortiz, E., Levesque, I. R., & Pike, G. B. (2015). MRI-based myelin water imaging: A technical review. *Magnetic Resonance in Medicine, 73*(1), 70-81.

Alonso, A., & Hernan, M. A. (2008). Temporal trends in the incidence of multiple sclerosis: A systematic review. *Neurology, 71*(2), 129-135. doi:10.1212/01.wnl.0000316802.35974.34 [doi]

Al-Radaideh, A. M., Wharton, S. J., Lim, S. Y., Tench, C. R., Morgan, P. S., Bowtell, R. W., . . . Gowland, P. A. (2013). Increased iron accumulation occurs in the earliest stages of demyelinating disease: An ultra-high field susceptibility mapping study in clinically isolated syndrome. *Multiple Sclerosis (Houndmills, Basingstoke, England), 19*(7), 896-903. doi:10.1177/1352458512465135; 10.1177/1352458512465135

Ashburner, J., & Friston, K. J. (2000). Voxel-based morphometry--the methods. *NeuroImage, 11*(6 Pt 1), 805-821. doi:10.1006/nimg.2000.0582 [doi]

Avants, B. B., Tustison, N. J., Song, G., Cook, P. A., Klein, A., & Gee, J. C. (2011). A reproducible evaluation of ANTs similarity metric performance in brain image registration. *NeuroImage, 54*(3), 2033-2044.

Bagnato, F., Hametner, S., & Welch, E. B. (2013). Visualizing iron in multiple sclerosis. *Magnetic Resonance Imaging, 31*(3), 376-384. doi:10.1016/j.mri.2012.11.011 [doi]

Bagnato, F., Hametner, S., Yao, B., van Gelderen, P., Merkle, H., Cantor, F. K., . . . Duyn, J. H. (2011). Tracking iron in multiple sclerosis: A combined imaging and histopathological study at 7 tesla. *Brain : A Journal of Neurology, 134*(Pt 12), 3602-3615. doi:10.1093/brain/awr278 [doi]

Bakshi, R., Benedict, R. H., Bermel, R. A., Caruthers, S. D., Puli, S. R., Tjoa, C. W., . . . Jacobs, L. (2002). T2 hypointensity in the deep gray matter of patients with multiple sclerosis: A quantitative magnetic resonance imaging study. *Archives of Neurology, 59*(1), 62-68. doi:noc10184 [pii]

Barbosa, J. H., Santos, A. C., Tumas, V., Liu, M., Zheng, W., Haacke, E. M., & Salmon, C. E. (2015). Quantifying brain iron deposition in patients with parkinson's disease using quantitative susceptibility mapping, R2 and R2*. *Magnetic Resonance Imaging,* doi:10.1016/j.mri.2015.02.021; 10.1016/j.mri.2015.02.021

Barkhof, F., Scheltens, P., Frequin, S. T., Nauta, J. J., Tas, M. W., Valk, J., & Hommes, O. R. (1992). Relapsing-remitting multiple sclerosis: Sequential enhanced MR imaging vs clinical findings in determining disease activity. *AJR.American Journal of Roentgenology, 159*(5), 1041-1047. doi:10.2214/ajr.159.5.1414773 [doi]

Barnett, M. H., & Prineas, J. W. (2004). Relapsing and remitting multiple sclerosis: Pathology of the newly forming lesion. *Annals of Neurology, 55*(4), 458-468.

Beaulieu, C., Plewes, C., Paulson, L. A., Roy, D., Snook, L., Concha, L., & Phillips, L. (2005). Imaging brain connectivity in children with diverse reading ability. *NeuroImage, 25*(4), 1266-1271.

Bender, B., & Klose, U. (2010). The in vivo influence of white matter fiber orientation towards B0 on T2* in the human brain. *NMR in Biomedicine, 23*(9), 1071-1076.

Bergsland, N., Horakova, D., Dwyer, M. G., Ramasamy, D., Havrdova, E., Seidl, Z., . . . Vaneckova, M. (2010). (2010). A five-year serial longitudinal study of deep gray matter atrophy in patients with multiple sclerosis. Paper presented at the *Neurology, , 74*(9) A235-A235.

Betts, M. J., Acosta-Cabronero, J., Cardenas-Blanco, A., Nestor, P. J., & Düzel, E. (2016). High-resolution characterisation of the aging brain using simultaneous quantitative susceptibility mapping (QSM) and R 2* measurements at 7T. *NeuroImage, 138*, 43-63.

Bilgic, B., Fan, A. P., Polimeni, J. R., Cauley, S. F., Bianciardi, M., Adalsteinsson, E., . . . Setsompop, K. (2014). Fast quantitative susceptibility mapping with L1-regularization and automatic parameter selection. *Magnetic Resonance in Medicine, 72*(5), 1444-1459.

Bilgic, B., Pfefferbaum, A., Rohlfing, T., Sullivan, E. V., & Adalsteinsson, E. (2012). MRI estimates of brain iron concentration in normal aging using quantitative susceptibility mapping. *NeuroImage, 59*(3), 2625-2635. doi:10.1016/j.neuroimage.2011.08.077 [doi]

Bloom, M., Burnell, E. E., MacKay, A. L., Nichol, C. P., Valic, M. I., & Weeks, G. (1978). Fatty acyl chain order in lecithin model membranes determined from proton magnetic resonance. *Biochemistry, 17*(26), 5750-5762.

Bouras, C., Giannakopoulos, P., Good, P. F., Hsu, A., Hof, P. R., & Perl, D. P. (1997). A laser microprobe mass analysis of brain aluminum and iron in dementia pugilistica: Comparison with alzheimer's disease. *European Neurology, 38*(1), 53-58.

Bowen, C. V., Zhang, X., Saab, G., Gareau, P. J., & Rutt, B. K. (2002). Application of the static dephasing regime theory to superparamagnetic iron-oxide loaded cells. *Magnetic Resonance in Medicine, 48*(1), 52-61.

Bramow, S., Frischer, J. M., Lassmann, H., Koch-Henriksen, N., Lucchinetti, C. F., Sørensen, P. S., & Laursen, H. (2010). Demyelination versus remyelination in progressive multiple sclerosis. *Brain, 133*(10), 2983-2998.

Browne, P., Chandraratna, D., Angood, C., Tremlett, H., Baker, C., Taylor, B. V., & Thompson, A. J. (2014). Atlas of multiple sclerosis 2013: A growing global problem with widespread inequity. *Neurology, 83*(11), 1022-1024. doi:10.1212/WNL.0000000000000768 [doi]

Calabrese, M., Agosta, F., Rinaldi, F., Mattisi, I., Grossi, P., Favaretto, A., . . . Rinaldi, L. (2009). Cortical lesions and atrophy associated with cognitive impairment in relapsing-remitting multiple sclerosis. *Archives of Neurology, 66*(9), 1144-1150.

Calabrese, M., Filippi, M., & Gallo, P. (2010). Cortical lesions in multiple sclerosis. *Nature Reviews Neurology, 6*(8), 438.

Carr, H. Y., & Purcell, E. M. (1954). Effects of diffusion on free precession in nuclear magnetic resonance experiments. *Physical Review, 94*(3), 630.

Cascio, C. J., Gerig, G., & Piven, J. (2007). Diffusion tensor imaging: Application to the study of the developing brain. *Journal of the American Academy of Child and Adolescent Psychiatry, 46*(2), 213-223. doi:10.1097/01.chi.0000246064.93200.e8 [doi]

Ceccarelli, A., Rocca, M. A., Pagani, E., Colombo, B., Martinelli, V., Comi, G., & Filippi, M. (2008). A voxel-based morphometry study of grey matter loss in MS patients with different clinical phenotypes. *NeuroImage, 42*(1), 315-322.

Ceccarelli, A., Filippi, M., Neema, M., Arora, A., Valsasina, P., Rocca, M. A., . . . Bakshi, R. (2009). T2 hypointensity in the deep gray matter of patients with benign multiple sclerosis. *Multiple Sclerosis (Houndmills, Basingstoke, England), 15*(6), 678-686. doi:10.1177/1352458509103611 [doi]

Ceccarelli, A., Rocca, M. A., Neema, M., Martinelli, V., Arora, A., Tauhid, S., . . . Filippi, M. (2010). Deep gray matter T2 hypointensity is present in patients with clinically isolated syndromes suggestive of multiple sclerosis. *Multiple Sclerosis (Houndmills, Basingstoke, England), 16*(1), 39-44. doi:10.1177/1352458509350310 [doi]

Chataway, J. *MS-SMART: Multiple Sclerosis-Secondary Progressive Multi-Arm Randomisation Trial-ClinicalTrials.Gov,*

Chataway, J., Schuerer, N., Alsanousi, A., Chan, D., MacManus, D., Hunter, K., . . . Nielsen, C. (2014). Effect of high-dose simvastatin on brain atrophy and disability in secondary progressive multiple sclerosis (MS-STAT): A randomised, placebo-controlled, phase 2 trial. *The Lancet, 383*(9936), 2213-2221.

Chawla, S., Kister, I., Herbert, J., Brisset, J., Dusek, P., Wuerfel, J., & Paul, F., Ge,Y. (2014). Assessment of iron deposition pattern in multiple sclerosis and neuromyelitis optica lesions with ultra-high field quantitative susceptibility mapping [Abstract]. *Multiple Sclerosis (Houndmills, Basingstoke, England), 20 S1* 14-66. doi:10.1177/1352458514546076 [doi]

Chen, J. C., Hardy, P. A., Kucharczyk, W., Clauberg, M., Joshi, J. G., Vourlas, A., . . . Henkelman, R. M. (1993). MR of human postmortem brain tissue: Correlative study between T2 and assays of iron and ferritin in parkinson and huntington disease. *AJNR.American Journal of Neuroradiology, 14*(2), 275-281.

Chen, W., Gauthier, S. A., Gupta, A., Comunale, J., Liu, T., Wang, S., . . . Wang, Y. (2014). Quantitative susceptibility mapping of multiple sclerosis lesions at various ages. *Radiology, 271*(1), 183-192. doi:10.1148/radiol.13130353 [doi]

Cheng, Y. C., Neelavalli, J., & Haacke, E. M. (2009). Limitations of calculating field distributions and magnetic susceptibilities in MRI using a fourier based method. *Physics in Medicine and Biology, 54*(5), 1169-1189. doi:10.1088/0031-9155/54/5/005; 10.1088/0031-9155/54/5/005

Cifelli, A., Arridge, M., Jezzard, P., Esiri, M. M., Palace, J., & Matthews, P. M. (2002). Thalamic neurodegeneration in multiple sclerosis. *Annals of Neurology, 52*(5), 650-653.

Cobzas, D., & Wilman, A.*Unpublished data.* Unpublished manuscript.

Cobzas, D., Sun, H., Walsh, A. J., Lebel, R. M., Blevins, G., & Wilman, A. H. (2015). Subcortical gray matter segmentation and voxel-based analysis using transverse relaxation and quantitative susceptibility mapping with application to multiple sclerosis. *Journal of Magnetic Resonance Imaging : JMRI, 42*(6), 1601-10. doi:10.1002/jmri.24951 [doi]

Cohen-Adad, J., Polimeni, J. R., Helmer, K. G., Benner, T., McNab, J. A., Wald, L. L., . . . Mainero, C. (2012). T 2* mapping and B 0 orientation-dependence at 7T reveal cyto-and myeloarchitecture organization of the human cortex. *NeuroImage, 60*(2), 1006-1014.

Connor, J., Menzies, S., St Martin, S., & Mufson, E. (1990). Cellular distribution of transferrin, ferritin, and iron in normal and aged human brains. *Journal of Neuroscience Research, 27*(4), 595-611.

Craelius, W., Migdal, M. W., Luessenhop, C. P., Sugar, A., & Mihalakis, I. (1982). Iron deposits surrounding multiple sclerosis plaques. *Archives of Pathology & Laboratory Medicine, 106*(8), 397-399.

Cronin, M. J., Wang, N., Decker, K. S., Wei, H., Zhu, W. Z., & Liu, C. (2017). Exploring the origins of TE-dependent QSM measurements in healthy tissue and cerebral microbleeds. *NeuroImage,* doi:S1053-8119(17)30063-0 [pii]

Cross, A., & Naismith, R. (2014). Established and novel disease-modifying treatments in multiple sclerosis. *Journal of Internal Medicine, 275*(4), 350-363.

de Rochefort, L., Liu, T., Kressler, B., Liu, J., Spincemaille, P., Lebon, V., . . . Wang, Y. (2010). Quantitative susceptibility map reconstruction from MR phase data using bayesian regularization: Validation and application to brain imaging. *Magnetic Resonance in Medicine : Official Journal of the Society of Magnetic Resonance in Medicine / Society of Magnetic Resonance in Medicine, 63*(1), 194-206. doi:10.1002/mrm.22187; 10.1002/mrm.22187

Deistung, A., Schafer, A., Schweser, F., Biedermann, U., Turner, R., & Reichenbach, J. R. (2013). Toward in vivo histology: A comparison of quantitative susceptibility mapping (QSM) with magnitude-, phase-, and R2*-imaging at ultra-high magnetic field strength. *NeuroImage, 65*, 299-314. doi:10.1016/j.neuroimage.2012.09.055; 10.1016/j.neuroimage.2012.09.055

DeLong, M., & Wichmann, T. (2009). Update on models of basal ganglia function and dysfunction. *Parkinsonism & Related Disorders, 15 Suppl 3*, S237-40. doi:10.1016/S1353-8020(09)70822-3 [doi]

Denk, C., Torres, E. H., MacKay, A., & Rauscher, A. (2011). The influence of white matter fibre orientation on MR signal phase and decay. *NMR in Biomedicine, 24*(3), 246-252.

Derache, N., Marie, R. M., Constans, J. M., & Defer, G. L. (2006). Reduced thalamic and cerebellar rest metabolism in relapsing-remitting multiple sclerosis, a positron emission tomography study: Correlations to lesion load. *Journal of the Neurological Sciences, 245*(1-2), 103-109. doi:S0022-510X(06)00111-0 [pii]

Dexter, D. T., Carayon, A., Javoy-Agid, F., Agid, Y., Wells, F. R., Daniel, S. E., . . . Marsden, C. D. (1991). Alterations in the levels of iron, ferritin and other trace metals in parkinson's disease and other neurodegenerative diseases affecting the basal ganglia. *Brain : A Journal of Neurology, 114 (Pt 4)*(Pt 4), 1953-1975.

Dexter, D. T., Wells, F. R., Lees, A. J., Agid, F., Agid, Y., Jenner, P., & Marsden, C. D. (1989). Increased nigral iron content and alterations in other metal ions occurring in brain in parkinson's disease. *Journal of Neurochemistry, 52*(6), 1830-1836.

Disanto, G., M Morahan, J., & V Ramagopalan, S. (2012). Multiple sclerosis: Risk factors and their interactions. *CNS & Neurological Disorders-Drug Targets (Formerly Current Drug Targets-CNS & Neurological Disorders), 11*(5), 545-555.

Du, Y. P., Jin, Z., Hu, Y., & Tanabe, J. (2009). Multi-echo acquisition of MR angiography and venography of the brain at 3 tesla. *Journal of Magnetic Resonance Imaging : JMRI, 30*(2), 449-454. doi:10.1002/jmri.21833 [doi]

Duyn, J. H., & Schenck, J. (2017). Contributions to magnetic susceptibility of brain tissue. *NMR in Biomedicine, 30*(4)

Eissa, A., Lebel, R. M., Korzan, J. R., Zavodni, A. E., Warren, K. G., Catz, I., . . . Wilman, A. H. (2009). Detecting lesions in multiple sclerosis at 4.7 tesla using phase susceptibility-weighting and T2-weighting. *Journal of Magnetic Resonance Imaging : JMRI, 30*(4), 737-742. doi:10.1002/jmri.21926 [doi]

Elkady, A. M., Cobzas, D., Sun, H., Blevins, G., & Wilman, A. H. (2018). Discriminative analysis of regional evolution of iron and myelin/calcium in deep gray matter of multiple sclerosis and healthy subjects. *Journal of Magnetic Resonance Imaging,*

Elkady, A. M., Cobzas, D., Sun, H., Blevins, G., & Wilman, A. H. (2017). Progressive iron accumulation across multiple sclerosis phenotypes revealed by sparse classification of deep gray matter. *Journal of Magnetic Resonance Imaging : JMRI,* doi:10.1002/jmri.25682 [doi]

Elkady, A. M., Sun, H., Walsh, A. J., Blevins, G., Zhuozi, D., & Wilman, A. H. (2015). (2015). Quantitative susceptibility mapping of lesions in multiple sclerosis. Paper presented at the *ISMRM 23rd Annual Meeting & Exhibition,* Toronto, Canada. 281.

Elkady, A. M., Sun, H., & Wilman, A. H. (2016). Importance of extended spatial coverage for quantitative susceptibility mapping of iron-rich deep gray matter. *Magnetic Resonance Imaging, 34*(4), 574-578. doi:10.1016/j.mri.2015.12.032 [doi]

Eshaghi, A., Bodini, B., Ridgway, G. R., García-Lorenzo, D., Tozer, D. J., Sahraian, M. A., . . . Ciccarelli, O. (2014). Temporal and spatial evolution of grey matter atrophy in primary progressive multiple sclerosis. *NeuroImage, 86*, 257-264.

Eshaghi, A., Prados, F., Brownlee, W., Altmann, D. R., Tur, C., Cardoso, M. J., . . . De Stefano, N. (2017). Deep grey matter volume loss drives disability worsening in multiple sclerosis. *Annals of Neurology,*

Eskreis-Winkler, S., Deh, K., Gupta, A., Liu, T., Wisnieff, C., Jin, M., . . . Spincemaille, P. (2014). Multiple sclerosis lesion geometry in quantitative susceptibility mapping (QSM) and phase imaging. *Journal of Magnetic Resonance Imaging : JMRI,* doi:10.1002/jmri.24745 [doi]

Fang, J., Bao, L., Li, X., van Zijl, P. C., & Chen, Z. (2017). Background field removal using a region adaptive kernel for quantitative susceptibility mapping of human brain. *Journal of Magnetic Resonance, 281*, 130-140.

Fernández-Seara, M., & Wehrli, F. (2000). Postprocessing technique to correct for background gradients in image-based R* 2 measurements. *Magnetic Resonance in Medicine, 44*(3), 358-366.

Fernandez-Ruiz, J., Lastres-Becker, I., Cabranes, A., Gonzalez, S., & Ramos, J. (2002). Endocannabinoids and basal ganglia functionality. *Prostaglandins, Leukotrienes and Essential Fatty Acids (PLEFA), 66*(2-3), 257-267.

Filippi, M., Preziosa, P., Copetti, M., Riccitelli, G., Horsfield, M. A., Martinelli, V., . . . Rocca, M. A. (2013). Gray matter damage predicts the accumulation of disability 13 years later in MS. *Neurology, 81*(20), 1759-1767. doi:10.1212/01.wnl.0000435551.90824.d0 [doi]

Foster, M., Zivadinov, R., Weinstock-Guttman, B., Tamano-Blanco, M., Badgett, D., Carl, E., & Ramanathan, M. (2012). Associations of moderate alcohol consumption with clinical and MRI measures in multiple sclerosis. *Journal of Neuroimmunology, 243*(1-2), 61-68. doi:10.1016/j.jneuroim.2011.12.007 [doi]

Fukunaga, M., Li, T. Q., van Gelderen, P., de Zwart, J. A., Shmueli, K., Yao, B., . . . Duyn, J. H. (2010). Layer-specific variation of iron content in cerebral cortex as a source of MRI contrast. *Proceedings of the National Academy of Sciences of the United States of America, 107*(8), 3834-3839. doi:10.1073/pnas.0911177107 [doi]

Ge, Y., Jensen, J. H., Lu, H., Helpern, J. A., Miles, L., Inglese, M., . . . Grossman, R. I. (2007). Quantitative assessment of iron accumulation in the deep gray matter of multiple sclerosis by magnetic field correlation imaging. *AJNR.American Journal of Neuroradiology, 28*(9), 1639-1644. doi:ajnr.A0646 [pii]

Gelfand, J. M. (2014). Multiple sclerosis: Diagnosis, differential diagnosis, and clinical presentation. *Handbook of clinical neurology* (pp. 269-290) Elsevier.

Geurts, J. J., & Barkhof, F. (2008). Grey matter pathology in multiple sclerosis. *The Lancet Neurology, 7*(9), 841-851.

Gilbert, G., Savard, G., Bard, C., & Beaudoin, G. (2012). Quantitative comparison between a multiecho sequence and a single-echo sequence for susceptibility-weighted phase imaging. *Magnetic Resonance Imaging, 30*(5), 722-730. doi:10.1016/j.mri.2012.02.008 [doi]

Grosenick, L., Klingenberg, B., Katovich, K., Knutson, B., & Taylor, J. E. (2013). Interpretable whole-brain prediction analysis with GraphNet. *NeuroImage, 72*, 304-321. doi:10.1016/j.neuroimage.2012.12.062 [doi]

Haacke, E. M., & Reichenbach, J. R. (2014). *Susceptibility weighted imaging in MRI: Basic concepts and clinical applications* John Wiley & Sons.

Haacke, E. M., Liu, S., Buch, S., Zheng, W., Wu, D., & Ye, Y. (2015). Quantitative susceptibility mapping: Current status and future directions. *Magnetic Resonance Imaging, 33*(1), 1-25. doi:10.1016/j.mri.2014.09.004 [doi]

Haacke, E. M., Makki, M., Ge, Y., Maheshwari, M., Sehgal, V., Hu, J., Grossman, R. I. (2009). Characterizing iron deposition in multiple sclerosis lesions using susceptibility weighted imaging. *Journal of Magnetic Resonance Imaging : JMRI, 29*(3), 537-544. doi:10.1002/jmri.21676; 10.1002/jmri.21676

Haacke, E. M., Xu, Y., Cheng, Y. C., & Reichenbach, J. R. (2004). Susceptibility weighted imaging (SWI). *Magnetic Resonance in Medicine : Official Journal of the Society of Magnetic Resonance in Medicine / Society of Magnetic Resonance in Medicine, 52*(3), 612-618. doi:10.1002/mrm.20198

Hagemeier, J., Ferdinand, S., Dwyer, M., Polak, P., Bergsland, N., Weinstock-Guttman, B., & Zivadinov, R. (2016). Quantitative susceptibility mapping study of deep gray matter iron at 3T in large cohort of multiple sclerosis patients (P4. 162). *Neurology, 86*(16 Supplement), P4. 162.

Hagemeier, J., Zivadinov, R., Dwyer, M. G., Polak, P., Bergsland, N., Weinstock-Guttman, B., . . . Schweser, F. (2017). Changes of deep gray matter magnetic susceptibility over 2years in multiple sclerosis and healthy control brain. *NeuroImage: Clinical,*

Hagemeier, J., Tong, O., Dwyer, M. G., Schweser, F., Ramanathan, M., & Zivadinov, R. (2015). Effects of diet on brain iron levels among healthy individuals: An MRI pilot study. *Neurobiology of Aging, 36*(4), 1678-1685. doi:S0197-4580(15)00043-3 [pii]

Hagemeier, J., Weinstock-Guttman, B., Bergsland, N., Heininen-Brown, M., Carl, E., Kennedy, C., . . . Zivadinov, R. (2012). Iron deposition on SWI-filtered phase in the subcortical deep gray matter of patients with clinically isolated syndrome may precede structure-specific atrophy. *AJNR.American Journal of Neuroradiology, 33*(8), 1596-1601. doi:10.3174/ajnr.A3030 [doi]

Hagemeier, J., Weinstock-Guttman, B., Heininen-Brown, M., Poloni, G. U., Bergsland, N., Schirda, C., . . . Zivadinov, R. (2013). Gray matter SWI-filtered phase and atrophy are linked to disability in MS. *Frontiers in Bioscience (Elite Edition), 5*, 525-532.

Hagemeier, J., Yeh, E. A., Brown, M. H., Bergsland, N., Dwyer, M. G., Carl, E., . . . Zivadinov, R. (2013). Iron content of the pulvinar nucleus of the thalamus is increased in adolescent multiple sclerosis. *Multiple Sclerosis (Houndmills, Basingstoke, England), 19*(5), 567-576. doi:10.1177/1352458512459289 [doi]

Haider, L., Simeonidou, C., Steinberger, G., Hametner, S., Grigoriadis, N., Deretzi, G., . . . Frischer, J. M. (2014). Multiple sclerosis deep grey matter: The relation between demyelination, neurodegeneration, inflammation and iron. *Journal of Neurology, Neurosurgery, and Psychiatry, 85*(12), 1386-1395. doi:10.1136/jnnp-2014-307712; 10.1136/jnnp-2014-307712

Hallgren, B., & Sourander, P. (1958). The effect of age on the non-haemin iron in the human brain. *Journal of Neurochemistry, 3*(1), 41-51.

Halterman, J. S., Kaczorowski, J. M., Aligne, C. A., Auinger, P., & Szilagyi, P. G. (2001). Iron deficiency and cognitive achievement among school-aged children and adolescents in the united states. *Pediatrics, 107*(6), 1381-1386.

Hametner, S., Wimmer, I., Haider, L., Pfeifenbring, S., Bruck, W., & Lassmann, H. (2013). Iron and neurodegeneration in the multiple sclerosis brain. *Annals of Neurology, 74*(6), 848-861. doi:10.1002/ana.23974 [doi]

Hammond, K. E., Metcalf, M., Carvajal, L., Okuda, D. T., Srinivasan, R., Vigneron, D., . . . Pelletier, D. (2008). Quantitative in vivo magnetic resonance imaging of multiple sclerosis at 7 tesla with sensitivity to iron. *Annals of Neurology, 64*(6), 707-713. doi:10.1002/ana.21582 [doi]

Haraguchi, T., Terada, S., Ishizu, H., Yokota, O., Yoshida, H., Takeda, N., . . . Uchitomi, Y. (2011). Coexistence of TDP-43 and tau pathology in neurodegeneration with brain iron accumulation type 1 (NBIA-1, formerly hallervorden-spatz syndrome). *Neuropathology : Official Journal of the Japanese Society of Neuropathology, 31*(5), 531-539. doi:10.1111/j.1440-1789.2010.01186.x; 10.1111/j.1440-1789.2010.01186.x

He, X., & Yablonskiy, D. A. (2009). Biophysical mechanisms of phase contrast in gradient echo MRI. *Proceedings of the National Academy of Sciences of the United States of America, 106*(32), 13558-13563. doi:10.1073/pnas.0904899106; 10.1073/pnas.0904899106

Heckemann, R. A., Hajnal, J. V., Aljabar, P., Rueckert, D., & Hammers, A. (2006). Automatic anatomical brain MRI segmentation combining label propagation and decision fusion. *NeuroImage, 33*(1), 115-126.

Hernández-Torres, E., Wiggermann, V., Li, D. K., Machan, L., Sadovnick, A. D., Hametner, S., & Rauscher, A.Iron loss occurs in the deep gray matter of multiple sclerosis patients. Paper presented at the *Proc. Intl Soc. Mag. Reson Med.* Hawaii. *, 25* 790.

Hildebrand, C., Remahl, S., Persson, H., & Bjartmar, C. (1993). Myelinated nerve fibres in the CNS. *Progress in Neurobiology, 40*(3), 319-384.

Holst, B., Siemonsen, S., Finsterbusch, J., Bester, M., Schippling, S., Martin, R., & Fiehler, J. (2009). T2' imaging indicates decreased tissue metabolism in frontal white matter of MS patients. *Multiple Sclerosis (Houndmills, Basingstoke, England), 15*(6), 701-707. doi:10.1177/1352458509103713 [doi]

Inglese, M., Park, S., Johnson, G., Babb, J. S., Miles, L., Jaggi, H., . . . Grossman, R. I. (2007). Deep gray matter perfusion in multiple sclerosis: Dynamic susceptibility contrast perfusion magnetic resonance imaging at 3 T. *Archives of Neurology, 64*(2), 196-202.

Jackson, J. D. (1999). Classical electrodynamics john wiley & sons. *Inc., New York,*

Jahanshad, N., Kohannim, O., Hibar, D. P., Stein, J. L., McMahon, K. L., de Zubicaray, G. I., . . . Thompson, P. M. (2012). Brain structure in healthy adults is related to serum transferrin and the H63D polymorphism in the HFE gene. *Proceedings of the National Academy of Sciences of the United States of America, 109*(14), E851-9. doi:10.1073/pnas.1105543109 [doi]

Jenkinson, M. (2003). Fast, automated, N-dimensional phase-unwrapping algorithm. *Magnetic Resonance in Medicine : Official Journal of the Society of Magnetic Resonance in Medicine / Society of Magnetic Resonance in Medicine, 49*(1), 193-197. doi:10.1002/mrm.10354

Kandel, B. M., Wolk, D. A., Gee, J. C., & Avants, B. (2013). Predicting cognitive data from medical images using sparse linear regression. *Information Processing in Medical Imaging : Proceedings of the ...Conference, 23*, 86-97.

Kermode, A. G., Tofts, P. S., Thompson, A. J., MacManus, D. G., Rudge, P., Kendall, B. E., . . . McDonald, W. I. (1990). Heterogeneity of blood-brain barrier changes in multiple sclerosis: An MRI study with gadolinium-DTPA enhancement. *Neurology, 40*(2), 229-235.

Khalil, M., Enzinger, C., Langkammer, C., Tscherner, M., Wallner-Blazek, M., Jehna, M., . . . Fazekas, F. (2009). Quantitative assessment of brain iron by R(2)* relaxometry in patients with clinically isolated syndrome and relapsing-remitting multiple sclerosis. *Multiple Sclerosis (Houndmills, Basingstoke, England), 15*(9), 1048-1054. doi:10.1177/1352458509106609 [doi]

Khalil, M., Langkammer, C., Pichler, A., Pinter, D., Gattringer, T., Bachmaier, G., . . . Fazekas, F. (2015). Dynamics of brain iron levels in multiple sclerosis: A longitudinal 3T MRI study. *Neurology, 84*(24), 2396-2402. doi:10.1212/WNL.0000000000001679 [doi]

Khalil, M., Langkammer, C., Ropele, S., Petrovic, K., Wallner-Blazek, M., Loitfelder, M., . . . Fazekas, F. (2011). Determinants of brain iron in multiple sclerosis: A quantitative 3T MRI study. *Neurology, 77*(18), 1691-1697. doi:10.1212/WNL.0b013e318236ef0e [doi]

Khalil, M., Teunissen, C., & Langkammer, C. (2011). Iron and neurodegeneration in multiple sclerosis. *Multiple Sclerosis International, 2011*, 606807. doi:10.1155/2011/606807; 10.1155/2011/606807

Koller, W. C., Cochran, J. W., & Klawans, H. L. (1979). Calcification of the basal ganglia: Computerized tomography and clinical correlation. *Neurology, 29*(3), 328-333.

Lancaster, J. L., Andrews, T., Hardies, L. J., Dodd, S., & Fox, P. T. (2003). Three-pool model of white matter. *Journal of Magnetic Resonance Imaging, 17*(1), 1-10.

Langkammer, C., Bredies, K., Poser, B. A., Barth, M., Reishofer, G., Fan, A. P., . . . Ropele, S. (2015). Fast quantitative susceptibility mapping using 3D EPI and total generalized variation. *NeuroImage, 111*, 622-630. doi:10.1016/j.neuroimage.2015.02.041 [doi]

Langkammer, C., Krebs, N., Goessler, W., Scheurer, E., Yen, K., Fazekas, F., & Ropele, S. (2012). Susceptibility induced gray-white matter MRI contrast in the human brain. *NeuroImage, 59*(2), 1413-1419. doi:10.1016/j.neuroimage.2011.08.045 [doi]

Langkammer, C., Liu, T., Khalil, M., Enzinger, C., Jehna, M., Fuchs, S., . . . Ropele, S. (2013). Quantitative susceptibility mapping in multiple sclerosis. *Radiology, 267*(2), 551-559. doi:10.1148/radiol.12120707 [doi]

Langkammer, C., Schweser, F., Krebs, N., Deistung, A., Goessler, W., Scheurer, E., . . . Reichenbach, J. R. (2012). Quantitative susceptibility mapping (QSM) as a means to measure brain iron? A post mortem validation study. *NeuroImage, 62*(3), 1593-1599. doi:10.1016/j.neuroimage.2012.05.049; 10.1016/j.neuroimage.2012.05.049

Laule, C., Vavasour, I. M., Leung, E., Li, D. K., Kozlowski, P., Traboulsee, A. L., . . . Moore, G. R. (2011). Pathological basis of diffusely abnormal white matter: Insights from magnetic resonance imaging and histology. *Multiple Sclerosis (Houndmills, Basingstoke, England), 17*(2), 144-150. doi:10.1177/1352458510384008; 10.1177/1352458510384008

Lebel, R. M., Eissa, A., Seres, P., Blevins, G., & Wilman, A. H. (2012). Quantitative high-field imaging of sub-cortical gray matter in multiple sclerosis. *Multiple Sclerosis (Houndmills, Basingstoke, England), 18*(4), 433-441. doi:10.1177/1352458511428464 [doi]

Lebel, R. M., & Wilman, A. H. (2010). Transverse relaxometry with stimulated echo compensation. *Magnetic Resonance in Medicine : Official Journal of the Society of Magnetic Resonance in Medicine / Society of Magnetic Resonance in Medicine, 64*(4), 1005-1014. doi:10.1002/mrm.22487 [doi]

Lee, J., Nam, Y., Choi, J. Y., Kim, E. Y., Oh, S., & Kim, D. (2017). Mechanisms of T2* anisotropy and gradient echo myelin water imaging. *NMR in Biomedicine, 30*(4)

Lee, J., van Gelderen, P., Kuo, L., Merkle, H., Silva, A. C., & Duyn, J. H. (2011). T2*-based fiber orientation mapping. *NeuroImage, 57*(1), 225-234.

Lee, J., Shmueli, K., Fukunaga, M., van Gelderen, P., Merkle, H., Silva, A. C., & Duyn, J. H. (2010). Sensitivity of MRI resonance frequency to the orientation of brain tissue microstructure. *Proceedings of the National Academy of Sciences of the United States of America, 107*(11), 5130-5135. doi:10.1073/pnas.0910222107 [doi]

LeVine, S. M. (1997). Iron deposits in multiple sclerosis and alzheimer's disease brains. *Brain Research, 760*(1-2), 298-303.

LeVine, S. M., & Chakrabarty, A. (2004). The role of iron in the pathogenesis of experimental allergic encephalomyelitis and multiple sclerosis. *Annals of the New York Academy of Sciences, 1012*, 252-266.

Li, L., & Leigh, J. S. (2001). *High-Precision Mapping of the Magnetic Field Utilizing the Harmonic Function Mean Value Property,*

Li, X., Liu, H., Harrison, D., Jones, C., Og, J., Calabresi, P., & Zijl, P. (2014). (2014). Magnetic susceptibility contrast variations in multiple sclerosis (MS) lesions observed at 7T. Paper presented at the *Proceedings of the 22nd Joint Annual Meeting of ISMRM-ESMRB,* Milan, Italy. abstract 0895.

Lim, I. A. L., Faria, A. V., Li, X., Hsu, J. T., Airan, R. D., Mori, S., & van Zijl, P. C. (2013). Human brain atlas for automated region of interest selection in quantitative susceptibility mapping: Application to determine iron content in deep gray matter structures. *NeuroImage, 82*, 449-469.

Liu, C. (2010). Susceptibility tensor imaging. *Magnetic Resonance in Medicine, 63*(6), 1471-1477.

Liu, C., Li, W., Tong, K. A., Yeom, K. W., & Kuzminski, S. (2015). Susceptibility-weighted imaging and quantitative susceptibility mapping in the brain. *Journal of Magnetic Resonance Imaging, 42*(1), 23-41.

Liu, T., Spincemaille, P., De Rochefort, L., Kressler, B., & Wang, Y. (2009). Calculation of susceptibility through multiple orientation sampling (COSMOS): A method for conditioning the inverse problem from measured magnetic field map to susceptibility source image in MRI. *Magnetic Resonance in Medicine, 61*(1), 196-204.

Liu, C., Li, W., Johnson, G. A., & Wu, B. (2011). High-field (9.4 T) MRI of brain dysmyelination by quantitative mapping of magnetic susceptibility. *NeuroImage, 56*(3), 930-938. doi:10.1016/j.neuroimage.2011.02.024 [doi]

Liu, J., Liu, T., de Rochefort, L., Ledoux, J., Khalidov, I., Chen, W., . . . Wang, Y. (2012). Morphology enabled dipole inversion for quantitative susceptibility mapping using structural consistency between the magnitude image and the susceptibility map. *NeuroImage, 59*(3), 2560-2568. doi:10.1016/j.neuroimage.2011.08.082 [doi]

Liu, T., Eskreis-Winkler, S., Schweitzer, A. D., Chen, W., Kaplitt, M. G., Tsiouris, A. J., & Wang, Y. (2013). Improved subthalamic nucleus depiction with quantitative susceptibility mapping. *Radiology, 269*(1), 216-223. doi:10.1148/radiol.13121991 [doi]

Lobel, U., Schweser, F., Nickel, M., Deistung, A., Grosse, R., Hagel, C., . . . Sedlacik, J. (2014). Brain iron quantification by MRI in mitochondrial membrane protein-associated neurodegeneration under iron-chelating therapy. *Annals of Clinical and Translational Neurology, 1*(12), 1041-1046. doi:10.1002/acn3.116; 10.1002/acn3.116

Loma, I., & Heyman, R. (2011). Multiple sclerosis: Pathogenesis and treatment. *Current Neuropharmacology, 9*(3), 409-416.

Lonsdale, K. (1939). Diamagnetic anisotropy of organic molecules. *Proc.R.Soc.Lond.A, 171*(947), 541-568.

Lounila, J., Ala-Korpela, M., Jokisaari, J., Savolainen, M., & Kesäniemi, Y. (1994). Effects of orientational order and particle size on the NMR line positions of lipoproteins. *Physical Review Letters, 72*(25), 4049.

Lublin, F. D., & Reingold, S. C. (1996). Defining the clinical course of multiple sclerosis: Results of an international survey. national multiple sclerosis society (USA) advisory committee on clinical trials of new agents in multiple sclerosis. *Neurology, 46*(4), 907-911.

Lublin, F. D., Reingold, S. C., Cohen, J. A., Cutter, G. R., Sorensen, P. S., Thompson, A. J., . . . Polman, C. H. (2014). Defining the clinical course of multiple sclerosis: The 2013 revisions. *Neurology, 83*(3), 278-286. doi:10.1212/WNL.0000000000000560 [doi]

MacKay, A., Whittall, K., Adler, J., Li, D., Paty, D., & Graeb, D. (1994). In vivo visualization of myelin water in brain by magnetic resonance. *Magnetic Resonance in Medicine : Official Journal of the Society of Magnetic Resonance in Medicine / Society of Magnetic Resonance in Medicine, 31*(6), 673-677.

Marques, J., & Bowtell, R. (2005). Application of a fourier-based method for rapid calculation of field inhomogeneity due to spatial variation of magnetic susceptibility. *Concepts in Magnetic Resonance Part B: Magnetic Resonance Engineering, 25*(1), 65-78.

Mehta, V., Pei, W., Yang, G., Li, S., Swamy, E., Boster, A., . . . Pitt, D. (2013). Iron is a sensitive biomarker for inflammation in multiple sclerosis lesions. *PloS One, 8*(3), e57573. doi:10.1371/journal.pone.0057573; 10.1371/journal.pone.0057573

Meiboom, S., & Gill, D. (1958). Modified spin-echo method for measuring nuclear relaxation times. *Review of Scientific Instruments, 29*(8), 688-691.

Minagar, A., Toledo, E. G., Alexander, J. S., & Kelley, R. E. (2004). Pathogenesis of brain and spinal cord atrophy in multiple sclerosis. *Journal of Neuroimaging, 14*(s3)

Montagne, A., Toga, A. W., & Zlokovic, B. V. (2016). Blood-brain barrier permeability and gadolinium: Benefits and potential pitfalls in research. *JAMA Neurology, 73*(1), 13-14.

Morris, C., Candy, J., Oakley, A., Bloxham, C., & Edwardson, J. (1992). Histochemical distribution of non-haem iron in the human brain. *Cells Tissues Organs, 144*(3), 235-257.

Muller, R. N., Gillis, P., Moiny, F., & Roch, A. (1991). Transverse relaxivity of particulate MRI contrast media: From theories to experiments. *Magnetic Resonance in Medicine, 22*(2), 178-182.

Nam, Y., Lee, J., Hwang, D., & Kim, D. (2015). Improved estimation of myelin water fraction using complex model fitting. *NeuroImage, 116*, 214-221.

Neema, M., Arora, A., Healy, B. C., Guss, Z. D., Brass, S. D., Duan, Y., . . . Khoury, S. J. (2009). Deep gray matter involvement on brain MRI scans is associated with clinical progression in multiple sclerosis. *Journal of Neuroimaging, 19*(1), 3-8.

Newberg, A., Alavi, A., & Reivich, M. (2002). Determination of regional cerebral function with FDG-PET imaging in neuropsychiatric disorders. *Seminars in Nuclear Medicine, 32*(1), 13-34. doi:S0001-2998(02)80037-X [pii]

Norton, W. T., & Cammer, W. (1984). Isolation and characterization of myelin. *Myelin* (pp. 147-195) Springer.

O'Gorman, C., Lucas, R., & Taylor, B. (2012). Environmental risk factors for multiple sclerosis: A review with a focus on molecular mechanisms. *International Journal of Molecular Sciences, 13*(9), 11718-11752.

Ontaneda, D., & Fox, R. J. (2017). Imaging as an outcome measure in multiple sclerosis. *Neurotherapeutics, 14*(1), 24-34.

Patrikios, P., Stadelmann, C., Kutzelnigg, A., Rauschka, H., Schmidbauer, M., Laursen, H., . . . Lassmann, H. (2006). Remyelination is extensive in a subset of multiple sclerosis patients. *Brain, 129*(12), 3165-3172.

Paul T. Callaghan. (1993). *Principles of nuclear magnetic resonance microscopy* Oxford University Press on Demand.

Paulesu, E., Perani, D., Fazio, F., Comi, G., Pozzilli, C., Martinelli, V., . . . Passafiume, D. (1996). Functional basis of memory impairment in multiple sclerosis: A [18F] FDG PET study. *NeuroImage, 4*(2), 87-96.

Peters, A. (2007). The effects of normal aging on nerve fibers and neuroglia in the central nervous system. In D. R. Riddle (Ed.), *Brain aging: Models, methods, and mechanisms* (). Boca Raton (FL): Taylor & Francis Group, LLC. doi:NBK3873 [bookaccession]

Pierpaoli, C. (2010). Quantitative brain MRI. *Topics in Magnetic Resonance Imaging : TMRI, 21*(2), 63. doi:10.1097/RMR.0b013e31821e56f8 [doi]

Pirpamer, L., Hofer, E., Gesierich, B., De Guio, F., Freudenberger, P., Seiler, S., . . . Schmidt, R. (2016). Determinants of iron accumulation in the normal aging brain. *Neurobiology of Aging, 43*, 149-155. doi:10.1016/j.neurobiolaging.2016.04.002 [doi]

Polman, C. H., Reingold, S. C., Banwell, B., Clanet, M., Cohen, J. A., Filippi, M., . . . Kappos, L. (2011a). Diagnostic criteria for multiple sclerosis: 2010 revisions to the McDonald criteria. *Annals of Neurology, 69*(2), 292-302.

Polman, C. H., Reingold, S. C., Banwell, B., Clanet, M., Cohen, J. A., Filippi, M., . . . Wolinsky, J. S. (2011b). Diagnostic criteria for multiple sclerosis: 2010 revisions to the McDonald criteria. *Annals of Neurology, 69*(2), 292-302. doi:10.1002/ana.22366 [doi]

Pott, F., Gingele, S., Clarner, T., Dang, J., Baumgartner, W., Beyer, C., & Kipp, M. (2009). Cuprizone effect on myelination, astrogliosis and microglia attraction in the mouse basal ganglia. *Brain Research, 1305*, 137-149.

Poynton, C., Lupo, J., Hess, C., & Nelson, S. (2014). (2014). Quantitative susceptibility mapping of huntington's disease at 7 tesla. Paper presented at the *Proceedings of the 22nd Joint Annual Meeting of ISMRM-ESMRB,* Milan, Italy. abstract 0895.

Pruessmann, K. P., Weiger, M., Scheidegger, M. B., & Boesiger, P. (1999). SENSE: Sensitivity encoding for fast MRI. *Magnetic Resonance in Medicine, 42*(5), 952-962. doi:10.1002/(SICI)1522-2594(199911)42:53.0.CO;2-S [pii]

Quinn, M. P., Gati, J. S., Klassen, M. L., Lee, D. H., Kremenchutzky, M., & Menon, R. S. (2014). Increased deep gray matter iron is present in clinically isolated syndromes. *Multiple Sclerosis and Related Disorders, 3*(2), 194-202. doi:10.1016/j.msard.2013.06.017 [doi]

Reichenbach, J. R., Barth, M., Haacke, E. M., Klarhofer, M., Kaiser, W. A., & Moser, E. (2000). High-resolution MR venography at 3.0 tesla. *Journal of Computer Assisted Tomography, 24*(6), 949-957.

Robinson, S., Grabner, G., Witoszynskyj, S., & Trattnig, S. (2011). Combining phase images from multi-channel RF coils using 3D phase offset maps derived from a dual-echo scan. *Magnetic Resonance in Medicine, 65*(6), 1638-1648.

Rocca, M. A., Mesaros, S., Pagani, E., Sormani, M. P., Comi, G., & Filippi, M. (2010). Thalamic damage and long-term progression of disability in multiple sclerosis. *Radiology, 257*(2), 463-469.

Roelcke, U., Kappos, L., Lechner-Scott, J., Brunnschweiler, H., Huber, S., Ammann, W., . . . Leenders, K. L. (1997). Reduced glucose metabolism in the frontal cortex and basal ganglia of multiple sclerosis patients with fatigue: A 18F-fluorodeoxyglucose positron emission tomography study. *Neurology, 48*(6), 1566-1571.

Rogosnitzky, M., & Branch, S. (2016). Gadolinium-based contrast agent toxicity: A review of known and proposed mechanisms. *Biometals, 29*(3), 365-376.

Ropele, S., Kilsdonk, I. D., Wattjes, M. P., Langkammer, C., de Graaf, W. L., Frederiksen, J. L., . . . Fazekas, F. (2014). Determinants of iron accumulation in deep grey matter of multiple sclerosis patients. *Multiple Sclerosis (Houndmills, Basingstoke, England), 20*(13), 1692-1698. doi:10.1177/1352458514531085 [doi]

Roxburgh, R. H., Seaman, S. R., Masterman, T., Hensiek, A. E., Sawcer, S. J., Vukusic, S., . . . Compston, D. A. (2005). Multiple sclerosis severity score: Using disability and disease duration to rate disease severity. *Neurology, 64*(7), 1144-1151. doi:64/7/1144 [pii]

Rudko, D. A., Solovey, I., Gati, J. S., Kremenchutzky, M., & Menon, R. S. (2014). Multiple sclerosis: Improved identification of disease-relevant changes in gray and white matter by using susceptibility-based MR imaging. *Radiology, 272*(3), 851-864. doi:10.1148/radiol.14132475; 10.1148/radiol.14132475

Salat, D. H. (2011). The declining infrastructure of the aging brain. *Brain Connectivity, 1*(4), 279-293.

Salat, D. H., Lee, S. Y., Yu, P., Setty, B., Rosas, H. D., & Grant, P. E. (2009). DTI in development and aging. *Diffusion MRI* (pp. 205-236) Elsevier.

Salomir, R., de Senneville, B. D., & Moonen, C. T. (2003). A fast calculation method for magnetic field inhomogeneity due to an arbitrary distribution of bulk susceptibility. *Concepts in Magnetic Resonance Part B: Magnetic Resonance Engineering, 19*(1), 26-34.

Sati, P., Silva, A. C., van Gelderen, P., Gaitan, M. I., Wohler, J. E., Jacobson, S., . . . Reich, D. S. (2012). In vivo quantification of T2 anisotropy in white matter fibers in marmoset monkeys. *NeuroImage, 59*(2), 979-985.

Sati, P., van Gelderen, P., Silva, A. C., Reich, D. S., Merkle, H., De Zwart, J. A., & Duyn, J. H. (2013). Micro-compartment specific T2 relaxation in the brain. *NeuroImage, 77*, 268-278.

Schafer, A., Wharton, S., Gowland, P., & Bowtell, R. (2009). Using magnetic field simulation to study susceptibility-related phase contrast in gradient echo MRI. *NeuroImage, 48*(1), 126-137. doi:10.1016/j.neuroimage.2009.05.093 [doi]

Schenck, J. F. (1992). Health and physiological effects of human exposure to Whole-Body Four-Tesla magnetic fields during MRI. *Annals of the New York Academy of Sciences, 649*(1), 285-301.

Schlemm, L., Chien, C., Bellmann-Strobl, J., Dörr, J., Wuerfel, J., Brandt, A. U., . . . Scheel, M. (2017). Gadopentetate but not gadobutrol accumulates in the dentate nucleus of multiple sclerosis patients. *Multiple Sclerosis Journal, 23*(7), 963-972.

Schmidt, M., Fung, G., & Rosales, R. (2007). (2007). Fast optimization methods for l1 regularization: A comparative study and two new approaches. Paper presented at the *European Conference on Machine Learning,* 286-297.

Schmidt, M., Fung, G., & Rosales, R. (2009). Optimization methods for l1-regularization. *University of British Columbia, Technical Report TR-2009, 19*

Schoonheim, M. M., Hulst, H. E., Brandt, R. B., Strik, M., Wink, A. M., Uitdehaag, B. M., . . . Geurts, J. J. (2015). Thalamus structure and function determine severity of cognitive impairment in multiple sclerosis. *Neurology, 84*(8), 776-783. doi:10.1212/WNL.0000000000001285 [doi]

Schweser, F., Deistung, A., Lehr, B. W., & Reichenbach, J. R. (2011). Quantitative imaging of intrinsic magnetic tissue properties using MRI signal phase: An approach to in vivo brain iron metabolism? *NeuroImage, 54*(4), 2789-2807.

Schweser, F., Martins, Ana Luiza Raffaini Duarte, Hagemeier, J., Lin, F., Hanspach, J., Weinstock-Guttman, B., . . . Zivadinov, R. (2017). Mapping of thalamic magnetic susceptibility in multiple sclerosis indicates decreasing iron with disease duration: A proposed mechanistic relationship between inflammation and oligodendrocyte vitality. *NeuroImage,*

Schweser, F., Deistung, A., Sommer, K., & Reichenbach, J. R. (2012). (2012). Disentangling contributions from iron and myelin architecture to brain tissue magnetic susceptibility by using quantitative susceptibility mapping (QSM). Paper presented at the *Proc. Int. Soc. Magn. Reson. Med. , , 20* 409.

Schweser, F., Hagemeier, J., Polak, P., Dwyer, M., Bergsland, N., Bertolino, N., . . . Zivadinov, R. (2016). (2016). Quantitative susceptibility mapping (QSM) in patients with clinically isolated syndrome (CIS) and multiple sclerosis (MS) - a large cohort study. Paper presented at the *Proceedings of the 22nd Joint Annual Meeting of ISMRM-ESMRB,* Milan, Italy. *, 24* abstract 0242.

Schweser, F., Sommer, K., Deistung, A., & Reichenbach, J. R. (2012). Quantitative susceptibility mapping for investigating subtle susceptibility variations in the human brain. *NeuroImage, 62*(3), 2083-2100. doi:10.1016/j.neuroimage.2012.05.067 [doi]

Shinohara, R. T., Goldsmith, J., Mateen, F. J., Crainiceanu, C., & Reich, D. S. (2012). Predicting breakdown of the blood-brain barrier in multiple sclerosis without contrast agents. *AJNR.American Journal of Neuroradiology, 33*(8), 1586-1590. doi:10.3174/ajnr.A2997 [doi]

Shmueli, K., de Zwart, J. A., van Gelderen, P., Li, T. Q., Dodd, S. J., & Duyn, J. H. (2009). Magnetic susceptibility mapping of brain tissue in vivo using MRI phase data. *Magnetic Resonance in Medicine, 62*(6), 1510-1522. doi:10.1002/mrm.22135 [doi]

Smith, S. M. (2002). Fast robust automated brain extraction. *Human Brain Mapping, 17*(3), 143-155. doi:10.1002/hbm.10062

Sood, S., Urriola, J., Reutens, D., O'Brien, K., Bollmann, S., Barth, M., & Vegh, V. (2016). Echo time-dependent quantitative susceptibility mapping contains information on tissue properties. *Magnetic Resonance in Medicine,* doi:10.1002/mrm.26281 [doi]

Sormani, M. P., & Bruzzi, P. (2013). MRI lesions as a surrogate for relapses in multiple sclerosis: A meta-analysis of randomised trials. *The Lancet Neurology, 12*(7), 669-676.

Stadelmann, C., Wegner, C., & Brück, W. (2011). Inflammation, demyelination, and degeneration—recent insights from MS pathology. *Biochimica Et Biophysica Acta (BBA)-Molecular Basis of Disease, 1812*(2), 275-282.

Steenwijk, M. D., Daams, M., Pouwels, P. J., Balk, L. J., Tewarie, P. K., Killestein, J., . . . Vrenken, H. (2014). What explains gray matter atrophy in long-standing multiple sclerosis? *Radiology, 272*(3), 832-842.

Stephenson, E., Nathoo, N., Mahjoub, Y., Dunn, J. F., & Yong, V. W. (2014). Iron in multiple sclerosis: Roles in neurodegeneration and repair. *Nature Reviews.Neurology, 10*(8), 459-468. doi:10.1038/nrneurol.2014.118; 10.1038/nrneurol.2014.118

Stuber, C., Morawski, M., Schafer, A., Labadie, C., Wahnert, M., Leuze, C., . . . Turner, R. (2014). Myelin and iron concentration in the human brain: A quantitative study of MRI contrast. *NeuroImage, 93 Pt 1*, 95-106. doi:10.1016/j.neuroimage.2014.02.026 [doi]

Sukstanskii, A. L., & Yablonskiy, D. A. (2014). On the role of neuronal magnetic susceptibility and structure symmetry on gradient echo MR signal formation. *Magnetic Resonance in Medicine : Official Journal of the Society of Magnetic Resonance in Medicine / Society of Magnetic Resonance in Medicine, 71*(1), 345-353. doi:10.1002/mrm.24629; 10.1002/mrm.24629

Sun, H., MacDonald, M. E., & Pike, G. B. (2015). (2015). Phase correction of a bipolar gradient-echo acquisition for quantitative susceptibility mapping. Paper presented at the *24th ISMRM Scientific Meeting, Singapore City, Republic of Singapore,* 2987.

Sun, H. (2015). *Quantitative Susceptibility Mapping in Human Brain: Methods Development and Applications,*

Sun, H., Walsh, A. J., Lebel, R. M., Blevins, G., Catz, I., Lu, J. Q., . . . Wilman, A. H. (2015). Validation of quantitative susceptibility mapping with perls' iron staining for subcortical gray matter. *NeuroImage, 105*, 486-492. doi:10.1016/j.neuroimage.2014.11.010; 10.1016/j.neuroimage.2014.11.010

Sun, H., & Wilman, A. H. (2013). Background field removal using spherical mean value filtering and tikhonov regularization. *Magnetic Resonance in Medicine : Official Journal of the Society of Magnetic Resonance in Medicine / Society of Magnetic Resonance in Medicine, 71*(3), 1151-7. doi:10.1002/mrm.24765 [doi]

Sun, H., & Wilman, A. H. (2014). Quantitative susceptibility mapping using single-shot echo-planar imaging. *Magnetic Resonance in Medicine : Official Journal of the Society of Magnetic Resonance in Medicine / Society of Magnetic Resonance in Medicine,* doi:10.1002/mrm.25316 [doi]

Suzuki, Y., Matsuzawa, H., Kwee, I. L., & Nakada, T. (2003). Absolute eigenvalue diffusion tensor analysis for human brain maturation. *NMR in Biomedicine, 16*(5), 257-260.

Tao, C., Simpson, S.,Jr, van der Mei, I., Blizzard, L., Havrdova, E., Horakova, D., . . . MSBase Study Group. (2016). Higher latitude is significantly associated with an earlier age of disease onset in multiple sclerosis. *Journal of Neurology, Neurosurgery, and Psychiatry, 87*(12), 1343-1349. doi:10.1136/jnnp-2016-314013 [doi]

Thompson, A. J., Banwell, B. L., Barkhof, F., Carroll, W. M., Coetzee, T., Comi, G., . . . Freedman, M. S. (2017). Diagnosis of multiple sclerosis: 2017 revisions of the McDonald criteria. *The Lancet Neurology,*

Tjoa, C. W., Benedict, R. H., Weinstock-Guttman, B., Fabiano, A. J., & Bakshi, R. (2005). MRI T2 hypointensity of the dentate nucleus is related to ambulatory impairment in multiple

sclerosis. *Journal of the Neurological Sciences, 234*(1-2), 17-24. doi:S0022-510X(05)00055-9 [pii]

Topfer, R., Schweser, F., Deistung, A., Reichenbach, J. R., & Wilman, A. H. (2015). SHARP edges: Recovering cortical phase contrast through harmonic extension. *Magnetic Resonance in Medicine, 73*(2), 851-856. doi:10.1002/mrm.25148 [doi]

Tóth, E., Szabó, N., Csete, G., Király, A., Faragó, P., Spisák, T., . . . Kincses, Z. T. (2017). Gray matter atrophy is primarily related to demyelination of lesions in multiple sclerosis: A diffusion tensor imaging MRI study. *Frontiers in Neuroanatomy, 11*, 23.

Trapp, B. D., & Nave, K. (2008). Multiple sclerosis: An immune or neurodegenerative disorder? *Annu.Rev.Neurosci., 31*, 247-269.

Trojano, M., Lucchese, G., Graziano, G., Taylor, B. V., Simpson Jr, S., Lepore, V., . . . Grammond, P. (2012). Geographical variations in sex ratio trends over time in multiple sclerosis. *PLOS One, 7*(10), e48078.

Tustison, N. J., Avants, B. B., Cook, P. A., Zheng, Y., Egan, A., Yushkevich, P. A., & Gee, J. C. (2010). N4ITK: Improved N3 bias correction. *IEEE Transactions on Medical Imaging, 29*(6), 1310-1320.

Uddin, M. N., Lebel, R. M., Seres, P., Blevins, G., & Wilman, A. H. (2015). Spin echo transverse relaxation and atrophy in multiple sclerosis deep gray matter: A two-year longitudinal study. *Multiple Sclerosis (Houndmills, Basingstoke, England),* doi:1352458515614091 [pii]

Van Gelderen, P., De Zwart, J. A., Lee, J., Sati, P., Reich, D. S., & Duyn, J. H. (2012). Nonexponential T2* decay in white matter. *Magnetic Resonance in Medicine, 67*(1), 110-117.

Vargas, W. S., Monohan, E., Pandya, S., Raj, A., Vartanian, T., Nguyen, T. D., . . . Gauthier, S. A. (2015). Measuring longitudinal myelin water fraction in new multiple sclerosis lesions. *NeuroImage: Clinical, 9*, 369-375.

Vercellino, M., Masera, S., Lorenzatti, M., Condello, C., Merola, A., Mattioda, A., . . . Cavalla, P. (2009). Demyelination, inflammation, and neurodegeneration in multiple sclerosis deep gray matter. *Journal of Neuropathology and Experimental Neurology, 68*(5), 489-502. doi:10.1097/NEN.0b013e3181a19a5a [doi]

Walsh, A. J., Blevins, G., Lebel, R. M., Seres, P., Emery, D. J., & Wilman, A. H. (2014). Longitudinal MR imaging of iron in multiple sclerosis: An imaging marker of disease. *Radiology, 270*(1), 186-196. doi:10.1148/radiol.13130474 [doi]

Walsh, A. J., Lebel, R. M., Eissa, A., Blevins, G., Catz, I., Lu, J. Q., . . . Wilman, A. H. (2013). Multiple sclerosis: Validation of MR imaging for quantification and detection of iron. *Radiology, 267*(2), 531-542. doi:10.1148/radiol.12120863 [doi]

Walsh, A. J., & Wilman, A. H. (2011). Susceptibility phase imaging with comparison to R2 mapping of iron-rich deep grey matter. *NeuroImage, 57*(2), 452-461. doi:10.1016/j.neuroimage.2011.04.017 [doi]

Wang, H., Suh, J. W., Das, S. R., Pluta, J. B., Craige, C., & Yushkevich, P. A. (2013). Multi-atlas segmentation with joint label fusion. *IEEE Transactions on Pattern Analysis and Machine Intelligence, 35*(3), 611-623.

Wang, Y. (2013). *Quantitative susceptibility mapping: Magnetic resonance imaging of tissue magnetism* CreateSpace.

Ware, A. L., Juranek, J., Williams, V. J., Cirino, P. T., Dennis, M., & Fletcher, J. M. (2014). Anatomical and diffusion MRI of deep gray matter in pediatric spina bifida. *NeuroImage: Clinical, 5*, 120-127.

Wharton, S., & Bowtell, R. (2015). Effects of white matter microstructure on phase and susceptibility maps. *Magnetic Resonance in Medicine, 73*(3), 1258-1269.

Wharton, S., & Bowtell, R. (2012). Fiber orientation-dependent white matter contrast in gradient echo MRI. *Proceedings of the National Academy of Sciences of the United States of America, 109*(45), 18559-18564. doi:10.1073/pnas.1211075109 [doi]

Wiggermann, V., Hernandez Torres, E., Vavasour, I. M., Moore, G. R., Laule, C., MacKay, A. L., . . . Rauscher, A. (2013). Magnetic resonance frequency shifts during acute MS lesion formation. *Neurology, 81*(3), 211-218. doi:10.1212/WNL.0b013e31829bfd63 [doi]

Wiggermann, V., Lee, L. E., Hernandez Torres, E., Li, D. K., MacKay, A. L., Vavasour, I. M., . . . Rauscher, A. (2014). (2014). Iron accumulation is a rare feature in multiple sclerosis lesions. Paper presented at the *Proceedings of the 22nd Joint Annual Meeting of ISMRM-ESMRB,* Milano. abstract 0894. Retrieved from http://cds.ismrm.org/protected/14MPresentations/abstracts/0894.pdf

Wiggins, C., Gudmundsdottir, V., Le Bihan, D., Lebon, V., & Chaumeil, M. (2008). (2008). Orientation dependence of white matter T2* contrast at 7 T: A direct demonstration. Paper presented at the *Proceedings of the 16th Annual Meeting of ISMRM, Toronto, Canada,* 237.

Williams, R., Buchheit, C. L., Berman, N. E., & LeVine, S. M. (2012). Pathogenic implications of iron accumulation in multiple sclerosis. *Journal of Neurochemistry, 120*(1), 7-25. doi:10.1111/j.1471-4159.2011.07536.x [doi]

Wisnieff, C., Ramanan, S., Olesik, J., Gauthier, S., Wang, Y., & Pitt, D. (2014). Quantitative susceptibility mapping (QSM) of white matter multiple sclerosis lesions: Interpreting positive susceptibility and the presence of iron. *Magnetic Resonance in Medicine : Official Journal of the Society of Magnetic Resonance in Medicine / Society of Magnetic Resonance in Medicine,* doi:10.1002/mrm.25420 [doi]

Worsley, K., Andermann, M., Koulis, T., MacDonald, D., & Evans, A. (1999). Detecting changes in nonisotropic images. *Human Brain Mapping, 8*(2-3), 98-101.

Wu, B., Li, W., Avram, A. V., Gho, S. M., & Liu, C. (2012). Fast and tissue-optimized mapping of magnetic susceptibility and T2* with multi-echo and multi-shot spirals. *NeuroImage, 59*(1), 297-305. doi:10.1016/j.neuroimage.2011.07.019; 10.1016/j.neuroimage.2011.07.019

Wu, B., Li, W., Guidon, A., & Liu, C. (2012). Whole brain susceptibility mapping using compressed sensing. *Magnetic Resonance in Medicine : Official Journal of the Society of Magnetic Resonance in Medicine / Society of Magnetic Resonance in Medicine, 67*(1), 137-147. doi:10.1002/mrm.23000 [doi]

Wu, G. F., & Alvarez, E. (2011). The immunopathophysiology of multiple sclerosis. *Neurologic Clinics, 29*(2), 257-278. doi:10.1016/j.ncl.2010.12.009 [doi]

Xu, X., Wang, Q., & Zhang, M. (2008). Age, gender, and hemispheric differences in iron deposition in the human brain: An in vivo MRI study. *NeuroImage, 40*(1), 35-42. doi:10.1016/j.neuroimage.2007.11.017 [doi]

Yablonskiy, D. A., & Haacke, E. M. (1994). Theory of NMR signal behavior in magnetically inhomogeneous tissues: The static dephasing regime. *Magnetic Resonance in Medicine, 32*(6), 749-763.

Yablonskiy, D. A., Luo, J., Sukstanskii, A. L., Iyer, A., & Cross, A. H. (2012). Biophysical mechanisms of MRI signal frequency contrast in multiple sclerosis. *Proceedings of the*

National Academy of Sciences of the United States of America, 109(35), 14212-14217. doi:10.1073/pnas.1206037109; 10.1073/pnas.1206037109

Yamada, N., Imakita, S., Sakuma, T., & Takamiya, M. (1996). Intracranial calcification on gradient-echo phase image: Depiction of diamagnetic susceptibility. *Radiology, 198*(1), 171-178. doi:10.1148/radiology.198.1.8539373 [doi]

Yao, B., Bagnato, F., Matsuura, E., Merkle, H., van Gelderen, P., Cantor, F. K., & Duyn, J. H. (2012). Chronic multiple sclerosis lesions: Characterization with high-field-strength MR imaging. *Radiology, 262*(1), 206-215. doi:10.1148/radiol.11110601 [doi]

Yao, B., Ikonomidou, V. N., Cantor, F. K., Ohayon, J. M., Duyn, J., & Bagnato, F. (2015). Heterogeneity of multiple sclerosis white matter lesions detected with T2*-weighted imaging at 7.0 tesla. *Journal of Neuroimaging : Official Journal of the American Society of Neuroimaging,* doi:10.1111/jon.12193; 10.1111/jon.12193

Yao, Y., Nguyen, T. D., Pandya, S., Zhang, Y., Hurtado Rua, S., Kovanlikaya, I., . . . Gauthier, S. A. (2018). Combining quantitative susceptibility mapping with automatic zero reference (QSM0) and myelin water fraction imaging to quantify iron-related myelin damage in chronic active MS lesions. *AJNR.American Journal of Neuroradiology, 39*(2), 303-310. doi:10.3174/ajnr.A5482 [doi]

Zhang, Y., Gauthier, S. A., Gupta, A., Chen, W., Comunale, J., Chiang, G. C., . . . Wang, Y. (2016). Quantitative susceptibility mapping and R2* measured changes during white matter lesion development in multiple sclerosis: Myelin breakdown, myelin debris degradation and removal, and iron accumulation. *AJNR.American Journal of Neuroradiology, 37*(9), 1629-1635. doi:10.3174/ajnr.A4825 [doi]

Zhang, Y., Zabad, R., Wei, X., Metz, L., Hill, M., & Mitchell, J. (2007). Deep grey matter "black T2" on 3 tesla magnetic resonance imaging correlates with disability in multiple sclerosis. *Multiple Sclerosis (Houndmills, Basingstoke, England), 13*(7), 880-883. doi:1352458507076411 [pii]

Zheng, W., Nichol, H., Liu, S., Cheng, Y. C., & Haacke, E. M. (2013). Measuring iron in the brain using quantitative susceptibility mapping and X-ray fluorescence imaging. *NeuroImage, 78*, 68-74. doi:10.1016/j.neuroimage.2013.04.022; 10.1016/j.neuroimage.2013.04.022

Zhou, D., Liu, T., Spincemaille, P., & Wang, Y. (2014). Background field removal by solving the laplacian boundary value problem. *NMR in Biomedicine, 27*(3), 312-319. doi:10.1002/nbm.3064 [doi]

Ziser, L., Meyer-Schell, N., Kurniawan, N. D., Sullivan, R., Reutens, D., Chen, M., & Vegh, V. (2017). Utility of gradient recalled echo magnetic resonance imaging for the study of myelination in cuprizone mice treated with fingolimod. *NMR in Biomedicine,* doi:10.1002/nbm.3877 [doi]

Zivadinov, R., Dwyer, M., Markovic-Plese, S., Hayward, B., Bergsland, N., Heininen-Brown, M., . . . Weinstock-Guttman, B. (2015). A pilot, longitudinal, 24-week study to evaluate the effect of interferon beta-1a subcutaneous on changes in susceptibility-weighted imaging-filtered phase assessment of lesions and subcortical deep-gray matter in relapsing–remitting multiple sclerosis. *Therapeutic Advances in Neurological Disorders, 8*(2), 59-70.

Zivadinov, R., Havrdová, E., Bergsland, N., Tyblova, M., Hagemeier, J., Seidl, Z., . . . Carl, E. (2013). Thalamic atrophy is associated with development of clinically definite multiple sclerosis. *Radiology, 268*(3), 831-841.

Zivadinov, R., Heininen-Brown, M., Schirda, C. V., Poloni, G. U., Bergsland, N., Magnano, C. R., . . . Dwyer, M. G. (2012). Abnormal subcortical deep-gray matter susceptibility-weighted imaging filtered phase measurements in patients with multiple sclerosis: A case-control study. *NeuroImage, 59*(1), 331-339. doi:10.1016/j.neuroimage.2011.07.045 [doi]

Zivadinov, R., Weinstock-Guttman, B., & Pirko, I. (2011). Iron deposition and inflammation in multiple sclerosis. which one comes first? *BMC Neuroscience, 12*, 60-2202-12-60. doi:10.1186/1471-2202-12-60; 10.1186/1471-2202-12-60